PLASMA NON-UNIFORMITY IN THE JET NEUTRAL BEAM INJECTION ION SOURCE - MEASUREMENT, SIMULATION AND DEVELOPMENT OF AN IMPROVED ION SOURCE.

A thesis for the degree of
PHILOSOPHIAE DOCTOR

Presented to
DUBLIN CITY UNIVERSITY

BY

DANIEL J. GODDEN BSc (Hons)
School of Physical Sciences
DUBLIN CITY UNIVERSITY

Joint Research Supervisors: Dr M B Hopkins
Dr D Ciric
External Examiner: Dr. R. Hemsworth

December 2000

I hereby certify that this material, which I submit for assessment on the programme of study leading to the award of PhD is entirely my own work and has not been taken from the work of others save and to the extent that such work has been cited and acknowledged within the text of my work.

Signed: D. Godlu *ID No.:* 96970014

Candidate

Date: 17/12/00

CONTENTS

5. PINI ION SOURCE DEVELOPMENT

Comparisons of experiments and theory with discussion

- Introduction
- Standard Supercusp
- Chequerboard
- Extended ion source
- Line Cusp
- Optimised Supercusp
- Summary and concluding remarks

6. QUANTIFICATION OF ION SOURCE PLASMA NON-UNIFORMITY

Describe three methods and illustrate on standard supercusp

- Beam divergence distribution
- 2D profiles
- Monte-Carlo

Compare and discuss results for supercusp, chequerboard, line-cusp, and optimised supercusp

7. COMPARATIVE ANALYSIS OF THE SC15S3 AND NSC_6 ION SOURCE MODELS

- Determine the difference in performance by comparing the modelled magnetic fields and Monte-Carlo model of the two source configurations

8. CONCLUSIONS

APPENDIX A

REFERENCES

Plasma non-uniformity in the JET Neutral Beam Injection ion source - measurement, simulation and development of an improved ion source.

ABSTRACT

For Neutral Beam Injection at JET an ion source is required with a high monatomic species yield It is now clear that the magnetic filter field arrangement used to enhance the monatomic species yield also produces non-uniformity in the ion source plasma density This property was known from Langmuir probe array measurements taken during development of the ion source Further experimental evidence is derived from the analysis of detailed spectroscopic and calorimetric measurements of extracted beams on the Neutral Beam Test Bed Non-uniformity of the ion source density results in reduced transmission of the extracted beam, with greater interception on beamline scraper elements The maximum power injected to the JET plasma from the Octant 4 Neutral Beam Injector is often limited by excessive beam interception on beamline scraper elements and not by the limits of the electrical power supplies A development programme was initiated to develop an ion source configuration to produce improved uniformity, without degrading the monatomic species yield This was approached in two ways -

1 Development of a Monte-Carlo model of the ion source
2 An experimental programme of source modification on the Neutral Beam Test Bed

The Monte-Carlo model was used to design and predict the performance of a new filter field arrangement It was anticipated that the new source configuration would give improved ion uniformity without significant degradation of the monatomic species yield When operated on the Test-Bed this ion source design showed a factor of 2 improvement in ion density uniformity, with the required monatomic species fraction for JET NBI Beams extracted from the new ion source have demonstrated improved beam transmission on the Test-Bed and a 33% reduction of beamline scraper power load on the Octant 4 NB Injector This is estimated to give a 5-8% increase in the neutral power injected into the JET plasma

1 - INTRODUCTION.

NEUTRAL INJECTION AS PLASMA HEATING FOR FUSION.

It has long been recognised m nuclear fusion research that some form of additional heating of magnetically confined plasmas is required Heating of fusion research plasmas was initially restricted to the ohmic heating produced by large currents induced in the plasma by using a toroidal plasma as the secondary winding of a transformer However, as the plasma resistivity decreases with mcreasmg plasma temperature, ohmic heating is restricted to a maximum practical electron temperature <5 keV Additional heating is therefore necessary to further raise the plasma temperature to levels where significant fusion reactions occur [1]

One scheme of providing this additional heating is to inject an energetic beam of neutral atoms across the confining magnetic field into the plasma Inside the plasma the neutral beam is quickly ionised and becomes trapped by the magnetic field The energetic particles then give up their energy to the rest of the plasma via collisions The energetic neutral beam is created by the neutralisation of an ion beam that has been accelerated to the required energy

The plasmas studied for nuclear fusion are those formed from the isotopes of hydrogen and it is ion beams formed from these isotopes that are, in general, used for neutral beam heatmg Two possibilities exist for the formation of accelerated hydrogen isotope ion beams, by using sources of either positive, or negative ions Positive hydrogen isotope ions are easily produced in abundance by ion source technologies that have existed for many years [2] In contrast the negative ion of hydrogen is only recently being produced m the required abundance by advances in ion source technology [3] The Negative Ion Neutral Beam injector installed on the JAERI JT60-U tokamak represents the current state of the art for this technology [4,5]

Table 1 1 gives a brief indication of the relative efficiencies of the state of the art neutral beam positive and negative ion sources, by comparing the ion yield and extracted ion density with the input power to the ion source

TABLE 1 1 Relative ion production efficiencies for the two most mature examples of ion production schemes for neutral beam heating in the Fusion community

Positive Ion Technology	**Negative Ion Technology**
JET	**JT60U**
60A $D^+/D_2^+/D_3^+$ at 130kW arc power	14 3A D^- at ~200kW arc power (aim 22A D^- at 300kW)
Ion density for extraction	Ion density for extraction
>200 mA cm^{-2}	8 5 mA cm^{-2} (13mA cm^{-2} target)

At the current time the production of positive ions is typically >5× more efficient than the production of negative ions, the efficiency being taken as the ion current generated per unit input power into the ion sources Also for a negative ion source an extraction area of typically 20× greater is required to produce a beam of similar current to a positive ion source The lower ion creation efficiency, combined with other technical difficulties of a negative ion source and beam extraction system (e g Caesium handling, electron co-extraction and negative ion stripping losses [3]) means that negative ion based neutral injection systems are only used when positive ion based injectors are no longer suitable This choice is driven fundamentally by the difference in the neutralisation efficiencies of positive and negative ions at the required energy of the neutral beam [6]

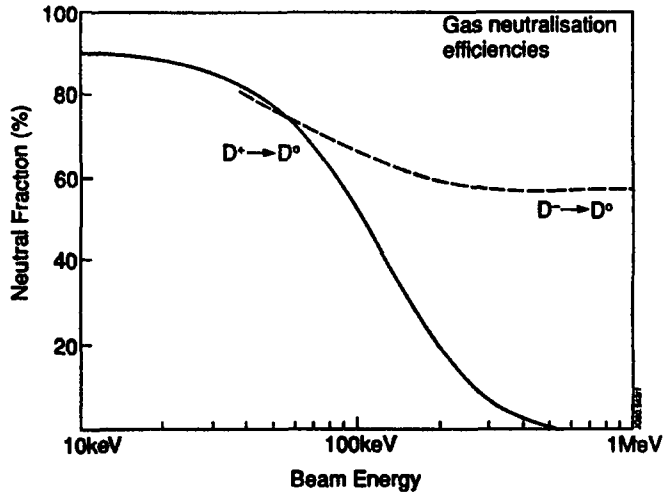

Figure 1 1 Neutral Fractions for D^+ and D^- ion beams emerging from

⇒ *Infinite gas target (D^+)*

⇒ *Energy dependent optimised gas target (D^-)*

Although the improved neutralisation efficiency of negative ions starts to become attractive at beam energies >50kV/nucleon, it is not until beam energies of >150kV/nucleon are required that the loss of positive ion neutralisation efficiency clearly outweighs the relative technical difficulties of negative ion production The choice of neutral energy in each fusion experiment is driven by the need for the energetic neutral to penetrate the foreseen plasma densities The attenuation of the neutral particles is dominated by ion impact ionisation, which can be approximated by

$$\lambda(m) = \frac{1}{18}\frac{1}{n(10^{19}m^{-3})}\frac{E(keV)}{A}$$

where

λ = the mean free path

n = the plasma density

E = the neutral energy

A = the neutral atomic number

For the JET project a value of E/A of 80 keV/nucleon was initially chosen by computation [7] with regard to the expected plasma density ($\sim 5\times10^{19}$ m^{-3}) and the JET plasma dimensions. In

this calculation the upper limit on beam energy is given the acceptable level of beam power that will "shine-through" the plasma to intercept the inner walls of the torus The lower limit is given by the lowest acceptable power deposition fraction close to the plasma axis

Figure 1 2(a) shows the cross sections for charge exchange and ionisation of deuterium beam neutrals by plasma ions and the effective electron impact ionisation cross sections for a Maxwellian plasma of varying electron temperature[6] From these cross sections the mean penetration distance of a deuterium neutral can be calculated through a given Maxwellian plasma, figure 1 2(b), in this case with density, ne, = 10^{20} m^{-3} at an electron temperature of 10keV For planned next step fusion devices where higher density plasmas ($\approx 10^{20}$ m^{-3}) are used in larger toroidal vessels, with equally increased plasma dimensions, then D^0 neutral energies of ≥1MeV are required to give the required neutral power deposition at the plasma core (marked by the distance a_{ITER} in figure 1 2(b))

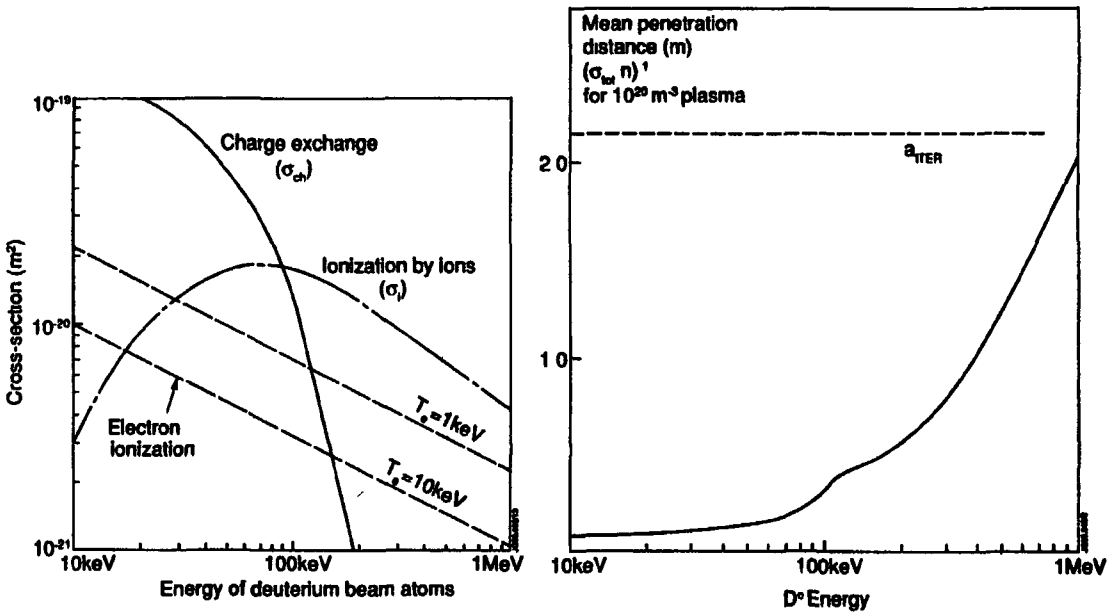

a) *b)*

Figure 1 2[6] a) Cross sections for charge exchange (σ_{ch}) and ionisation (σ_i) of deuterium beam neutrals by plasma ions and the effective cross section $<\sigma_{ei}V>$ for ionisation by electron impact in a Maxwellian plasma of varying temperatures (T_e) b) Mean penetration distance ($l = (\sigma_{tot} n_e)^{-1}$) for a deuterium neutral in a spatially constant plasma with density (ne) = 10^{20} m^{-3} and Maxwellian average electron temperature = 10keV a_{ITER} indicates the minor radius of the proposed ITER tokakmak

THE JET NEUTRAL BEAM INJECTORS

Originally (circa 1979) the JET NBI system was specified to provide ≈10MW of 80keV H^0 beams with future modification to 160keV D^0 beams[7] After 20 years of development the neutral beam heating at JET is now implemented in two separate injectors, each of which comprises eight beamlines integrated into a single vacuum enclosure, the Neutral Injector Box (NIB) A schematic layout of the JET torus and neutral injectors is shown in figure 1 3 The injectors are located to inject through ports on Octants 4 and 8 of the JET device so that half the beams have a radius of tangency of 1 85m (tangentiual beams – 2 passes thought the plama) and half have a radius of tangency of 1 31 (normal beams – single pass through the plasma)

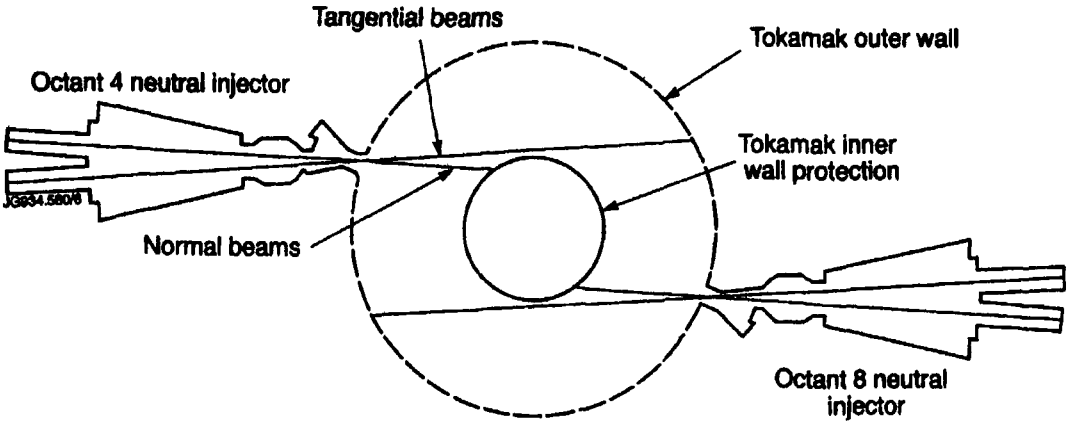

Figure 1 3 Plan view of the JET torus and NBI system

The Injectors are operated with a variety of beam species (H, D, T ^{3}He and ^{4}He) at voltages ≤80kV or ≤160kV depending on the configuration of the accelerator geometry and power supplies Typical positive ion beam powers available m each injector, at the time of writing, using the Hydrogen isotopes are shown in table 1 2

TABLE 1 2 Typical ion beam performance figures for the two JET Neutral injectors

Beam Species	**Octant 4 Injector**	**Octant 8 Injector**
H	8 × 70kV/60A	8 × 110kV/30A
D	8 × 80kV/55A	8 × 140kV/30A
T	8 × 80kV/45A	8 × 160kV/30A

Routinely the two injectors are operated in Deuterium to provide a combined total maximum neutral power of 20MW In the Tritium phases of the JET project using the 160keV injector to inject T^0, with D^0 beams from the 80keV injector [8], gave a record injected neutral power of 22 3MW This power injected into a 50 50 DT plasma mix gave JET the current record fusion power of 16 7MW [9]

The Neutral injectors are located on opposite sides of the JET tokamak and inject through ducts located on the centres of Octants 4 and 8 The two neutral injectors used are of essentially identical design, the power supply modules used are each capable of providing a current of 60A at 80kV Four pairs of these power supply modules are used in each injector each pair arranged either a) in parallel to produce, at maximum, 2 beams of 80keV at 60A each or b) in series to produce 2 beams of 160keV at 30A each Currently a common power supply arrangement is used in each injector, so the Octant 4 injector is configured to produce 8 beams of 60A at 80keV and the Octant 8 injector produces 8 beams of 30A at 160keV

The elevation and plan view section schematics, figures 1 5 and 1 6, show the axes of the beam injection into the JET plasma The more perpendicular ('normal') beams aim at the inner wall of the torus and the more tangential beams cross the plasma twice, aiming at the outer wall of the torus The plan view shows the location of the calorimeter panels that are opened to intercept the beams to allow short pulse operation of the Injector asynchronously with the JET plasma Alongside the calorimeter panels are the inam beam defining box scrapers used to protect downstream components from exposure to the neutral beam During the injector pulses the power intercepting the box scraper and the back surface of the closed calorimeter panels must be kept below prescribed limits to prevent damage to these components The sidewalls of the NIB are completely covered by the large LHe cryopumps, with LN_2 shields, to maintain the required NIB vacuum during the Injector pulses Each Injector can be isolated from the torus vacuum by a rotary valve placed between the NIB and Torus port The duct into the torus is protected by an arrangement of tiles and scraper elements

Figure 1.4 Picture of the JET Tokamak with one of the two Neutral Injectors in the right side foreground. The high voltage side of the NIB is visible, with the column of 4 'normal' bank PINIs. Beyond the PINIs is the SF6 tower used to carry the HV power transmission lines to the PINIs from the power supply wing.

Figure 1.4 shows a photograph of one of the Neutral Injectors in position with the JET Tokamak in the torus hall, an indication of the scale of the JET device and the neutral injector can be determined from the man standing on top of the torus transformer limbs. The overall design of the Neutral Injector is shown in the cut-away drawing of figure 1.4, with the major components labelled. The height of the Neutral Injector Box (NIB) vacuum vessel is approximately 7m. The 8 beams are provided from 8 Positive Ion Neutral Injector (PINI) modules that are mounted in two columns of four on the outside of the NIB. The schematic shows the location of the Central Support Column on which the deflection magnet are located. The magnets deflect the un-neutralised components of the beams extracted from the PINIs onto the Full and Fractional Energy Ion Dumps.

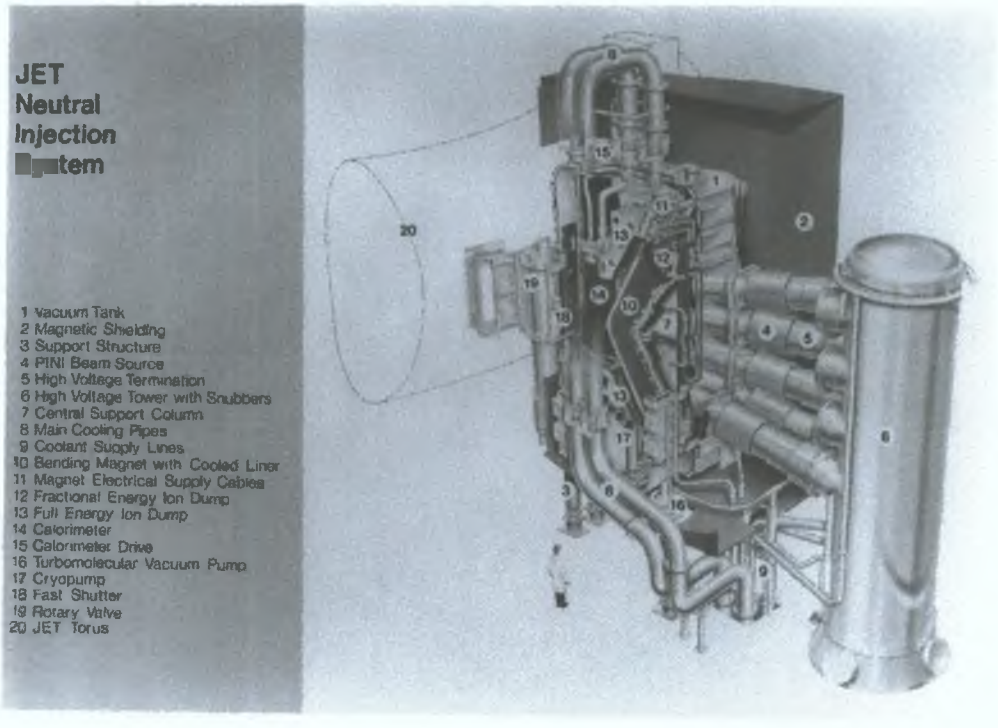

Figure 1.5 Cut-away drawing of the JET Neutral Beam Injector

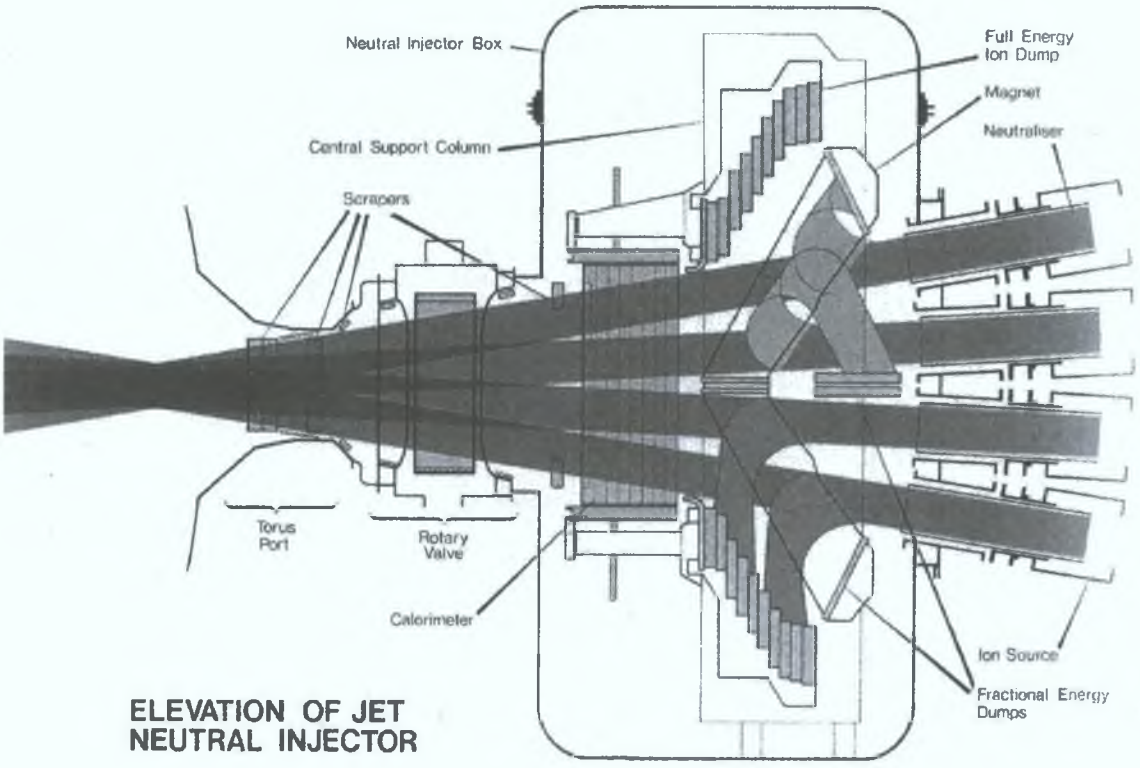

Figure 1.6 Elevation section schematic of the JET Neutral Beam Injector

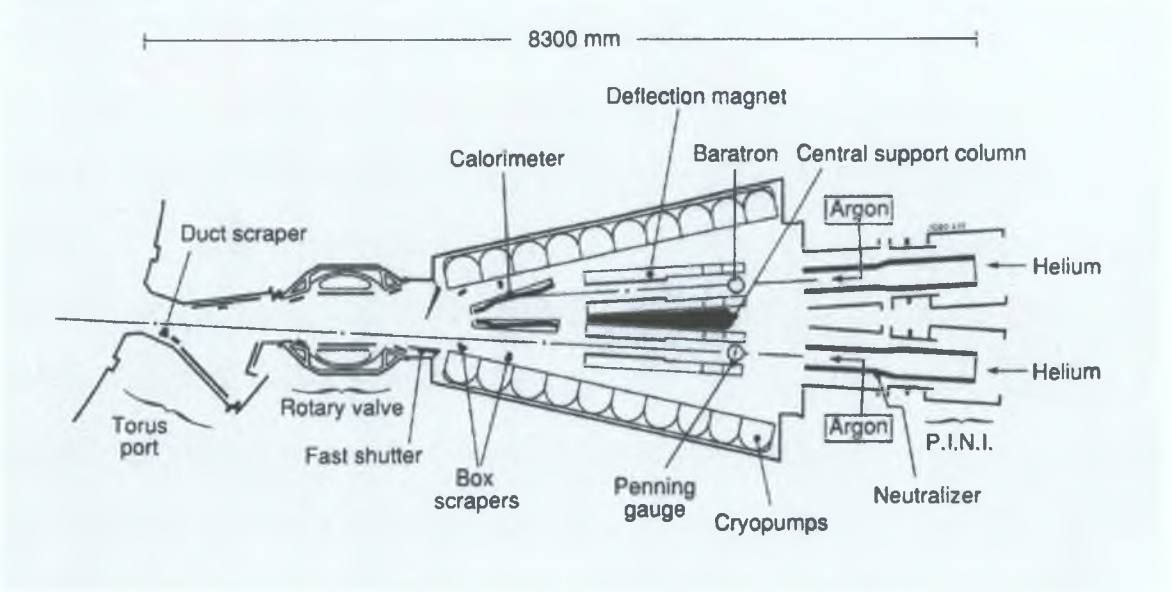

Figure 1.7 Plan section schematic of the JET Neutral Beam Injector

The Neutral Injector positioned at Octant 4 on the JET tokamak, with 8 PINIs operating at a nominal 80kV 60A (D_2) produces up to 1 6MW of neutral power per PINI This is significantly more than the 0 95MW of neutral power produced from the 140kV 30A (D_2) PINIs on Octant 8 Consequently the increased neutral power extracted per PINI on the Octant 4 injector leads to greater power interception on beamline scraper elements In particular the power falling on the Octant 4 injector box scraper and calorimeter back panel can often approach the designed safe limits at beam powers less than the power supply maximum rating In these circumstances it is necessary to reduce the extracted beam power, sometimes as low as 1 2MW per PINI to allow safe operation of the injector at long (10s) pulse lengths It is the power interception on these scraper elements that can limit the neutral power available for injection to the JET plasma from the Octant 4 injector, rather than the power supply limit

1.2.1 THE POSITIVE ION NEUTRAL INJECTOR (PINI)

The PINI module consists of the ion source, extraction aperture array and the first stage of the gas cell neutraliser A hinged support plate is used to attach the PINI to the outer wall of the NIB Upstream of the grounded support tube and flange the large porcelain insulator acts as the vacuum enclosure Inside the vacuum enclosure the accelerator grids are mounted onto precision-ground post insulators which determine the exact grid alignment and separation The ion source is mounted onto the high voltage side of the accelerator grids A transformer is mounted onto the back of the ion source to provide the AC heating currents for the 24 tungsten filament cathodes from a single 3 phase feed The power supply to drive the arc discharge is connected across arc load resistors, in series with the filaments, and the body of the ion source (anode) with a maximum rated output of 200V, 1300A The arc and filament power supplies are mounted on a High Voltage deck that is floated to the electrical potential of the source and first (plasma) grid

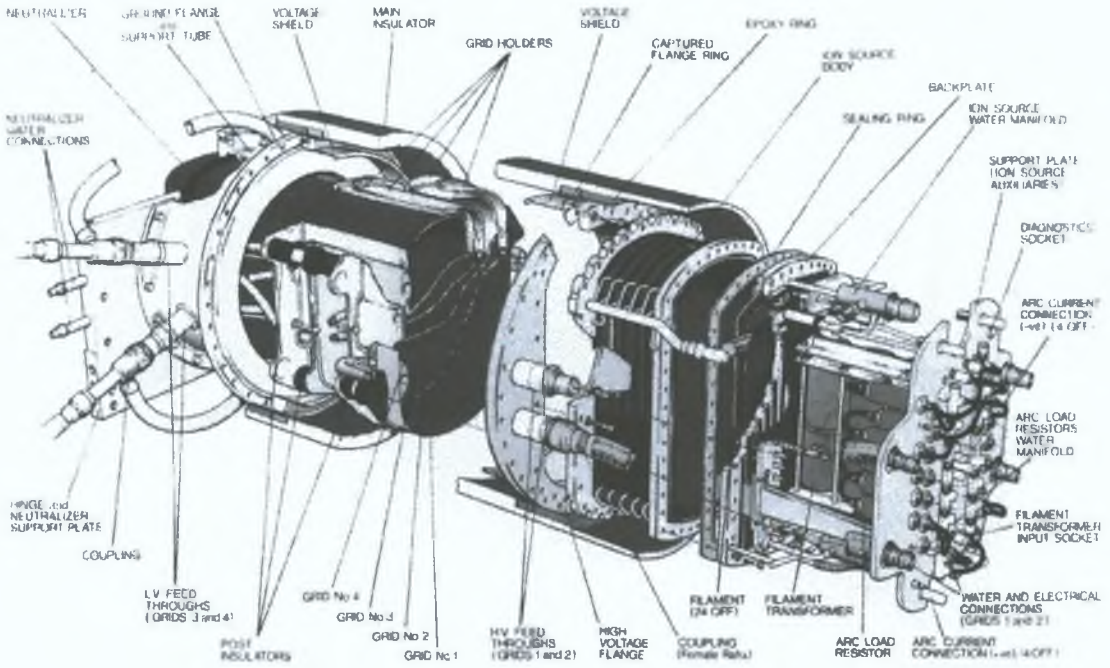

Figure 1.8 Exploded schematic of the Positive Ion Neutral Injector (PINI) module

The beam extraction aperture array produces 262 individual beamlets from a total area of $450\times180mm^2$. The extraction grids are configured in either a 3 (triode) or 4 (tetrode) grid system, both of which use a common grid naming system. In both cases the ground grid (grid 4) and the electron suppression grid (grid 3) are used with an identical design. The electron suppression grid is biased to a maximum of -3kV (typically –2.5 to –2.8kV) to prevent electrons produced downstream of the accelerator from being accelerated back into the ion source. For the 3 grid extraction system grid 2 is omitted, power to this grid in the 4 grid design is provided by a dividing resistor from the grid 1 voltage to ground. The typical value used of the dividing resistor produces a grid 2 potential of $10/99^{ths}$ of the grid 1 voltage. The grid 1 designs used in the 3 and 4 grid systems have some significant differences in the aperture diameters and aperture offsets.

Focussing the extracted beamlets into a single beam, which has a typical divergence <0 6deg, that can be transmitted through the duct at a distance of 8 3m downstream and into the JET plasma is achieved by two methods

A) Each grid is constructed in two halves, which are inclined towards each other in the vertical (y-axis) plane The inclination angle is 8 3mrad, which produces a focal length of 14m

B) Each grid half is drilled with a pattern of apertures that are offset between grid 1 and grid 3 Each beamlet is thus steered about the central beamlet of each grid half with focal lengths of 14m in the vertical (y-axis) plane and 10m in the horizontal (x-axis) plane

Beam focussing is illustrated in more detail in section 3 3 1 of Chapter 3

1.2.2 THE PINI ION SOURCE

Development of the plasma ion source for the JET PINI was undertaken independently at both Culham and Fontenay-aux-Roses (FAR) laboratories Eventually the magnetic multipole source developed at Culham was chosen for use by JET primarily because of its lower operating gas pressure than the FAR periplasmatron source The initial configuration of the multipole source, with a "chequerboard" magnet configuration, produced an unacceptably low proton fraction, which would give both a low power for the full energy neutral component and high power loading on the fractional energy beam dumps The species composition typically achieved by the ion source in this configuration is 68 27 5 (% H^+ H_2^+ H_3^+) where a proton yield of >85% is required for neutral beam injection at JET The term "chequerboard" originates from the arrangement of the permanent magnets on the outer walls of the ion source In this arrangement the adjacent magnets in each row have opposite polarity, as well as the magnets in the adjacent rows Viewed in the plane of each wall of the source the magnetic polarity thus appears to alternate, like the colours of a chequerboard ("checkerboard")

Following work in the USA it was discovered that the proton yield of the multipole ion source could be enhanced by using a magnetic filter field to divide the source into two regions [10,11,12] The filter field acts to isolate the plasma region into which the primary electrons are emitted from the region of plasma close to the extraction aperture array The filter field strength used is sufficiently weak to allow ions and the colhsional, slow (thermal), electrons to pass through The filter field is of sufficient strength, however, to reflect the fast primary electrons, keeping them away from the region close to the extraction aperture array In this way a plasma region with lower electron temperature is created close to the extraction grid In this region the conditions are suitable for an enhanced monatomic species fraction since -

1) No primaries are available for further ionisation of the neutral source gas

$$e_{>15\,4eV} + H_2 \rightarrow H_2^+ + 2e$$

2) The molecular ions are preferentially removed at low electron energies by dissociative attachment

$$e + H_2^+ \rightarrow H + H \text{ and } e + H_3^+ \rightarrow H_2 + H$$

The act of confining the primary electrons away from the magnetically unshielded first extraction grid also increases the ionisation efficiency of the source The confinement time of the primary electron is increased giving a greater probability that more of the primary energy will be used in the creation of ions

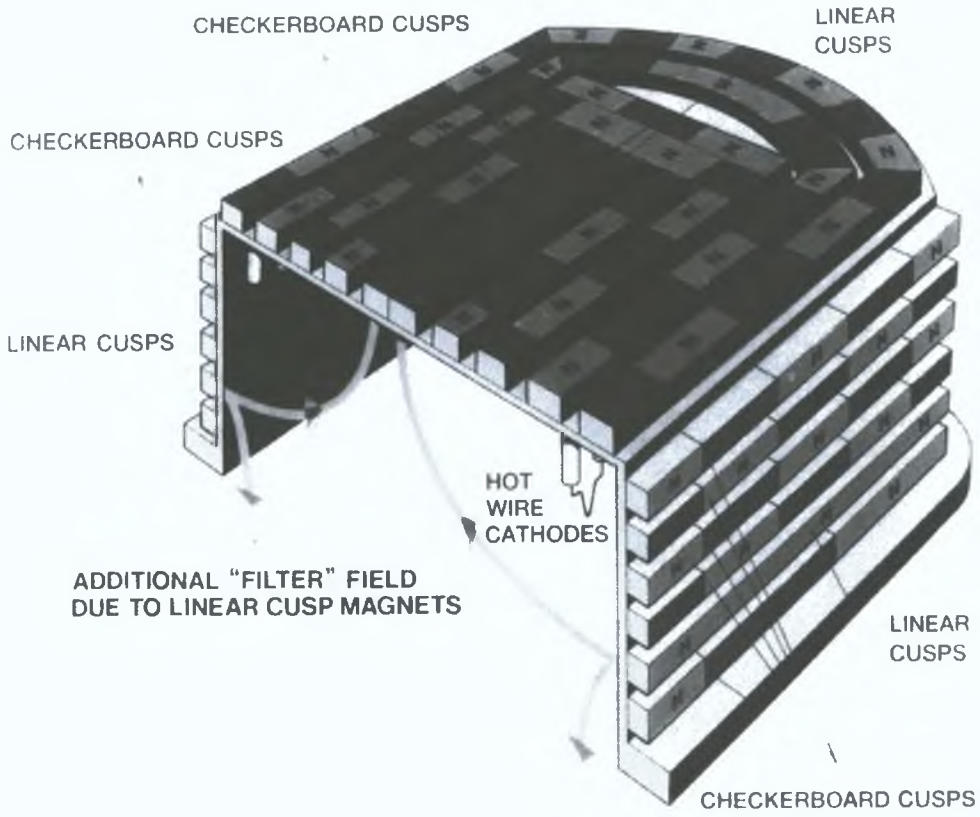

Figure 1.9 Schematic of the PINI ion source showing the chequerboard and filter field magnet pattern.

The filter field configuration used in the ion source chosen for the JET PINI is of the 'super-cusp', or 'tent', filter design [13] The filter field is created by having two lines of equal polarity magnets over the central region of the backplate and along the base of the source walls. The magnet polarities are aligned so that a long-range field links between the base of the source walls and the centre of the source backplate, resembling the structure of a ridge tent. The species yield achieved from the source with this filter configuration is typically 85:10:5 (% H^+:H_2^+:H_3^+), an acceptable proton yield for the JET neutral injectors.

At the time of development at Culham a multiple Langmuir probe array was used to assess the uniformity of the ion source [14]. At that time it was noted that the addition of the filter field to the ion source gave an increase in the non-uniformity of the plasma. After many magnet configurations were tested the pattern labelled SC15S3 was chosen as the best combination of species yield and non-uniformity, having a uniformity of ±8% over the extraction area.

The ion source has maximum internal dimensions of 580mm×300mm×210mm (length×width×depth), the endplates are a curved design with a radius of 290mm. The permanent magnets used are SmCo with a remnant induction of 0.85T, and are positioned 3mm away from the internal walls. The source body is manufactured from oxygen free, high-conductivity copper onto which the water-cooling pipes are brazed

1.3 The JET Neutral Beam Test Bed

The Neutral Beam Test Bed [15] is installed in the Hot Cell adjacent to the JET Torus Hall, with sufficient shielding to allow operation of Deuterium beams at 160keV. The Test Bed uses identical components to the Neutral Injectors wherever possible. The Test Bed is able to operate 2 PINIs simultaneously, although most frequently a single PINI is used. The NIB used for the Test Bed is attached to a target tank with a horizontal Y-shaped beam dump located 12m downstream of the PINI. At the exit from the NIB are the Box Scrapers, with an aperture of 150×700mm^2, similar to those present in the actual Injector boxes.

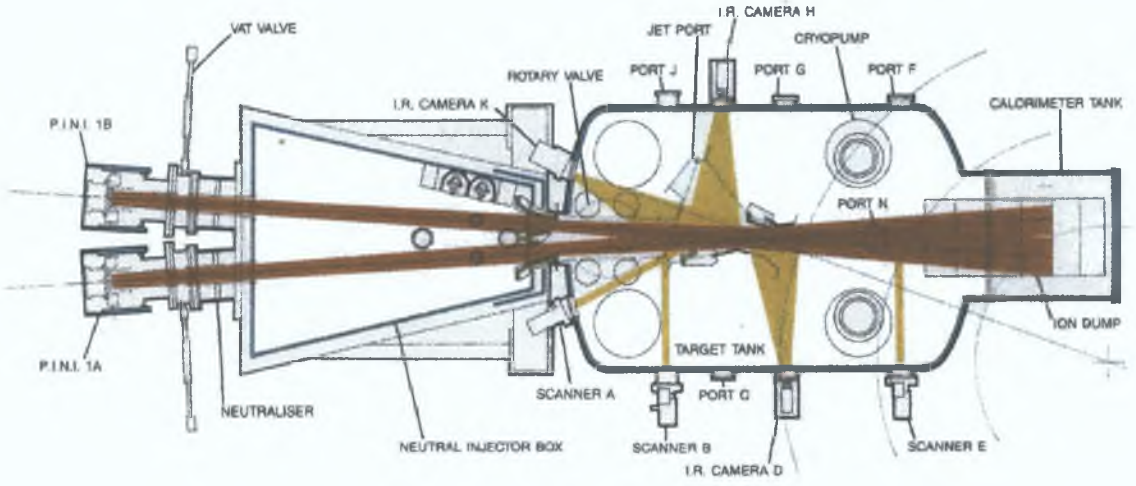

Figure 1.10 Schematic of the JET Neutral Beam Test-Bed layout.

The Test Bed NIB is generally used without the deflection magnets used in the actual injectors, allowing the full mixed ion/neutral beam to be transported to the beam dump. The target tank initially housed a simulation of the duct scrapers and torus wall to test the beam transmission into the JET plasma. These components are no longer in place allowing excellent

access. to the composite ion/neutral beam for the detailed beam diagnostics that are now available on the Test-Bed

1.3.1 BEAM DIAGNOSTICS USED ON THE NB TEST BED.

Figure 1.11 shows in schematic for the layout of the diagnostics used on the Test Bed beamline.

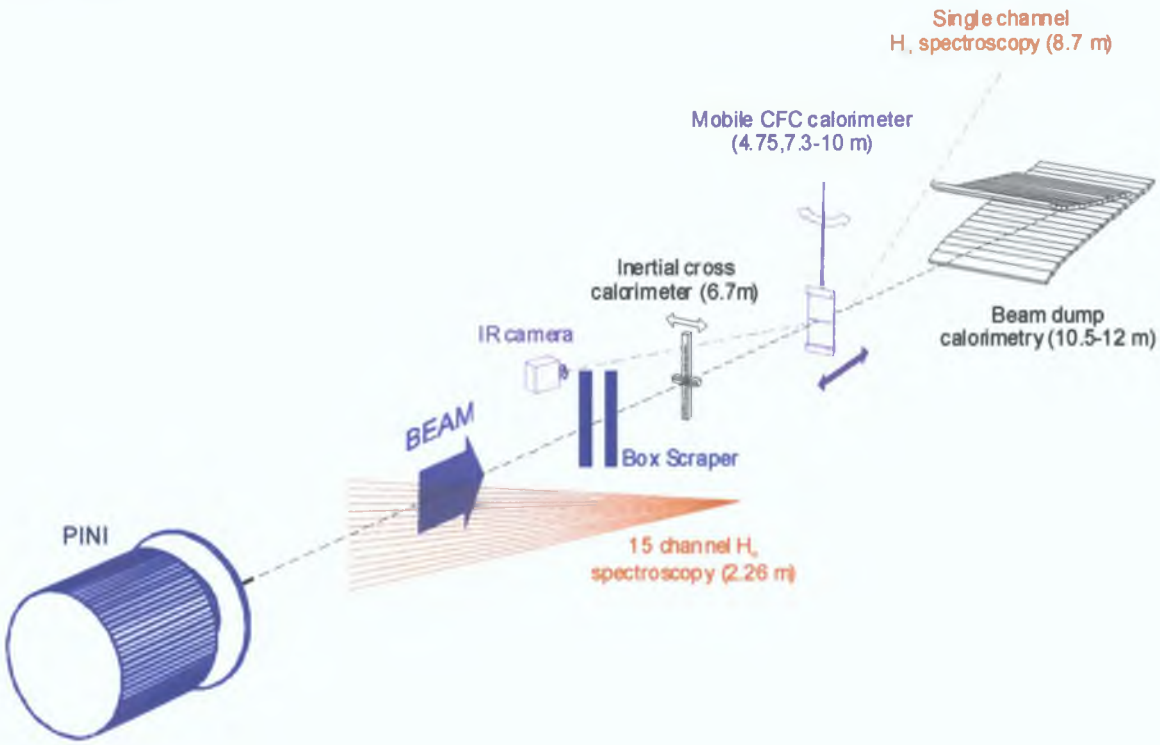

Figure 1.11 Schematic of the diagnostics used on the JET Neutral Beam Test Bed beamline

The primary diagnostic used on the beamline is the water calorimetry of the ion dump, box scraper and PINI components. These are the critical diagnostics as they determine where the beam power is falling, since excessive power interception on any beamline component has the potential to create serious beamline damage. These are however reasonably coarse diagnostics of the extracted beam, the ion dump has the greatest resolution with measurements taken at 50mm intervals across the vertical (y) centre axis of the beam and at 100mm intervals across 3 lines of the horizontal x-axis. This allows a profile of the beam on the ion dump to be established, for a given extraction voltage the beam current at which the minimum profile

width on the ion dump occurs is then defined as the 'optimum' value, which is used as the standard condition for further beam operations

The inertial cross calorimeter was constructed to give a more detailed profile of the beam at a distance close to the start of the JET duct The calorimeter has 32 thermocouples embedded in a copper cross shape to give points at ≈5 mm intervals across the horizontal (x) and vertical (y) centre axes of the beam The cross calorimeter is exposed to short beam pulses and the peak response temperature from each thermocouple is used to determine the beam profile This diagnostic has now been largely superceded by the more detailed calorimetry available from the Carbon Fibre Composite tile calorimeter [16]

1.3.2 CFC TILE CALORIMETER

A 20mm thick 400×200mm^2 block of Carbon Fibre Composite (CFC) material (Mitsubishi MFC-1A) is placed at the centre of the beam in the Neutral Beam Test Bed The CFC tile can be positioned at 4 8m or between 7 and 10m downstream of the source The tile is exposed to short beam pulses, of duration dependent on the expected peak beam power density Typically the beam pulse lengths used are between 0 5 and 0 1s for peak power densities of 5 to 100MW/m^2 The anisotropy of the thermal conductivity of the CFC in directions parallel (k_z) and perpendicular ($k_{x,y}$) to the beam direction allow a thermal image of the beam footprint to be retained The ratio of thermal conductivities ($k_z/k_{x,y} \approx 20$) is practically constant over the operating range of the tile, this ratio means that thermal equilibrium is reached in the direction parallel to the beam after a few seconds, whilst the lateral thermal equilibrium is achieved after ~10 minutes

The surface temperature of the CFC tile is measured by an AGEMA 900 SW infrared camera at an image rate of 15Hz The imaging system has an accuracy of 1% over an operating range of 0-2000°C Using the known thermal properties of the MFC-1A material it is possible to recreate the beam power density profile directly from the measured temperature profile Images of the tile are taken shortly prior to the beam exposure and then 2-3s after exposure when the tile has reached thermal equilibrium in the beam direction The images are converted to a power density profile transformed to the spatial x,y coordinates of the tile The resolution of the imaging system depends on the distance between the camera and the tile, but

for the typical imaging distance of 3.0m between the camera and the tile the profile resolution is $2.5 \times 2.5 mm^2$.

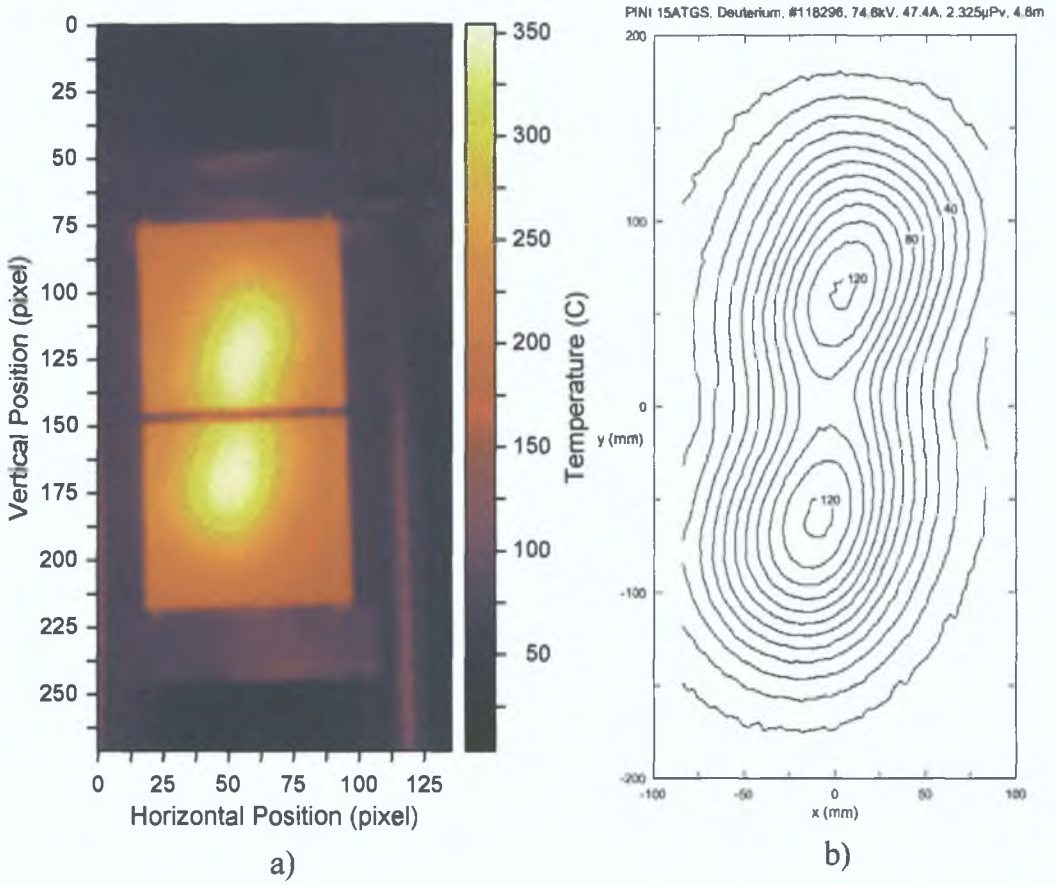

Figure 1.12 CFC tile calorimeter data a) Raw thermal image of the CFC tile after exposure. b) Analysed power density profile.

1.3.3 MULTI-CHANNEL SPECTROMETER

In addition to the detailed calorimetry of the beam the Doppler shifted Balmer-α light emission from collisions of energetic neutral hydrogen with residual gas molecules in the beam path is collected by a multi-channel spectrometer [17]. This light is used to determine the species composition of the fast hydrogen neutral components of the beam (at the full, ½ and $1/3^{rd}$ energy). A method [18,19] that has been used frequently in the past to give information on the properties of the original ion species from which these energetic neutrals

are produced (i.e. H^+, H_2^+ and H_3^+). On the Neutral Beam Test Bed the light previously has been collected from a region, 8.7m downstream, close to the beam centre and used to give the line averaged data across a single line of sight. A newer multi-channel diagnostic was constructed at the Neutral Beam Test Bed to provide spatially resolved measurements of the beam parameters at a distance of 2.26m downstream. The Balmer-α light emission is focussed onto an array of 15 optical fibres that transport the light over 50m into the Neutral Beam Test bed control room. Here the light is refocused onto the entrance slit of a 0.5m visible light monochromator. The combination of the optical fibres and light collection lens gives 15 circular collection areas of 10mm diameter equally displaced across ±190mm of the beam vertical (y) axis. A CCD array detector simultaneously acquires each of the 15 individual spectra, the CCD image is then transferred to the JETNET PC network for subsequent display and analysis.

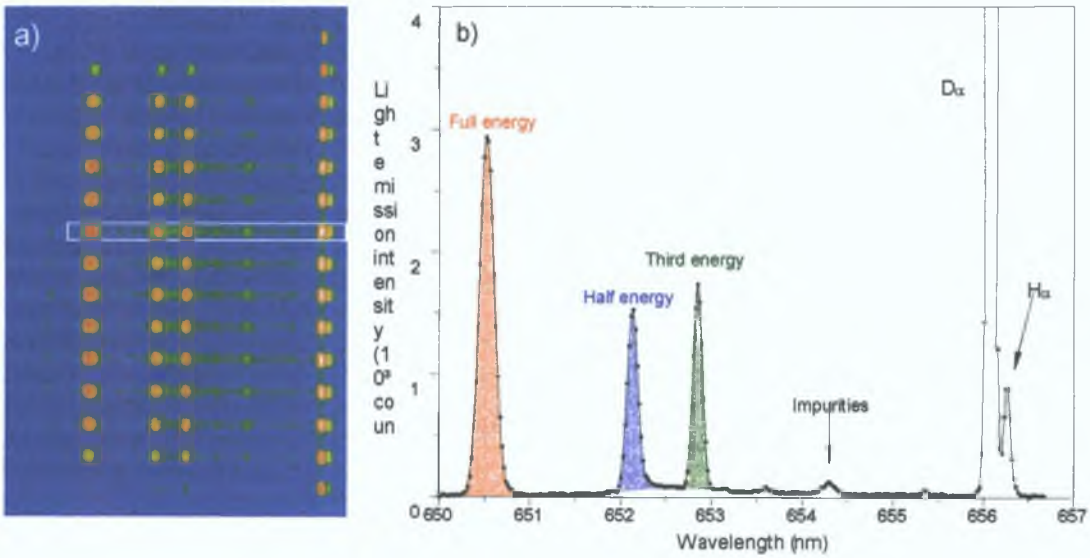

Figure 1.13 Multi-channel spectrometer data a) Raw CCD array image of the 15 spectral images. b) Analysed spectrum of the image section highlighted in a). Data from a 140kV 30A Deuterium beam.

Figure 1.13 shows a sample image acquired by the CCD array, with the analysis of one of the fibre spectral images. Each spectrum is analysed to give the best-fit Gaussian area and width

of each shifted line This allows the relative abundance and divergence of each of the beam species to be calculated, once the instrumental transfer function has been included

It is the quality and resolution of the data from the CFC tile calorimeter and the multi-channel spectrometer, available in recent years, that has allowed the investigation of the uniformity of the ion source from beam measurements on the Neutral Beam Test Bed

1.4 SCOPE OF THESIS

Given that the neutral power available from the Octant 4 injector can be limited by power interception on beamline scrapers, rather than by the limits of the power supply It is clear that if beam interception can be reduced from the 80kV 60A (D_2) tetrode accelerator PINIs used on this Octant then the benefit would be twofold

1) Reducing the power lost on beamline scrapers will inevitably lead to a greater fraction of the power transmitted to the JET plasma

2) Sufficient reduction of the power intercepting the beamlme scrapers, e g by enough to allow the PINIs to be operated at the maximum of the power supply rating, will increase the total neutral power available for injection

Given the cost of installing new neutral beam injectors, currently estimated at €2 8×10^6 per MW, it is therefore very cost effective to maximise the performance of the already installed neutral injectors

Two main factors that influence the power interception of beam power on the scraper elements are -

1) **Beam divergence** given by accelerator optics and ion source uniformity
2) **Beam alignment** given by the mechanical construction of the ion accelerator

This thesis concerns the efforts made to study the causes and effects of ion source non-uniformity The Neutral Beam Test Bed is used to diagnose the effects of source non-uniformity and determine the degree of source non-umformity from the beamlme diagnostics The experimental study is supported by the construction of a computer simulation of the ion source This study is then applied to a work program to produce an ion source that has improved uniformity, but with all the other required characteristics of the JET NBI ion source

2 EXPERIMENTAL EVIDENCE AND CONSEQUENCES OF ION SOURCE PLASMA NON-UNIFORMITY.

One of the mechanisms causing increased beam power interception on the beamline scraper elements is believed to be increased beam divergence due to non-uniformity in the ion density provided by the ion source at the plane of the beamlet extraction array The important evidence that increased beam transmission, with reduced interception on beamlme scrapers, could be obtained by using an ion source with a uniform ion density came from Neutral Beam Test Bed measurements These measurements compared beams extracted from a standard super-cusp filter source with those extracted from a source with only the basic chequerboard magnet pattern

2.1 COMPARISON OF BEAMS FROM SUPER-CUSP AND CHEQUERBOARD SOURCES

The standard ion source used on the PINIs has a 'super-cusp' filter field, also often called a 'tent filter', to enhance the monatomic species yield The magnet pattern chosen for the standard super-cusp source was denoted SC15S3 during the development programme at Culham The magnet arrangement of one of these ion sources has been modified to remove the filter field and leave only the basic chequerboard magnet pattern On the Neutral Beam Test Bed the same PINI accelerator grid assembly (11AT) was used to extract beams from a standard ion source, using the SC15S3 super-cusp magnet pattern, and from the source using the chequerboard only magnet pattern (without a filter field) It is important in this case to use the same accelerator grid assembly so that the potential effects of differing mechanical grid alignments do not confuse the comparison of the two sources

Calorimetric measurements of the cooling water flowing through the beam dump and scraper elements of the Test-Bed shows the distribution of the beam power from each PINI configuration One of the significant differences in the beam performance was a larger transmission of the beam extracted from the chequerboard source to the Test-Bed beam dump Correspondingly, the power loading on the beam defining (box) scrapers is reduced when the chequerboard source is used Figures 2 1 and 2 2 show the comparison of the fraction of the

total beam power falling on the beam dump and box scraper – as a function of the beam perveance. The figures show that beam transmission is improved by almost 10% of the full power, and that the power interception on the box scraper is nearly halved.

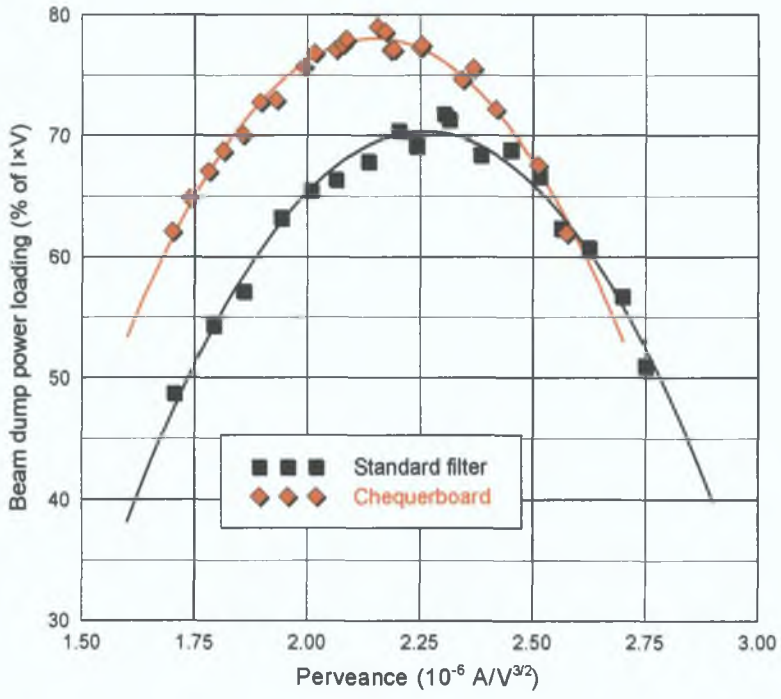

Figure 2.1: Comparison of beam power transmitted to the Test-Bed beam dump for a standard filter source and a chequerboard only source.

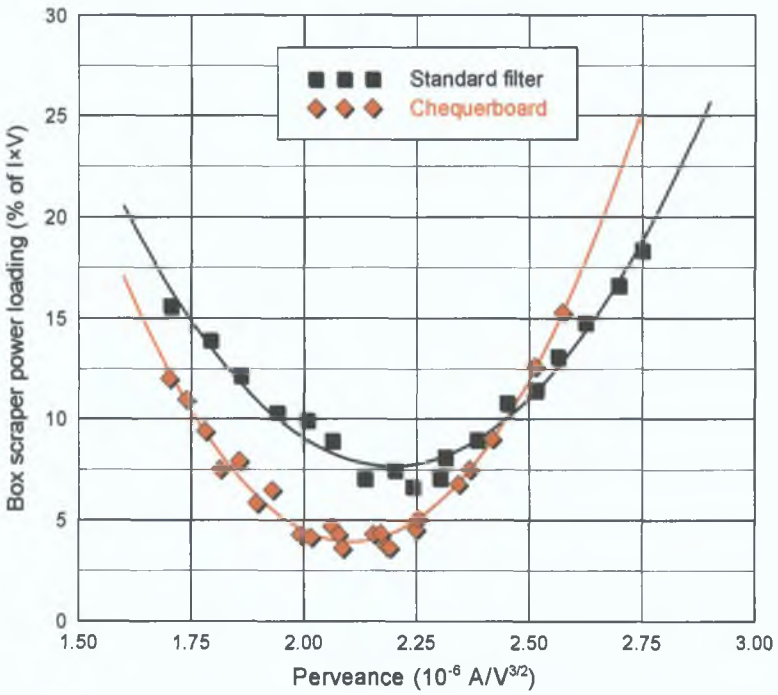

Figure 2.2: Test-Bed Box Scraper power loading comparison for standard and chequerboard only sources

The difference between the perveance where the minimum box scraper interception, and maximum beam transmission, occurs is consistent with the different species composition of the beams extracted from the two ion sources. In figures 2.1 and 2.2 the maximum transmission occurs at a total beam perveance of 2.10μPv using the chequerboard source and 2.25μPv with the super-cusp source. The unit of perveance, Pv, defined as 1 $A \times V^{-3/2}$, is derived from Child's Law, where for a planar diode : -

$$\frac{I}{V^{3/2}} = \frac{4\sqrt{2}\,\varepsilon_0}{9z^2}\sqrt{\frac{q}{m}} \qquad (1)$$

hence the maximum transportable beam perveance is a constant depending on the beam charge/mass ratio (q/m) and diode gap length, z.

The chequerboard only source typically produces a measured species yield ratio of 68:27:5 (% $D^+:D_2^+:D_3^+$), compared to the 85:10:5 (% $D^+:D_2^+:D_3^+$) species yield ratio typically measured for the SC15S3 super cusp source. These species ratios give an effective beam mass of

2 74amu for the chequerboard source and 2 40amu for the super-cusp source The perveance at which the minimum beam divergence is obtained scales with the square root of the effective beam mass (equation 1) Using the super-cusp optimum perveance of 2 25μPv, the chequerboard source should have an optimum perveance at $2\,25\,\mu Pv \times \frac{\sqrt{2\,4}}{\sqrt{2\,75}} = 2\,10\,\mu Pv$, exactly as is measured

Since the same accelerator grid stack is used for the measurement of both sources, with a common value of mechanical misalignment, the increase in beam transmission must be due to a difference between the two ion sources This is consistent with previous evidence [14] that the chequerboard source produces a more uniform ion density at the extraction plane of the ion source than the super-cusp source A uniform ion density across the extraction array means that all beamlets are extracted at the minimum divergence at the point of overall beam optimum perveance For a non-uniformity there will be no overall beam perveance where all the beamlets are extracted at minimum divergence, leading to total beam of larger divergence, once the beamlets are superimposed

However the chequerboard ion source is not suitable for use on the neutral beam injectors at JET because the poorer monatomic species yield would result in significantly reduced power in the full energy neutrals, reducing the penetration of the delivered neutral power to the JET plasma core The monatomic species fraction from the super-cusp source is, however, of the required level (>80%) for adequate full energy neutral delivery

Further evidence of ion source non-uniformity is given by the analysis of the extracted beams measured with the multi-channel spectrometer and Carbon Fibre Composite tile calorimeter diagnostics

2.2 Evidence from Multi-channel spectrometer measurements

The multi-channel spectrometer uses a CCD array to acquire the spectrally resolved image of the light delivered to a monochromator from 15 fibre optic channels aligned vertically across the ion beam The imaging point is located 2 26m downstream of the extraction grids, past the

end of the neutraliser. Analysis of the data provides horizontal (x) line averaged data on beam intensity, species composition and divergence across a vertical (y-axis) line of ±190mm about the beam centre. A more detailed description of this diagnostic is given, previously, in section 1.5 of Chapter 1.

2.2.1. SC15S3 SUPER-CUSP ION SOURCE

The multi-channel spectrometer was used to measure the properties of a beam extracted from a super-cusp ion source, using a high current tetrode accelerator. The analysis of a spectral image taken at a beam perveance of 2.303μPv is shown in the following figures. This beam perveance is close to the 'optimum' beam perveance of 2.25μPv, which gives the highest transmission to the Test-Bed beam dump (see figure 2.1).

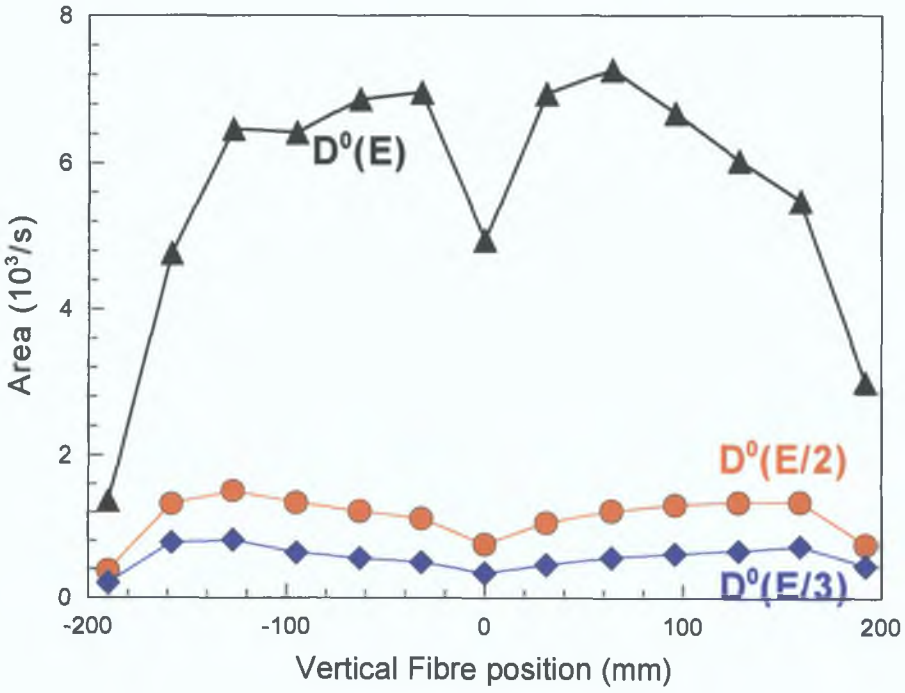

Figure 2.3. Line intensity (integrated area of each line) profile of the D^0 – full, ½ and 1/3rd energy components in a beam extracted from an SC15S3 super-cusp ion source (at 'optimum' perveance). PINI 18AT, a high current tetrode accelerator

Figure 2.3 shows the intensity of the measured species spectral line as a function of the optical fibre position, projected to the plane of the beam centre line. The monatomic species is the largest fractional component of the beam, and shows effectively the beam intensity over the y-axis of the beam. The central dip in the intensity profile is where the line of sight for this fibre views between the beamlets from the two half grids, here there is a large gap between the first row of extraction apertures of each grid half, refer to figure 3.3 in chapter 3. The reduction in the intensity towards the outer edges of the profile is where the edges of the beam are seen.

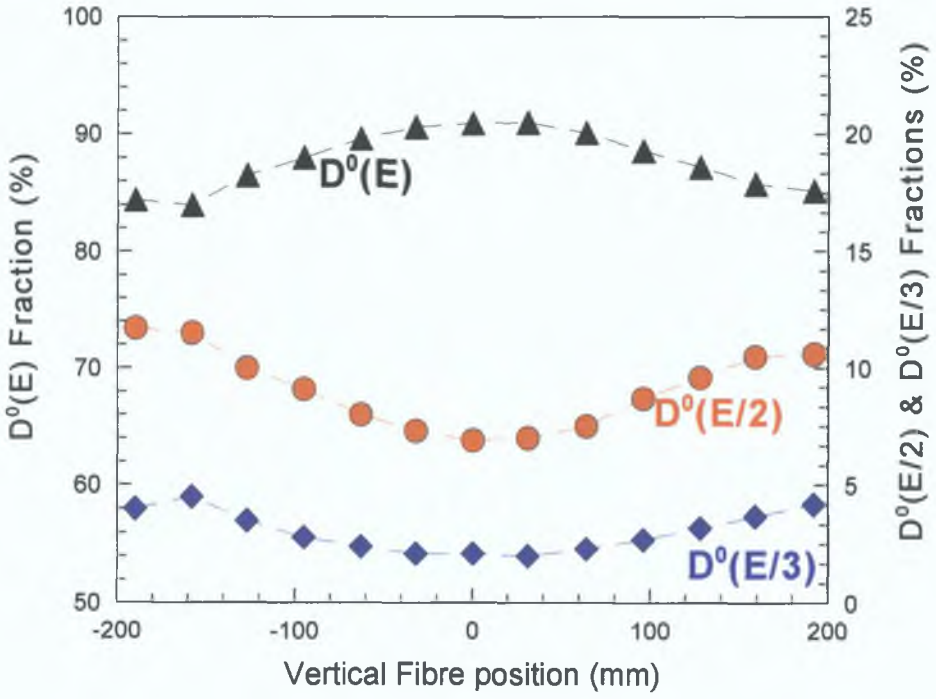

Figure 2.4. Species fraction profile of the D^0 – full, ½ and 1/3rd energy components of a beam extracted from an SC15S3 super-cusp ion source (at 'optimum' perveance). Data taken from PINI 18AT, a high current tetrode accelerator

The distribution of the species fraction is then calculated across the vertical (y-axis) profile, figure 2.4. The D^+ (full energy) fraction in the beam is clearly non-uniform across the vertical line, due mainly to the reduction in D_2^+ (½ energy) towards the centre of the source. This

would be consistent with either a) increased D_2^+ dissociation or b) reduced D_2^+ production towards the source centre.

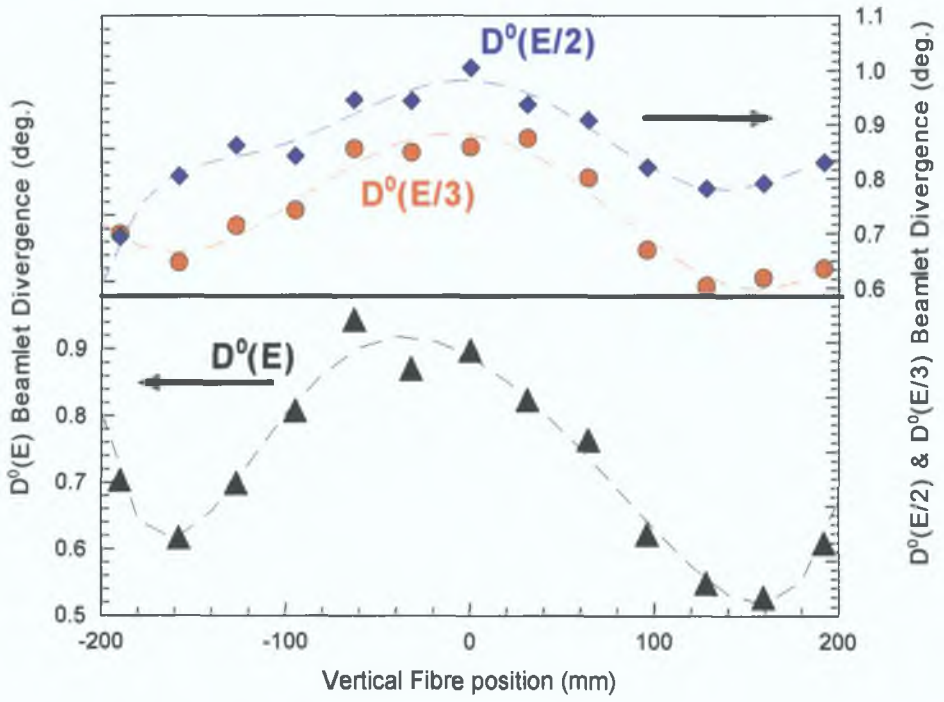

Figure 2.5. Vertical (y-axis) beamlet divergence profile of the D^0 – full, ½ and 1/3rd energy components of a beam extracted from an SC15S3 super-cusp ion source (at 'optimum' perveance). PINI 18AT a high current tetrode accelerator

The width of each species emission line is then used to determine the beamlet divergence of each species over the vertical (y) profile of the beam. Figure 2.5 shows that at the 'optimum' perveance, the minimum D^+ (full energy) beamlet divergence occurs towards the outer edge of the vertical profile, with the central beamlets showing the maximum divergence. The same pattern is generally repeated in the D^0 ½ and 1/3rd energy (D_2^+ and D_3^+) divergence profiles.

The analysis of the spectroscopic data was then repeated for a scan of the beam perveance. The beam perveance is varied by changing the extracted beam current at a fixed extraction potential. Figure 2.6 shows how the D^+ (full energy) beamlet divergence profile evolves through the perveance scan. At low perveance the minimum divergence occurs close to the

centre of the profile, as the perveance increases the point where the minimum divergence occurs moves gradually towards the outer edge of the profile.

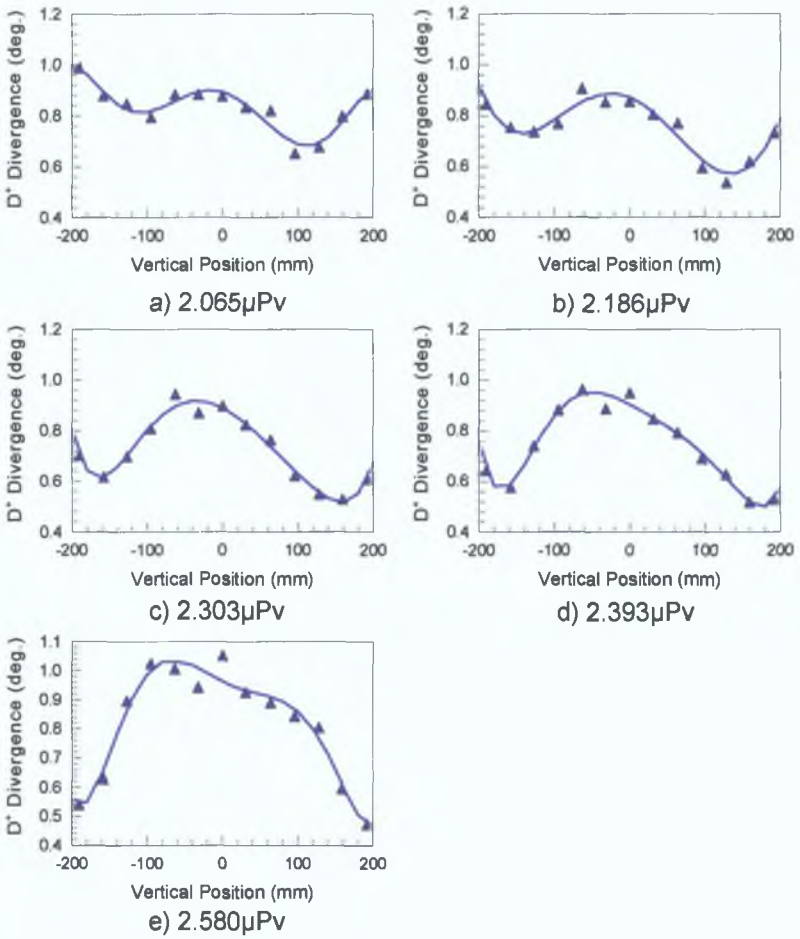

Figure 2.6 Evolution of the D^0 full energy (from D^+) beamlet divergence profile through a scan in beam perveance (fixed extraction voltage, varying beam current). All graphs have the same Y axis scale for divergence (0.4 to 1.2 deg.). Using PINI 18AT with SC15S3 super-cusp ion source.

This data can be summarised in a plot that shows the beam perveance where each local beamlet minimum divergence is seen, as a function of the vertical (y) position. The perveance where each minimum divergence occurs is interpolated by fitting a quadratic polynomial to the divergence data for each fibre location, corrected for the relative change in measured species composition across the beam.

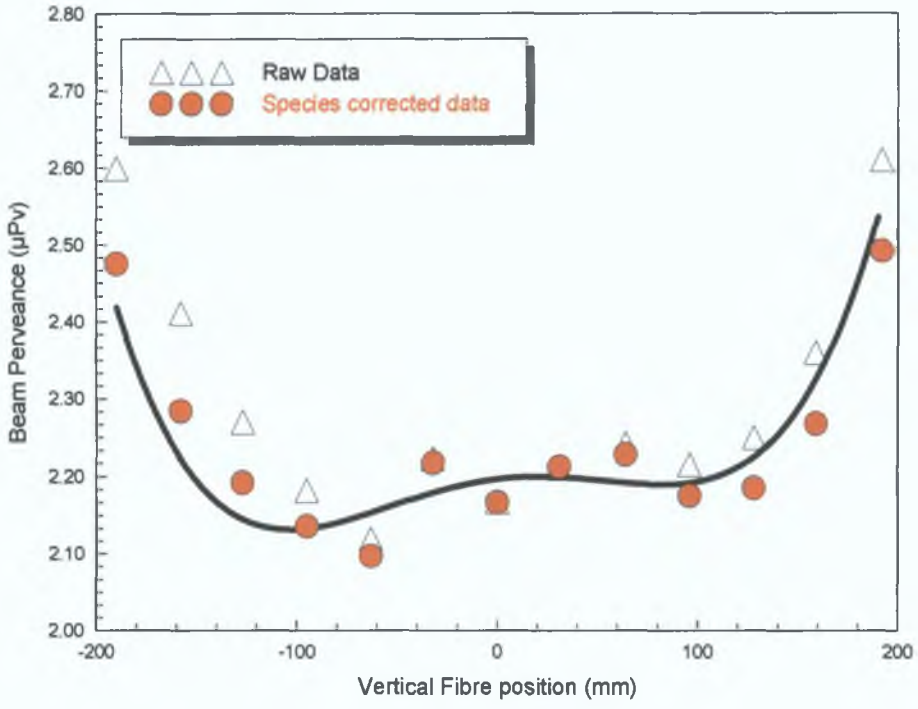

Figure 2.7. The vertical (y) distribution of the beam perveance where the local minimum beam divergence occurs. For a fixed extraction gap and extraction potential this is equivalent to the inverse of the current density distribution. The 'Raw data' shown on the plot is before the correction to compensate for the measured species composition change across the profile. (Using the perveance scan of PINI 18AT).

This figure (2.7) is a strong piece of evidence for non-uniformity of the ion density in the source, since for an array of identical extraction apertures, with constant accelerator gap lengths at uniform extraction potentials, the local minimum beamlet divergence will only occur when the local source ion density is at the correct value. As the global current density is varied during a perveance scan the local ion density reaches the condition for minimum divergence at different values of total ion current for different vertical (y) locations.

2.2.2 CHEQUERBOARD ONLY ION SOURCE

The same analysis of the spectroscopic data of a beam extracted from a chequerboard ion source shows, as expected, evidence of a more uniform ion density. In this case the data is taken from another high current tetrode, PINI 6AT.

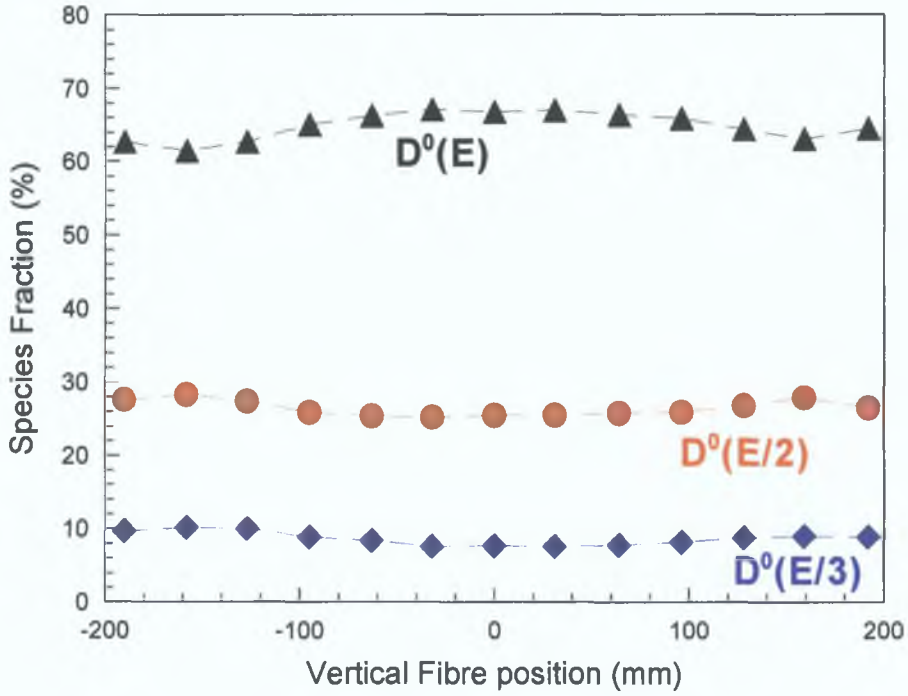

Figure 2.8. Vertical (y) species fraction profile of the D^0 – full, ½ and 1/3rd energy components of a beam extracted from a chequerboard ion source (at 'optimum' perveance). PINI 6AT, a high current tetrode accelerator

Figure 2.8 shows the distribution of the beam species fractions taken from a beam with a perveance of 2.10μPv, which gives the greatest transmission to the Test Bed beam dump (see figure 2.1). The monatomic species yield for this source is, as expected, lower at approximately 65% D^+ (full energy), with a greater fraction of D_2^+, 29%, (½ energy) than the super-cusp ion source. Although there are some small differences in the species yield across the vertical measuring plane, this is not as pronounced as the distribution observed for the super-cusp source.

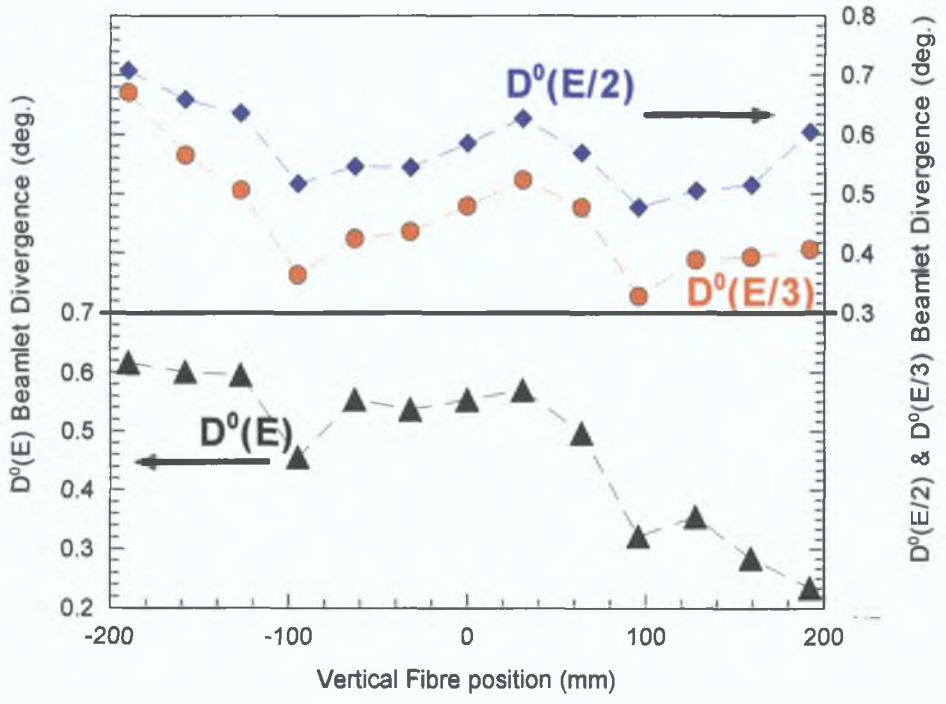

Figure 2.9. Vertical (y) beamlet divergence profile of the D^0 – full, ½ and 1/3rd energy components of a beam extracted from a chequerboard ion source (at 'optimum' perveance). PINI 6AT a high current tetrode accelerator

The divergence distribution calculated at the 'optimum' beam perveance for each species is shown in figure 2.9. This figure shows a beamlet divergence that is generally constant over the range 0 to -200mm with a decreasing value over the 0 to + 200mm range. This can be interpreted as showing a difference in the accelerator grid gaps between the upper and lower accelerator grid halves, which lead to a different beamlet divergence being obtained from each grid half under otherwise identical conditions.

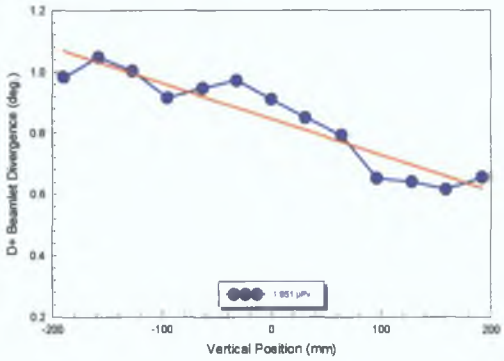

a) 1.851 μPv

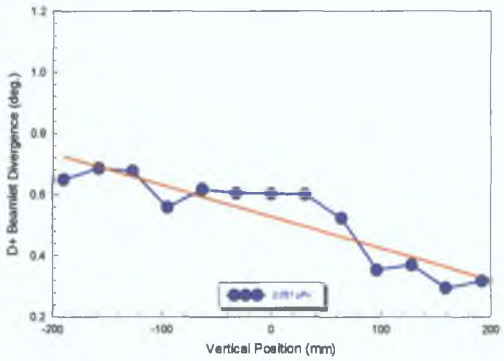

b) 2.051 μPv

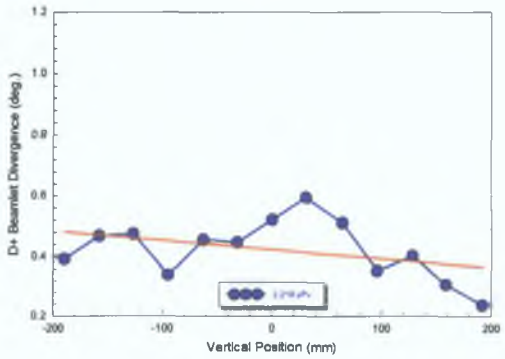

c) 2.219 μPv

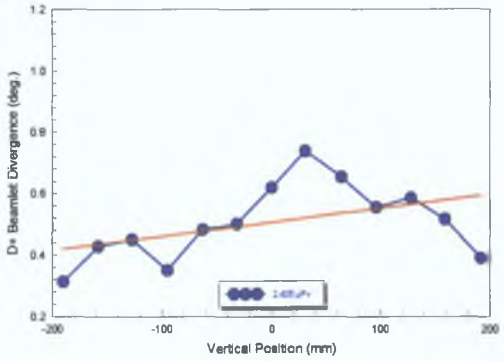

d) 2.405 μPv

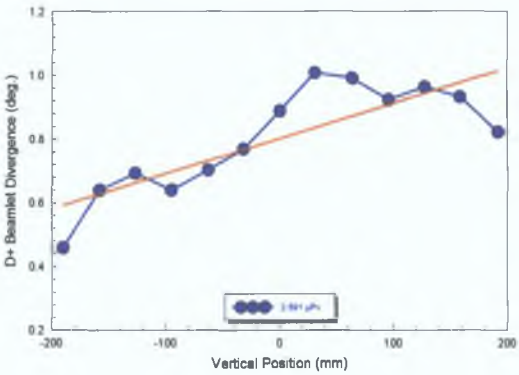

e) 2.591 μPv

Figure 2.10 Evolution of the D^0 full energy (D^+) beamlet divergence profile through a scan in beam perveance. All graphs have the same Y axis scale for divergence (0.2 to 1.2 deg.). Using PINI06AT with a chequerboard ion source.

The plot of the beamlet divergence profile through the scan in beam perveance shows clearly the discrepancy that exists between the beam extracted from the two grid halfs. Under the optimum beam perveance the upper grid half has the lower beamlet divergence, and above the optimum perveance the lower grid half has a lower beamlet divergence. This effect introduces an apparent gradient across the beamlet divergence profile, if this gradient is removed then it

can be seen that each profile through the perveance scan has essentially a uniform distribution

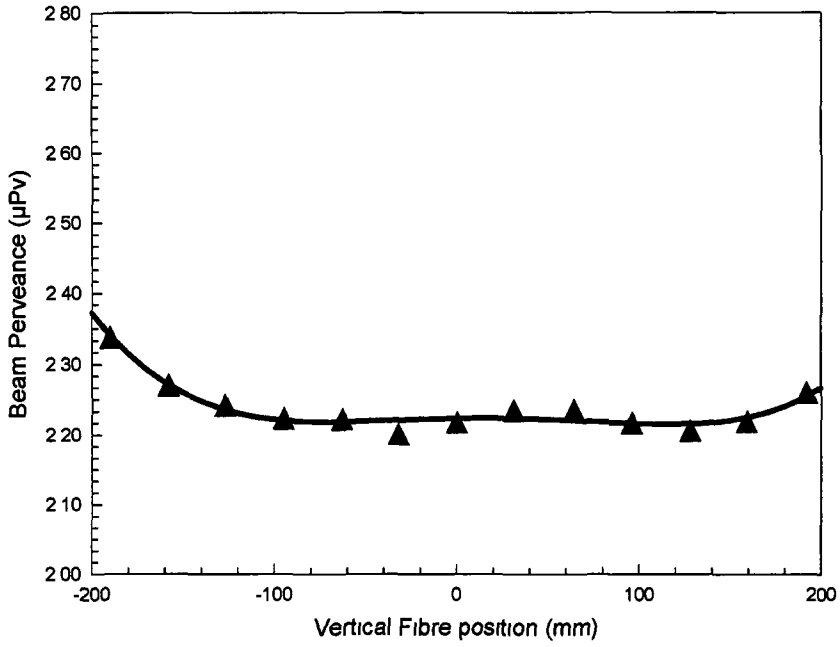

Figure 2 11 The vertical (y) distribution of the beam perveance where the local minimum beam divergence occurs - in this case corrected for the discrepancy between the beams extracted from each grid half This is plotted on the same y-axis scale as figure 2 7 so that a direct comparison can be made (Using the perveance scan of PINI 6AT)

Removing the apparent gradient across each beamlet divergence profile allows the plot of the beam perveance where the minimum beamlet divergence occurs to be recalculated to remove the effect of the discrepancy between the behaviour of the two grid halves This is shown in figure 2 11 with an identical y-axis range to the similar plot of the super-cusp ion source in figure 2 7, again adjusted for the (small) change in species composition across the beam This shows a that the source must be producing a much more uniform ion density distribution, once the distorting effect of the accelerator grid misalignment has been removed

2.3 Evidence from Infrared Calorimeter measurements

The JET Neutral Beam Test-Bed routinely obtains detailed beam power density profiles using a unidirectional Carbon Fibre Composite (CFC) tile calorimeter The tile is exposed to short beam pulses and the large difference in transverse to longitudinal heat conductivity allows an image of the beam power footprint to be retained An AGEMA THV 900 SW Infrared Camera system records this temperature distribution, and the data is transferred to the JET PC network for analysis Using an image of the tile taken shortly before the beam pulse and a second image taken 2-3 second after the pulse, when the tile has reached thermal equilibrium in the beam direction, the power density profile can then be calculated, using the known thermal properties of the material

2.3.1. SC15S3 super-cusp ion source

The infrared image of the beam footprint is taken at a distance of 4 8m downstream for a scan in beam perveance The analysed footprint images are shown in figure 2 12, where the tile temperature rise has been converted to a beam power density The 3 images shown in figure 2 12 are at beam perveances of 2 050μPv, 2 310μPv and 2 578μPv - values below, at and above the 'optimum' perveance for this beam

In each case the distance between the beam centres formed from each grid half is measured The point on each grid half where the maximum power density is seen will depend on 2 factors - 1) the focal length of the local offset aperture steering and 2) the local beamlet divergences As the focal length of the accelerator is a fixed function of the geometry of the extraction aperture array, it is apparent that any difference in the relative location of the maximum power density of each grid half will be due to changes in the local beamlet divergence

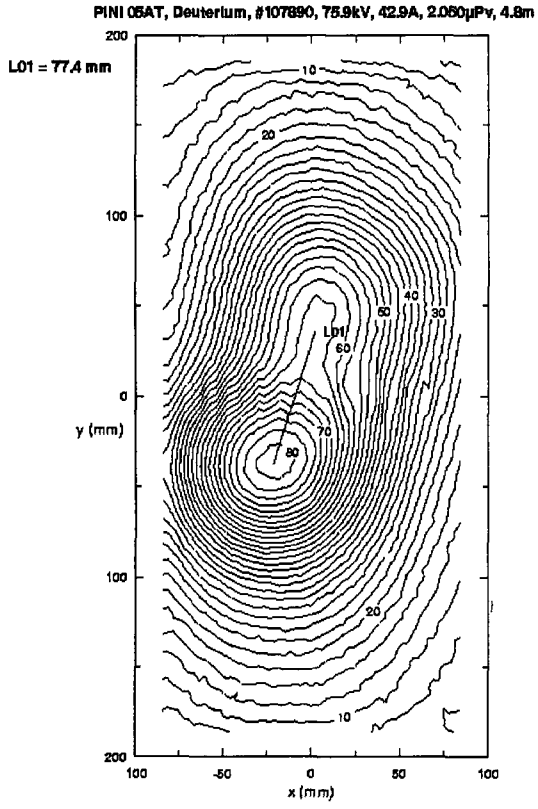

a) 2 050μPv

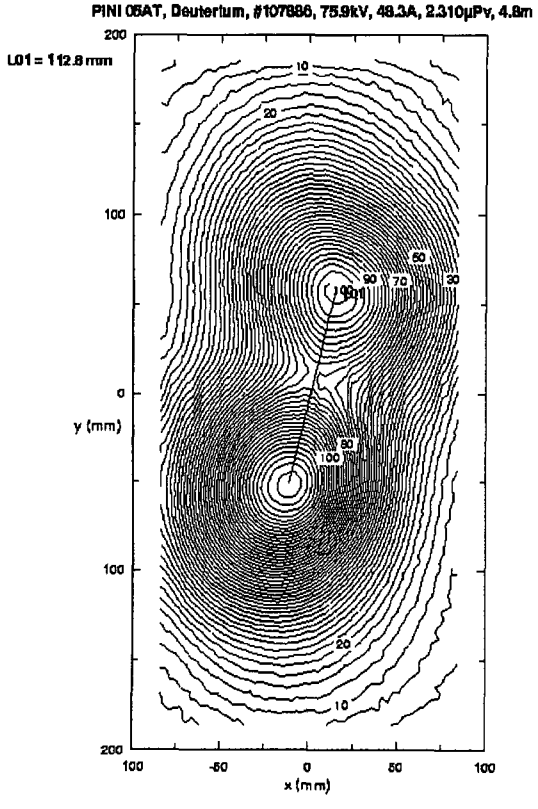

b) 2 310μPv

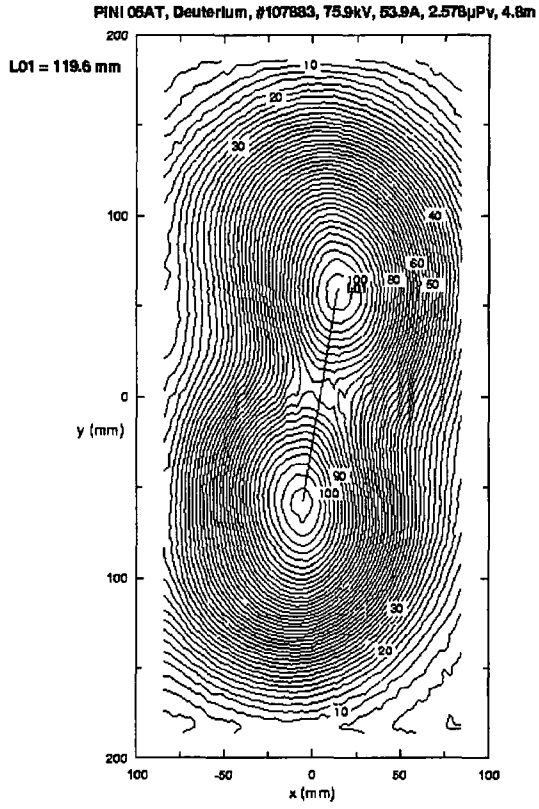

c) 2 578μPv

Figure 2 12 Beam power density footprints taken at a distance of 4 8m downstream from PINI 05AT with a super-cusp ion source during a scan in beam perveance

As Figure 2.12 illustrates, the distance between the points in each grid half with maximum power density increases with increasing beam perveance, this is summarised in figure 2.13. For comparison the distance between the grid half beam centres is shown for a narrow range perveance scan measured at 4.8m with a chequerboard ion source.

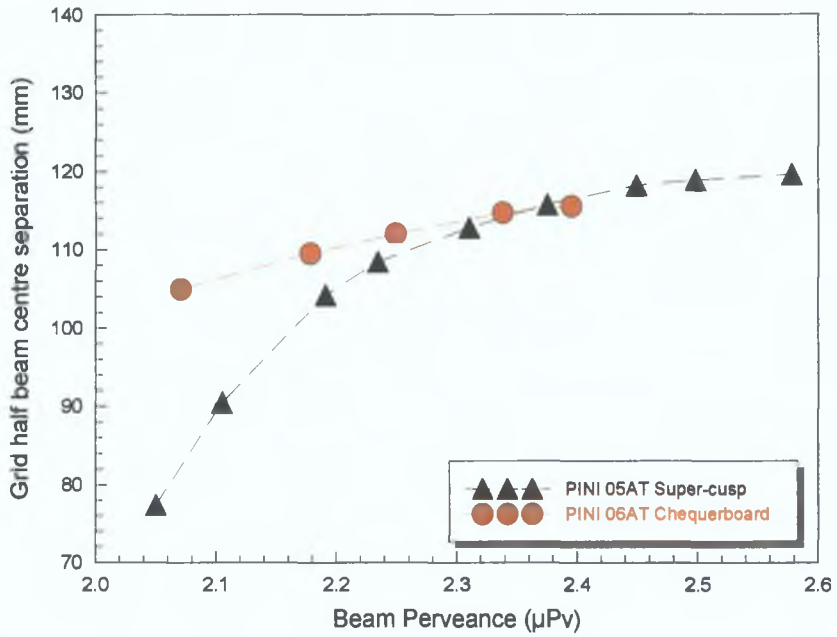

Figure 2.13. The distance between the beam centres formed from each grid half as a function of the beam perveance. The data is shown from PINIs 05AT with a super-cusp ion source and 06AT with a chequerboard ion source.

Although there is some small increase of the beam centre separation with the chequerboard source it is nowhere near as large as for the super-cusp source. This behaviour is interpreted as showing that for the super-cusp source the beamlets with minimum divergence move from the centre of the source to the outer edges as the ion source current is increased. So as the beam perveance is increased the location where the highest power occurs in each grid half moves towards the outer edge of the ion source. This is consistent with the experimental observations of the super-cusp ion source with the multi-channel spectrometer, that show the minimum beamlet divergence moving from the centre of the ion source to the edges with increasing beam perveance. The more uniform profile seen in the beams from the chequerboard source is also consistent with only the small changes seen between the separation of the beam centres from the chequerboard footprint images.

2.4 CONSEQUENCES OF AN ION SOURCE NON-UNIFORMITY ON BEAM EXTRACTION

The effect of a non-uniform density distribution in the ion source on the properties of beam extracted from a multi-aperture array can be illustrated in figure 2 14 For a uniform extraction aperture array, at a fixed extraction potential, there will be a given beamlet current at which the minimum divergence occurs At beamlet currents other than this the beamlet divergence is increased For a non-uniform ion density it is not possible to have all beamlets extracted at the minimum divergence, so the total beam divergence is always larger than the minimum beamlet divergence For this purpose a parabolic density profile is assumed, which is reasonably consistent with the measured distribution shown in figure 2 7 As the total beam current is increased the location of the minimum divergence beamlets moves progressively from the centre to the edge of the extraction aperture array (A→D) The minimum total beam divergence is seen, at case C, when the beam is formed from beamlets with the smallest maximum deviation from the minimum divergence

For a non-uniform source density it is the permanent presence of beamlets that are with greater than the minimum divergence that leads to an overall increased divergence of the combined beam It is this increased total beam divergence that is responsible for the increased beam interception on beamline scraper elements when a non-uniform source is compared to a uniform source

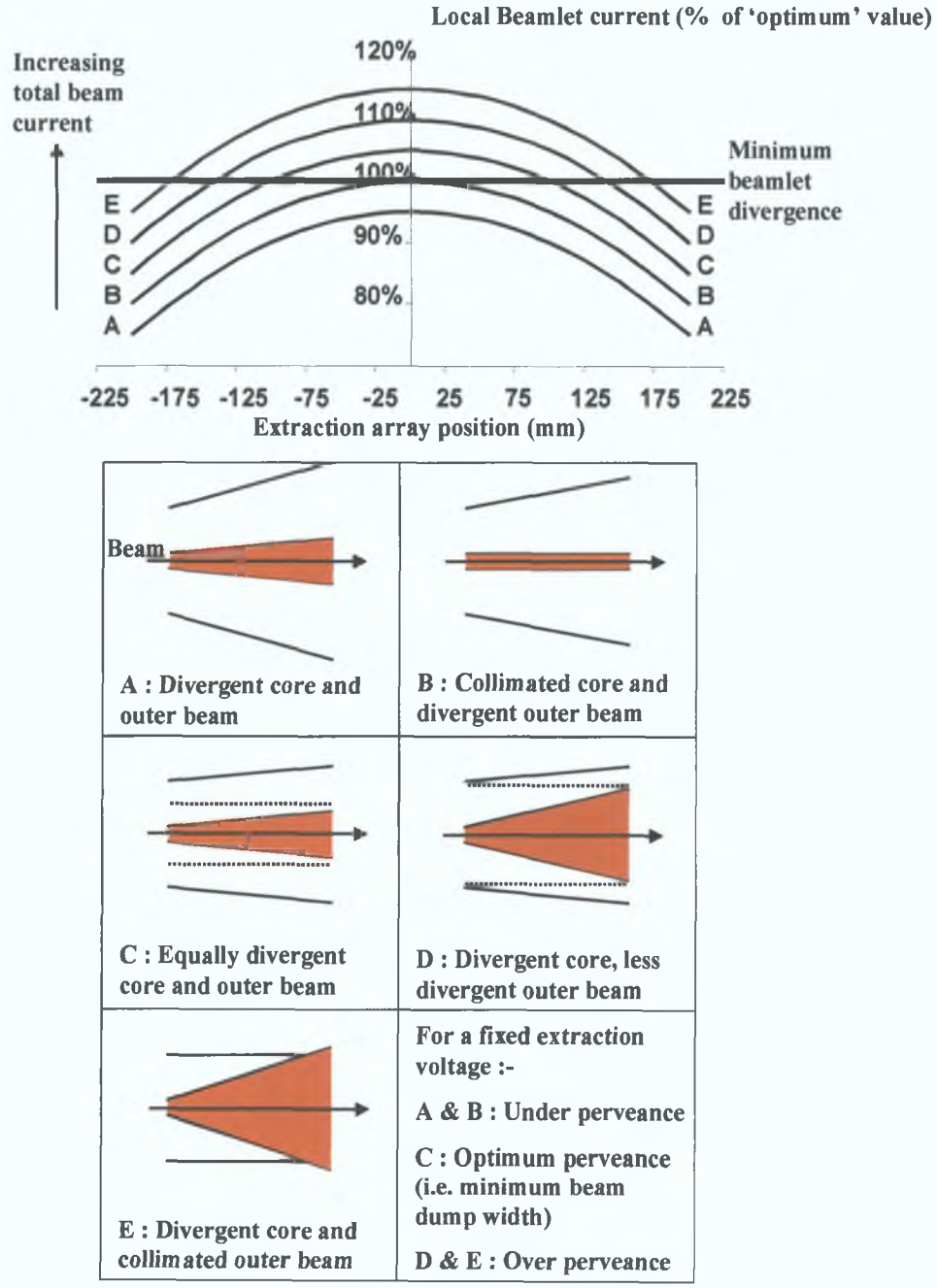

Figure 2.14: Schematic of effect of ion density non-uniformity on extracted beam quality.

2.5 CHAPTER SUMMARY

Using the same PINI accelerator grid stack on the Neutral Beam Test bed with a standard SC15S3 super-cusp ion source and a chequerboard ion source has shown -

1) Increased beam transmission of 10% of the full beam power for the chequerboard ion source
2) Corresponding factor of 2 reduction in box scraper power loading for the beam from the chequerboard source compared to the beam extracted from the super-cusp ion source

Even though the accelerator grid array used has consistent mechanical alignments between the extraction of the two beams

It is believed that this improved beam performance is attributable to the difference in the ion density uniformity between the chequerboard and super-cusp ion sources This assertion is further reinforced by measurements of the beam with the multi-channel spectrometer and infrared tile calorimeter diagnostics that are available on the Neutral Beam Test-Bed The analysis of these measurements both show a non-umformity in the divergence of the beamlets extracted from the array of accelerator apertures, when a super-cusp ion source is used This non-uniformity in beamlet divergence is due to a non-uniformity in source ion density for a given array of identical extraction apertures In contrast the measurements of beams extracted from a chequerboard ion source show a reasonably uniform distribution of beamlet divergence, once some discrepancies introduced between the alignment of each grid half are removed

The chequerboard source, however, is not suitable for use on the JET neutral beam injectors due to the reduced monatomic species yield This would give an insufficient fraction of the beam power at the full energy required for penetration to the core of the JET plasma

It is the aim of this work to develop a model of the ion source to allow investigation of the cause of the non-uniformity introduced on the ion density by the presence of the super-cusp filter field This model will then be used to attempt to develop an ion source that produces a

more uniform ion density without degrading to monatomic species yield given by the existing super-cusp design

3 SIMULATION OF THE TWO DIMENSIONAL BEAM PROFILES OBSERVED WITH THE CFC TILE CALORIMETER

3.1. INTRODUCTION

The JET Neutral Beam Test-Bed routinely obtains detailed beam power density profiles of conditioned Positive Ion Neutral Injector modules (PINIs) using a unidirectional Carbon Fibre Composite (CFC) tile calorimeter, see section 1 3 2 of Chapter 1 The tile is exposed to short beam pulses and the large difference in transverse to longitudinal heat conductivity allows an image of the beam power footprint to be retained An AGEMA TVM 900S Infrared Camera system records this temperature distribution, and the data is transferred to the JET PC network for analysis Using an image of the tile taken shortly before the beam pulse and a second image taken 2-3 second after the pulse, when the tile has reached thermal equilibrium in the beam direction, the power density profile can then be calculated, usmg the known thermal properties of the material

Power density profiles have been obtamed usmg PINIs running in either H_2/D_2 or He gases Using D_2 gives the profile of a composite beam containing D^+, D^0, D_2^+, D_2^0, D_3^+ and D_3^0, as the JET Neutral Beam Test-Bed does not currently have a magnet to separate the residual ions from the neutralised beam component The advantage of usmg He gas is that it gives a simpler beam of He^+ and He^0 only, as no molecular ions are created

The beam profiles are normally measured at a distance of 8 3m from the end of the final extraction grid, this is the distance at which the neutral beam passes through the duct into the JET plasma Recently the CFC tile has been positioned at a distance of 4 8m downstream so that detailed profiles at the equivalent location to the calorimeter panels used in the Neutral Injector Boxes (NIBs) can be measured One of the critical factors in the safe operation of the neutral injector beamline is the power falling on the beam defining scrapers, this power must be kept below the acceptable limit to avoid damaging these components In particular the beam power falling on the box scraper element can limit the amount of power that can be safely extracted from the PINIs, thus reducmg the power that can be mjected into the JET

plasma Having a detailed set of profiles at 4 8m allows us to determine how the beam from each PINI will intercept the Box Scrapers

Earlier simulations of the beam profiles have concentrated on reproducing single line profiles taken through the beam mid point in the vertical (y-axis) and horizontal (x-axis) directions [20] The simulation code now attempts to reproduce the full beam power profile

3.2. CODE DESCRIPTION

The aim of these simulations is to attempt to reconstruct the ion density profile at the beam extraction plane directly from the beam power profile measurements This relies on having good knowledge of the offset aperture steering [21] and the beamlet current-divergence relationship Both of these parameters have been determined from experimental measurements and modelling with the 3D accelerator design code KOBRA3-INP [22,23,24]

This simulation attempts to produce a fit to the **whole** beam profile, although some trimming of the measured beam profile is performed This trimming removes data points below 10% of the peak value and those in the outer few millimetres of the tile This trimming allows the simulation routine to concentrate on fitting the central part of the beam profile rather than getting distracted by the noise in the low level and edge data points Figure 3 1 shows both the raw and trimmed profiles of a measured beam power density profile

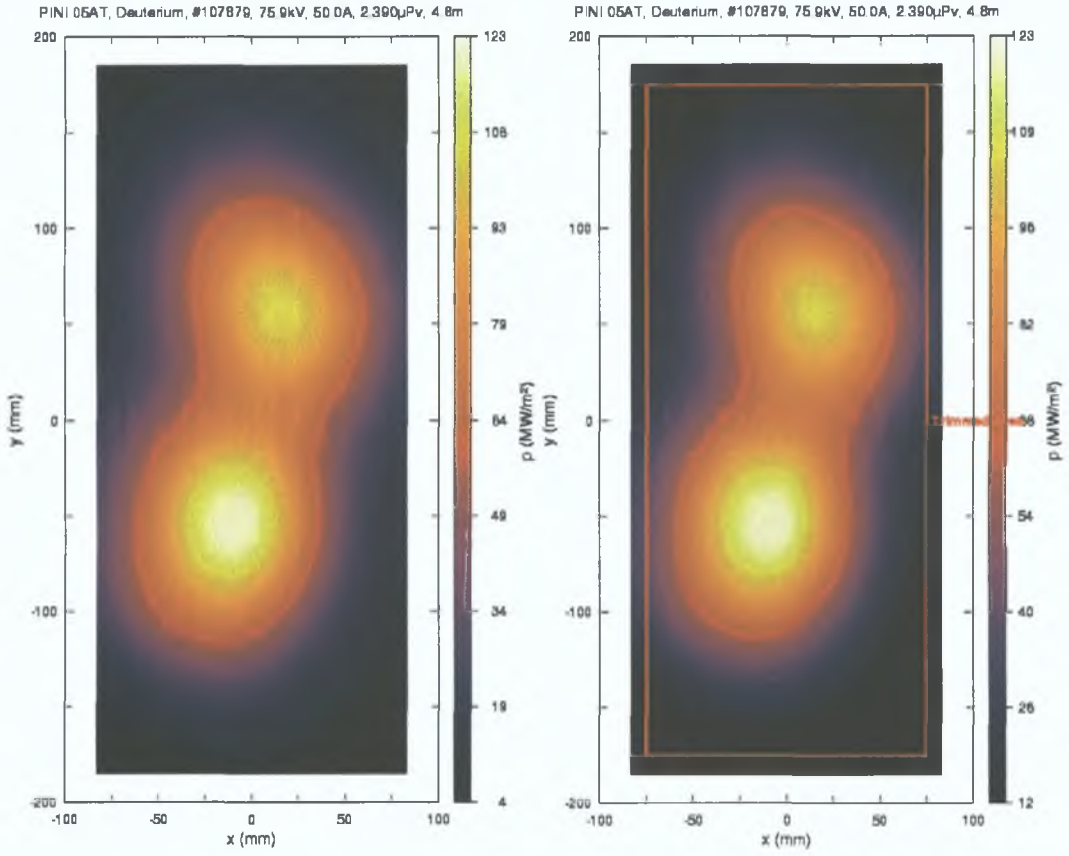

Figure 3.1 :- Raw and trimmed (red box) beam profiles used.

The simulation individually models all 262 beamlets present in the PINI extraction array. Each beamlet is described by a gaussian distribution and is assigned an individual value of current, divergence and steering angle.

The current distribution for each beamlet, in the x-y axes shown by figure 3.1 $i_{beamlet}(x,y)$, is defined from the total beamlet current, $I_{beamlet}$, at a given point downstream, z, by:-

$$i_{beamlet}(x,y) = I_{beamlet}\, e^{-\left(\frac{x-x_{centre}}{X_{initial}+z\theta_x}\right)^2} e^{-\left(\frac{y-y_{centre}}{Y_{initial}+z\theta_y}\right)^2}$$

where x_{centre} and y_{centre} are the beamlet centre point at the distance z, calculated from the initial positions ($X_{initial}$ and $Y_{initial}$)

and the x and y steering angles, Φ_x and Φ_y

$$x_{centre} = x_{initial} + z\Phi_x \text{ and } y_{centre} = y_{initial} + z\Phi_y$$

the gaussian width (at 2 standard deviations) is calculated from the defined initial widths, $X_{initial}$ and $Y_{initial}$, and the beamlet divergences, θ_x and θ_y

For the model of the JET PINI, with circular beam apertures the x and y beamlet divergences are given equal values The calculation of the beamlet gaussian width can also treat convergent beamlets by using a given value of beamlet emittance to calculate the minimum beamlet focal width, however for the JET PINI modelling all the beamlets are divergent so this calculation is not required

At a given distance along the beamline the gaussian current distribution for each beamlet at this point is calculated The contributions of each individual beamlet profile are then summed at this distance to produce the total beam distribution In order to reduce the processing time the sum of the beamlets is only calculated using beamlets that are within a distance of 2 standard deviations from each other

The simulation allows comparison of either the full power density profiles or profiles normalised to the peak power density Comparing normalised profiles enables the simulation to find the conditions that produce the correct beam shape, without having to match the absolute values of the profile After a reasonable normalised fit has been achieved it is then simpler to find the conditions to simulate the real beam profile

The simulation obtains a best fit to either the normalised or full profile by minimising either the square of the difference or the average percentage deviation between the two distributions, depending on the choice of the user

The methods used are -

Difference square - Minimum value of $\sum (Z_{real} - Z_{simulated})^2$

Average % Deviation - Minimum value of $\frac{\sum \left| \frac{(Z_{real} - Z_{simulated})}{Z_{real}} \right| * 100\%}{Npts}$

Each beam defining parameters, described in section 3 3 below, is varied individually by the user to find the minimum value of the Difference Square or the Percentage Deviation A simple algorithm is used by the code to iterates to the nearest best fit value by perturbing the chosen parameter and using a reducing step interval to hunt for the minimum value of the Difference Square or Percentage Deviation As each parameter is adjusted in turn the user moves to the best overall fit to the measured beam profile With the number of unknown variables used by the code it is possible to find some solutions that may only be a 'local' minimum in the difference square or percentage deviations This code requires the user to have some knowledge and experience of the accelerator parameters to avoid letting the code find unrealistic solutions that may appear to reproduce the measured beam profiles, or prevent the minimisation routmes getting 'trapped' by local minima

A 32bit Visual Basic program has been written to perform the minimisation This code uses the core routine used previously to simulate the single line profiles, in effect the main additions have been the profile comparison routme, the minimisation codes and a routme to generate the initial beamlet conditions A sample of the code front panel is shown in figure 3 2

The program initially requests the user to open the data file (* grd) of the profile that the user requires to simulate The user is then prompted to give the extents of the region to be removed from the measured profile by the trimming routine, a default set limits is given that can be accepted At this point the user can either a) enter the beam voltage, beam current, profile distance, PINI type and beam species of the measured power density profile or b) choose to load in the results of a previous simulation. If the user has a data set of the known beamlet current divergence relation for the beam species measured then this can be entered by clicking

on the 'New I-div' button, otherwise the default is used for the given accelerator type. At this point the user must decide whether to fit to the normalised or actual beam profile. The user then selects the parameter for the code to find the best value solution. The user is then expected to find the best values individual parameters until no further improvement can be made in the difference between the simulated and measured profiles.

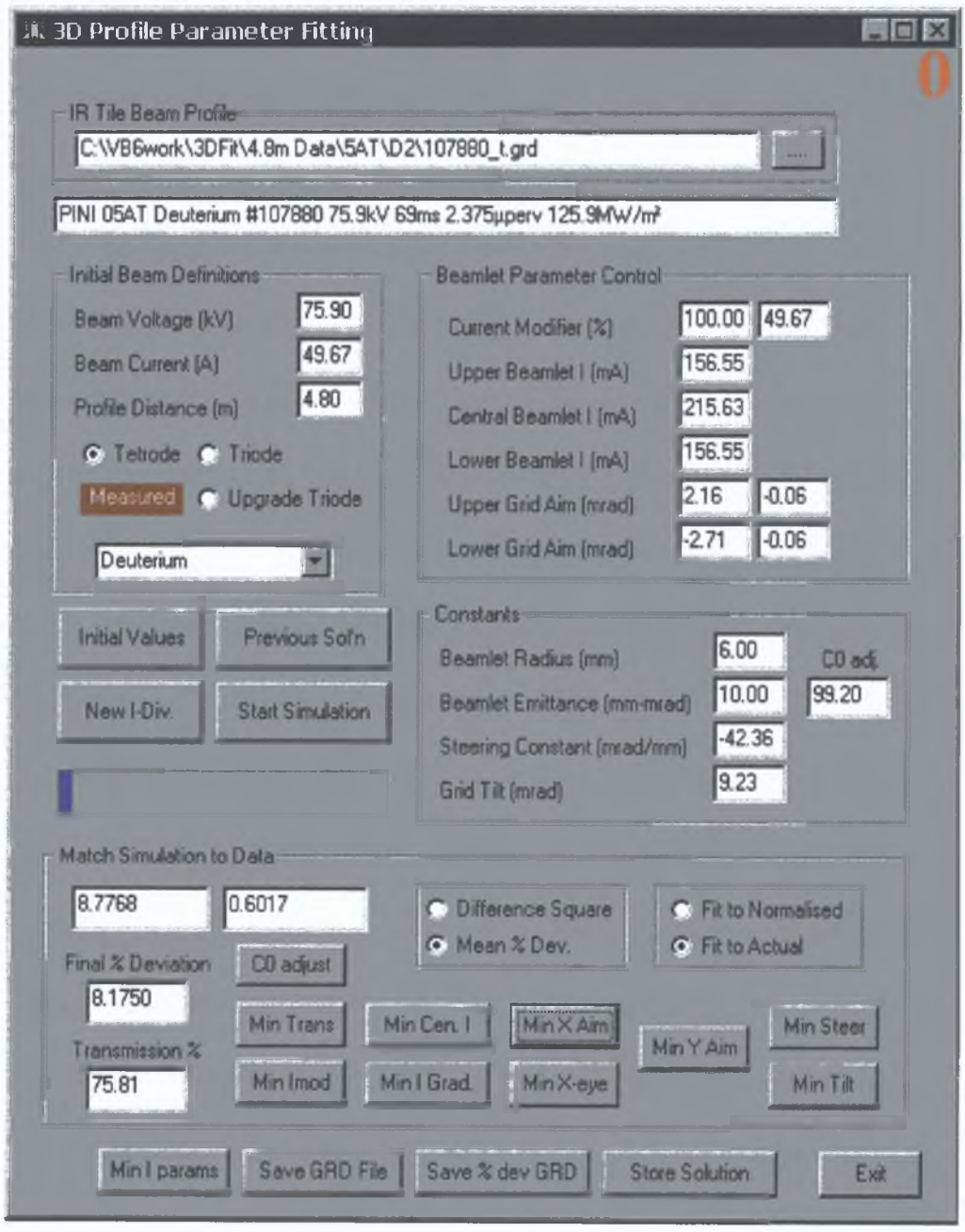

Figure 3.2: Front Panel of 3Dfit code

3.3 BEAM PARAMETERS

It has been attempted to produce as simple a list as possible of the parameters that can describe most of the observed beam behaviour These parameters and their influence on the beam are described briefly in Table 3 1 below, and in more depth in the following sections

TABLE 3 1 Beam defining parameters used in the simulation

PARAMETER	UNIT	EFFECT
Current Modifier	%	$Beamlet\ I = \left[\frac{Total\ Measured\ I}{262}\right] \times \mathrm{Im}od$ Simulates transmission of beam to CFC tile This simulates the loss of beam when the tile is placed downstream of the box scraper
Transmission	%	Simulates IR Window transmission for the absolute value profile comparison (can change depending on window's exposure history)
Central Beamlet Current	mA	Non-uniformity definition (see below)
Beamlet Current Gradient	mA	Non-uniformity definition (see below)
X steering	mrad	Global X aim (to centre compared profiles)
Y steering	mrad	Global Y aim (to centre compared profiles)
X-eye ("cross-eye")	mrad	Grid half horizontal (x-axis) misalignment (simulate observed cross-eye feature of PINIs)
Grid tilt	mrad	Mechanical vertical (y-axis) focusing (nominally 8 3 mrad ≡ 14m focal length) Gives location where the two grid half beams will merge
Steering constant	mrad/mm	Offset aperture steering (nominal values are 36 mrad/mm for the tetrode and 17 mrad/mm for the triode) Gives the vertical (y axis) and horizontal (x axis) focusing property of each grid half

3.3.1 BEAM STEERING AND FOCUSING

The PINI extraction system combines the beams from 262 individual beamlets to form the final extracted beam The required steering and focusing of the beamlets is achieved by two methods -

1 The apertures in each beamlet extraction system are offset relative to the beamlet centre line This produces an electrostatic deflection in the beamlet proportional to the relative offset By this method each beamlet is individually steered about the centre of each grid half to produce a focal point at some distance along the beamline (***Steering Constant***)

2 Each grid half is also tilted in the vertical (y) plane so that the two focused beams from each grid half are combined at the required point (***Grid Tilt***)

A schematic layout of the extraction apertures is shown in figure 3 3

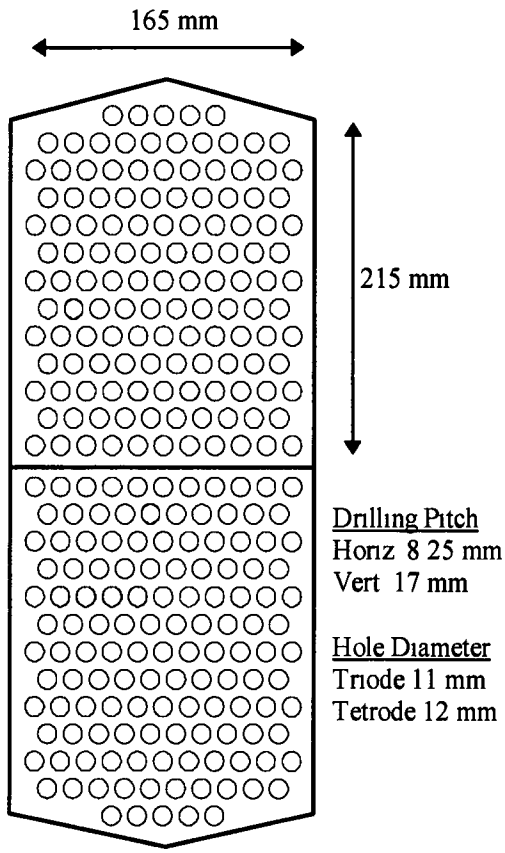

Figure 3 3 Extraction grid aperture drilling pattern

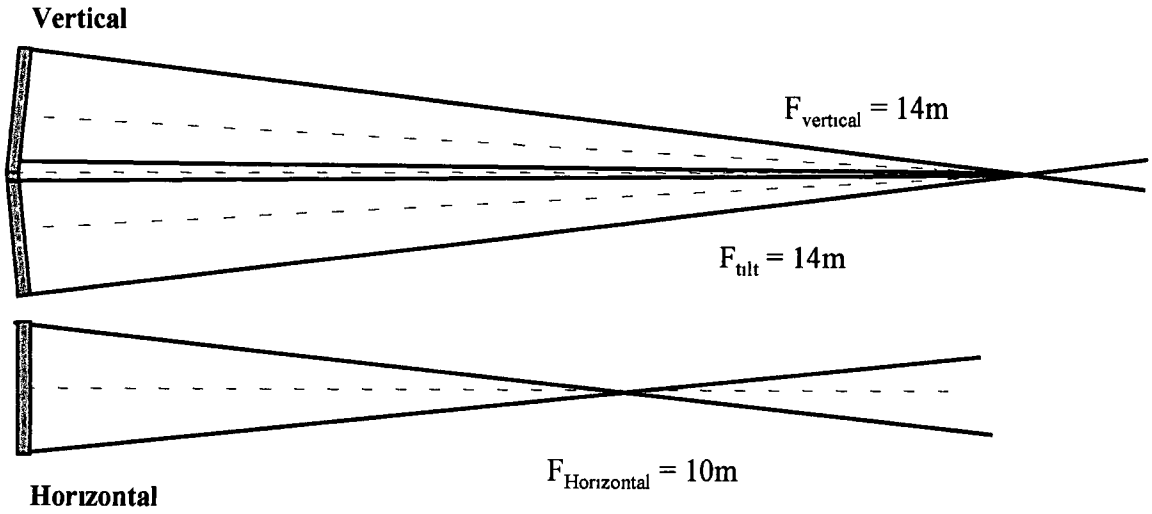

Figure 3 4 Focusing Scheme of the JET PINI beam

Figure 3 4 is a schematic of the focusing pattern, showing the focal points given by offset aperture steering and vertical grid tilt The ***Grid Tilt*** and ***Steering Constant*** parameters

described in Table 3 2 above cover these two beam focusing methods The beamlet steering constant is calculated from the KOBRA3-INP 3D model of the extraction system with offset apertures

Table 3 2 shows the beamlet steering constants derived from both the measured beam focal lengths and the 3D accelerator code KOBRA3-INP The steering constants and focal lengths are shown for the two different accelerator configurations currently used routinely by the JET Neutral Beam Injectors

TABLE 3 2 Beam Profile Model Parameters (with equivalent grid focal lengths)

PINI Measured	**Steering Constant (mrad/mm)**		**Vertical Tilt (mrad)**	**Vertical Focal Length(m) y axis**	**Horizontal Focal Length (m) x- axis**
	Measured	KOBRA3 Simulation			
24AT (80kV Tetrode)	40	42	8 3	14 17	10 16
17BT (140kV Triode)	14	14 5	8 3	13 28	9 53

The parameters ***X steer*** and ***Y steer*** are applied to the beamlets of both of the grid halves to produce a global steering of the beam, this allows the simulated profile to be aligned with the measured power density profile The ***X eye*** parameter is applied in opposite directions to each grid half to simulate the observed horizontal (x axis) separation of the beams from each grid half Figure 3 5 illustrates the cross-eye of a beam extracted from an 80kV tetrode accelerator (PINI 05AT), it is this cross-eye phenomenon that contributes significantly to extra beam power loading on beam line scrapers as the effective beam width is increased by this horizontal misalignment

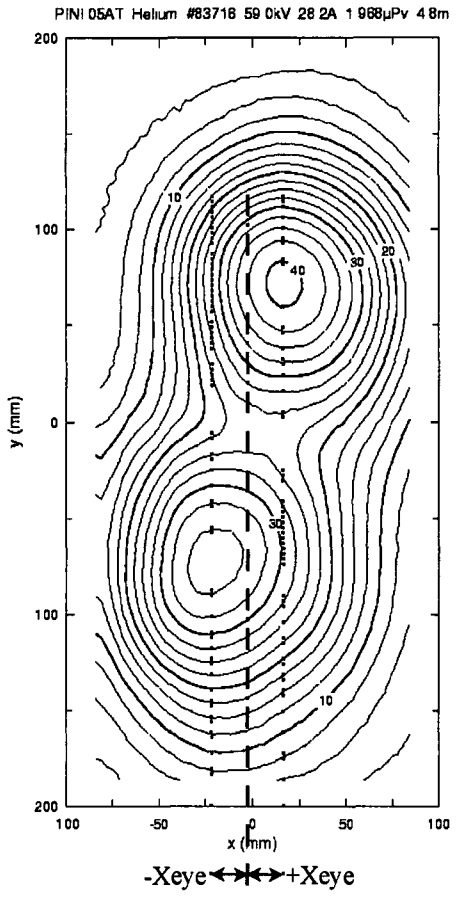

Figure 3 5 - Measured beam power density profile from PINI 05AT, showing clearly the vertical (y) separation of the beams produced by each grid half - and the longitudinal separation that is known as beam cross-eye

3.3.2 ION DENSITY UNIFORMITY

The ion density uniformity profile is defined by giving the value of the centre beamlet current When the value of the centre beamlet current is changed the code recalculates the values of the outermost beamlet currents for each grid half (I_{upper} and I_{lower}) so that the correct total beam current is maintained The individual beamlet currents are calculated by a quadratic expression to generate a parabolic profile, and the total beam current is the sum of all the beamlet currents

For the upper and lower grid halves the vertical beamlet current profile is given by:-

$$I_{beamlet} = I_{centre} + \left(\frac{I_{upper} - I_{centre}}{Y_{upper}^2} \right) y_{beamlet}^2 \qquad \text{and} \qquad I_{beamlet} = I_{centre} + \left(\frac{I_{centre} - I_{lower}}{Y_{lower}^2} \right) y_{beamlet}^2$$

where Y_{upper} and Y_{lower} are the vertical distances of the rows of beamlet apertures furthest from the grid centre. $y_{beamlet}$ is the vertical position of the beamlet for which the current is calculated. (the horizontal (x) and vertical (y) axes for this calculation are shown in figure 3.1)

In addition the horizontal beamlet current profile is similarly calculated by using double the value of the vertical gradient, chosen since the horizontal (x) width of the source is almost exactly half that of the vertical (y) dimension. This generates a profile with a parabolic shape in both directions, this distribution is chosen as a reasonable approximation to the beamlet divergence profiles seen by the multi-channel spectrometer. The profile shown in Chapter 2, figure 2.7 of the beam perveance where the minimum beamlet divergence occurs can be reasonably approximated with a quadratic polynomial. This simplified definition of non-uniformity is used in the simulation in order to reduce the number of unknown variables in the simulation and best-fit routines to a manageable level.

A global gradient I_{grad} is also allowed across the whole vertical (y) length of the ion source.

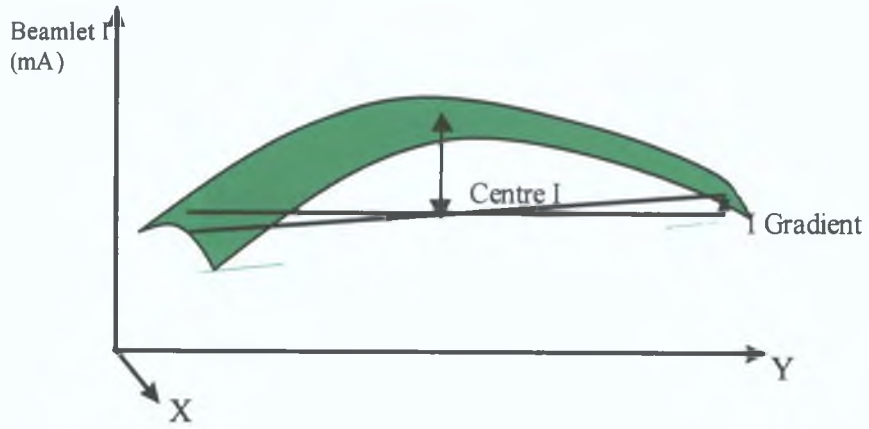

Figure 3.6: Schematic of the source non-uniformity simulation

3.3.3 BEAMLET DIVERGENCE

The simulation uses a beamlet divergence relation derived from multi-channel spectroscopic measurements. Initially the measurements of PINIs 23BT and 14AT were used to produce a standard current-divergence relation for each PINI type, now that these measurements are taken more routinely the code can now accept the measures current-divergence relation for each individual PINI. The data shown in figure 3.7 is the beamlet divergence measured at the centre and uppermost fibres, expressed as an equivalent beamlet perveance (i.e. beam perveance divided by 262). It is clear that the beamlet current–divergence relationship changes across the accelerator. This is possibly as a result of accelerator grid bending changing the first gap distance across the accelerator array [25]. The fibre closest to the point with no vertical (y) offset aperture steering (at the half grid centre) appears to give a good compromise between the two extremes. A quadratic fit to this fibre position data is then used to derive the beamlet divergence from the local beamlet perveance during simulation

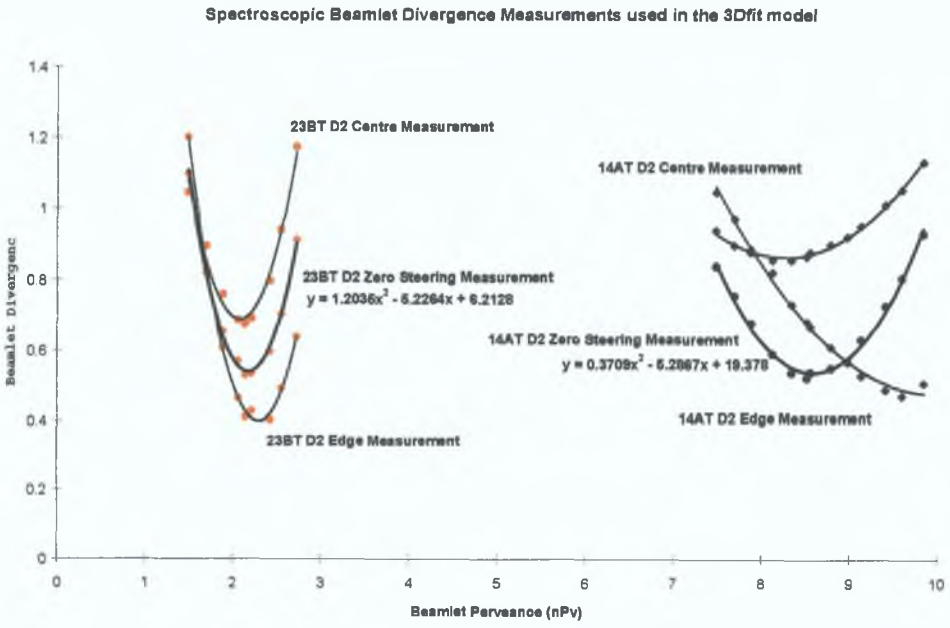

Figure 3.7: Beamlet perveance – divergence relationship used in the 3Dfit model

This data is used for the modelling of PINIs where is no data has been taken from the multi-channel spectrometer. Where good spectroscopic data is available the measured beamlet-

current divergence relationship can be entered into the model to override the generic data The code allows the data measured for each individual grid half to be entered, at the zero offset aperture steering point

3.4. SAMPLE SIMULATION

To illustrate the operation of the 3Dfit simulation this section shows the results of using the 3Dfit code to simulate the beam power density profile the high voltage triode PINI 23BT, extracting a helium beam

3.4.1. 23BT 132KV HE BEAM

The beam power density profiles from this PINI were chosen for initial analysis since a good set of both IR calorimeter profiles and spectroscopy measurements are available The beam profiles were simulated across a perveance scan from 0 359μPv to 0 522μPv, where the 'optimum' perveance from beam dump measurements is 0 437μPv

Figure 3 8 below shows the contour plots to compare the actual and simulated profiles of the 23BT He beams at 0 437μPv The final minimised value of the average percentage deviation between the two profiles 3 46%

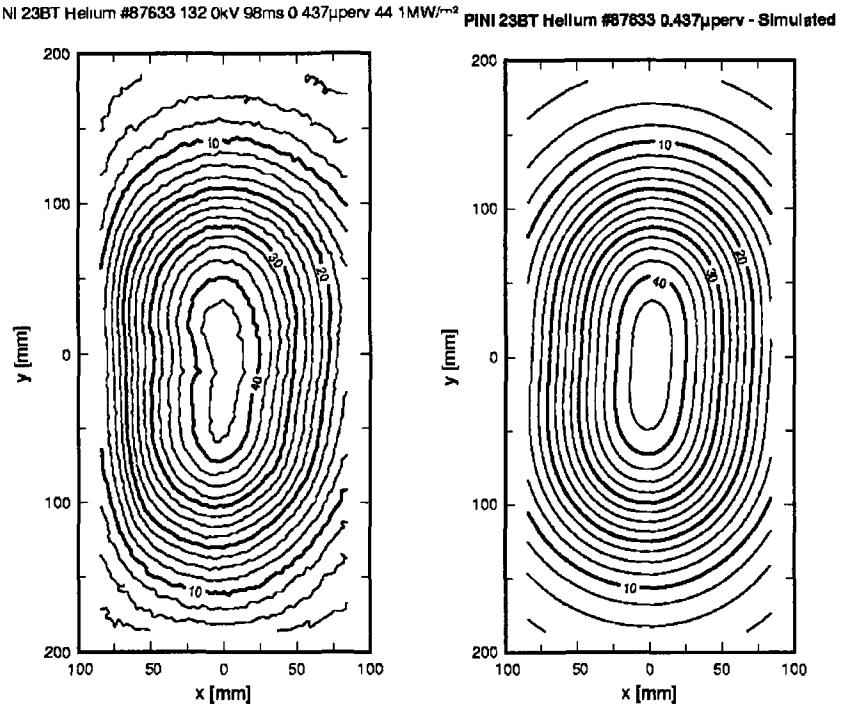

Figure 3 8 - Measured and Simulated Beam profiles of 23BT He

The model appears to lose some of the detail of the profile peak, but matches the bulk of the profile reasonably well This is acceptable, as one of the intended purposes for these simulations is to provide information on scraper loadings, which will require better simulation of the beam edges than necessarily knowing the details of the beam centre

A summary of the simulation parameters required to model the profiles measured in a perveance scan is given in the figures below

The two graphs below (figures 3 9 and 3 10) show the beamlet current non-uniformity generated by the model with the resulting beamlet divergence distribution The plots show the beamlet current and divergence profiles along the vertical (y) centreline of the extraction array

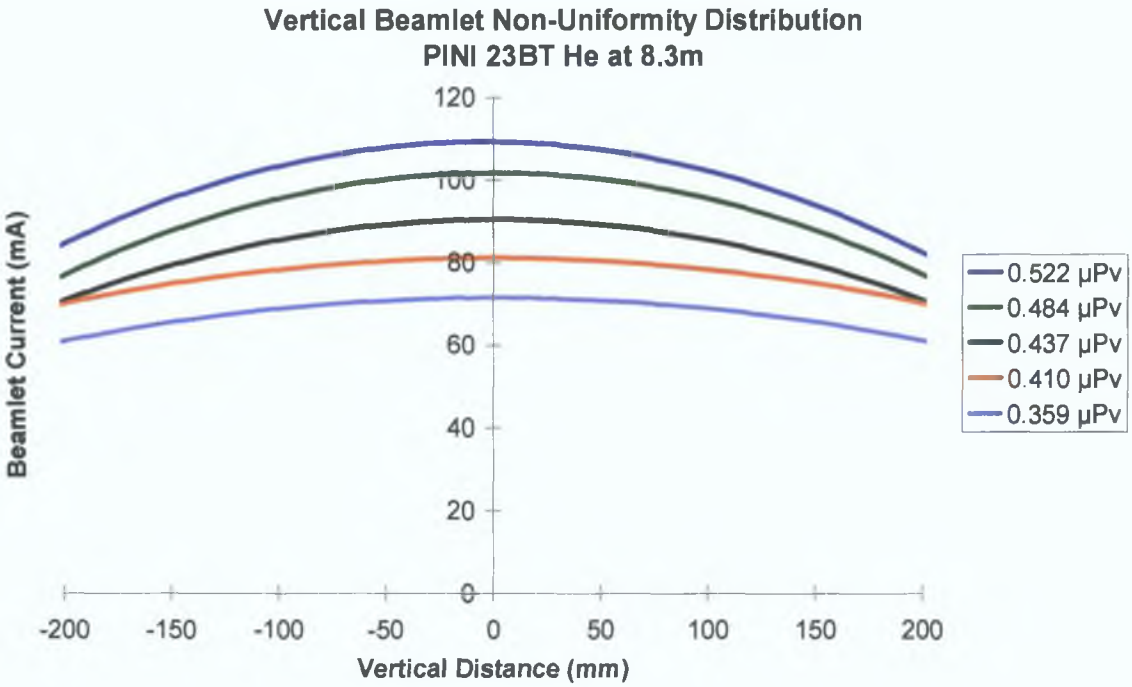

Figure 3.9: - Vertical (y) Beamlet current distribution vs. perveance

The beamlet divergence distribution generated by the simulation agrees quite well with the multi-fibre spectroscopic measurements (figure 3.10). In both the 3Dfit simulation and the spectrometer measurements the position where the minimum beamlet divergence occurs moves from the centre towards the outside of the beam, with increasing beam perveance.

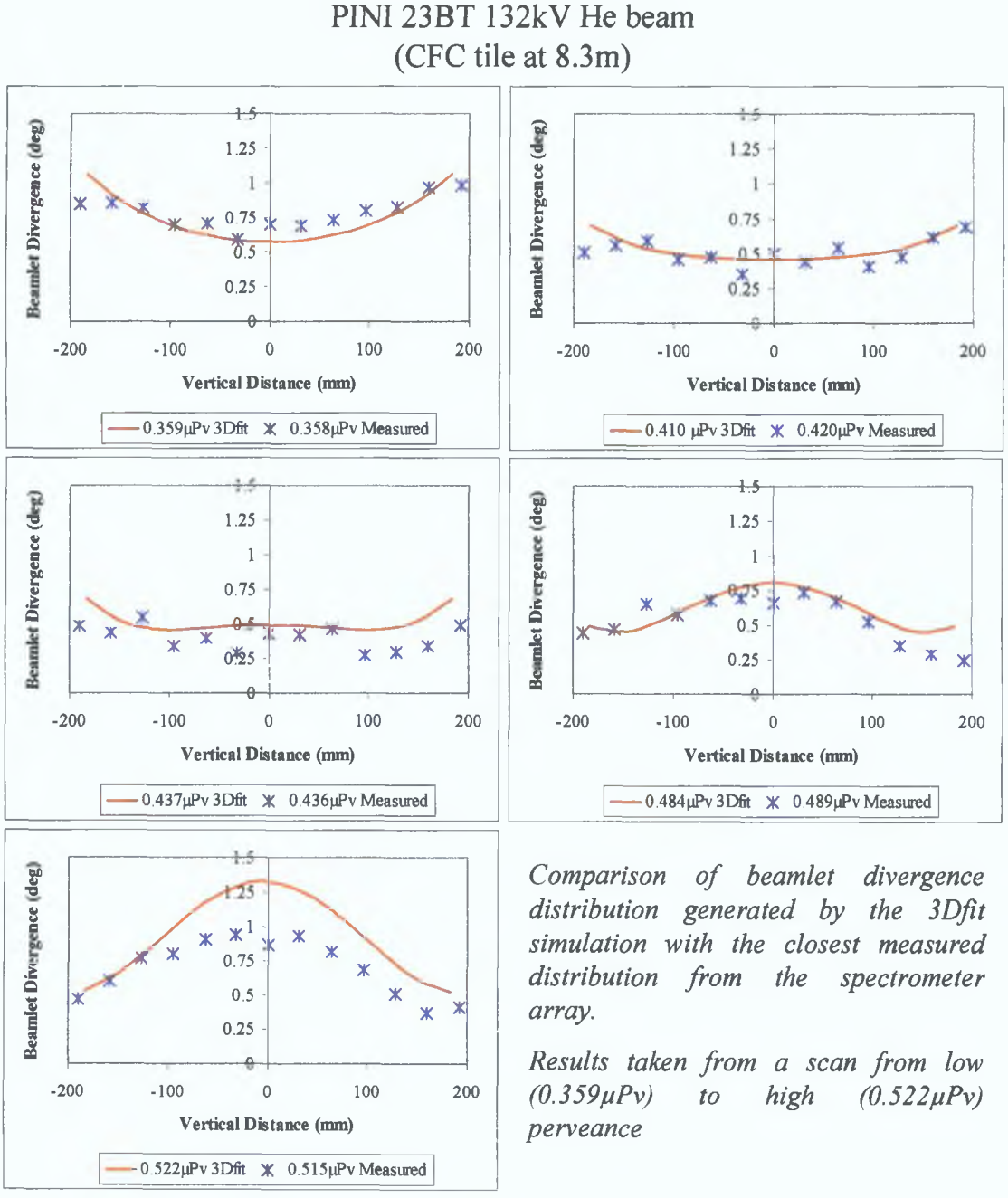

Comparison of beamlet divergence distribution generated by the 3Dfit simulation with the closest measured distribution from the spectrometer array.

Results taken from a scan from low (0.359μPv) to high (0.522μPv) perveance

Figure 3.10: - Vertical (y) Beamlet divergence distribution vs. perveance

For the profiles shown in figure 3.9 a non-uniformity parameter is defined from the root mean square (RMS) deviation of the actual profile from an equivalent uniform profile, over the length of the vertical (y) centreline. This calculation is discussed in more detail in Chapter 6,

but is given here as an example In this case the mean RMS deviation of the current profiles shown in figure 3 9 from a uniform profile is 6 8%

3.5 CHAPTER SUMMARY

A code has been written to analyse the detailed beam power density footprints measured on the Carbon Fibre Composite tile exposed to beams on the Neutral Beam Test Bed This analysis uses known properties of the accelerator aperture extraction array and a model of the ion source non-umformity The ion uniformity model describes the ion density distribution in the ion source with a parabolic shape, which is generally consistent with the measurements of the multi-channel spectroscopic array The code finds best-fit values for each parameter so that the difference between the simulated and measured power density profiles is minimised This has successfully reproduced the power density footprints measured for a variety of beams extracted from different PINI types with different beam species, m this chapter the example of PIN23BT is given, a 140kV/30A triode accelerator extracting a He beam The 3Dfit code is used in the following chapters to give quantitative measures of the non-uniformity of the ion sources tested

4 ION SOURCE MODELLING

4.0 INTRODUCTION

In parallel with an experimental program of ion source development, a Monte Carlo code was developed to simulate and attempt to predict the behaviour of various ion source configurations This method was chosen based on the successes of S Ido and others to model ion sources in a similar way [26,27,28] This computer model follows single charged particle trajectories through a simulation of the 3D magnetic field that is present in the ion source This model does not include the effect of electric fields, all results are due to the motion of charged particles in the magnetic field alone A Monte Carlo method is then used to randomly determine the routes of the most significant particle interaction paths The initial aim of this code is to follow the primary electrons, emitted from the filament cathodes, to determine where the bulk of the ionisation of the neutral source gas occurs Once the regions where the ionisation of the source gas are identified, this is used as the initial conditions of an ion trajectory simulation Following ion trajectories through the source, in a similar way to the primary electron trajectories, allows the simulation software to derive the ion density distribution through the ion source

4.1 JET PINI ION SOURCE MAGNETIC FIELD ARRANGEMENT

The ion source used in the JET PINI is a water-cooled copper chamber with approximate internal dimensions of 580mm ×300 mm × 210 mm (length × width × depth) Over the external walls of the source are arrays of SmCo magnets which are arranged to give partial confinement of the plasma [29] The source is evacuated using an arrangement of turbo-molecular and Liquid Helium cryo-adsorption vacuum pumps, with a continuous flow of feed gas (Isotopes of Hydrogen or Helium) into the source resulting in a typical gas pressure of 4 μbar Internal to the chamber are 24 filaments (length and diameter) which are heated to emission by an AC power source, distributed via the filament transformer mounted at the back of the PINI In addition to the AC heating, 80-100 Volts DC voltage is applied to the filaments resulting in up to 1300 Amps of DC current to the grounded chamber walls

In total 363 SmCo permanent magnets are used on the external surface of the PINI ion source The basic arrangement used is a chequerboard pattern, which produces the strong short-range multpole fields required for good plasma confinement In addition to this, some of the magnets are arranged to produce a weaker long range field that reaches from the centre of the ion source backplate to near the base of the ion source walls This 'filter' field acts to isolate the extraction region of the ion source from the primary electrons emitted from the filaments This effectively separates the ion source into regions of distinctly different electron temperature, a hot region where the primary electrons are present and a cooler region where only primaries of reduced energy can reach The region of higher electron temperature is where the source gas ionisation mainly occurs, in the cooler region dissociation processes are dominant, leading to an enhancement of the monatomic species yield

The source magnet configuration of most interest is the super-cusp configuration SC15S3 used in all of the JET PINI ion sources to date This was chosen after some development as giving a good combination of arc efficiency, monatomic species yield and ion uniformity Figure 4 1 shows a schematic of the magnet pattern used, with the reference coordinate frame used in these simulations

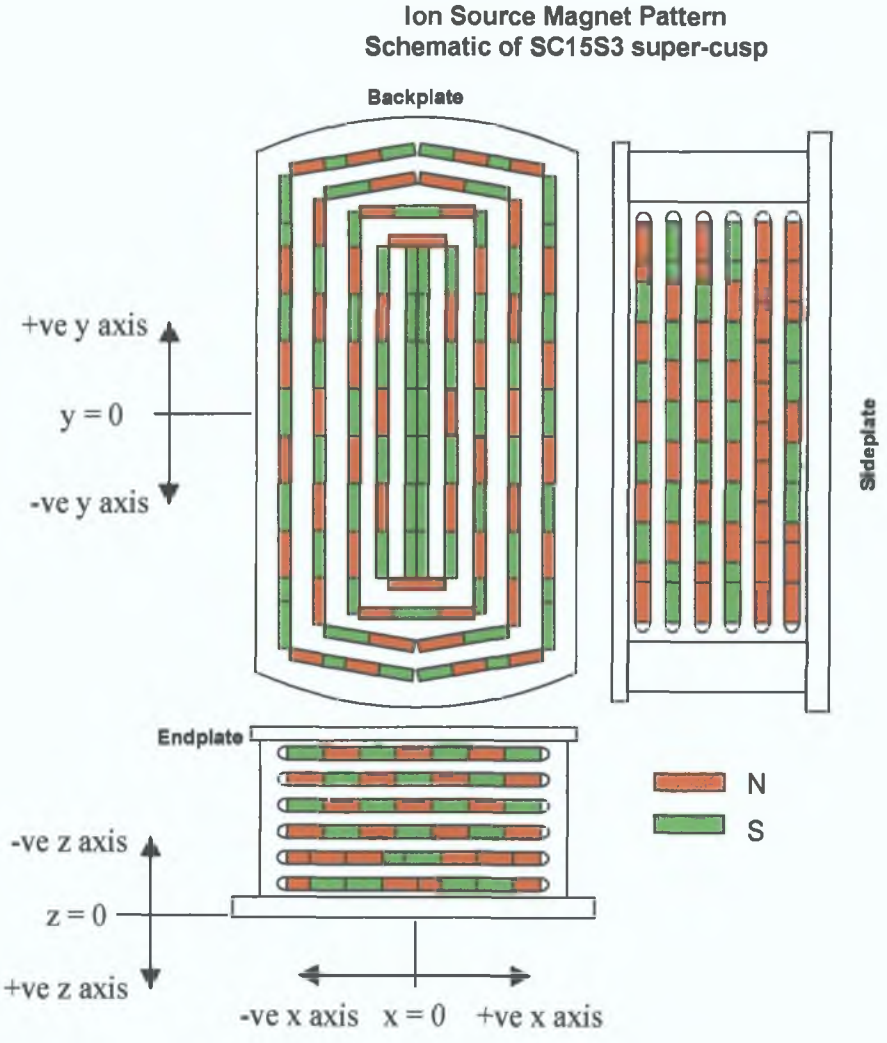

Figure 4.1 Schematic of the SC15S3 super-cusp magnet configuration (viewed from the outside of the ion source)

4.2 MAGNETIC FIELD MODEL

Each of the ion source magnets is defined by its position, orientation, size and field strength, the components of the vector of magnetic field $\vec{B}(r)$ are calculated using analytical expressions. The magnetic modelling code produces a 3D-field map of each component (B_x, B_y and B_z) of the magnetic induction with a predefined mesh density, by superimposing the field of individual magnets. This mesh of field points is stored for later use by trajectory

tracing codes [See Appendix A for a detailed description of the permag32 exe code] In order to find the magnetic field at any given point within the mesh a fifth order polynomial fit is used in each direction to interpolate the field components at that point This provides a good method of determining fields unless regions very close to the magnet surface are considered, here the magnetic field gradients are very high, leading to significant errors in interpolation

A full 3D model of this field in the SC15S3 ion source has been calculated at a mesh resolution of 5mm Graphical output of the modelled field map indicating the structure of the super-cusp is shown in figure 4 2 below

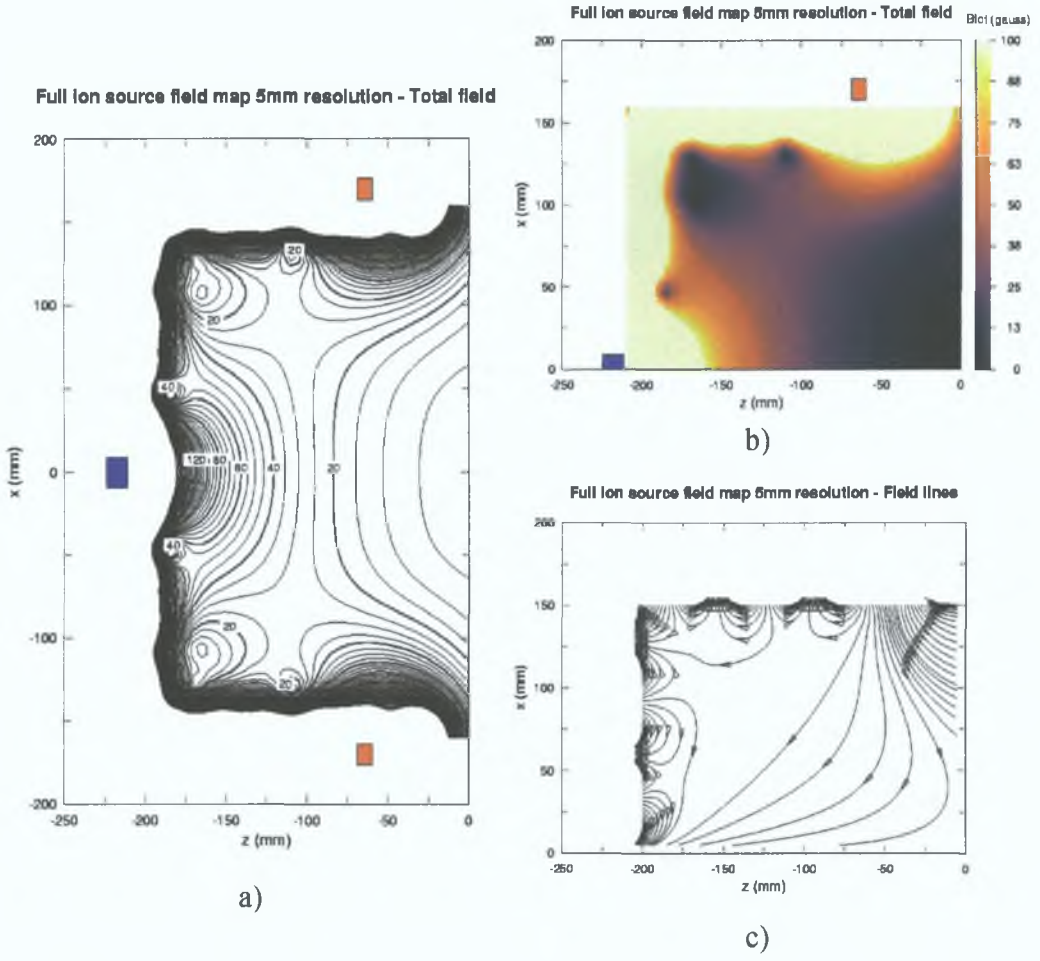

Figure 4.2 Magnetic model of the SC15S3 super-cusp configuration a) A contour plot of the mid plane across the ion source (short direction) where z=0 is the extraction plane and the back plate is at z=-210mm. The magnets responsible for the super cusp field are highlighted. b) A contour band plot of the super-cusp field that more clearly shows the saddle of the cusp field. c) A field line plot that shows both the long-range fields of the super-cusp and the short-range fields of the chequerboard magnet pattern close to the source walls.

Figure 4.2c shows the field lines of the super-cusp field across a half section of the source through the plane across the centre of the short dimension of the ion source. An indication of the filter field strength can be seen from the total field contour plot of figure 4.2a. Typically the filter field has a peak strength of ~30 Gauss.

4.3 SINGLE TRAJECTORY TRACING

The first step in the ion source model is to produce particle trajectories in the magnetic field pattern modelled inside the ion source The differential equation of the particle trajectory is solved by a stepwise controlled Runge-Kutta integration For this model, electric fields are not considered so the particle motion is governed by the Lorentz force alone

The equation of motion $m\frac{d^2s}{dt^2} = Bev$ is solved in each plane of motion

The trajectory is split into small integration steps of the order of a few mm The trajectory is traced over this integration step with an initially low number of intermediate points, the integration is then repeated with a doubled number of steps and the end points of the trajectory calculation is compared This process is repeated until the difference in the trajectory endpoints falls below a given error value, typically <0 1%

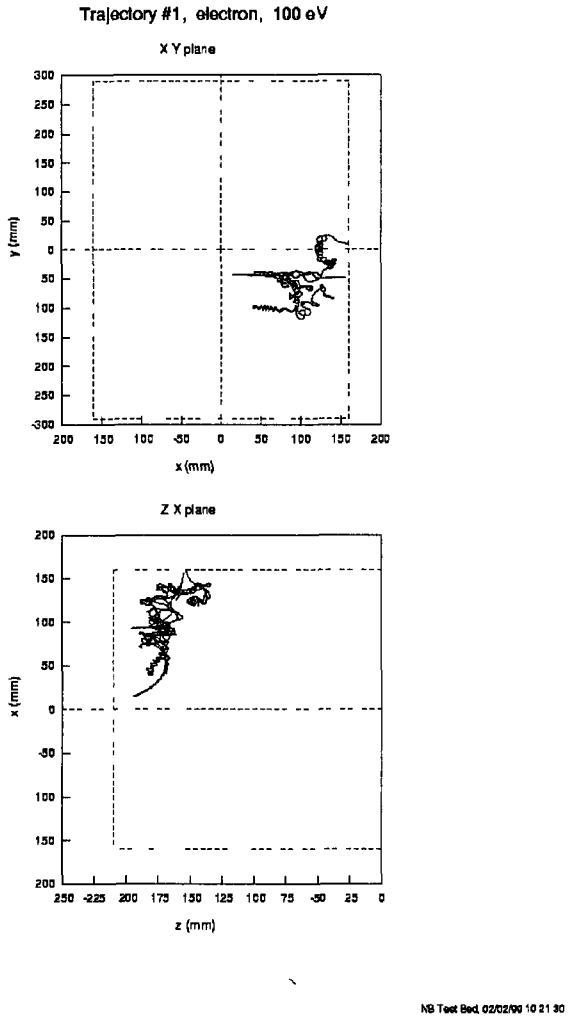

Figure 4 3 Single 100 eV electron trajectory in the SC15S3 super cusp field The XY plane is viewed from the front of the ion source and the ZX plane is the same as that shown in the field plots of figure 4 2

The first step in this model is to calculate particle trajectories without interaction, primarily to confirm the correct function of the code This also gives an early indication of the primary electron confinement provided by the super-cusp and chequerboard fields Figure 4 3 shows a single 100eV electron launched from a filament location and traced for a total path length of 2 5m, before the electron is lost to the source wall

The electron trajectory shown in the ZX plot is clearly confined behind the super-cusp field, and can also be seen to precess around the ion source in the XY plot, perpendicular to the

super-cusp field It is useful to compare this trajectory plot with figure 4 2c above to show the line of the filter field in the ZX plane

4.4 ELECTRON INTERACTIONS

The step that turns particle trajectory tracing into a model of the ion source is the addition of particle interactions The first phase of this step of the modelling is to add the significant interactions of the primary electrons The primary electrons are launched from the filaments with an initial energy of the order of 100 eV, which drives the ionisation of the neutral source gas

The most significant interactions of the primary electrons, in terms of having the shortest mean free path, are elastic, ionisation and dissociation collisions Specifically these reactions are -

Elastic	$e + H_2 \rightarrow e + H_2$	(ELA)
Ionisation	$e + H_2 \rightarrow H_2^+ + 2e$	(ION)
Dissociation	$e + H_2 \rightarrow 2H + e$	(DIS)

Other reactions with smaller cross sections, or those with cross sections that are only significant below the H_2 ionisation potential are not considered in this model Of the reactions investigated during the construction of this model the excitation reactions of the H_2 source gas appear to generally fall into the latter category The main aim of this model is to provide information on the ionisation reactions of the primary electrons and so the primary electron trajectory tracing will be halted once the electron energy falls below the ionisation potential In the case of the JET PINI ion source the plasma density is typically only a few percent of the filling gas density For this reason primary electron interactions are not considered with the plasma ion population, as no reactions with large enough cross sections to compensate for the 2 orders of magnitude reduction in target (plasma ion) density were identified

The energy dependant cross-sections for each of the above reactions with the neutral source gas are obtained from a database [30] A Chebyshev polynomial fitting routine is used to

interpolate continuous data across the electron energy region of interest (typically 0 to 100eV). The mean free path (L_{REAC}) for each reaction is then calculated for a given source gas density (N_0) as a function of the electron energy (E_p): -

$$L_{REAC}(E_p) = \frac{1}{\sigma(E_p)N_0}.$$

A sample calculation of the individual mean free paths, as a function of the electron energy, for a typical source gas density of 3.8×10^{19} m^{-3} is shown in figure 4.4

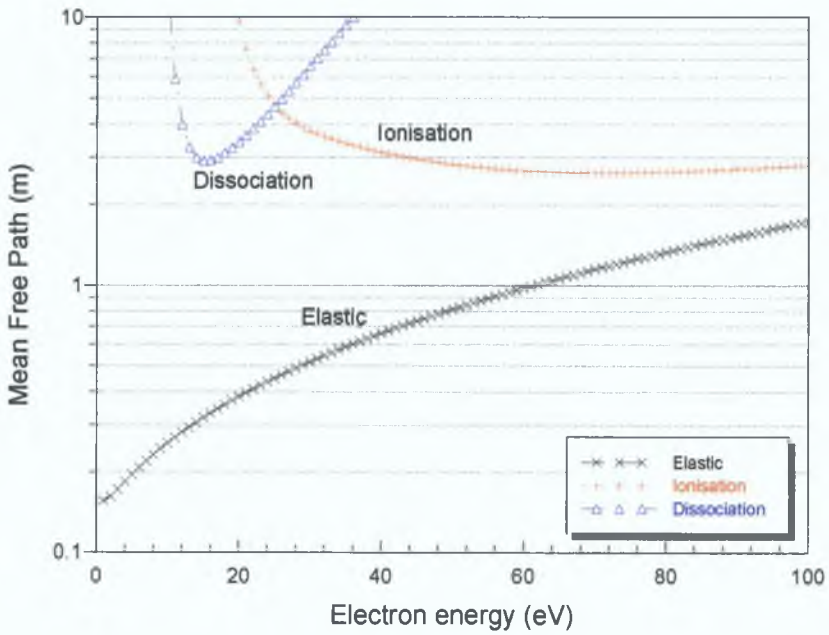

Figure 4.4:- Mean Free Path Lengths for the Elastic, Ionisation and Dissociation processes for electrons with a 3.8×10^{19} m^{-3} H_2 density

Using one random number per reaction, in this case 3 numbers $R_{1\text{-}3}$ chooses the electron trajectory length. A trajectory length is calculated for each reaction with the random numbers

$$l_{ELA} = -\lambda_{ELA}\log_e(R_1)$$
$$l_{ION} = -\lambda_{ION}\log_e(R_2)$$

$$l_{DIS} = -\lambda_{DIS} \log_e(R_3)$$

the reaction that gives the minimum trajectory length is thus chosen. The trajectory calculation then follows an electron for this (minimum) trajectory length, at which point the interaction occurs.

The relative probability of each reaction being chosen will thus be proportional to the relative values of the inverse of each of the mean free path lengths. The resulting reaction probability distribution for the mean free path example of figure 4.4 is given below in figure 4.5, normalised to a total probability of 1.

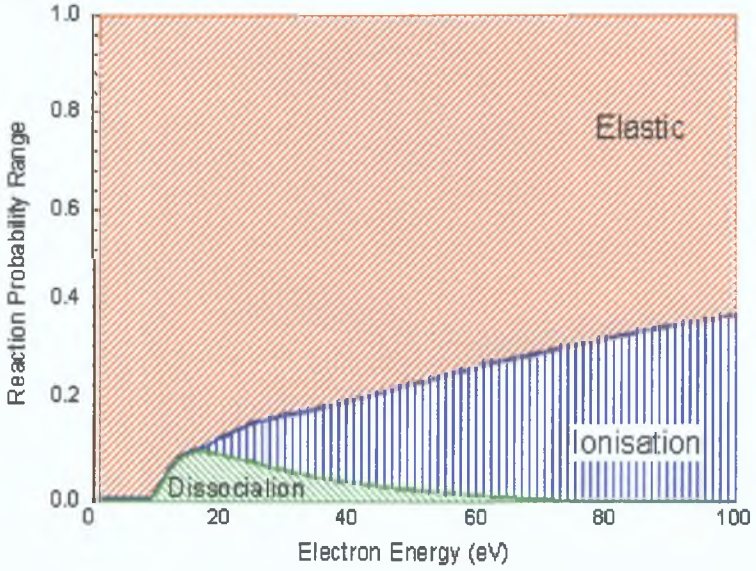

Figure 4.5:- Probability function generated from the mean free path lengths given in figure 4.4. (at 3.8×10^{19} m^{-3} H_2 density)

4.4.1 ELASTIC COLLISIONS

When an elastic collision is chosen the electron continues its trajectory with an unchanged energy. The electron trajectory is then given a random deflection equally weighted in all directions. Although this is not necessarily the most physically realistic model, the intention of this is to provide an extra degree of randomisation into the model. In this way, it is

intended that repeating models with identical initial conditions will quickly produce many different outcomes This should further remove any bias given by the use of multiple runs with identical initial conditions

4.4.2 DISSOCIATION REACTION

The dissociation reaction is treated by reducmg the electron energy by the reaction threshold energy (8 5eV) plus a random amount of the remaining energy -

$$\Delta E = E_{THRES} + Rnd(0\ \ 1)\left[E_p - E_{ITHRES}\right]$$

This attempts to simulate some transfer of energy to the dissociated H atoms The electron trajectory is then continued without deflection, it seemed unnecessary to calculate the electron deflection in this case given that elastic collisions produce a large degree of extra randomisation into an already eccentric electron trajectory

4.4.3 IONISATION REACTION

The ionisation reaction, being of most interest in this part of the simulation, is given a more rigorous treatment The Binary Encounter Approximation [31,32] gives a theoretical model of the doubly differential cross-section for the ionisation reaction This expresses the cross-section as a function of the ejected electron energy, W, and its angular distribution, θ

$$\frac{\partial\sigma}{\partial W\,\partial\theta} = \sigma(W,\theta)$$

As with the dissociation reaction it was decided that for this simulation the angular deflection could be neglected for this reaction, the most important factor here is a realistic model of electron energy loss

Integrating the doubly differential cross-section gives the single differential cross-section as a function of ejected electron energy -

$$\frac{\partial\sigma}{\partial W} = \int \sigma(W,\theta)\, d\theta = \frac{S}{I(t+2)}\left[\frac{1}{(w+1)^2} + \frac{4}{3(w+1)^3} + \frac{1}{(t-w)^2} + \frac{4}{3(t-w)^3} - \frac{1}{(w+1)(t-w)}\right]$$

where I is the molecular ionisation threshold potential (15 4eV), the dimensionless variables $w = W/I$ and $t = T/I$, with T being the primary electron energy Also $S = 4\pi a_0^2 N(R/I)^2$, with a_0 the Bohr radius, N the number of electrons in the target and R the Rydberg energy (13 6eV)

Further integrating gives the total ionisation cross-section, which then simply gives the probability distribution for the ejected electron energy -

$$P(W) = \frac{\sigma(W)}{\sigma_{ion}}$$

This is turned into a form where a random number, x, chosen in the range 0 to 1 selects the ejected energy by integrating the probability distribution

$$W(x) = \frac{\int_0^W P(W)\, dW}{\int P(W)\, dW}$$

Sample calculations of these probability functions for a primary electron energy of 100eV are given in figure 4 6 These show that an electron ejected with high energy is as likely to occur as a primary with a small energy loss The simulation then continues with the most energetic particle remaining from this reaction

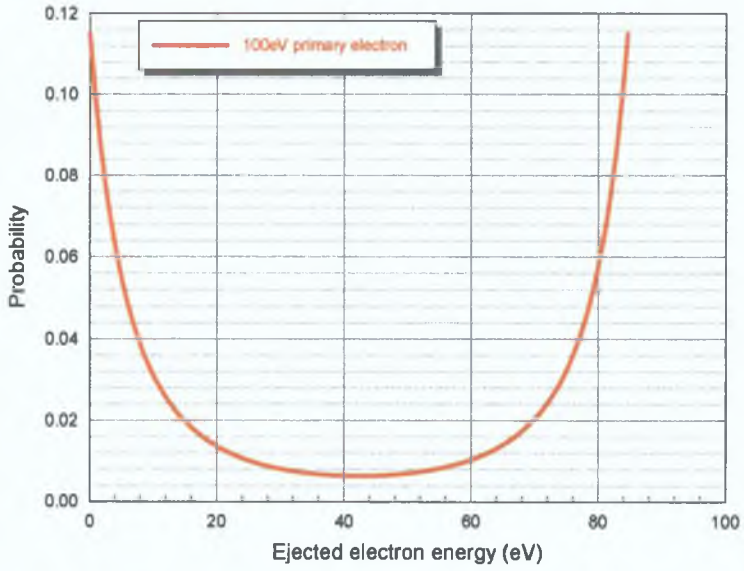

a)

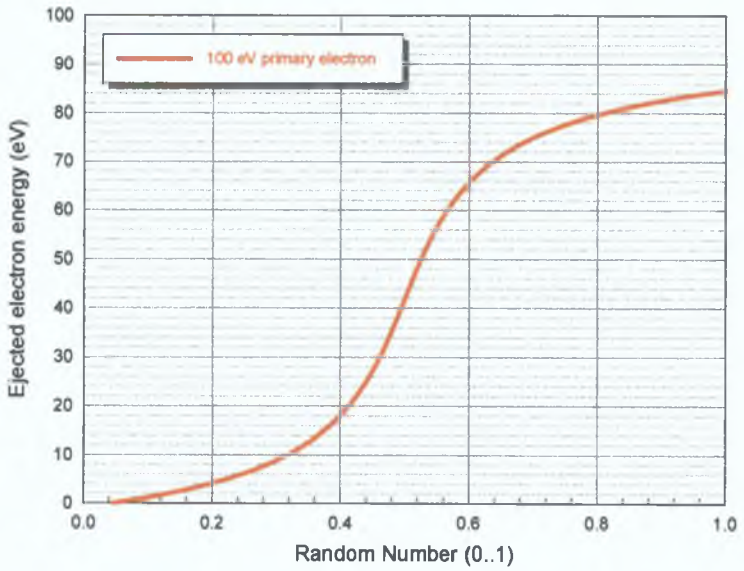

b)

Figure 4.6: - a) The probability function, given by the Binary Encounter Approximation to the H_2 ionisation, for an ejected electron energy given a 100 eV primary electron. b) The probability function modified so that a random number chosen in the range (0..1) selects the ejected electron energy.

The secondary electron from the ionisation collision, i.e. the lower energy particle, is stored if its energy exceeds the minimum threshold energy for the model. After the first run of the code is completed then the file of secondary particles is read and these electron trajectories are

traced, generating a further secondary file if necessary The results from tracing these secondaries are added to the results of the initial run of the model This stops any systematic errors building from tracing only the highest energy electron resulting from each collision

4.4.4 COULOMB COLLISIONS

The energetic primary electrons also experience collisions with the thermal background of electrons In the case of the PINI ion source, the plasma density is typically a few percent of the source gas density The energy loss of the primary electrons is expressed by [33,34] -

$$\frac{d}{dt}E_p = -\upsilon_\varepsilon^{\alpha/\beta} E_p$$

where E_p is the primary electron energy, in the case where $E_p > T_e$,

where T_e is the 'background' electron temperature,

and $\upsilon_\varepsilon^{\alpha/\beta} \approx 7.7\times10^{-6}\,\psi(x)E_p^{-3/2}\,n_e\,\lambda_{\alpha\beta}$

where $x = \frac{E_p}{T_e}$, $\psi(x) = \frac{2}{\sqrt{\pi}}\int_0^x dt\, t^{1/2}\, e^{-t}$ and $\lambda_{\alpha\beta}$ is the Coulomb Logarithm

where for thermal electron-electron collisions of $T_e \le 10\ eV$, $\lambda_{ee} = 23 - \ln\left(n_e^{1/2}T_e^{-3/2}\right)$

The primary energy loss is calculated in the form eV/m and the total energy loss for the path length between interactions is calculated This is then subtracted from the primary electron energy after the interaction process has been calculated

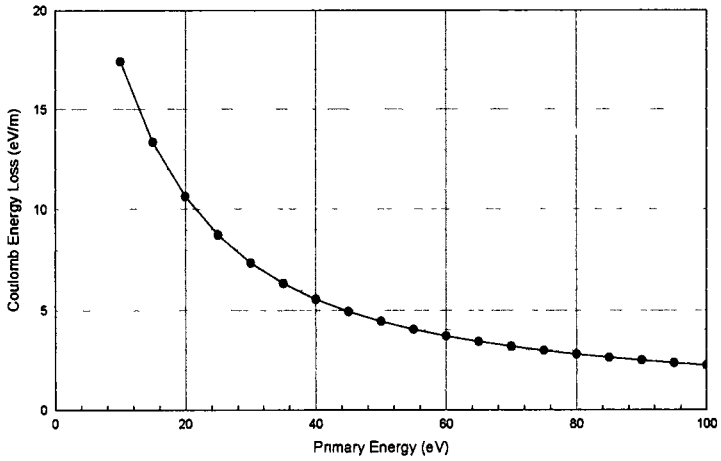

Figure 4 7 - The electron-electron Coulomb collision energy loss for a primary electron moving through a background electron density $n_e = 1\,5\times10^{18}\,m^{-3}$, *with temperature* $T_e = 5eV$

As with all Monte-Carlo codes the statistical significance of the resulting output is a function of the number of trajectories that are traced by the model - and the time required to produce the simulation In the following sections of this chapter concerning use of this model most of the examples are shown with input data sets chosen to run within a working day (or overnight) on a 350MHz Intel Pentium II PC with 128Mb RAM, running Microsoft Windows NT 4 These mput data sets give results that are meaningful to experienced users in a reasonable time Clearly at the current rate of evolution of processing performance available to the PC user the same working time will, in the near future, be able to produce results of improved statistical significance To ensure that multiple simulations using an identical set of initial conditions do not produce an identical outputs, the random number generator sequence used by Visual Basic is initialised with a starting seed generated as a function of the system clock time – so that the same random number sequence is unlikely to be repeated

4.5 MODELLING THE SC15S3 SUPER-CUSP ION SOURCE

The SC15S3 super-cusp is the standard source magnet configuration used in the JET PINI ion sources A 3D magnetic field map has been calculated at a resolution of a 5mm mesh within

the walls of the source body (sections 4 1 and 4 2) This field map will be used to trace single electron trajectories with the inclusion of the collision processes described above
The initial conditions for the primary electrons are generated using a Microsoft Excel spreadsheet that randomly generates launch locations randomly along the length of each of the 24 filaments, with the initial launch plane set to be perpendicular to each filament For this simulation the initial electron energy is set equal to the potential difference applied between the filaments and the source body (anode) As a first approximation, this is the maximum energy that can be given to electrons as they are accelerated from the filaments across the sheath and into the plasma It is simply assumed for the operation of this model that the energy is gained in one single step across the sheath at the filament Future simulations will need to assess whether this approximation will need to be replaced with a refined estimate of the actual energy electron distribution emitted from the filaments

Running the model repetitively with the same initial conditions builds up a large number of electron trajectories, randomised by the collision processes The location of each interaction point is logged for subsequent analysis and display

Qualitative output is easily obtained by projecting the interaction points onto planes parallel to the source walls This gives a visual representation of the areas in which the primary electrons are confined – and the regions where the ionisation reaction primarily occurs

In the case shown in figure 4 8 a source gas density of $3\ 81\times10^{19}$ m^{-3} (equivalent to a gas pressure of 4μbar at 750K) has been used This is estimated from the known source input gas flow, conductance of the extraction aperture array and previous measurements [35] of the neutral molecular temperature in similar ion sources, which suggest a temperature ≤0 1eV The model here has used an initial population of 1194 primary electrons, each launched with an energy of 100eV from points at the filament locations Each electron was then traced until its energy fell below 10eV, it hit a source wall or the pre-set iteration control parameters were exceeded The secondary electrons produced from the ionisation reactions are then traced until each of these has an energy less than 10eV (or passed through any of the other boundary conditions) Including these electrons gives a total number of trajectories traced of 2558 in this example

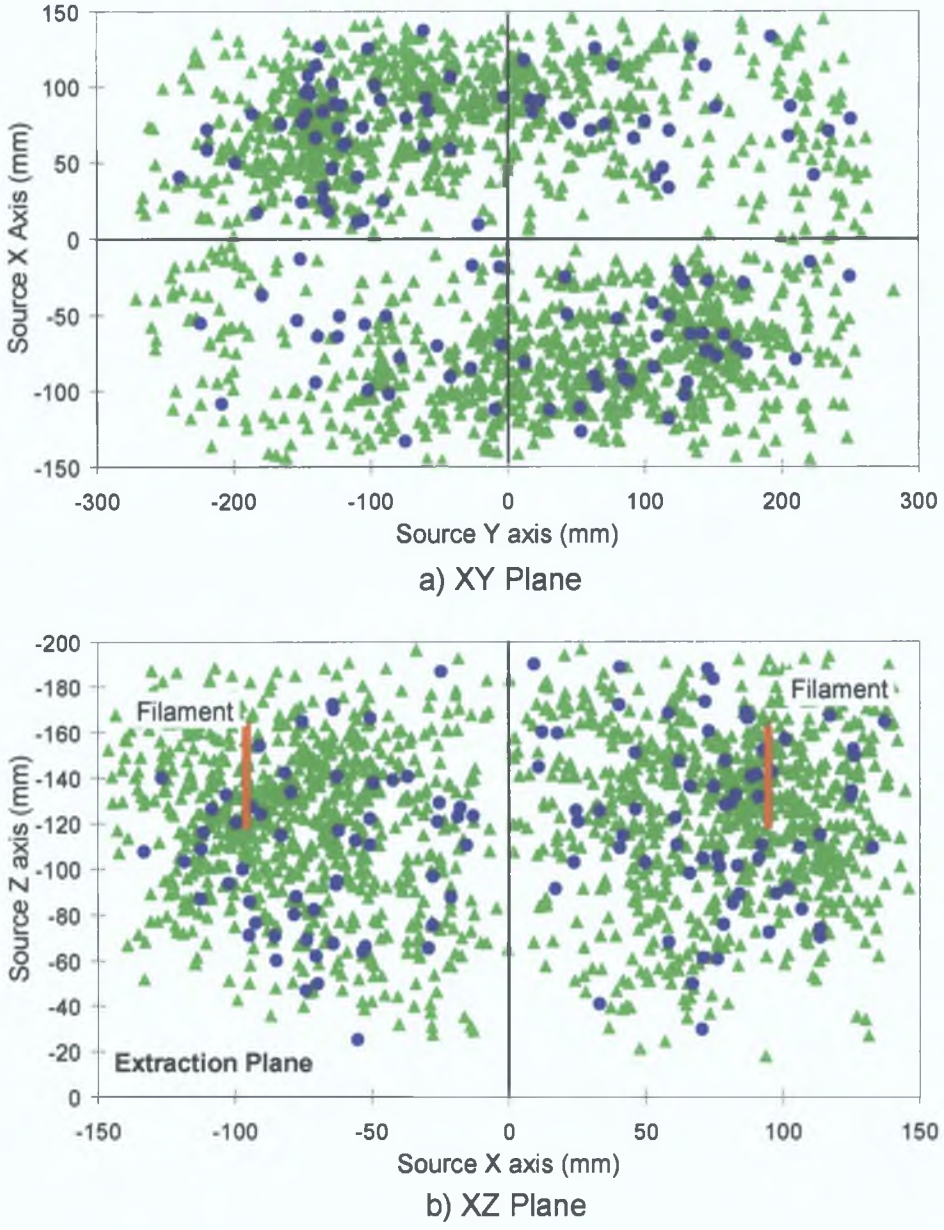

Figure 4.8: - Projections of the inelastic interaction points for 100eV electrons launched from the filaments on a) the ZX plane and b) the XY plane.
(Symbols mark - ● Dissociation and ▲ Ionisation points)

Projecting all the inelastic interaction points onto planes perpendicular to the source walls gives a qualitative view of the ion production regions in the source. For the super-cusp configuration above it appears that the ionisation is concentrated into two lobes close to the sides of the ion source. Inspecting the XY plane view shows that the density of ionisation

points is concentrated into 2 diagonally opposite quadrants of the plot This result from the (anti-clockwise) precession of the electron trajectories across the super-cusp filter field, however when the electrons reach the source end plates, the field structure at this point stops the precession, effectively 'stalling' the electrons in each of these two quadrants If the filter-field was continuous across the transition from the source side walls to end plates then the electron trajectories would be expected to precess uniformly around the source (in a clockwise direction in this case) The ionisation region does appear to be fairly well confined behind the super-cusp field with very few interaction points plotted close to the extraction plane (z=0)

4.5.1 ANALYSIS OF THE SC15S3 MODEL

The secondary electrons produced by the ionisation collision reactions in the model of the SC15S3 super-cusp above are used in a second iteration The distribution of the secondary energy is determined by the Binary Encounter Approximation calculation described above Figure 4 9 shows the secondary electron energy distribution generated from the SC15S3 super-cusp model above For the 1194 primary electrons launched at 100eV in this model 1059 secondary electrons are generated, of which 35% are above the 10eV minimum energy The secondary electrons generate an additional 1 3% ionisation reactions and 52% more dissociation reactions above those generated by the first iteration of primary electrons alone

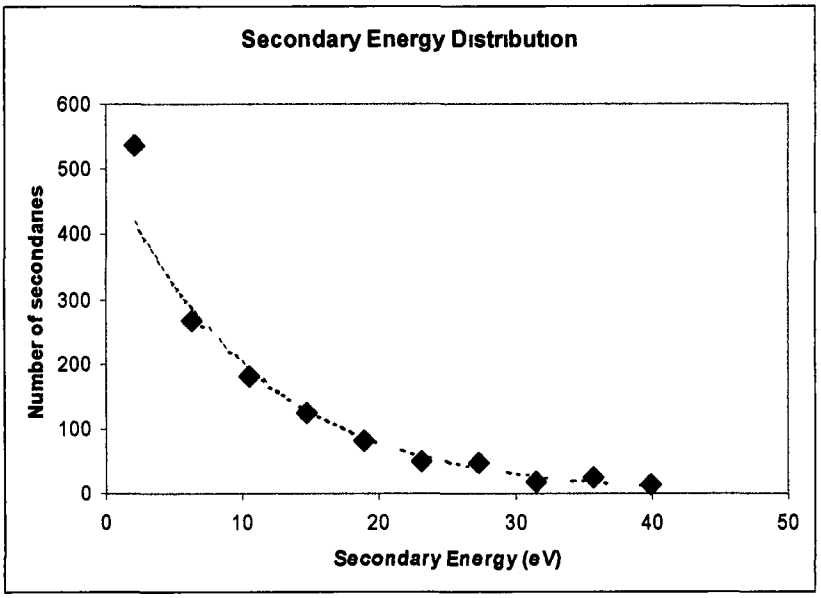

Figure 4 9 - Secondary electron energy distribution for 100eV primary electrons used in the SC15S3 super-cusp model

Once the secondary electron trajectories have been calculated some analysis of the model is possible In this case 1194 primary electrons are launched to give a total of 1069 ionisation reactions - giving a ratio of 0 90 H_2^+ ions per primary electron Of all the electron trajectories modelled (primary and secondary) 15 7% are lost to the source walls Further analysis shows that 5 8% of the total number of electrons hit Grid 1, of these 71% have an energy >90eV (i e within 10% of the launching energy) This figure indicates the proportion of primary electrons that are not confined by the filter field and move with little interaction directly to the extraction plane The presence of fast electrons at the extraction plane will produce H_2^+ ions in this region, degrading the monatomic species fraction of the extracted beam This 'primary electron leakage fraction' should be a good qualitative indicator of the likely monatomic species yield available from a given ion source magnet design This information can be derived from calculating both the fraction of the primaries that reach Grid 1 and the average energy (a quantity analogous to the floating potential of a Grid 1 that is electrically insulated from the rest of the source body)

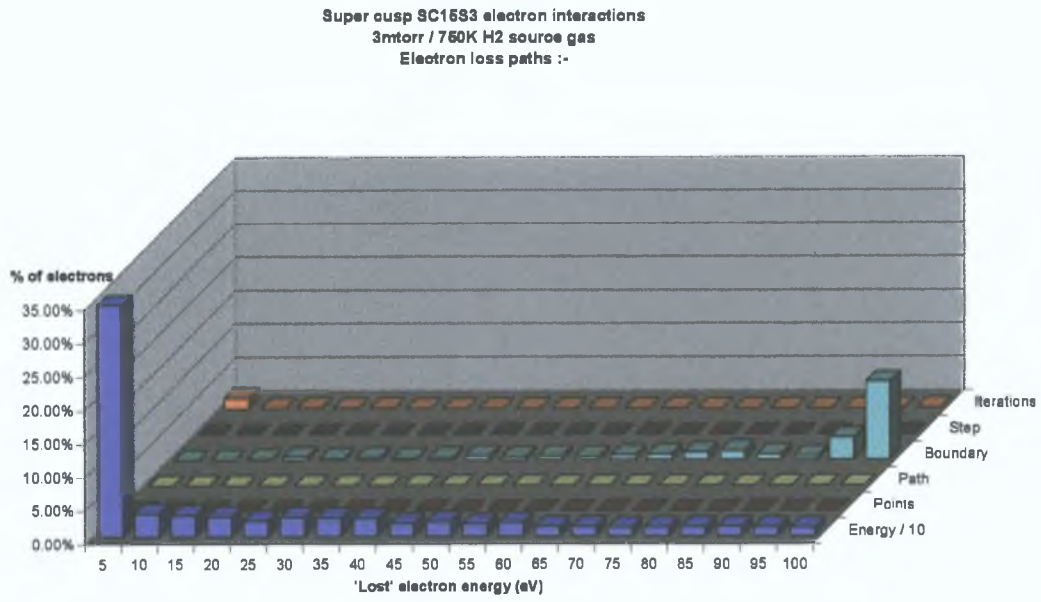

Figure 4.10: - Electron trajectory endpoint conditions for the SC15S3 super-cusp model (primaries + secondaries)

Figure 4.10 shows a summary plot of the electron trajectory endpoint conditions. The majority of the electron trajectories are terminated when the electron energy is below the 10eV minimum threshold, the next largest group is the primaries that are not confined by the filter field and move with few interactions to grid 1.

4.6 PARAMETER SCANS USING THE SC153 MODEL

4.6.1 NEUTRAL GAS DENSITY

The effect of key parameters on the primary electron model of the SC15S3 super-cusp source has been investigated. Firstly the neutral gas filling density has been varied to investigate how the ion production efficiency and electron confinement depends on the source gas density was run with a fixed set of initial conditions for 1194 primary electrons, using an initial energy of 100eV. The primary and secondary electron trajectories were then calculated and the ratio of H_2 ionisations to the number of primaries was calculated, along with the fraction of primary

electrons lost to grid 1. Figure 4.11 shows these quantities plotted as a function of the source gas density.

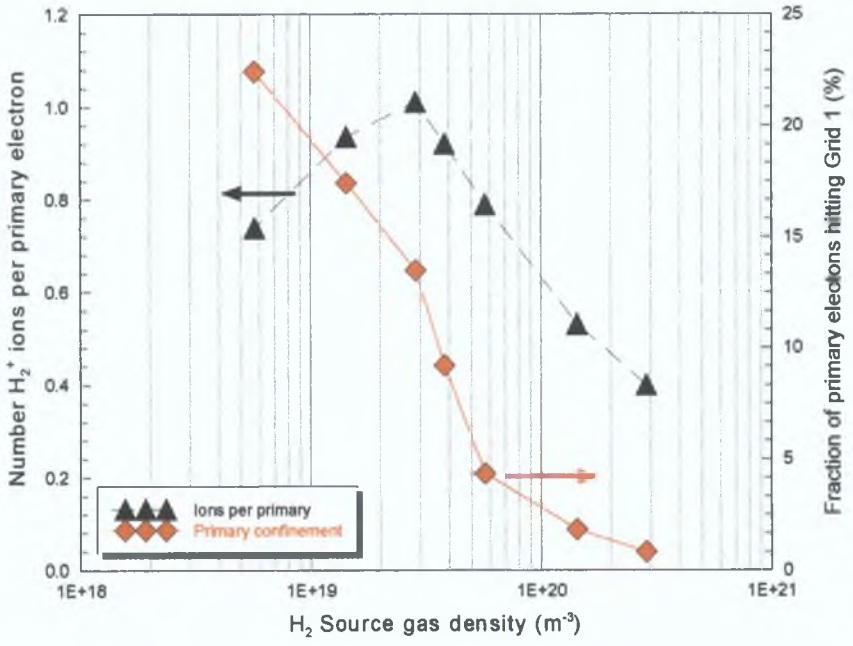

Figure 4.11: - Ion production efficiency and primary electron confinement expressed as a function of the H_2 neutral gas density.

This graph shows that there is a filling gas density where the ion production efficiency is maximised. At lower gas densities the electron mean free path length is long and there is increased loss of primaries to the source walls, giving less chance for ionisation reactions to occur. At higher source gas densities the electrons lose energy more quickly to the coulomb collisions with the electron background, again reducing the chance of ionisation collisions occurring. In this simulation, however, the approximation is used that a constant fraction of the source gas density is assumed to be ionised to produce the 'background plasma' density for the coulomb energy loss calculation. The only proper way to get around this approximation would be to run the simulations iteratively feeding back the calculated ionisation fraction (as the number of ion per primary) into the coulomb energy loss model. However due to the processing time currently required to produce single simulation output with acceptable statistics the analysis of this model will continue using the constant ionisation approximation.

Goede et al. [36] express the ion production efficiency derived from measurement of a large magnetic multipole ion source (one of the forerunners of the JET ion sources) with the inverse of the source gas pressure. If the source gas densities of figure 4.11 are converted to an equivalent source pressure (at a fixed nominal gas temperature [750K]) the data can be plotted in a similar way (Figure 4.12)

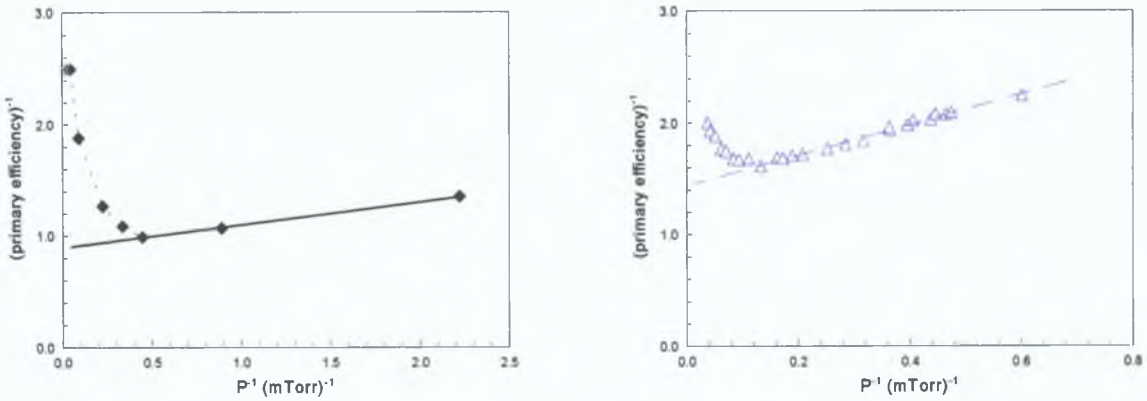

a) SC15S3 model

b) Measured 'multipole' source data

Figure 4.12: - Ionisation efficiency (inverse) vs. inverse source H_2 gas pressure for a) SC15S3 super-cusp b) measured in a large multipole ion source

The model of the primary electrons in the SC15S3 super-cusp source shows the same behaviour as the experimental observations made by Goede et al in the multipole source and later with the SC15S3 source at JET [37]. At lower gas pressures both the model and measurement show good agreement with the relation

$$\frac{1}{\varepsilon} = a + \frac{b}{P_s}$$

where a and b are constants, ε is the ionisation efficiency and P_S the source gas pressure. At higher source pressures both graphs show a similar reduction in ionisation efficiency. Using the linear fit shown in figure 4.12 the intercept gives the value of the inverse efficiency at infinite gas density, the slope of the linear fit gives the value of the electron confinement time, these values are compared to the measured values of the SC15S3.source [37]

TABLE 4 1 Comparison of quantities derived from measurements of the Sc15S3 source with the Monte-Carlo model analysis

	SC15S3 Measured	SC15S3 Model
$\left(\frac{I_{ARC}}{I_{TOT}}\right)_{\infty}$	0.54 to 0.75	0.89
τ_e	0.05 to 0.13μs	1.5μs

The model give a reasonable agreement with the infinite gas density effciency, but appear to over-estimate the electron confinement time significantly

4.6.2 PRIMARY ELECTRON ENERGY

The primary electrons in this model are launched perpendicular to the filaments at an initial energy equal to the potential difference between the filament cathodes and the source body anode This assumes that the electrons emitted from the filaments are accelerated across a sheath that is significantly shorter than the electron mean free path length The model was run at fixed neutral gas density, at the point where maximum ionisation efficiency occurs for the 100eV electrons See figure 4 11

After calculation the trajectories of both the primary and secondary electrons the ionisation efficiency was calculated, i e the number of ionisation reactions per primary electron This is plotted in figure 4 13 as a function of the initial primary energy It can be seen that the ionisation efficiency increases with increasing electron energy, but with a step change around 75eV, leading to a different linear relationship at higher energies This step change appears to result in the model from an increase in the fraction of electrons lost to the source wall at the launching energy, due mainly to the increased effective mean free path of the higher energy electrons Hence at higher initial electron energies there is a greater probability of loss to the source wall before an inelastic interaction occurs

A more useful quantity however is the arc efficiency of the ion source, which is defined as the number of ions extracted per unit of input arc power (A/kW) It is this quantity that is generally measured experimentally Thus given that the initial number of primaries used in

each run of the model is constant (equivalent to a fixed arc current) then dividing the calculated ionisation efficiency by the initial electron energy gives a quantity equal to the ionisation efficiency per unit of arc power.

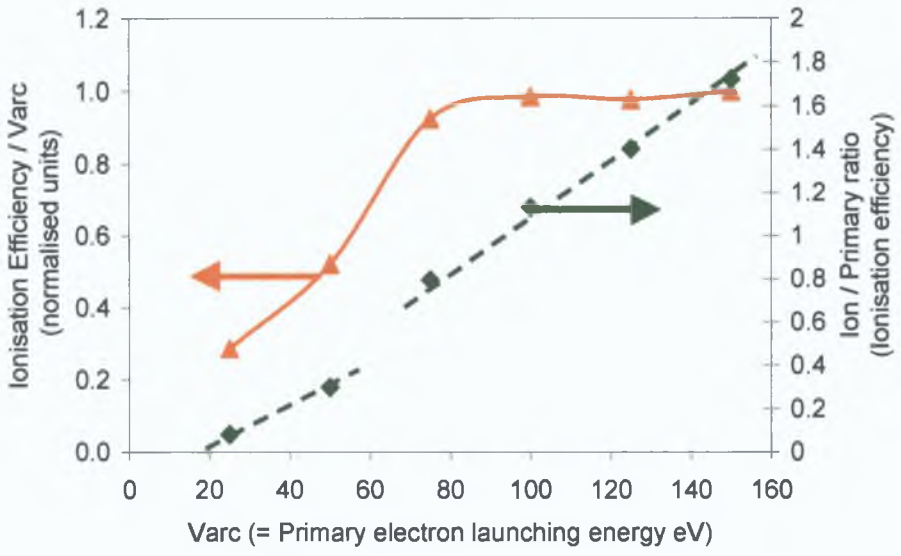

Figure 4.13: - Ionisation and Arc efficiencies derived from the Monte-Carlo model of the SC15S3 super-cusp ion source.

Figure 4.14 shows the measured arc efficiency as a function of the arc potential in the SC15S£ source. This figure shows that there is no arc efficiency increase above an arc potential of about 80V. This behaviour is well known in this ion source and is the reason why a nominal arc potential of 80 - 100 V is used [7].

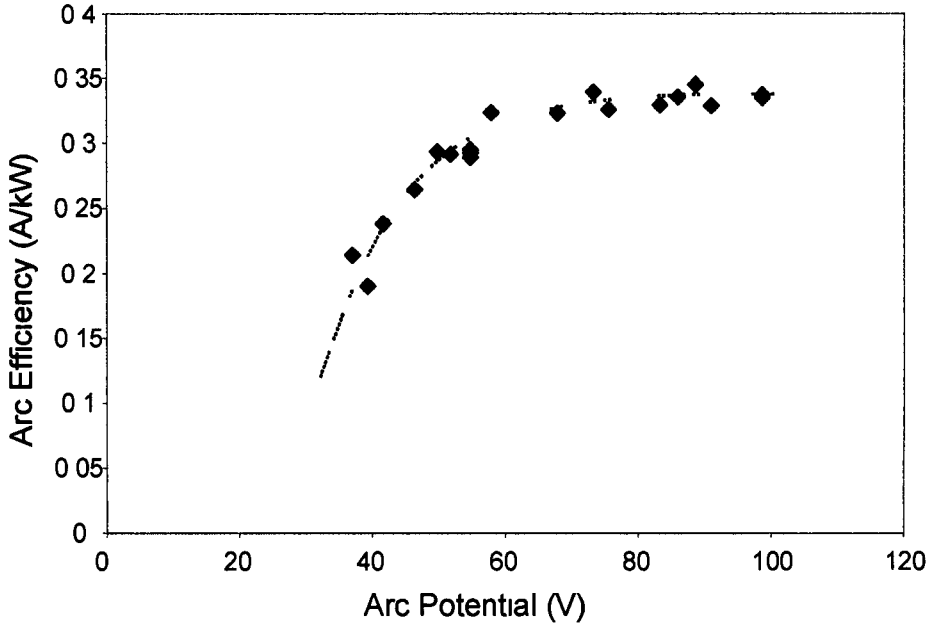

Figure 4 14 - Measured arc efficiency of the SC15S3 ion source as a function of arc potential

4.7 PLANE CROSSING CODE

The full trajectory of each particle traced in the simulation can be stored in a binary file for subsequent processing Instead of plotting the projections of the interaction points onto a given measurement plane, a good visualisation of the particle density can be obtained by counting the trajectories crossing a given measurement plane A simple code to parse though the binary file of the trajectories and bin the crossing points of a given plane has been written A contour plot of the resulting binned datafile can then be generated, along with individual line profiles

Figure 4 15 shows the electron trajectory crossing density for a plane parallel to the extraction plane (and source backplate) at a depth of 125mm into the ion source (75 mm from the source backplate) where the primary electrons are confined behind the filter field The data is obtained for this plot using $5\times5mm^2$ bins To produce a more clearly visible plot the details of the electron density map are suppressed above a density of 50% of the maximum density

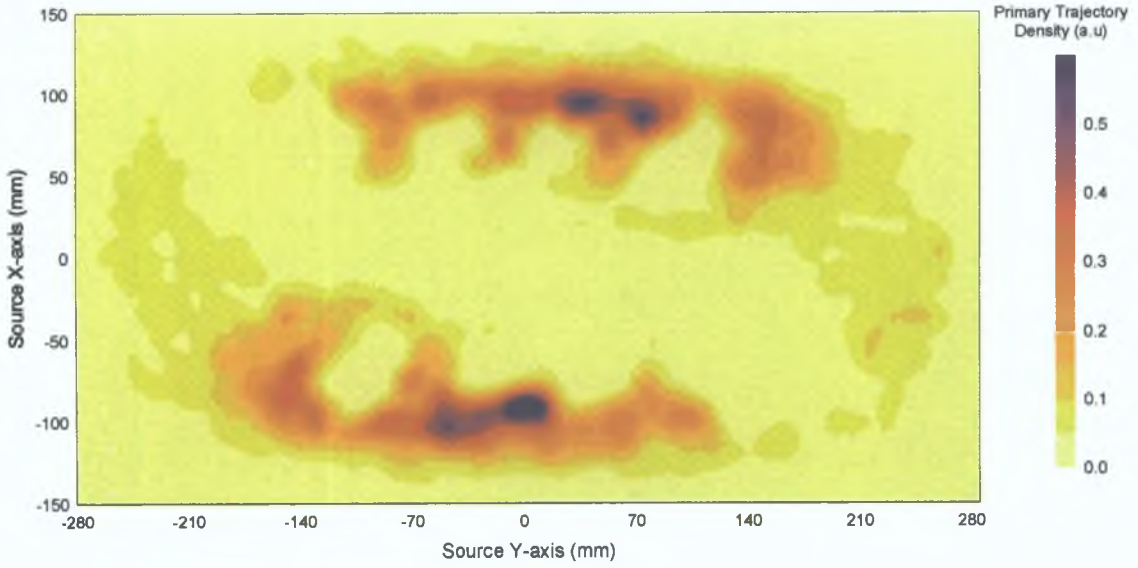

Figure 4.15: - Electron trajectory crossing map of an XY measurement plane at z=-125mm in the SC15S3 super-cusp electron trajectory model.

The image of figure 4.15 should be compared with figure 4.8b, and shows more clearly the electron trajectory density in the driver region of this super-cusp ion source. What this plot does not show, however, is the density of the ion production - as this simple code cannot distinguish the energy of each trajectory that it counts crossing the measurement plane.

4.8 ION TRAJECTORY TRACING

A simple simulation was constructed to follow H_2^+ ion trajectories from the locations generated by the primary electron model, using a method similar to that for the electron trajectories. The intention of this simulation was to give information on how the H_2^+ ions will move through the source, with the aim of providing initial conditions for subsequent H^+ and H_3^+ ion trajectory simulation.

As with the model of the primary electrons the trajectories of the H_2^+ ions are traced only through the magnetic field in the source. The effects of electric fields in the source are not included in this simulation. To estimate the mean free path of the H_2^+ ions as they move through the ion source the interactions with the shortest mean free paths are considered.

$H_2^+ + H_2$	[Elastic]
$H_2^+ + H_2 \rightarrow H_2 + H_2^+$	[Charge exchange]
$H_2 + H_2^+ \rightarrow H + H^+ + H_2^+$	[Dissociation]
$H_2^+ + H_2 \rightarrow H_3^+ + H$	[H_3^+ production]
$H_2^+ + e \rightarrow H^+ + H + e$	[Dissociative excitation]

The reactions are treated in an identical way as the electron interactions, for the neutral H_2 interactions a Chebyshev polynomial fit is used over the valid range of the cross-sections In the case of the Dissociative excitation reaction a constant rate coefficient, $\sigma v_{electron}$, of 10^{-7} cm^3s^{-1} is used as this reaction is quite insensitive to the value of the electron temperature chosen[35] The mean free path length of each reaction is then calculated for a given neutral gas target density and H_2^+ ion energy Individual random numbers are used to generate a trajectory path length, l_{REAC} for each reaction from the individual mean free paths, λ_{REAC}

$$l_{ELA} = -\lambda_{ELA} \log_e(R_1)$$
$$l_{CX} = -\lambda_{CX} \log_e(R_2)$$
$$l_{DIS} = -\lambda_{DIS} \log_e(R_3)$$
$$l_{H3+} = -\lambda_{H3+} \log_e(R_4)$$
$$l_{H+} = -\lambda_{H+} \log_e(R_5)$$

The reaction with the minimum trajectory length generated above is selected to occur once the trajectory has been followed for this length These give a relative probability of selecting each reaction proportional to the values of the mean free path of each reaction A sample calculation of the relative probabilities, derived from the calculated mean free paths is shown in figure 4 16, normalised to a total probability of 1

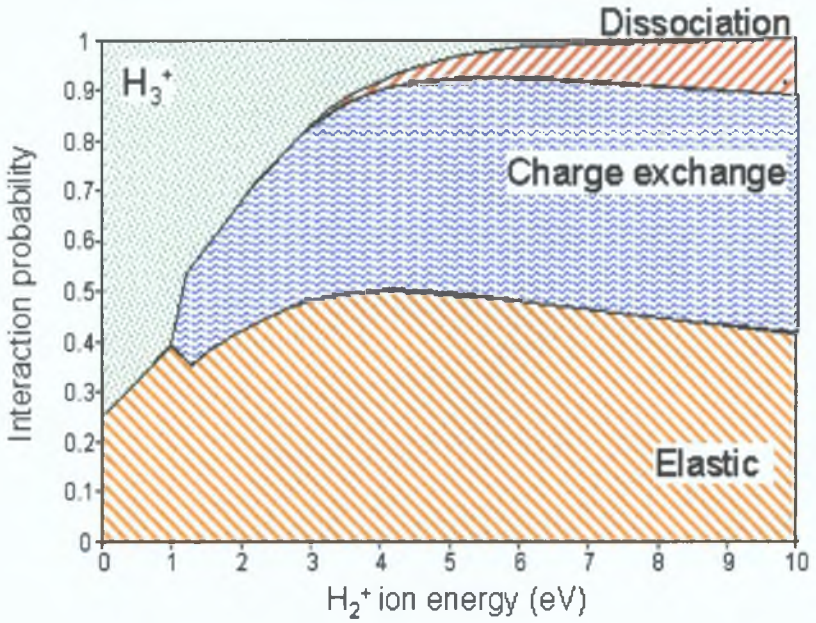

Figure 4.16: - H_2^+ ion interaction probabilities used in the H_2^+ ion trajectory model. A random number generated in the range (0..1) is used to select the process that occurs

As a first approximation, in each of the inelastic collisions the energy of the H_2^+ ion is reduced by a random amount up to 50% of the initial energy, except for the H^+ and H_3^+ producing reactions where the trajectory is terminated. In a similar way to the electron model the elastic collision does not alter the ion energy but is used to give a randomised deflection to the H_2^+ ion trajectory.

The H_2^+ ion trajectories are followed until the ion either hits a boundary wall, an H^+ or H_3^+ ionisation occurs or its energy falls below a pre-set value.

Inspection of the H_2^+ ion trajectory density distribution shows that this simple model appears to reproduce the measured ion density distribution, without needing to further calculate the paths of the H^+ trajectories. Given that H_2^+ is the most abundant ion generated by the primary electrons it seems reasonable that this ion is the source of a large fraction of the H^+ ions, mainly through the dissociative excitation reactions with the electron population. As this reaction has a rate coefficient that is remarkably insensitive to the variation of electron temperature found in the ion source the H+ creation will only be weakly affected by the local

electron temperature variations in the source beyond the driver region Since for this ion source geometry the H_2^+ ionisation points are generally only within a small number of mean free path lengths of being lost to the source walls It appears that to a simple approximation the formation of the majority of the H^+ ions will be coincident with the short H_2^+ ion trajectories followed in this simple model

4.8.1 MONTE CARLO MODEL OF H_2^+ ION TRAJECTORIES IN THE SC15S3 SUPER-CUSP

The Monte-Carlo model of the ion source has been used to trace the trajectories of primary electrons through the SC15S3 super-cusp ion source The primary electron calculations generate a map of the ionisation regions in the source, which is used as the starting point for tracing H_2^+ ion trajectories through the source The distribution of H_2^+ ion trajectories crossing a plane close to the extraction plane is then calculated

Figure 4 17 shows the density map created by counting the number of H_2^+ ion trajectories crossing a measurement plane parallel to the extraction plane In this case 64000 H_2^+ ions are generated at the ionisation locations determined by running a model of 1164 primary electrons The ions are each given an initial energy randomly chosen from a normal distribution with a mean value of 0 5eV, with a standard deviation of 0 25eV The ion trajectories are traced until their energy falls below 0 01eV or a collision with a source wall is detected

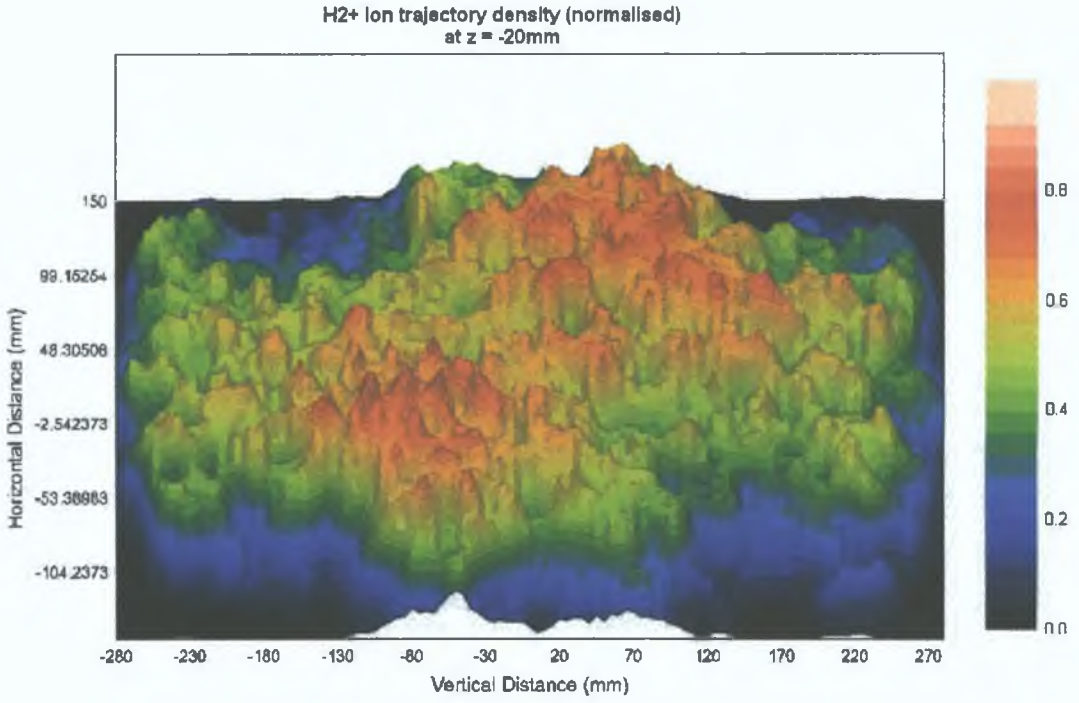

Figure 4.17. Distribution of H_2^+ ion trajectories close to the extraction plane SC15S3 Super-cusp ion source 64000 ions [0.5eV mean, 0.25eV std. dev.]

This density map clearly shows that the H_2^+ ion trajectories are not distributed uniformly over the extraction plane. There is a quite strong concentration of trajectories towards the centre of the source, mainly in two lobes offset across the centreline.

From this density map a vertical (y-axis) centreline ion density can be derived similar to that obtained from the analysis of the spectroscopic and calorimetric measurements. In order to compare with the profiles generated from the analysis of measured data, a quadratic polynomial is fitted to this profile over a range equivalent to the vertical width of the extraction array. This vertical line density profile is plotted in figure 4.18.

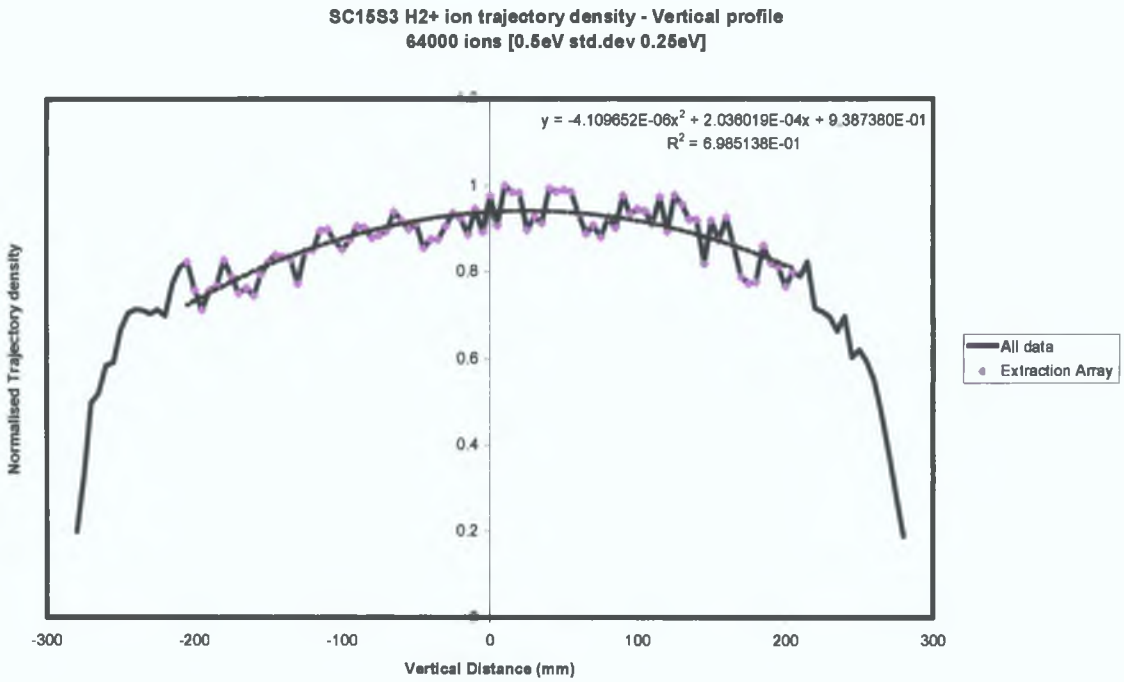

Figure 4.18. Vertical (y axis) profile of the trajectory density map, with quadratic polynomial fit to the width of the extraction array.

The quadratic fit to this profile shows a RMS deviation from a uniform distribution of 5.3%. This value is compared with a similar definition used for the ion density profiles inferred from the experimental measurements. As a measure of the quality of the quadratic fit across the extraction array the R^2 value is also calculated, where

$$R^2 = 1 - \frac{SSE}{SST},\ SSE = \sum \left(Y_i - \hat{Y}_j\right)^2 \text{ and } SST = \left(\sum Y_i^2\right) - \frac{\left(\sum Y_i\right)^2}{n}$$

(Thus $R^2 = 1$ is a perfect fit of the trendline to the data)

These examples use the R^2 implementation available in the polynomial line fitting functions provided in Microsoft Excel.

4.8.2 PARAMETER SCANS OF THE SC15S3 H_2^+ ION MODEL

4.8.2.1 INITIAL NUMBER OF H_2^+ IONS

The model of the H_2^+ ion trajectories in SC15S3 super-cusp was, in the first cases, run with 15000 ions, each ion given an energy randomly chosen between 1eV and 3eV Repetitive runs of this model were used to give a total of 90000 calculated trajectories For each run of 15000 ions the trajectory density profile close to the extraction plane was calculated and the results added to the previous run The R^2 deviation of the quadratic fit to the central part of the vertical (y) ion density profile was then plotted as a function of the total number of ion trajectories

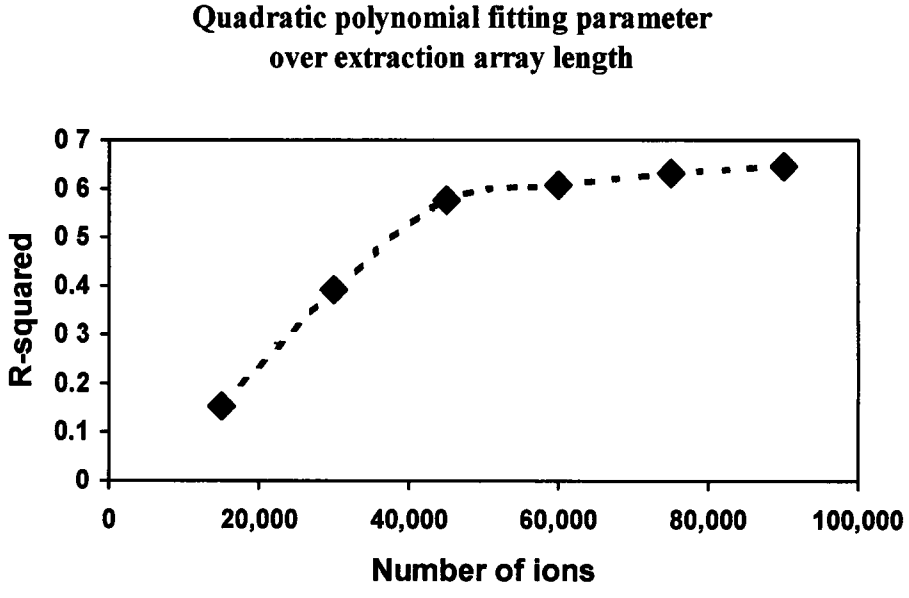

Figure 4 19 - R^2 parameter for a quadratic polynomial fit to the vertical (y) H_2^+ ion density profile, plotted against the total number of ion trajectories modelled

Figure 4 19 shows that there is no benefit from modelling significantly more than 60000 trajectories This is convement as with the current PC hardware used a 60000 ion model takes 12-18 hours to complete on the target 350MHz Intel Pentium II PC with 128Mb RAM, using Windows NT 4, enabling the results to be obtained overnight

4.8.2.2 H_2^+ ION ENERGY

The H_2^+ ion trajectory model was run with a fixed number of ions (64155) but varying the initial conditions of the ion energy. The individual ion energies were selected at random from a normal distribution with a given mean and standard deviation energy. The choice of ion energy for this model is a compromise between the likely ion thermal energy Previous measurements of the ion energy in similar positive ion sources suggest that a mean ion energy in the range of a few $1/10^{ths}$ eV can be expected in the JET PINI ion sources [35] and giving each particle sufficient energy to move far enough through the ion source to get a significant number of ions at the extraction plane. For an initial ion thermal energy distribution of 0.1eV mean with a 0.05eV standard deviation, for a starting set of 64155 ions this gives only 6489 trajectories that cross a plane close to the extraction plane. This low number of crossing points gives a large scatter on the density profile, making it difficult to produce an analysis of the non-uniformity.

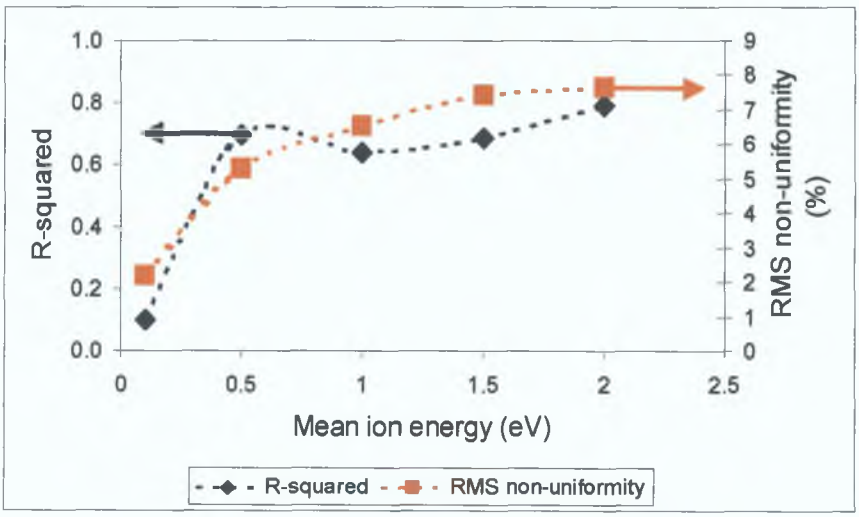

Figure 4.20: - R^2 parameter for a quadratic polynomial fit to the vertical (y) H_2^+ ion density profile and the non-uniformity factor for a model with varying initial ion energy.

Increasing the initial ion energy to 0.5eV with a standard deviation of 0.25eV gives a total of 21593 trajectories crossing the measuring plane close to the extraction plane. This is a sufficient number to give an ion density non-uniformity profile with a reasonable quadratic

fit In fact increasing the ion energy further (to 1 0, 1,5 and 2 0eV) does not significantly change either the non-uniformity profile or polynomial fit quality

Thus it seems that a good compromise of using ≈60000 ions with an initial energy distribution in the expected range, given by a normal distribution with a mean energy close of 0 5eV and 0 25eV standard deviation, gives reasonable ion density uniformity predictions, within an acceptable processmg time

4.9 CHAPTER SUMMARY

A Monte-Carlo model of the JET PINI ion source has been created The code uses a simulation of the 3D magnetic field that is produced m the ion source by the external array of permanent magnets The first part of the model was to trace the trajectories of the primary electrons launched from the tungsten filaments The trajectory calculation was extended to include some of the more significant interactions, including most importantly the H_2^+ ionisation reaction This enables the model to produce information on the regions of the ion source where the ionisation of the neutral source gas occurs In addition analysing the statistic of the Monte-Carlo model give predictions on the behaviour of the ionisation efficiency as a function of both source gas density and initial electron energy The predicted behaviour of the ionisation efficiency, and derived arc efficiency, agrees well with experimental observation of the ion source

Extending the model to further simulate the trajectories of H_2^+ ions through the ion source now leads to predictions of the ion density profile at the extraction plane of the ion source The non-uniformity profile generated for the JET PINI ion source agrees well with that derived from experimental observations

5 PINI ION SOURCE DEVELOPMENT.

The improved beam transmission observed on the Neutral Beam Test-bed, by simply replacing the super-cusp ion source on a PINI with a chequerboard ion source, was used as the basis for an experimental development programme The aim of this development work was to produce an ion source design that gives improved beam transmission, by way of a more uniform ion density, but without degrading the monatomic species yield or the ion production efficiency This experimental programme was initiated prior to the start of the development of the Monte Carlo ion source model, although as the code started to become operational it was able to support the experimental programme Eventually the Monte Carlo model was sufficiently developed to define the next steps to be taken m the experimental programme

5.1 PERFORMANCE OF THE SC15S3 ION SOURCE

As the reference source configuration for this development programme detailed information about its configuration and performance is required The super-cusp configuration SC15S3 was chosen after a process of modification and measurement of various magnet configurations at Culham [7] The majority of the source development was carried out using a Langmuir probe array [38] to determine the ion source performance and uniformity The measurements taken now on the Neutral Beam Test-Bed are all from the analysis of data from beam diagnostics, where it is attempted to infer the ion source conditions under its operating mode, with a large extracted ion current In addition this work m many cases has to be 'piggy backed' onto the normal operation of PINIs on the TestBed and Neutral Injectors, so modifications for source diagnostics to PINIs, that would make them incompatible with JET operations, were not permissible

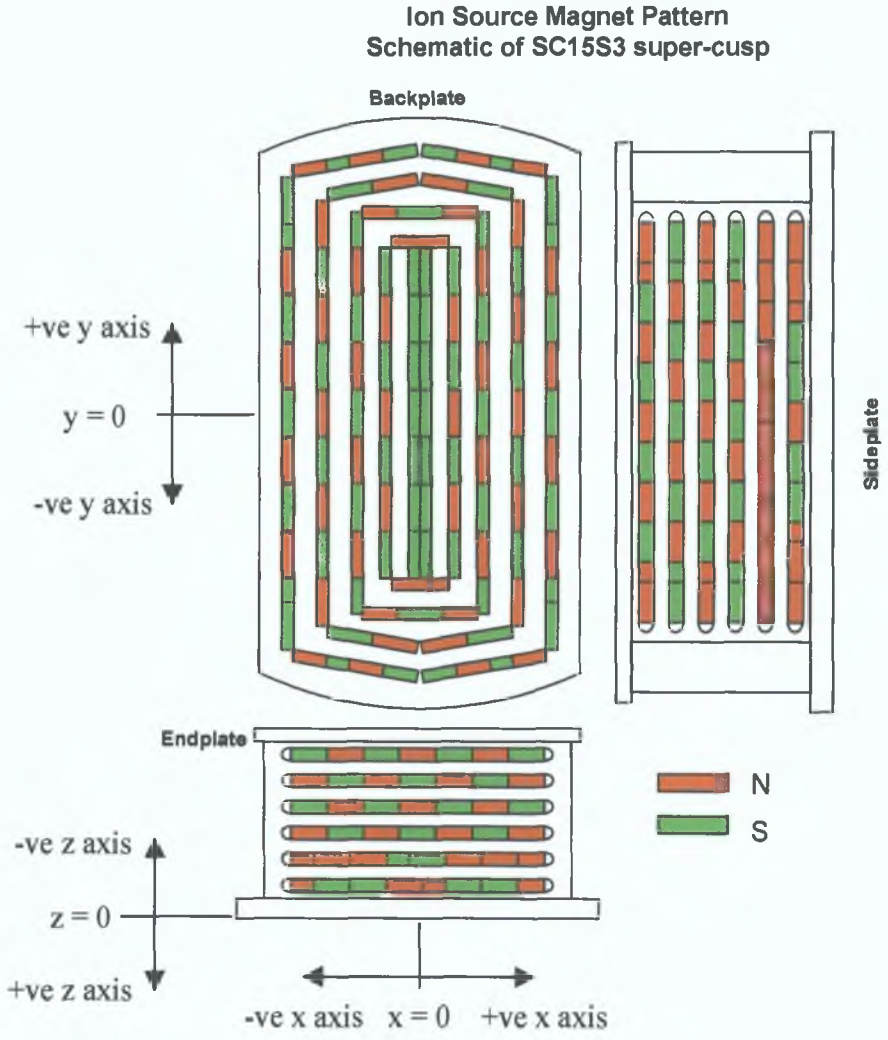

Figure 5.1: Schematic of the SC15S3 super-cusp magnet pattern, viewed from the on the external surface of the ion source.
[Figure reproduced from Chapter 4 (figure 4.1)]

The SC15S3 magnet pattern arrangement shown in figure 5.1 gave, at the time, the best compromise of monatomic species yield, arc efficiency and ion density uniformity. The arc efficiency is sufficient to allow an extraction of a 60A ion current from the source at the required source gas flow of 12-15 $mbls^{-1}$ (with a similar separate gas flow into the neutraliser) at an arc current of 1200A (at 80 - 100V).

Figure 5.2 below shows the arc efficiency of the SC15S3 super cusp ion source operated in H_2, D_2 and He gases. In this case the arc efficiency is defined as the ion current extracted per kA of arc current (whilst maintaining a fixed arc potential of 100V at all arc currents).

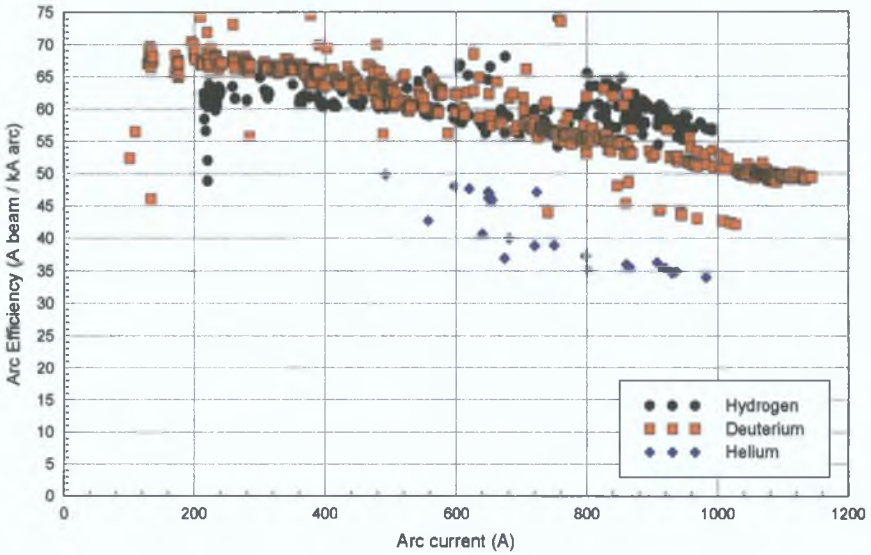

Figure 5.2: Arc efficiency of the SC15S3 super cusp source (using a high current tetrode accelerator).

This figure shows that the arc efficiency falls slowly with increasing arc current, but allows an ion current of 60A (D^+/H^+) to be extracted at an arc current of 1200A. One of the important parameters is the species composition extracted from this ion source, along with the required D^+ ions a fraction of D_2^+ and D_3^+ ions are accelerated. These will produce D^0 neutrals with 1/2 and 1/3 of the full energy beam with a consequently shorter penetration depth into the JET plasma. Typically the species composition expected from this source at nominal operating conditions is 88% D^+ : 9% D_2^+ : 3% D_3^+. Figure 5.3 shows how the species composition of the extracted ion beam reaches the nominal values as the arc power is increased.

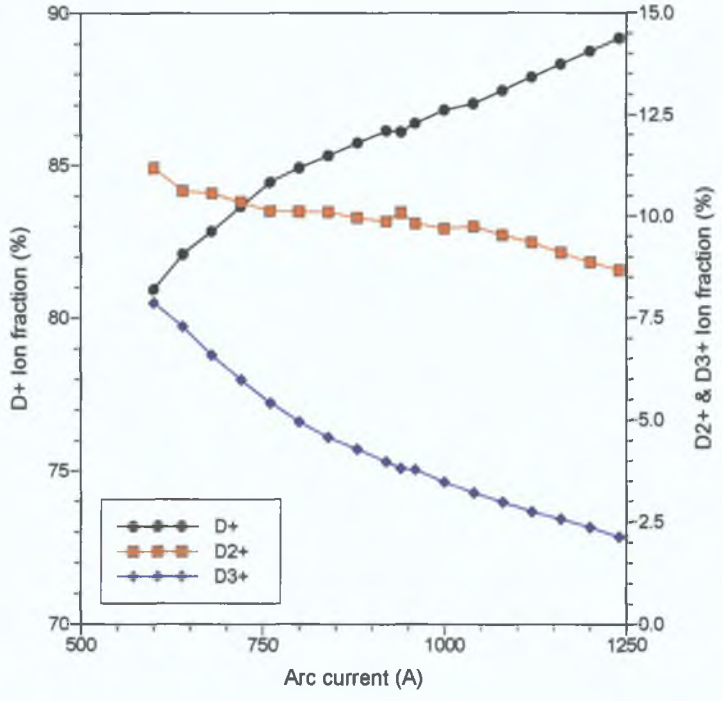

Figure 5.3: Species yield of the SC15S3 super-cusp ion source (using a high current tetrode accelerator)

A detailed discussion of the non-uniformity measurements has been given in *Chapter 2*. However, in brief, the uniformity of the ion density across the extraction plane of the accelerator array can be illustrated from multi-channel spectroscopic measurements. Figure 5.4 (previously shown in Chapter 2) shows the global beam perveance at which the local minimum beamlet divergence occurs, measured across the vertical (y) dimension of the extraction array. Since these measurements are made at a fixed extraction voltage the determining factor for the local beamlet divergence is the local ion density. Figure 5.4 thus shows what is effectively the inverse of the ion density uniformity, the ion density profile is thus peaked towards the centre of the source. The beamlets in the centre of the source reach the minimum divergence at low values of total beam current, whereas the outer beamlets only reach their minimum divergence at higher values of total beam current.

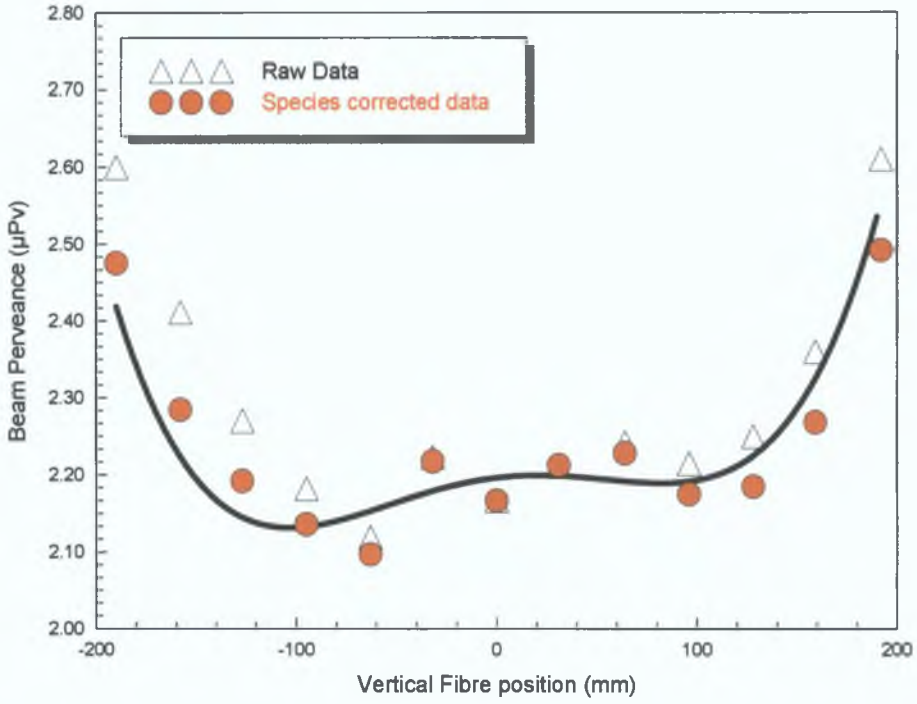

Figure 5.4: Uniformity of the ion density across the SC15S3 filter source – [Figure reproduces from Chapter 2 (figure 2.7)]

Thus, it is clear that for a given total beam perveance not all of the individual beamlets will be extracted with the same divergence. It is this spread of beamlet divergences that appears to be responsible for an increased effective total beam divergence, which inevitably leads to higher beamline scraper loading and reduced beam transmission.

5.2 Performance of the Chequerboard only ion source

One of the JET ion source bodies was modified to remove the super-cusp magnet pattern to leave the chequerboard pattern only, i.e. reverting to a simple multipole bucket source. The pattern used is essentially the same as that shown in figure 5.1, but with the filter rows made into a chequerboard pattern. This source was tested on a variety of PINI accelerator stacks, the best comparisons with SC15S3 source data are made using the high current tetrode accelerator - which is when the improved beam transmission and reduced box scraper loading were first observed (see chapter 2)

The arc efficiency of the chequerboard only source is slightly lower than that of the SC15S3 super-cusp source. This lower arc efficiency of the chequerboard source makes it difficult to achieve an extracted beam current of 60A (D_2) within the limit of the arc power supply. Figure 5.5 shows a comparison of the ion current extracted from the two ion sources, as a function of the demanded arc current.

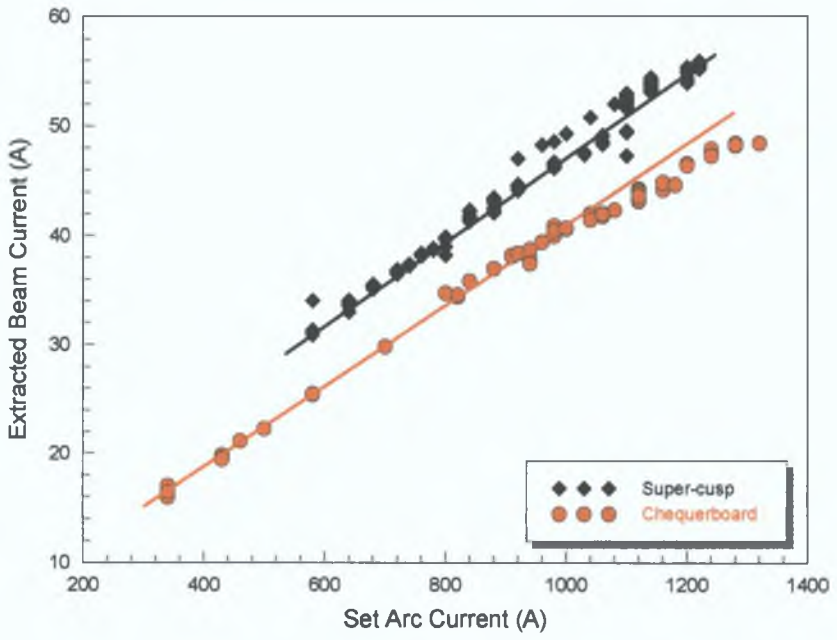

Figure 5.5 Arc efficiency comparison of the chequerboard only ion source with the standard filter source (using a high current tetrode accelerator and D_2 source gas). Data taken at a source gas flow of 12 mb l s^{-1}, and an Arc Voltage of 80V

The monatomic species yield of the chequerboard is of course worse than the super-cusp ion source since the main purpose of the super-cusp field is to enhance the monatomic species yield. In this case the species fractions at full arc power are 68% D^+ : 27% D_2^+ : 5% D_3^+., the evolution of the species yield with increasing arc current is shown in figure 5.6,

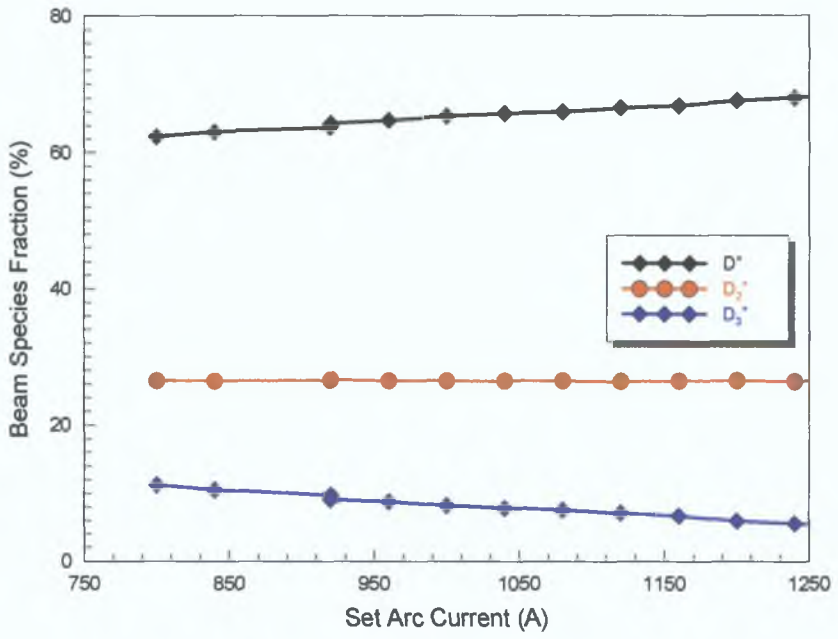

Figure 5.6 Species fractions measured from the chequerboard only ion source (using a high current tetrode accelerator and D2 source gas)

The ion density uniformity though is better than that of the super-cusp source. For a given global beam perveance, all the beamlets are extracted with similar divergence. Figure 5.7 shows a comparison of the local minimum divergence in the vertical (y) plane of the extraction array, as with figure 5.4 above these graphs show the inverse of the ion density. For the chequerboard source the ion density is clearly much more uniform over the whole dimension of the extraction array. In this case at a global beam perveance of 2.2μPv all the beamlets are extracted at (or very close to) the minimum divergence.

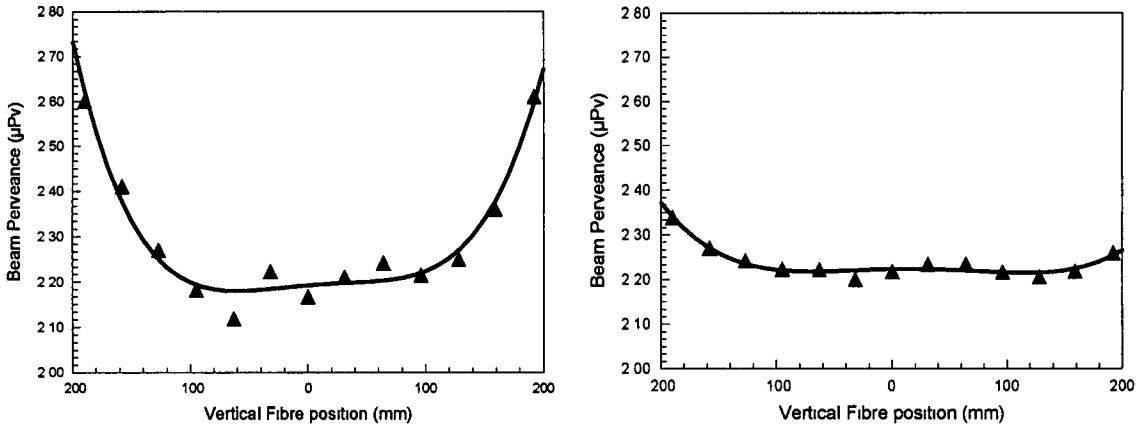

Figure 5 7 Comparison of chequerboard and standard ion source beamlet uniformity (using data uncorrected for the species change)

Reproduced from Chapter 2 (figures 2 7 and 2 11)

5.3 EXTENDED ION SOURCE

Initially it was postulated that the stray magnetic field from the super-cusp that is present at the extraction plane was responsible for the observed ion non-uniformity. A comparison of the magnetic field across the extraction planes of a super-cusp and chequerboard ion source is shown in figure 5.7 below. The extraction aperture array occupies approximately ±200mm in the vertical (y) direction and ±100mm in the horizontal (x) direction. Over the large majority of these ranges the chequerboard source has a field less than 1Gauss. However the super cusp source only produces a small central region of low field (<1Gauss) and the majority of the extraction array has a field of between 2- 5 Gauss.

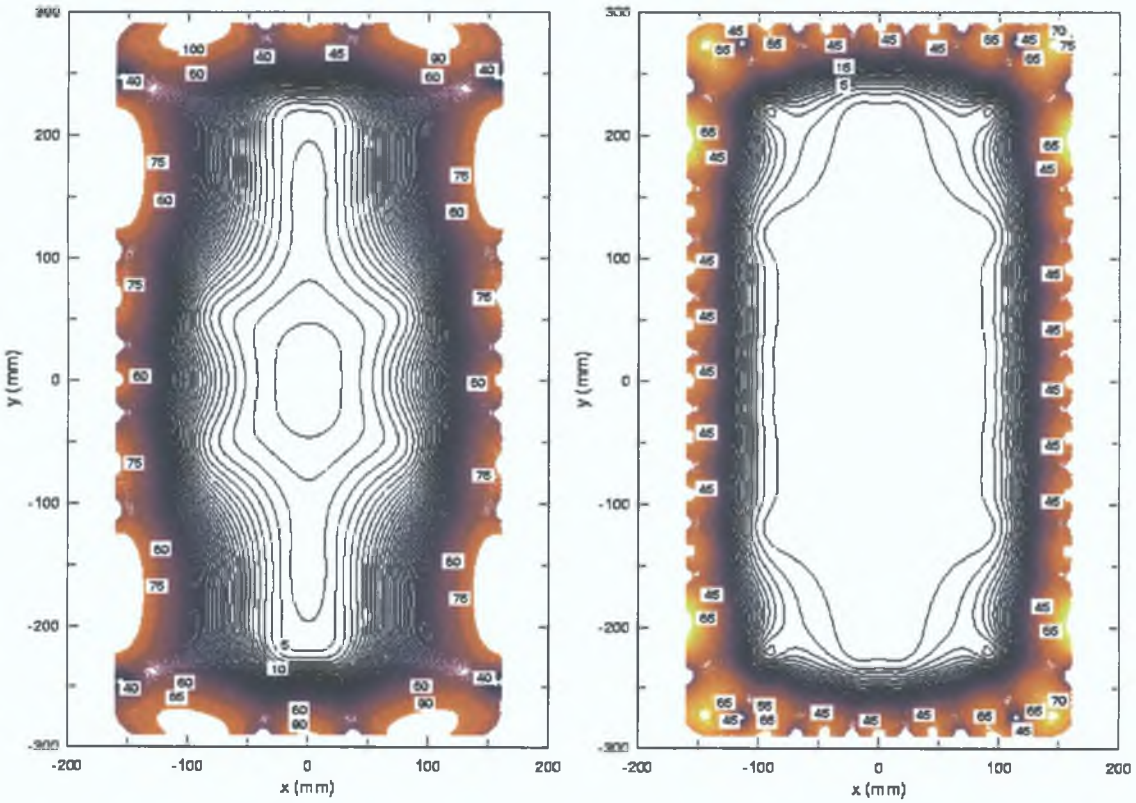

Figure 5.8: Comparison of the total magnetic field at the extraction plane of a) the SC15S3 super-cusp and b) the chequerboard only ion sources. The contours are in 1G increments, to a 100G maximum.

To attempt to produce a field free volume in front of the extraction plane a new ion source was manufactured with a 33% increase in depth The extended length was covered in a chequerboard pattern whilst the SC15S3 super cusp magnet pattern was maintained as closely as possible over the rest of the source

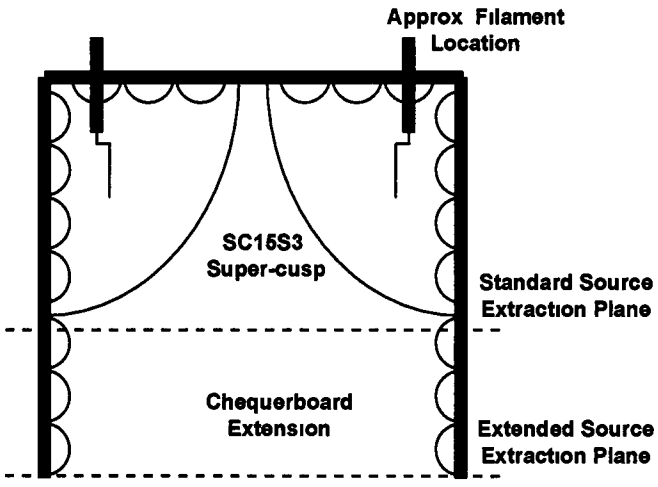

Figure 5 9 Schematic of the Extended Ion source design

During the mechanical design of the extended source body, it was considered necessary to add reinforcing bars to the sidewalls of the source This action was taken to prevent the extended ion source walls from buckling when the internal volume was evacuated In order to mount these reinforcing bars to the source walls it was necessary to leave extra spaces in the magnet pattern of each row However care was taken to keep the magnet pattern as close as possible to the original SC15S3 pattern

5.3.1 Extended Ion Source Performance

When operated on the Neutral Beam Test-Bed a PINI using this extended ion source was found to have significantly degraded arc efficiency, although the monatomic species yield was found to be m excess of 90% In addition, it was clear that the ion uniformity was no better than the standard length source with the SC15S3 super-cusp

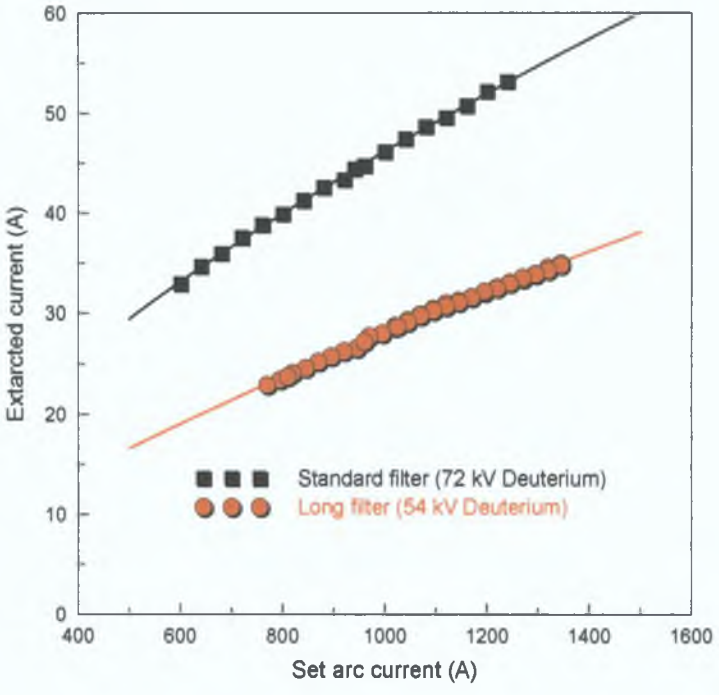

Figure 5.10 Arc efficiency of the extended filter source, compared to the standard SC15S3 filter source.

The arc efficiency of this source was too poor to allow a beam to be extracted at voltages higher than 60kV, the maximum D^+ current obtained was 35A – where >50A is required to run the beam at 80kV. Thus, all the beam characterisation measurements had to be performed at <60kV, this data must then be compared with data taken from other beams at 70-80kV.

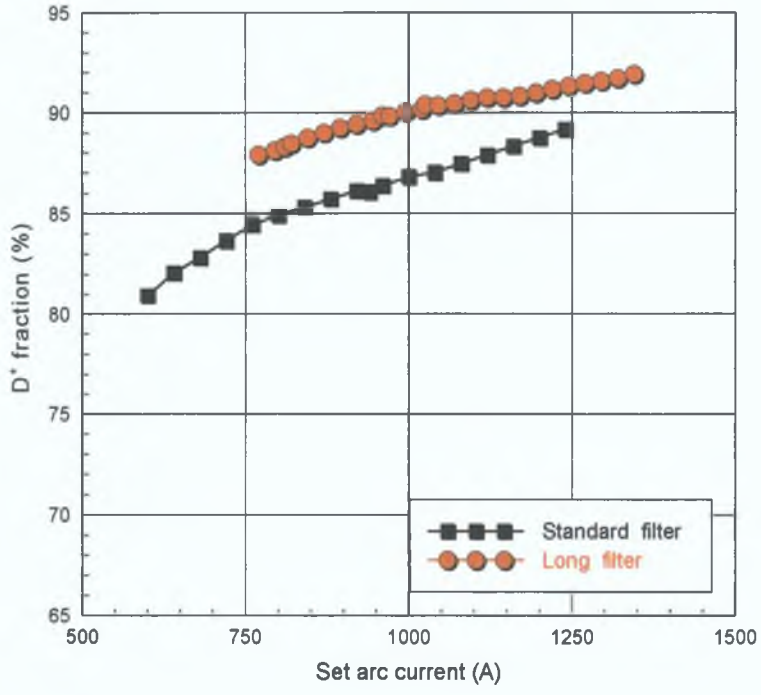

Figure 5.11 Monatomic species yield comparison for the extended ion source and the standard SC15S3 ion source

The monatomic species yield of the extended ion source was the best yet measured, with a maximum D^+ content of 92%. Comparing the plot of the beam perveance profile at which the local minimum divergences occur show that the ion density profile for the deepened ion source is actually slightly more non-uniform than for the standard super-cusp source.

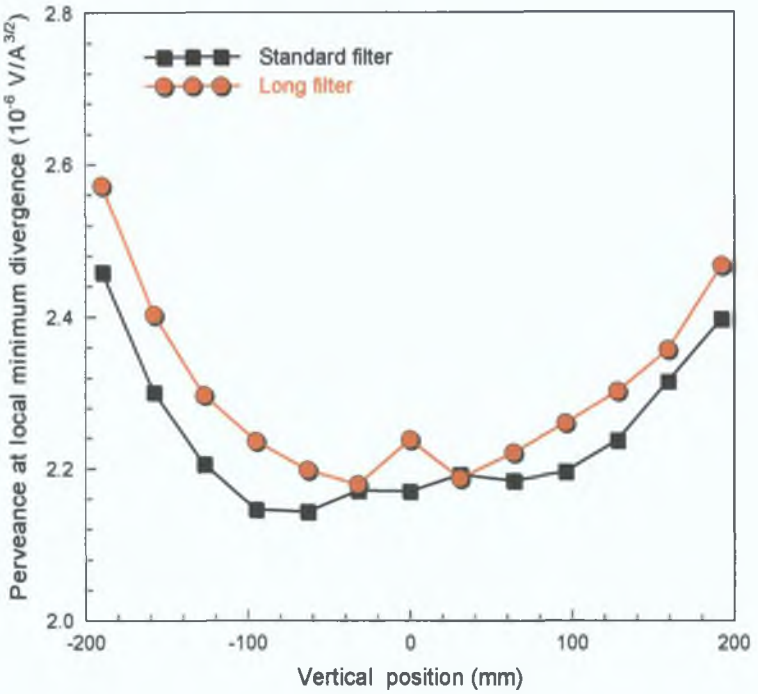

Figure 5.12 Comparison of local beamlet divergence minima for the extended and standard ion sources

It was clear that the arc efficiency of this ion source was too poor to enable this source to be used on the high current PINIs. There was some concern that the extra spacing introduced into the magnet pattern to accommodate the source wall support bars was increasing the effective wall loss area, giving a loss of primary electron confinement, and that this could explain the reduced arc efficiency. It was therefore decided to configure this source with a chequerboard only magnet pattern so that it would be clear whether the performance loss was due to these 'gaps' in the confinement field pattern

When operated as a chequerboard only source, it was found that the extended source gave an arc efficiency performance identical to that of a standard source body with a chequerboard only magnet pattern. The clear distinction of the extended source was that the monatomic species yield increased to 75%, from the 65% usually expected with a standard source in this configuration. The ion density uniformity across the extraction array was also essentially uniform, the same as observed from the standard chequerboard only source.

The test of the extended source with a chequerboard only field pattern showed clearly that the loss of performance was due to the positioning of the filter field away from the extraction plane

It was thus becoming clear that our initial theory, that the ion source non-uniformity was produced by the stray magnetic field at the extraction plane from the filter, was not necessarily correct

5.4 Line Cusp Magnetic Configurations

A review of current high power positive ion sources in use reveals that the source used by JAERI employs a rather different magnetic field configuration Figure 5 14 shows a schematic drawing of the source reproduced from [39] This ion source uses bands of magnets arranged in a line cusp pattern around the source, with a comparatively large spacing between rows (50mm compared to 30mm in the JET sources) The filaments are then placed close to the side wall of the source behind the field created between line cusp rows The 'filter field' is thus produced directly by the longer range of the fields used to provide confinement In addition the ion production region is kept close to the wall and extends along almost all of the depth of the ion source This achieves something close to the aims that we have after the results of the extended ion source tests, where we require an ion production source to compensate the loss to the source walls It is claimed that this source gives good arc efficiency, monatomic species yield and ion density uniformity [40]

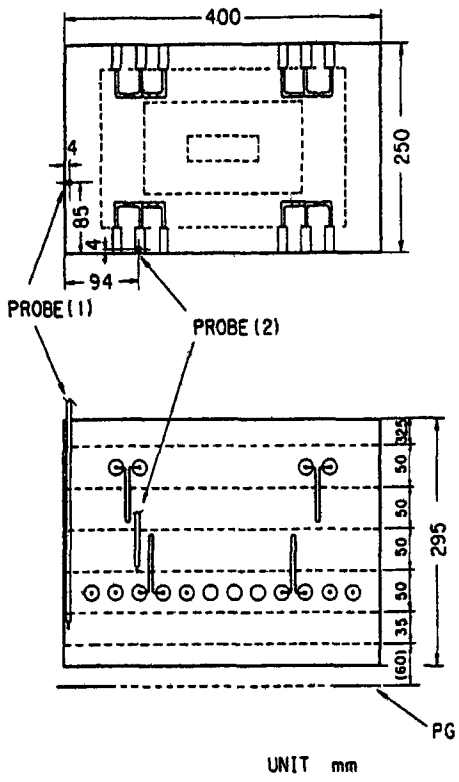

FIG 2 Developed view of the arc chamber Dotted lines show the cusp lines and hairpin-shaped line filaments

Figure 5 14 JAERI Positive ion source schematic (reproduced from [39])

Clearly, the important difference between the JAERI design and the PINI ion source design is the filament location The PINI ion source has filaments fed through from the back plate and cannot be modified to use side wall mounted filaments Thus, we can only use a reconfiguration of the magnet pattern to attempt to emulate the JAERI design

Two different line cusp magnet configurations were tried using the standard depth PINI ion source

5.4.1 LINE CUSP A

Our first attempt to modify the magnet pattern was to put bands of doubled magnets (stacked on top of each other) around the ion source, but leaving the intermediate rows empty A

chequerboard only pattern was primarily used on the back plate but with an outer single line cusp row to attempt to compensate for the field from the uppermost double line cusp band.

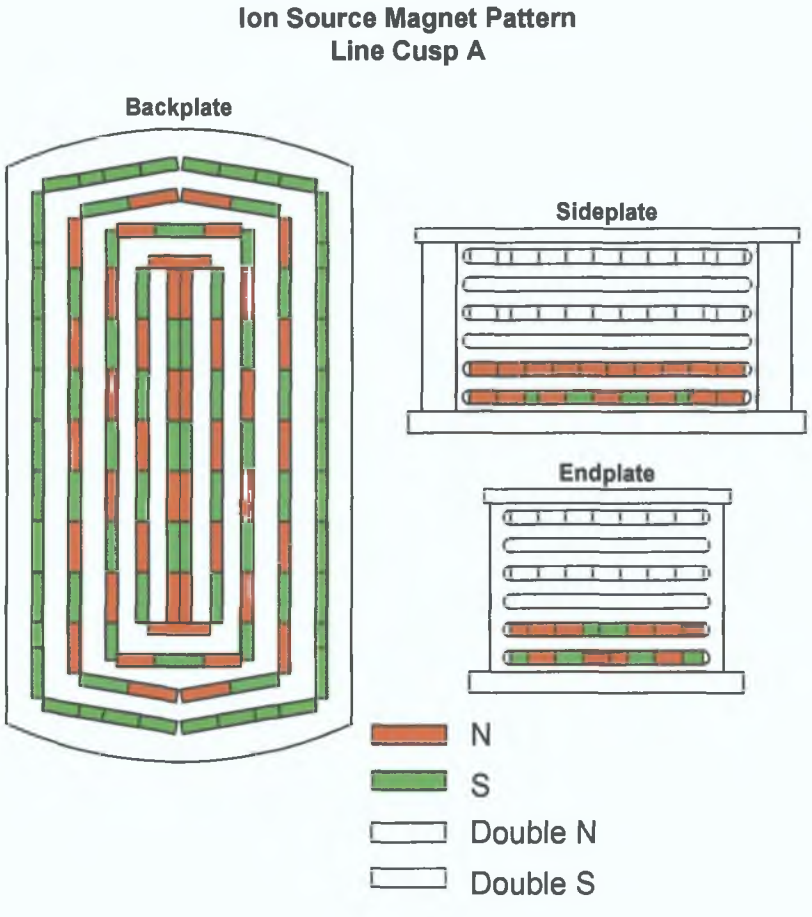

Figure 5.15 Schematic of the Line Cusp A magnet configuration

In addition, the filament stems were rotated so that now the filaments are placed closer to the source wall. Figure 5.16 shows a field line plot of the calculated field across the source centre half section plane, across the horizontal (x) axis, showing a projection of the filament geometry onto this plane. The field lines of this figure indicates that the electrons emitted from the filaments can be expected to be confined close to the source wall and backplate.

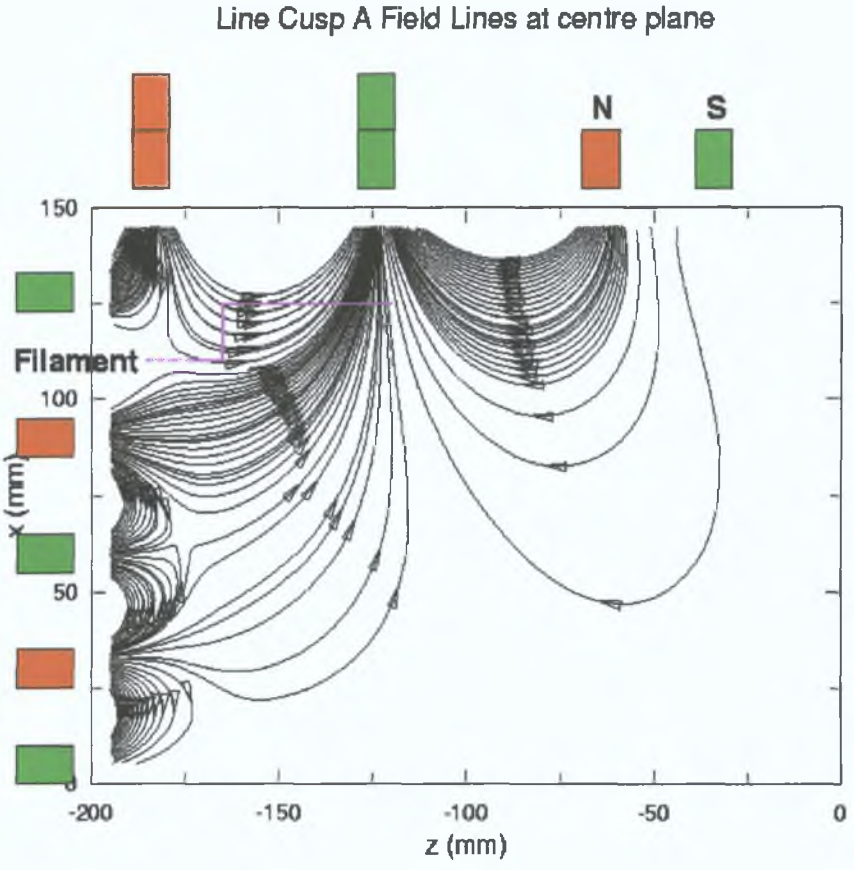

Figure 5.16 Field line plot of a centreline ½ section through the modelled field of the Line Cusp A magnet configuration.

5.4.1.1 Line Cusp A Performance

The initial operation of a source with this magnet configuration was found to have very low arc efficiency. We could only extract 6A of ions for an arc current of 600A. It was therefore impossible to continue with the source in this configuration. It was postulated, and confirmed by subsequent modelling of the primary electron trajectories, that the double magnet configuration was too effective at confining the primary electrons to the rear of the source. It was decided to make modifications to this source in situ to try to weaken the line cusp rows. The 'piggy backed' magnets were removed from the double magnet bands and extra magnets added to the backplate to try to push a weakened line cusp field forward to the extraction plane.

A model of the reconfigured magnet pattern confirms that this has given a situation where some of the filament is now emitting into the lower of the two line cusps, i.e. closer to the extraction plane.

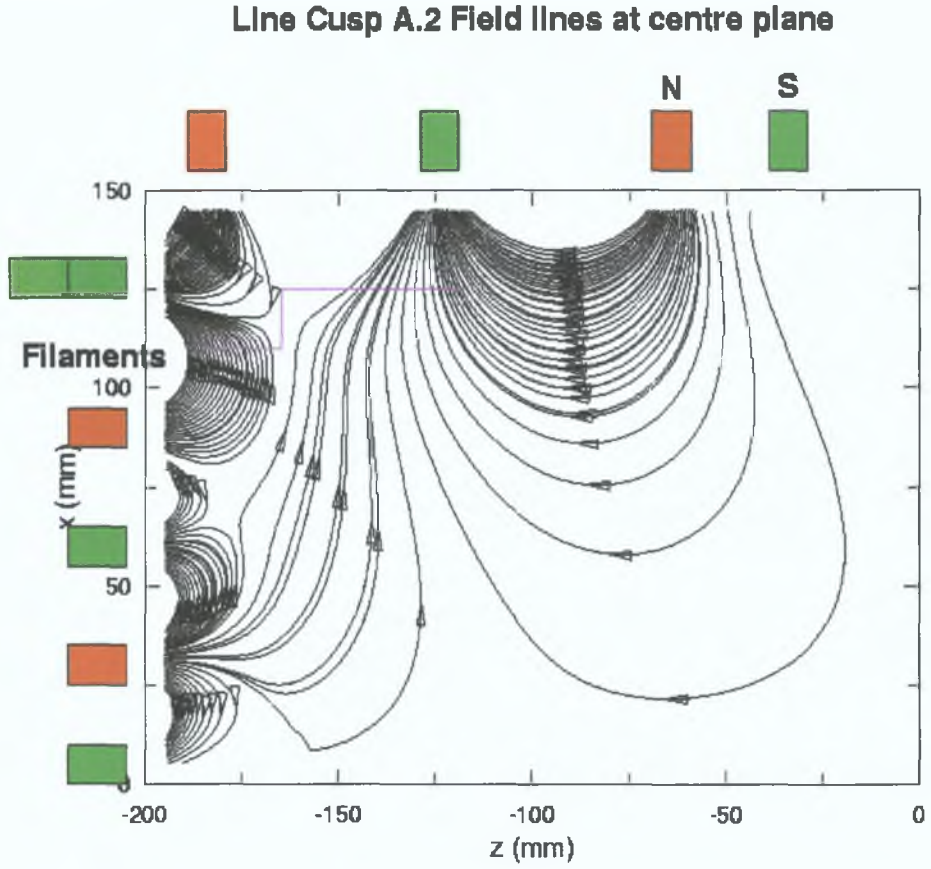

Figure 5.17 Field line plot of a centreline ½ section through the modelled field of the modified Line Cusp A.2 magnet configuration.

This modification had the desired effect, the arc efficiency returned to a value close to that achieved in the standard super cusp source. The arc efficiency value achieved for this configuration was ≈10% lower than the super-cusp efficiency. This enabled a complete characterisation of the beam parameters to be performed. The monatomic species yield for this configuration had a peak value of 83% D^+, less than the super-cusp source but still generally acceptable.

The uniformity appeared to be marginally better than the standard super-cusp source, a larger more uniform central part to the profile can be seen, although the edges of the beam shows evidence of non-uniformity again.

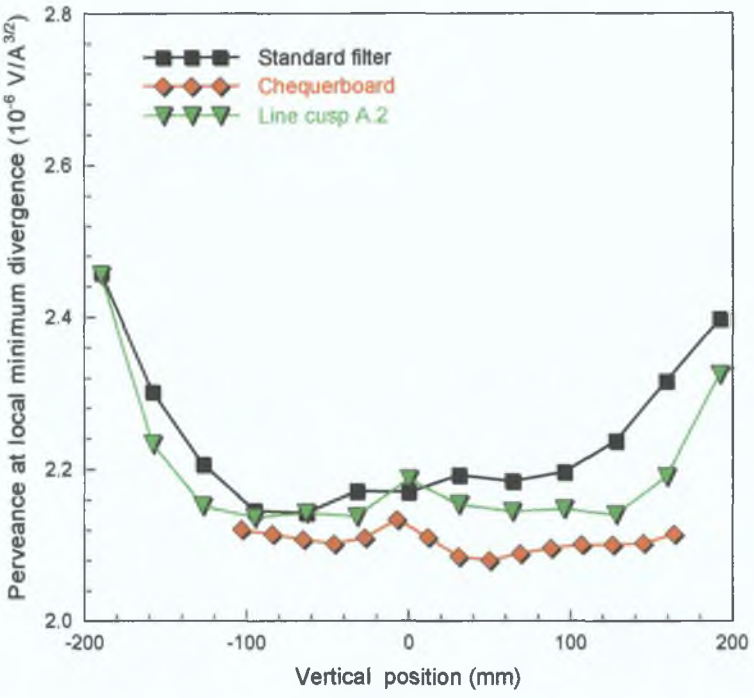

Figure 5.18 Minimum beamlet divergence uniformity compared for super-cusp. chequerboard and line-cusp A.2 sources.

This does lead to some improvement in beam transmission to the Test-Bed beam dump, giving a value between that of the chequerboard and super-cusp sources.

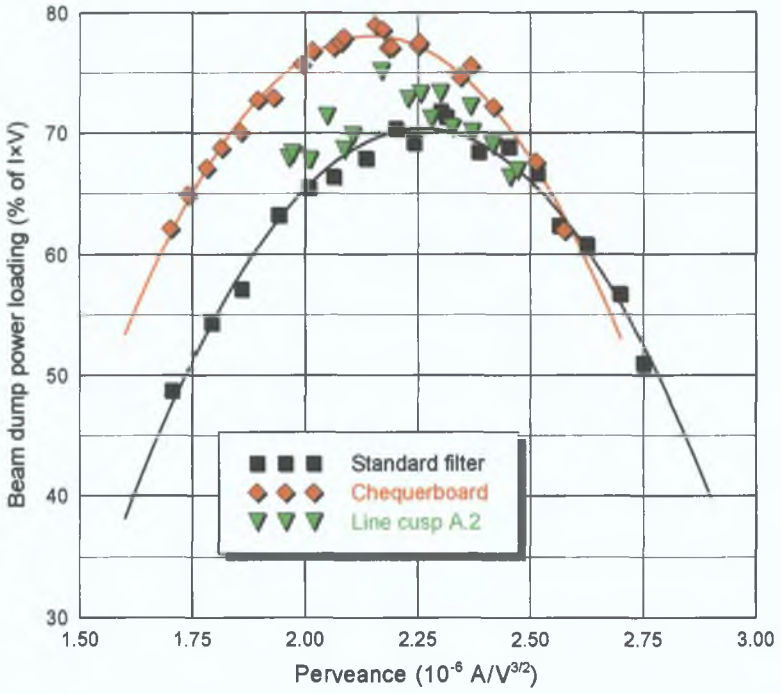

Figure 5.19 Beam transmission to the Test-Bed beam dump compared for super-cusp, chequerboard and line-cusp A.2 sources

Debatably, the source with the A.2 line cusp configuration has improved performance over the standard super-cusp source. Although the 10% reduced arc efficiency would make this source difficult to operate at high power, the improved transmission could compensate for a small loss of monatomic species yield.

5.4.1.2 Line Cusp A Source Model

At the same time as the experimental program, some of the new magnetic field arrangements were simulated with the newly developed Monte Carlo primary electron trajectory code, which at that time was starting to produce 3D maps of the ion production regions.

The primary electron trajectories in the first line cusp configuration (A.1) were modelled and a plot of the resulting ionisation interactions is shown in figure 5.20

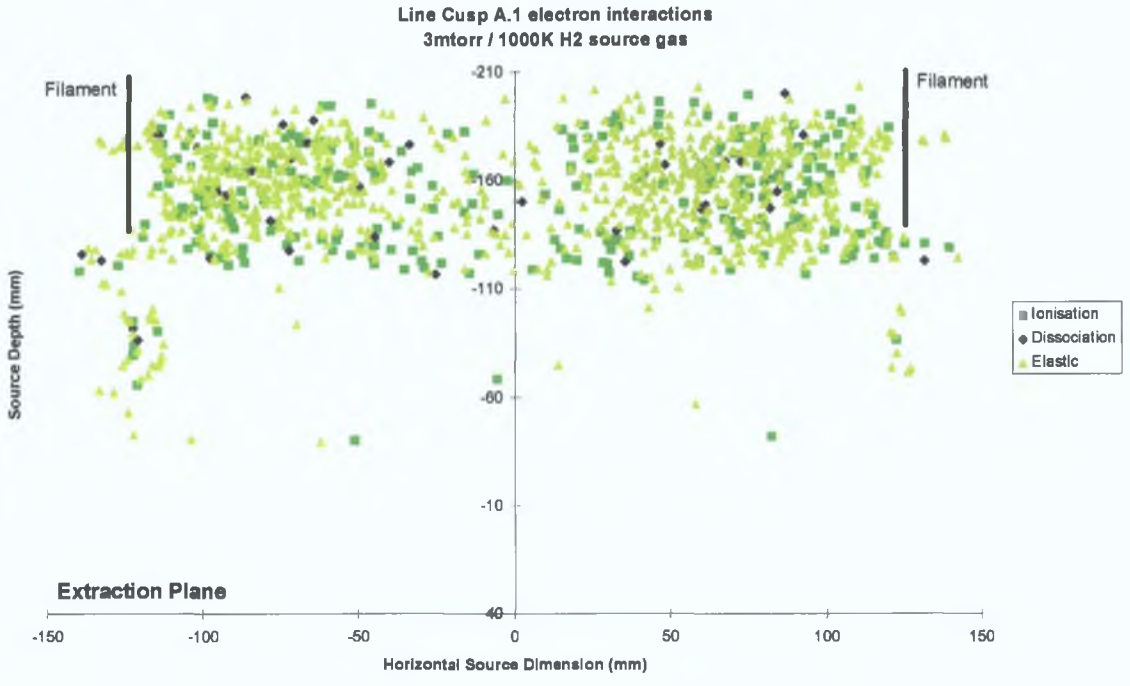

Figure 20 Primary electron interaction points mapped onto a vertical (y) cross-section through the line-cusp A magnet configuration.

This figure clearly shows that the ion production region is very well confined towards the back of the ion source, agreeing qualitatively with our observation of a very poor arc efficiency which is indicative of an extremely low ion density available at the extraction plane.

Figure 5.21 shows the results of the same model run with the modified line-cusp A.2 configuration. It can be clearly seen that the weakening of the line cusp allows primary electrons to move closer towards the extraction plane of the ion source, although the primaries are still sufficiently confined to prevent reaching the extraction region directly. This model is consistent with our observation of improved arc efficiency in the line-cusp A.2 configuration, by showing that the ion production region has been moved closer to the extraction plane. In addition the fact that the primaries appear to be reasonably well confined away from the extraction plane is consistent with the 83% monatomic species yield observed.

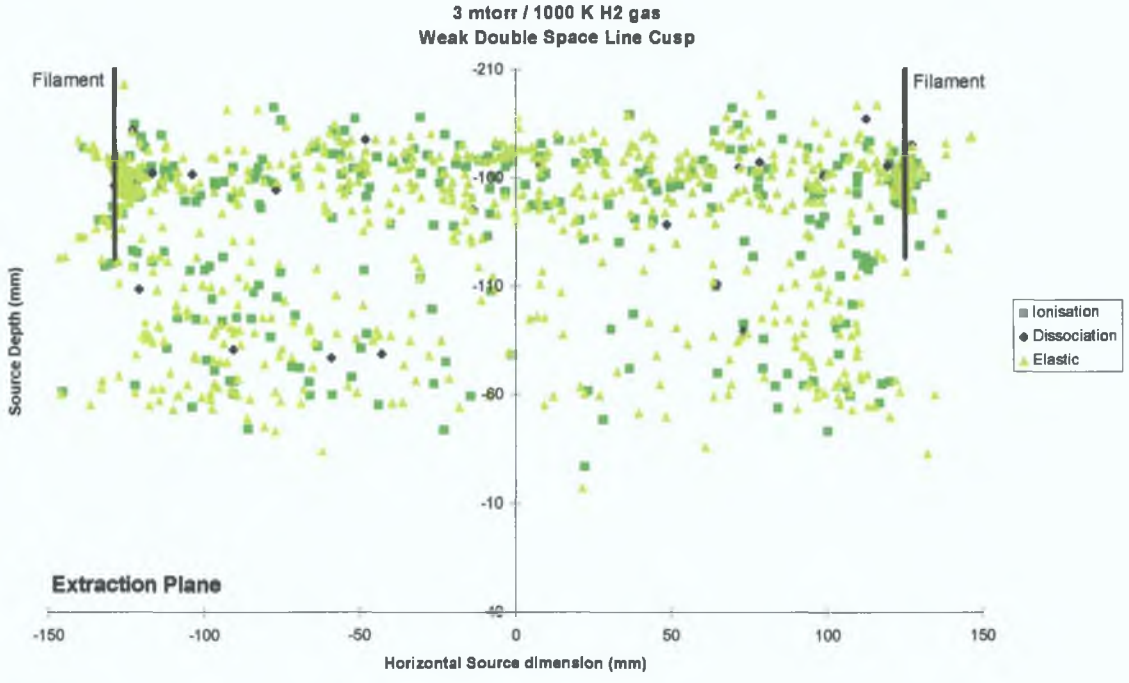

Figure 5.21 Primary electron interaction points mapped onto a vertical (y) cross-section through the line-cusp A.2 magnet configuration.

5.4.2 LINE CUSP B

With confidence that our knowledge of how to modify the magnetic field pattern was now heading in the right direction there was room in this phase of the experimental program for one more configuration. With the next configuration, we tried to produce a large single line cusp that would reach along the whole depth of the source. It was apparent from the earlier line cusp configuration that we had sufficient field to keep primary confinement with only a single depth row of line cusp magnets. We therefore made the new magnet pattern with two single line cusp rows on the source side walls separated by a chequerboard magnet pattern to maintain high electron confinement.

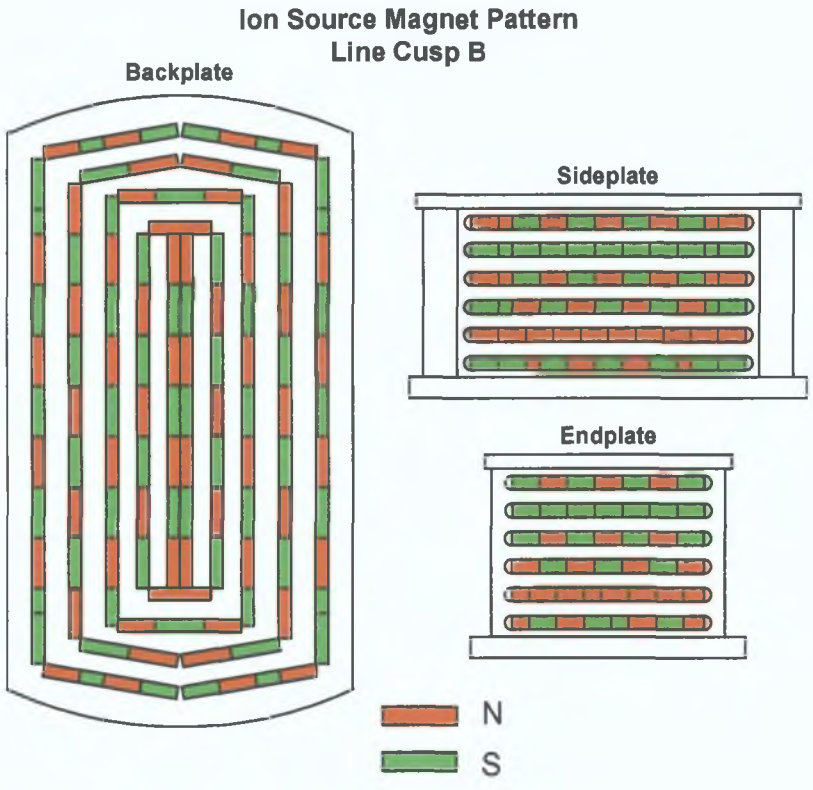

Figure 5.22 Schematic of the line-cusp B magnet configuration

5.4.2.1 Line Cusp B Source Model

In this case the electron trajectory model was run with the new magnet configuration prior to the experimental tests. This enabled some level of performance prediction to take place before committing to the installation of the PINI on the Test-Bed. The output from the model of the line-cusp B configuration shown in figure 5.23, shows that the primary electrons are well confined around the walls of the source. The ionisation region does, however, also extend well down the depth of the source walls close to the extraction plane.

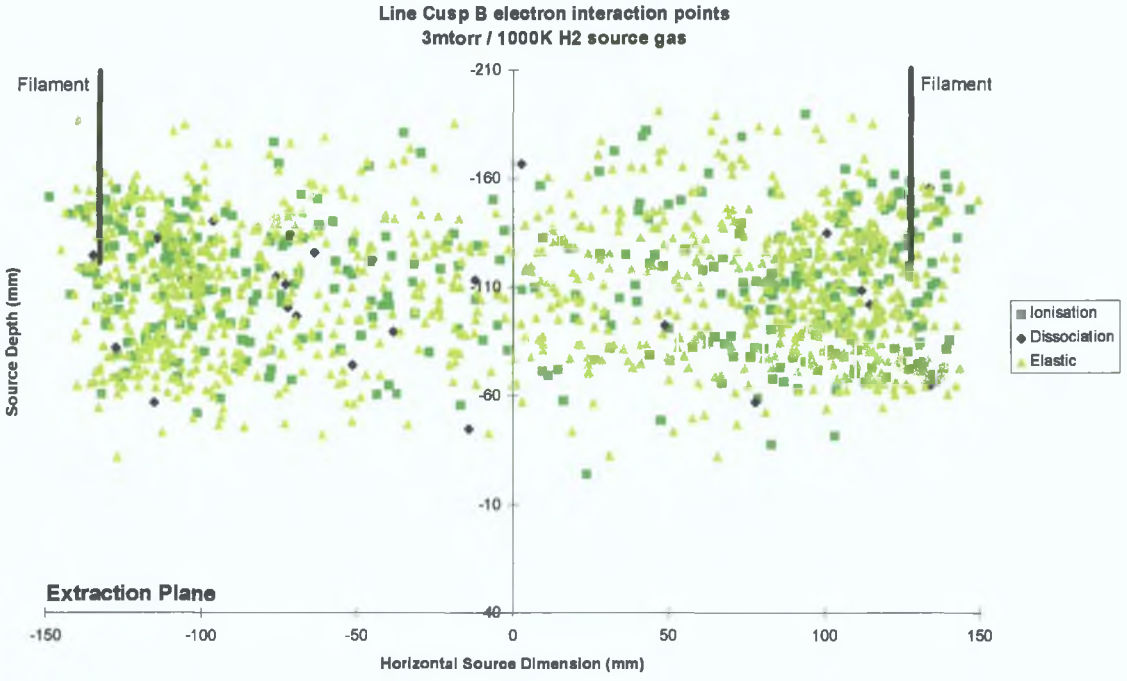

a)

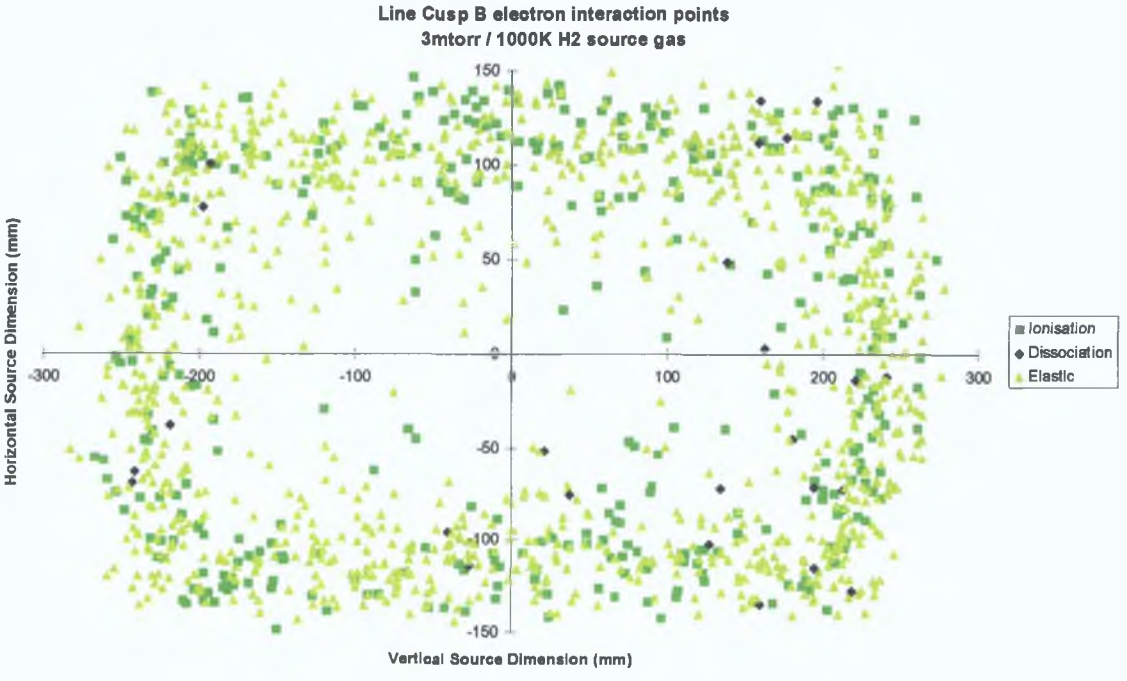

b)

Figure 5.23 Projection of all primary electron interaction points onto planes in the ***a)*** *YZ and* ***b)*** *XY planes of the source for the line-cusp B magnet configuration.*

It was thus expected that this source will have an arc efficiency comparable to the super-cusp and line cusp A.2 configurations. Also a clear absence of primary electrons crossing the confinement field should indicate that a reasonable monatomic species yield could be achieved. We also appear now to have created a source of ions around the source wall to compensate for the loss of ions from the plasma centre to the walls.

5.4.2.2 LINE CUSP B PERFORMANCE

As anticipated this ion source exhibited an arc efficiency as good as that achieved with the standard super-cusp ion source, allowing a full characterisation of the beam properties up to full power.

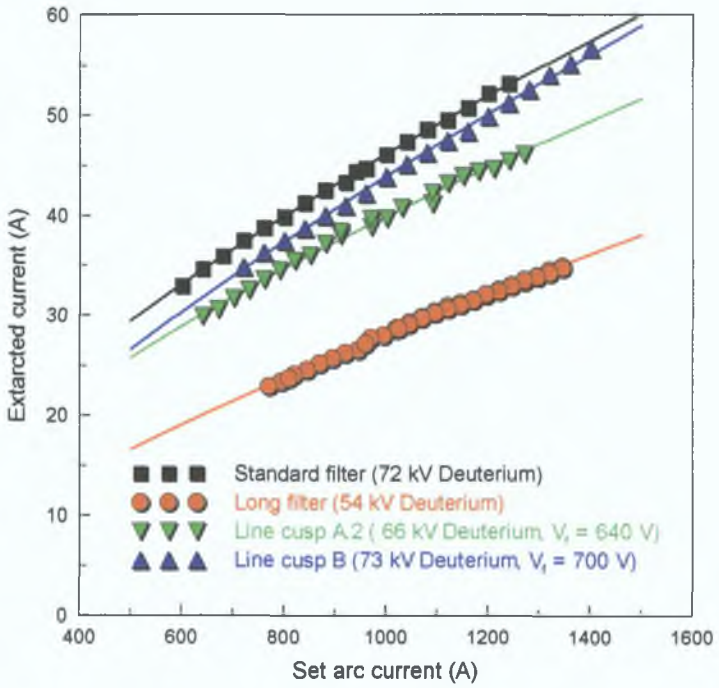

Figure 5.24 Comparison of arc efficiency of the line cusp sources with the standard and extended super-cusp sources.

This line cusp configuration achieved a maximum monatomic species yield of 84% D^+, which compares very well with the 85-88% generated by the standard super-cusp source. It is the measurement of ion density uniformity that is of most interest with this source. The figure 5.25 below shows, that with this source configuration the lowest central beamlet divergence

actually occurs at high overall beam perveance (i.e. current). Thus we have inverted the density profile normally seen, where the ion density is peaked in the centre and falls towards the edges of the source, to give a profile where the ion density is higher at the edges and falls towards the centre of the source.

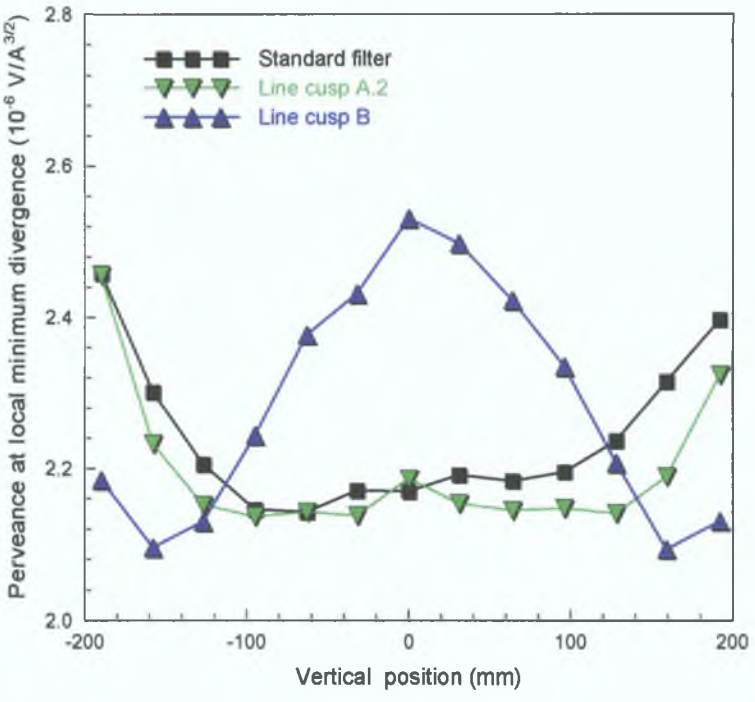

Figure 5.25 Local optimum perveance for the two line cusp configurations compared with the super-cusp source

This may not be the optimum ion density profile as it is still quite non-uniform, but we have demonstrated a capability to modify the ion density profile, which is encouraging. This source does however seem to give improved beam transmission over the standard super-cusp source, but not as much as is achieved with the chequerboard only source.

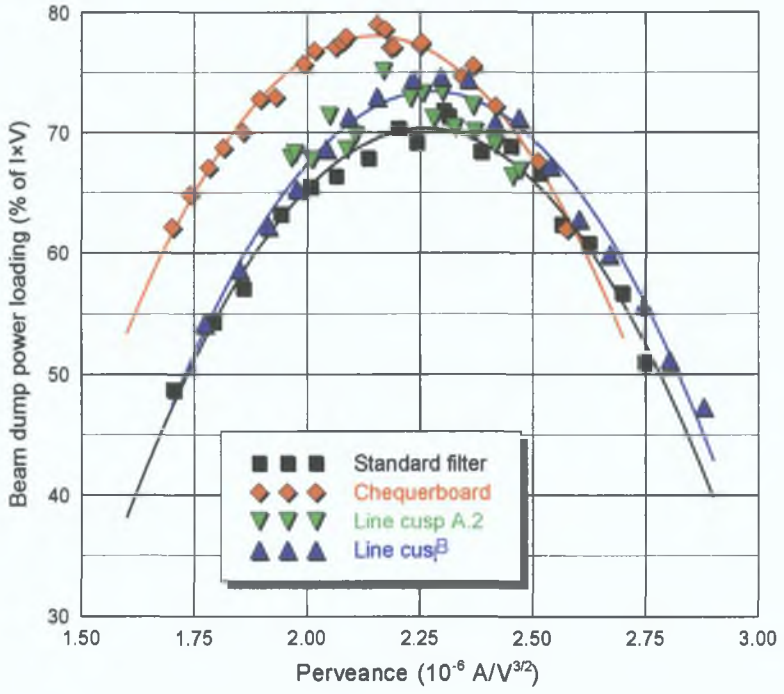

Figure 5.26 Comparison of Test-Bed transmission for beam extracted from Line cusp sources with the standard super cusp and chequerboard only sources.

Finally, we can compare to optimum beam perveances seen as the minimum beam width on the Test-Bed beam dump. This shows how closely the final line cusp configurations compare to the super cusp source, even though the sources have two completely different methods of producing primary electron confinement.

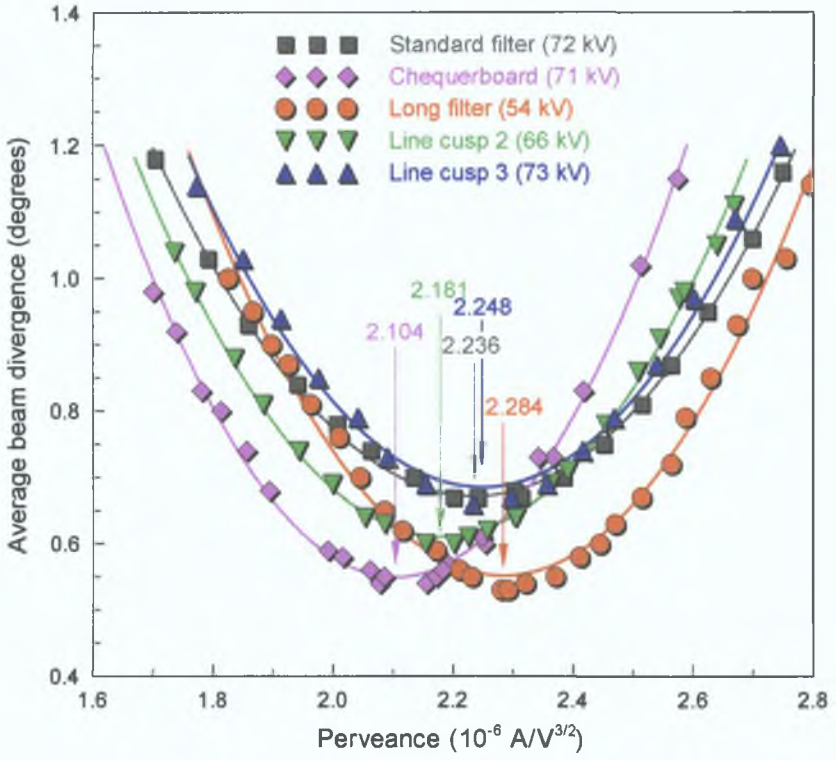

Figure 5.27 Comparison of optimum perveance on the Test-Bed beam dump with PINI 11AT with all the source configurations used in this development.

5.5 New Ion Source Design

One of the primary aims of this work was to decide whether to set of new ion source currently under design should be built as standard or extended sources. Once it was clear that the extended source could not work on the JET PINIs, the decision was made to construct the new sources at standard depth.

For the new ion sources it was decided to retain the existing source backplates and build new source bodies only. At this time it was decided that to allow greater flexibility in the choice of new magnet patterns that space for a possible extra row of magnets would be placed along the source walls. Tests of the previous line cusp configuration showed that each positioning row on the source body would not necessarily need to be populated with magnets. Without lengthening the depth of the ion source the space for an extra magnet row was found by

reducing the inter row spacing. Thus a design was chosen with 7 rows of magnets at 23.5 mm separation, compared to the previous deign of 6 rows at 30.0 mm separation.

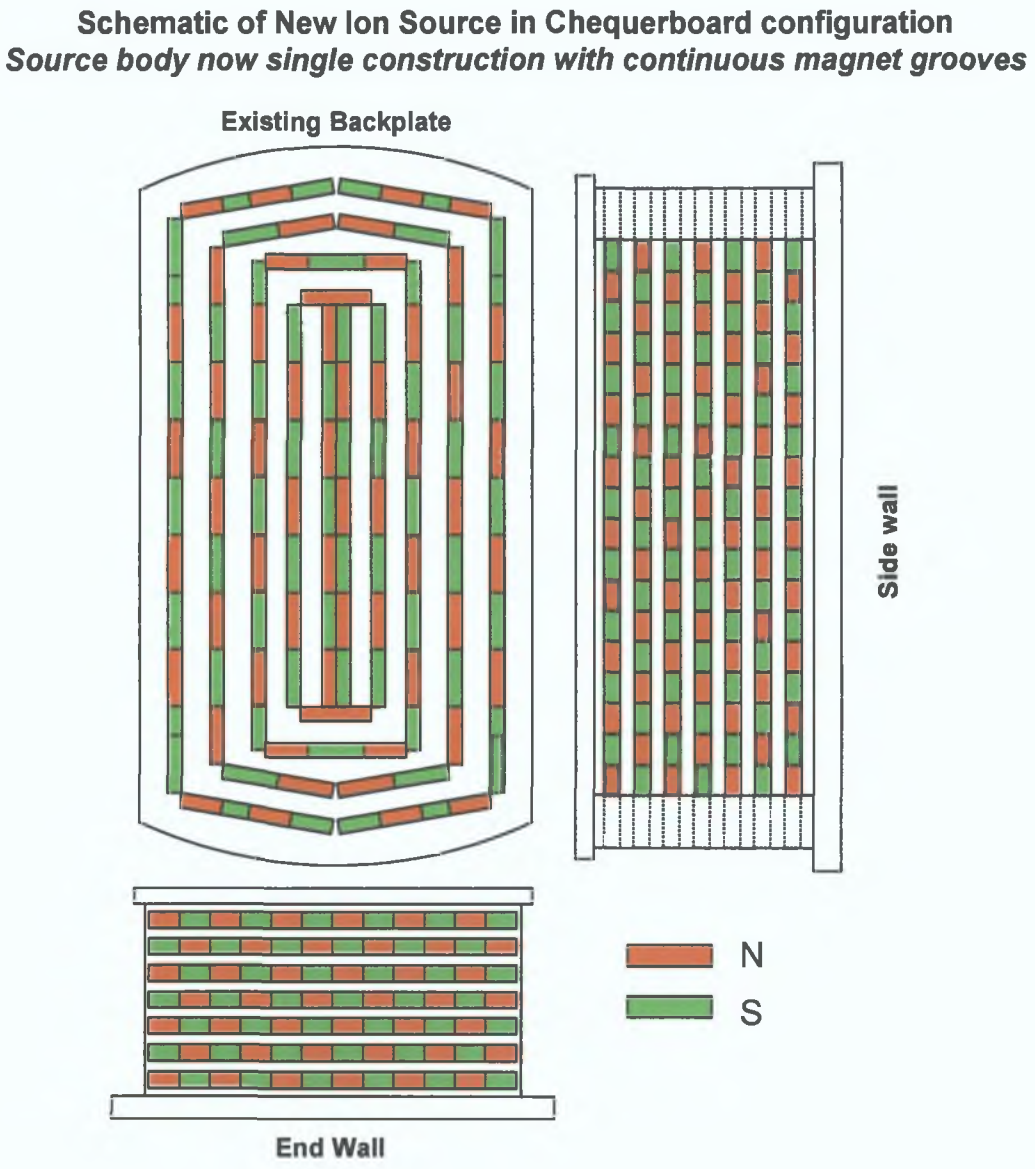

Figure 5.28 Schematic of the new ion source body design, in chequerboard configuration. Note now the source body is one single construction, with continuous magnet groves around the wall circumference.

A schematic view of the new ion source construction is shown in figure 5.28. In addition to a reduction in the magnet row spacing, to accommodate an extra row, the source body is now constructed as a single piece [41]. This has allowed the grooves that hold the magnets to be

made continuous around the circumference of the body Hence the magnet now form a continuous band around the whole source, without the previous gap the existed at the joint between the separately constructed side and end plate sections

The other significant change is the choice on magnets that are used on the source body In order to have greater flexibility in magnet designs a common magnet length of 27mm was chosen for the source walls, compared to the 46mm magnets generally used in the SC15S3 design This new magnet length was chosen so that a symmetric magnet pattern could be used with 9 magnets either side of the centreline of the sidewall and 6 either side of the end wall As line cusp configurations were considered for this source, magnet with a stronger remnant field were chosen so that long-range line cusp filter field could be formed The new magnets have a remnant induction of 0 97T compared to the 0 85T of the magnet previously used

5.5.1 Initial Configuration (NSC_1)

Initially the new ion source body was configured with a magnet pattern as close as possible to the SC15S3 pattern, so that a reference source performance could be obtained with the new construction This would also give us a fall back position should further magnet pattern optimisations prove to be unsuccessful

A schematic of the magnet pattern chosen to resemble the SC15S3 magnet pattern is shown in figure 5 29 A single line cusp is used along the source side walls with a break of reversed magnets across the centreline of the end plates The rest of the source body is covered in a chequerboard pattern, which is arranged to give axes of symmetry across the centre line of both the side and end walls The backplate retains the original magnets and magnet pattern - only the source body magnet pattern is modified

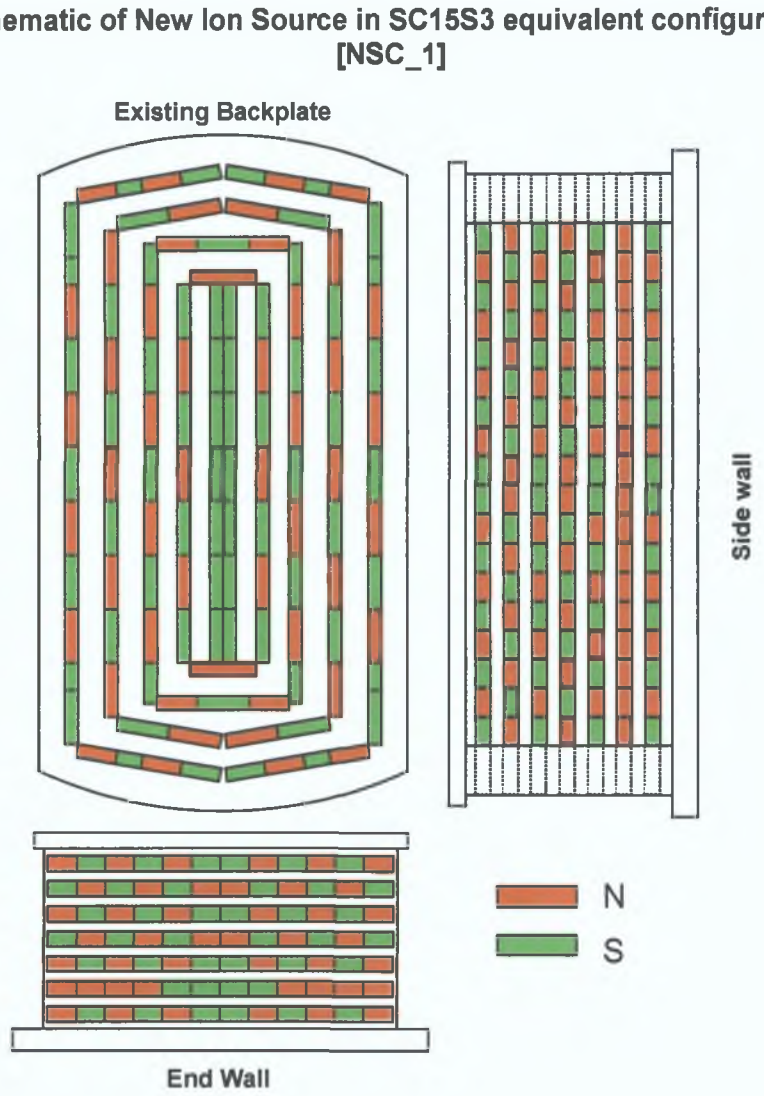

Figure 5.29 Schematic of the magnet pattern used for the new ion source body, chosen to be as close as possible to the SC15S3 magnet pattern. Labelled NSC_1.

An ion source was constructed with this NSC_1 magnet configuration and mounted onto PINI 6AT, a high current tetrode accelerator. This PINI was then operated on the Neutral Beam Test-bed. Immediately it was clear that the beam from this PINI was not behaving in the same way as from an SC15S3 super-cusp source. The box scraper power loading was seen to be higher, at 10% of the beam power compared to 7% for the SC15S3 source. The perveance at which the minimum power loading occurred, and minimum beam dump width, was also higher at 2.5μPv, compared to 2.3μPv.

Measurements of the beam with the multi-channel spectrometer soon confirmed these initial observations. The monatomic species yield from this source was greater than for the SC15S3 source, with an extra 2% of the species total as D^+, across the whole of the measured beam. The species yield measured across the new source configuration NSC_1 is shown in figure 5.30, compared to that from the SC15S3 super-cusp source.

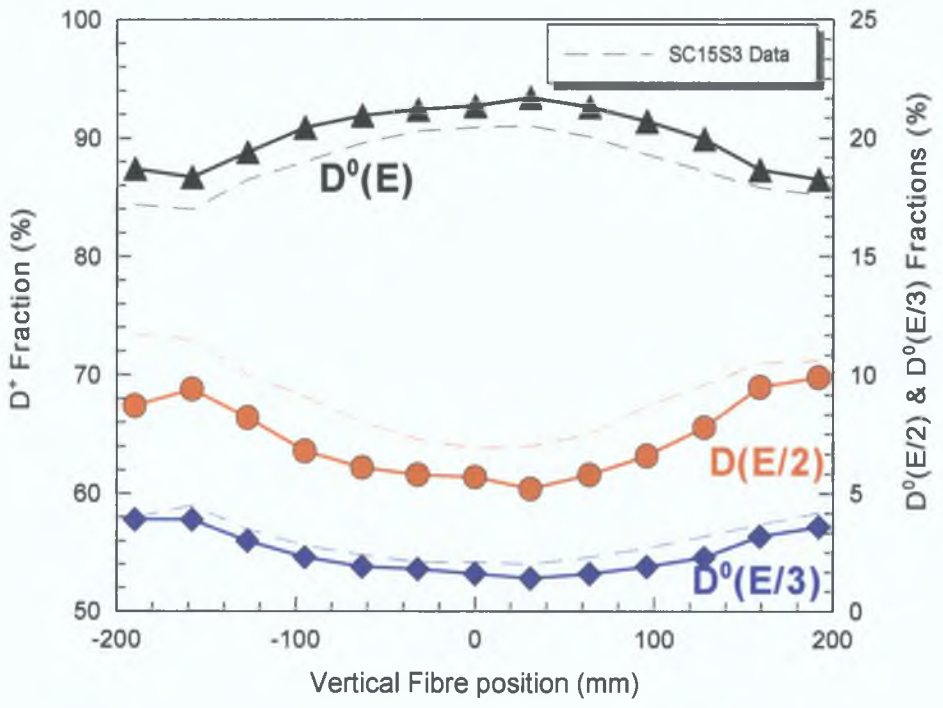

Figure 5.30 Comparison of the Deuterium beam species yield obtained from the NSC_1 and SC15S3 super-cusp ion sources (shown as the measure full, ½ and 1/3rd energy D^0 components of the beam).

Plotting the total beam perveance where the local minimum beamlet divergence is seen for the beam from the NSC_1 ion source shows that this ion source produces a larger non-uniformity in the ion density than is given by the SC15S3 super-cusp source. A comparison of this source with the SC15S3 super-cusp and chequerboard sources is shown in figure 5.31.

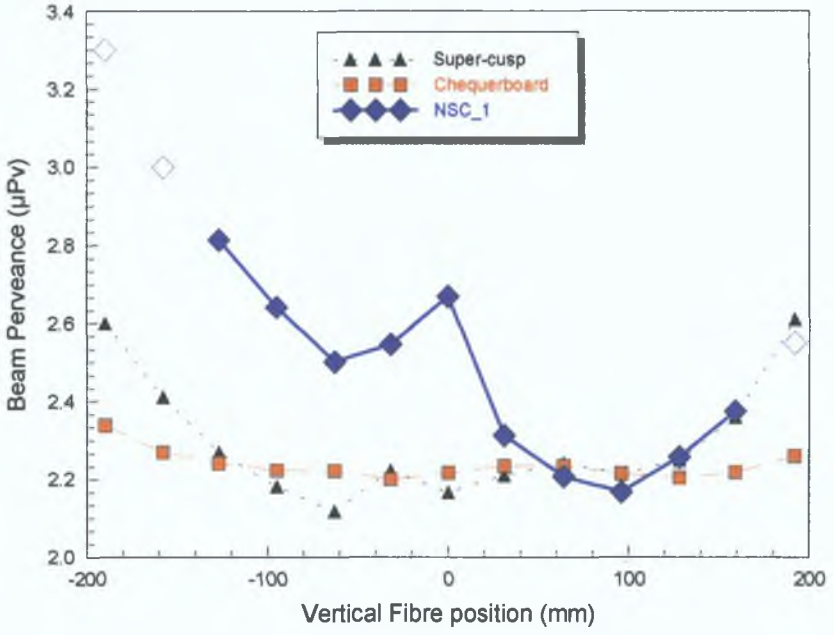

Figure 5.31 Comparison plots of the total beam perveance at the local minimum beamlet divergence for the NSC_1, SC15S3 and chequerboard ion sources. [In the case of the NSC_1 plot the open symbols refer to points generated by interpolating from outside of the data measured in the perveance scan]

It is clear that the NSC_1 configuration is not suitable for use, although the monatomic species yield is high, this is achieved at the expense of significantly degraded ion uniformity.

This magnet pattern was simulated with the magnetic field mapping code, to compare with the model already obtained of the SC15S3 source. As in the case of the SC15S3 magnet configuration the NSC_1 magnet pattern produces stray magnetic field across the extraction plane. Figure 5.32 shows the total magnetic field in the plane of the extraction array, with an indication of the extent of the array. This shows that over the majority of the extraction array the magnetic field exceeds 5 Gauss, reaching 20Gauss at the array edges.

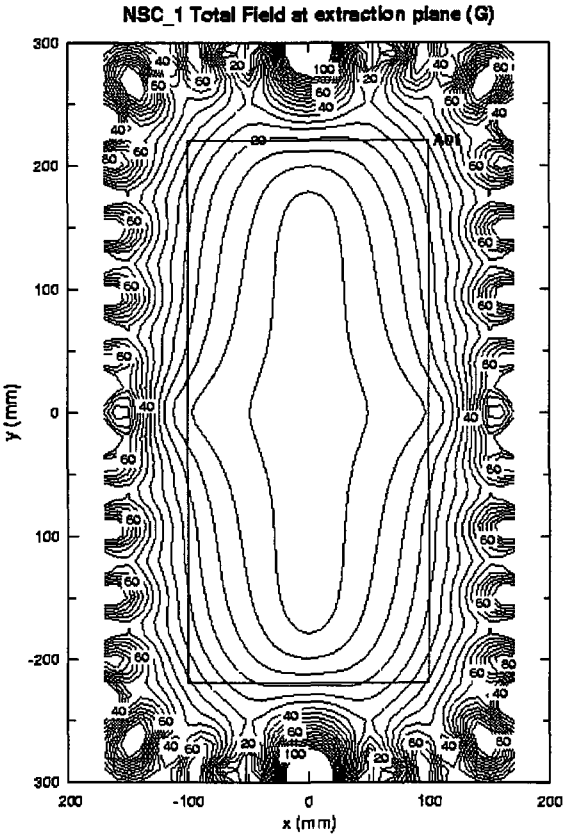

Figure 5 32 Total magnetic field modelled in the plane of the extraction aperture array The box marks the outer extents of the extraction array

A direct comparison can be given by comparing the magnetic field that extends between the side walls and the source backplate The plots of the simulated total field in the plane across the short XZ axis of the NSC_1 and SC15S3 ion sources are shown in figure 5 32

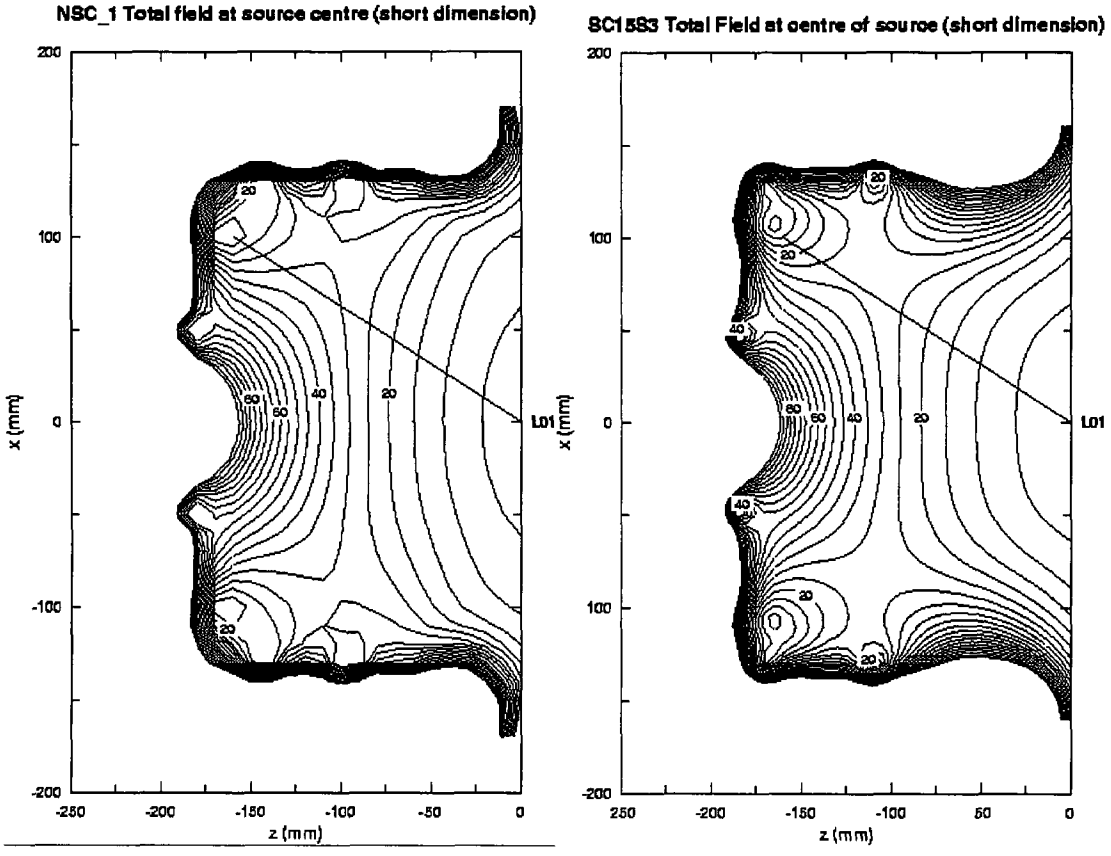

Figure 5 33 Comparing the field modelled trough the centre of the source in the XZ plane (across the short dimension of the ion source) The field is calculated along the line marked on both plots from filament stem (z=-160mm) to extraction plane centre (z=0mm)

To give a quantitative comparison the field along a line from the filament stem location to the centre of the extraction is calculated Comparing the peak fields and the integrals of the total B field along this line will give some indication of the relative strengths of the filter field generated in each source configuration

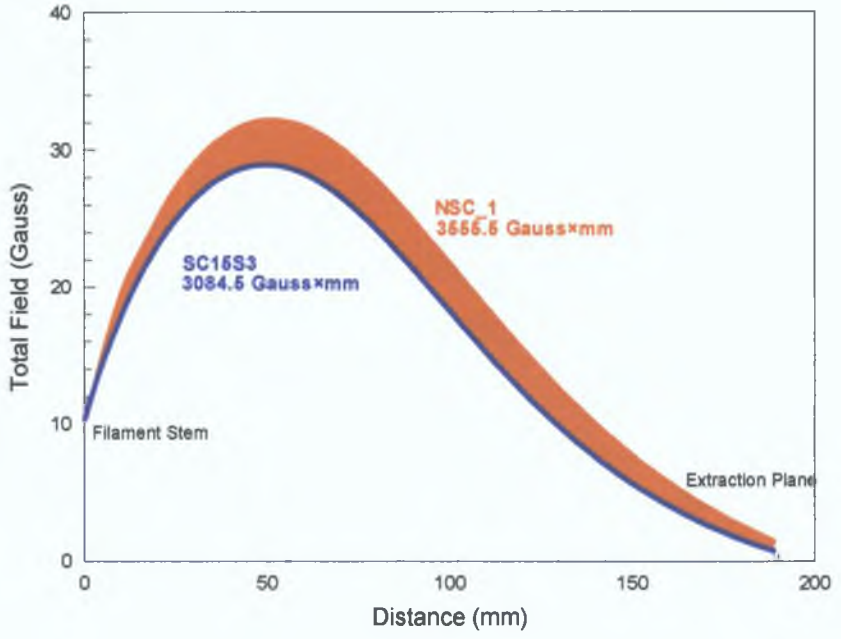

Figure 5.34 Total magnetic field plotted along the lines shown in figure 5.33. The origin is at the filament stem location with the end of the line at the centre of the extraction plane. Also shown is the integral of the curves in Gauss mm.

The filter field in the NSC_1 source is clearly stronger, with a greater peak strength, 32G, compared to 29G and larger integral 3555.5 G mm, compared to 3084.5 G mm. It appears from this information that the new magnets with the higher remnant field of 0.97T used in the new source bodies are creating a filter field that is stronger than with the older 0.86T magnets used for the SC15S3 source bodies. It was thus decided to find a magnet configuration that produces a weaker filter field but still using the new high strength magnets.

5.5.2 CONFIGURATION NSC_6

The interim magnet configurations NSC_2 to NSC_4 were attempts to weaken the filter field by changing the orientation of some of the magnets during the experimental programme - which had only small effects on the source performance. The configuration labelled NSC_5 was in fact a chequerboard only test of the source. It was felt necessary run a chequerboard configuration to confirm that the construction techniques used for the new ion source body were not themselves influencing the source performance. This test confirmed that the new

source body configured with a chequerboard source behaved in the same way as the previous chequerboard configurations

The configuration NSC_6 was chosen after some effort to produce magnetic field maps of the NSC_1 to NSC_4 configurations and then design a new magnet pattern based on the experience gained with these For this configuration rotation of every third magnet of the filter magnet row was used to substantially weaken the filter field In addition the chequerboard pattern over the rest of the source body was modified to be continuous around the source body - rather than being symmetric across the centre line of the side and end walls

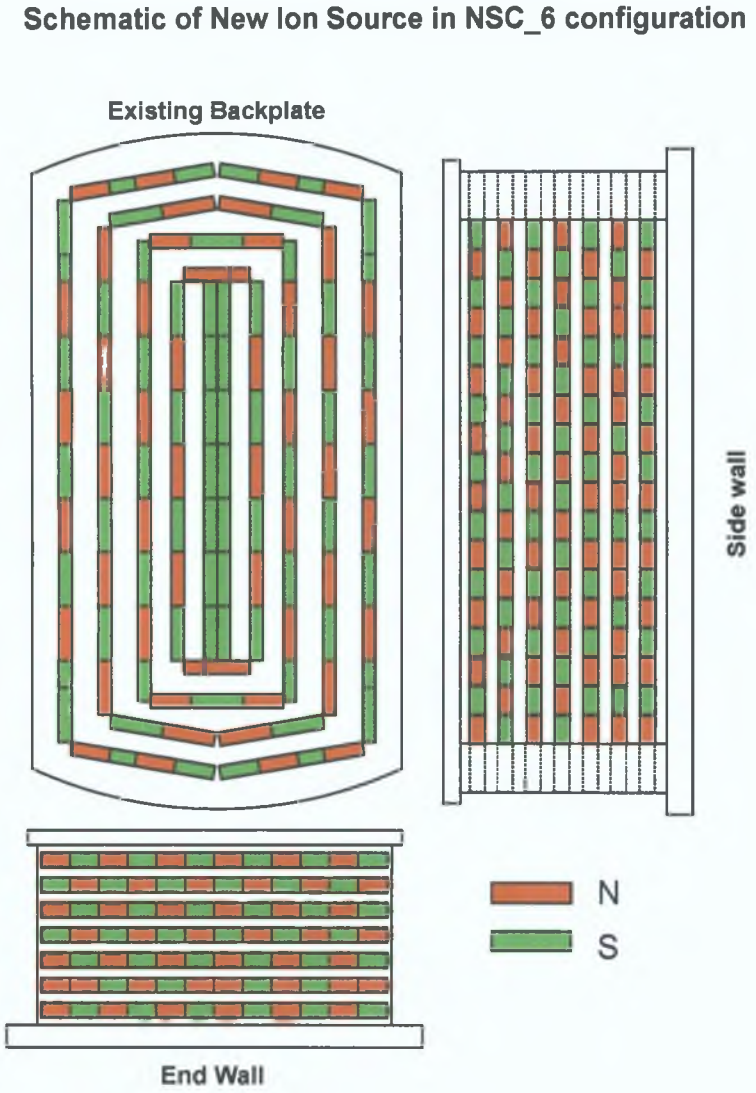

Figure 5.35 Schematic of the magnet pattern used for the NSC_6 super-cusp on the new ion source body. The filter row is weakened by rotating every third magnet.

The magnetic field maps produced by the calculation program are shown in figure 5.36. By weakening the filter row the stray magnetic field present across the extraction aperture array is substantially reduced. Over the majority of the extraction array the total field is less that 5 Gauss, only reaching 10 Gauss towards the extremes of the array.

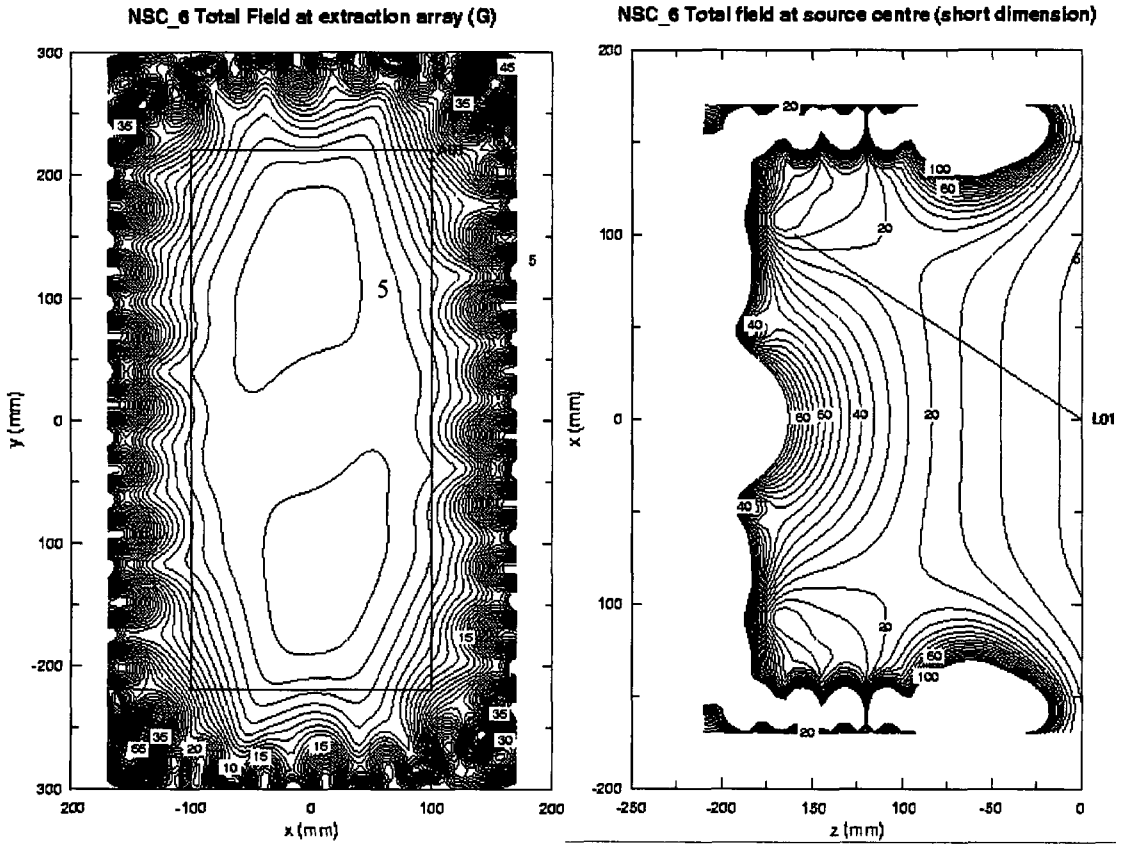

Figure 5 36 Calculated magnetic field maps in the XY extraction array plane and XZ source short dimension plane The box on the XY plot marks the approximate extents of the extraction array

The plot of the total field through the centre XZ plane of the source is also shown, to compare with the NSC_1 and SC15S3 magnet arrangement the total magnetic field is plotted along the line running from the filament stem location to the extraction plane This shows that the peak field of the filter along this line is 24 Gauss, compared to the 29 Gauss of the SC15S3 and 32 Gauss of the NSC_6 configurations

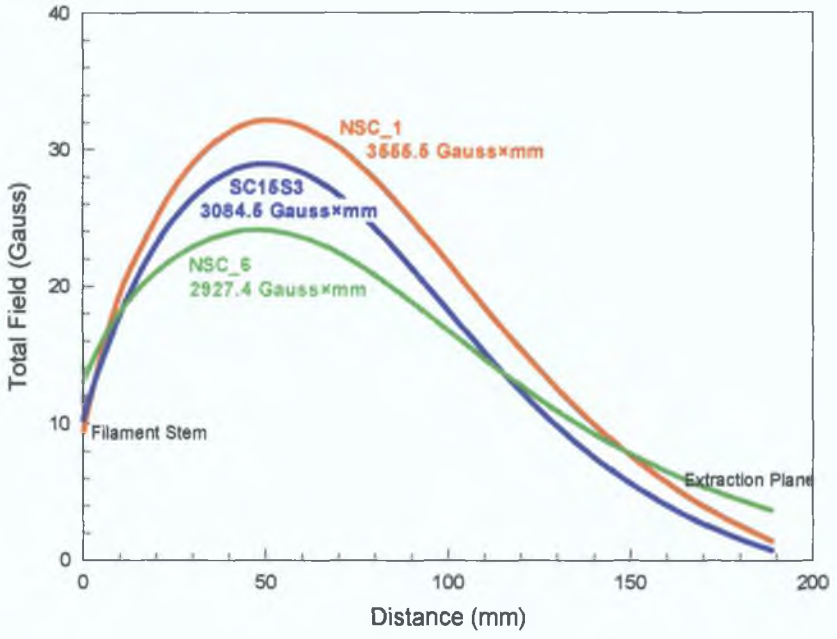

Figure 5.37 Total magnetic field plotted along the lines shown in figures 5.33 and 5.36. The origin is at the filament stem location with the end of the line at the centre of the extraction plane. Also shown is the integral of the curves in Gauss mm.

The integral of the total field along the line from the filament steam to the centre of the extraction plane is also reduced in the NSC_6 configuration, with a 17% reduction to 2927.4 Gauss mm.

The NSC_6 magnet configuration was then modelled with the Monte-Carlo trajectory modelling code, prior to any experimental work being undertaken on the Test-Bed. The primary electron trajectories are followed from the filament positions, as described in Chapter 4. For this case the ratio of the number of ionisation reactions per primary electron is 0.84, lower than the ratio of 0.90 calculated from the model of the SC15S3 source at the same initial conditions (i.e. 100eV primaries, 3 mtorr, 750 K). The general confinement of the primaries in the NSC_6 configuration, away from the plasma facing grid 1, is however comparable to that calculated from the SC15S3 source, with only 2.9% of the primary electron reaching grid 1 with energies >90eV, compared to a figure of 4.1%. These calculations indicate that the monatomic species yield should be similar to the SC15S3

source, but the NSC_6 source will probably show a reduced arc efficiency. Figure 5.38 shows a projection of all the inelastic collisions in the XZ plane of the ion source, this figure indicates the good confinement of the primary electrons away from the plane of the extraction aperture array, at z = 0.

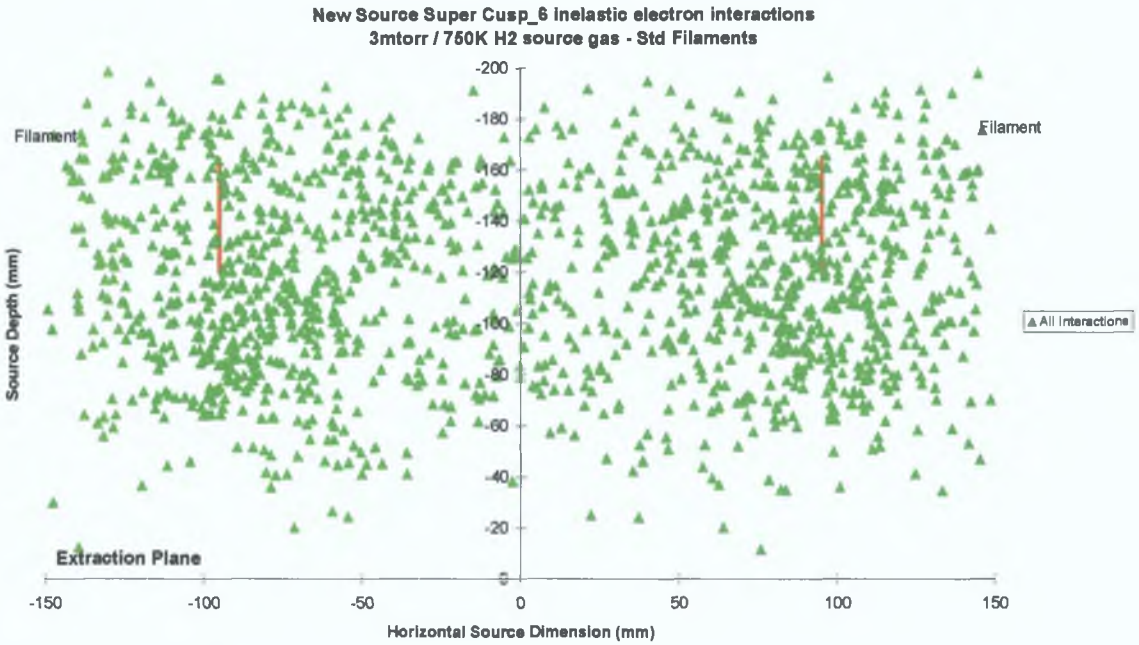

Figure 5.38 Projection of the inelastic collisions of the primary electrons onto the XZ plane, i.e. through the filter field.

The ionisation points are then used as the initial conditions to trace H_2^+ trajectories through the rest of the ion source. The density of the H_2^+ ion trajectories crossing the plane of the extraction aperture array is then used to give the likely ion density uniformity. This analysis is discussed in detail in the following chapter, but the model of the H_2^+ ion trajectories gives a prediction of the ion uniformity better than that obtained with the SC15S3 source. It is for this reason that this configuration was then selected for further experimental testing on the neutral beam test bed.

Firstly it was clear that the arc efficiency of this source was indeed reduced compared to the SC15S3 ion source (apparently consistent with the reduction in filter strength). However it was possible to recover an arc efficiency comparable to the standard super-cusp by increasing the gas flow into the NSC_6 ion source from 6.7 to 13 mbar.l.s^{-1} (figure 5.39). This higher

level of source gas flow is equivalent to that used routinely in the Octant 4 neutral injectors. So there will be no unacceptable effects on the NIB vacuum, backstreaming electron power or beam loss in the accelerator grids. This first observation is consistent with the predicted reduction in the ion per primary ratio, calculated by the NSC_6 configuration by the Monte Carlo model of the primary electron trajectories.

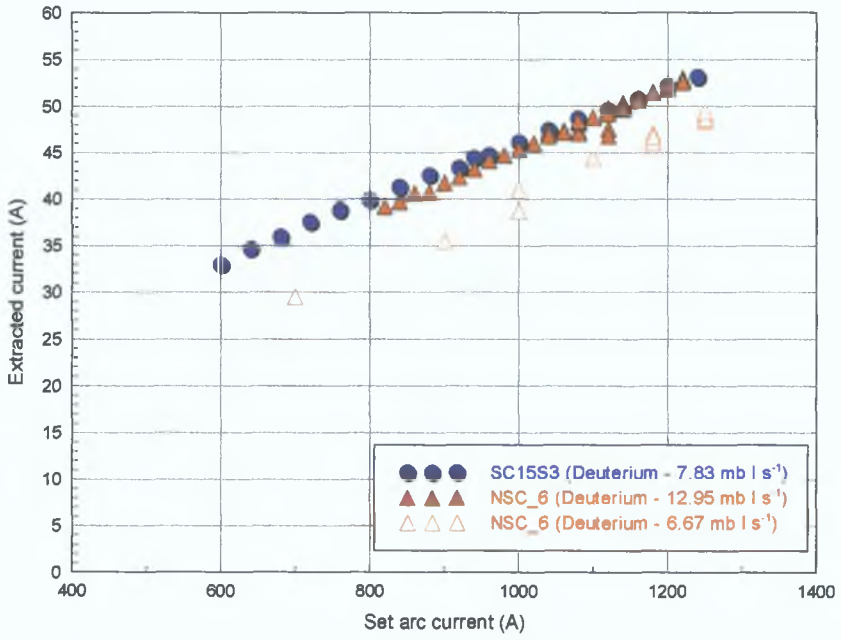

Figure 5.39. Arc efficiency of the NSC_6 ion source configuration, compared to the standard SC15S3 configuration.

As the testing of the ion source progressed it was clear that there was increased transmission to the beam dump, with a corresponding reduction in the power load intercepting the box scraper. The transmission of the beam to the Test Bed beam dump for a PINI using the NSC_6 ion source is shown in figure 5.40, compared to the previous transmission shown for the SC15S3 and chequerboard sources.

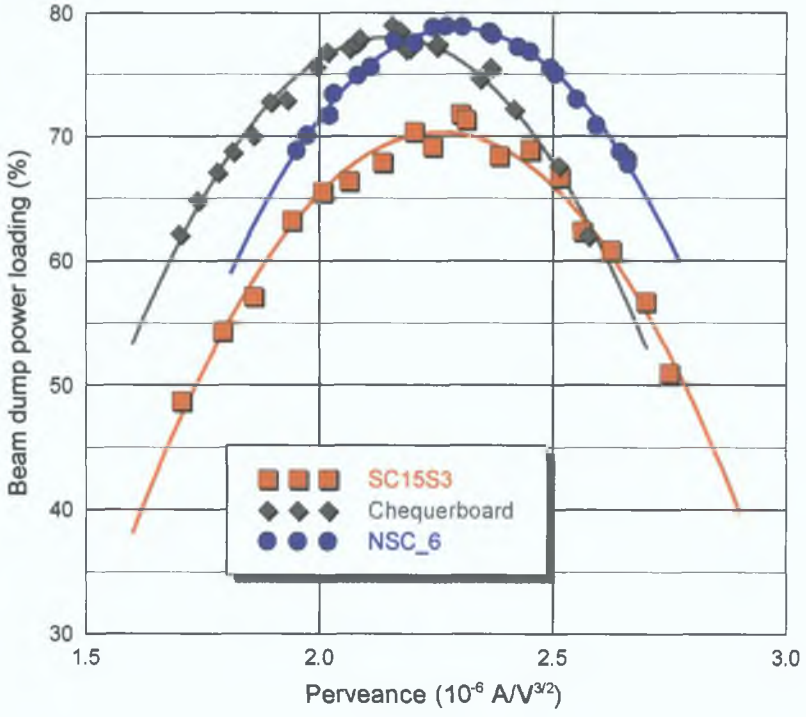

Figure 5.40 Comparison of the beam transmission to the Test-Bed beam dump between the SC15S3, chequerboard and NSC_6 ion sources.

The NSC_6 source thus appears to produce a beam transmission comparable with that obtained with the chequerboard only source. Some care must be taken however in interpreting the plots in figure 5.40 as the same accelerator assembly was not used for the NSC_6 tests as that used to obtain the SC15S3 and chequerboard source data. However, in general the transmission difference seen between similar accelerator assemblies is not usually greater than ±5%, so it is reasonable safe to say that the NSC_6 source provides improved beam transmission.

Measuring the beam with the multi-channel spectrometer now gives the information on the monatomic species yield of the NSC_6 source and an initial indication of the ion density uniformity at the extraction array.

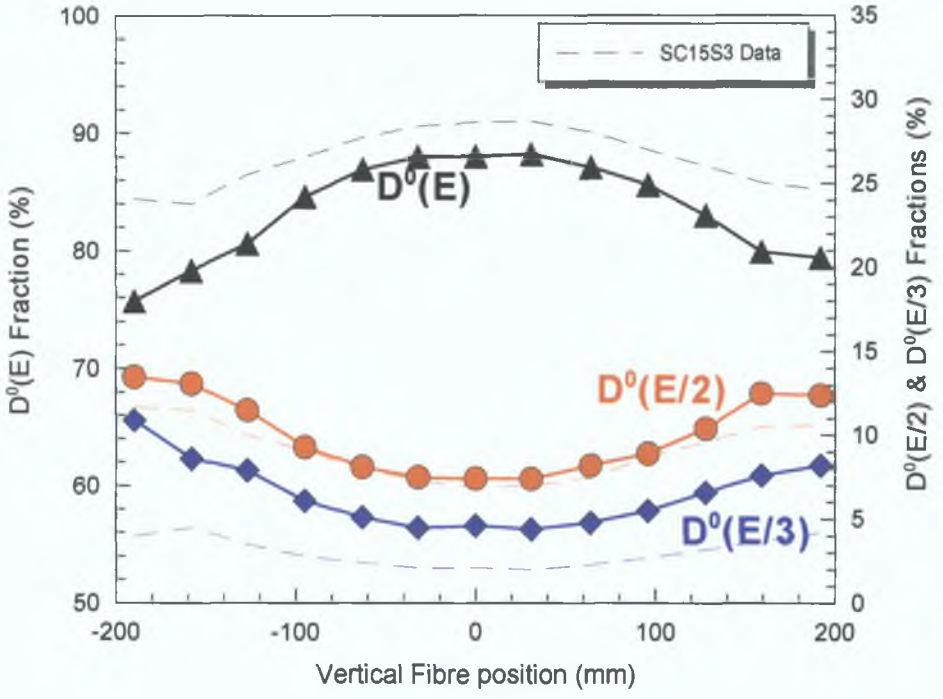

Figure 5.41 Comparison of the Deuterium beam species yield obtained from the NSC_6 and SC15S3 super-cusp ion sources.

The monatomic species yield of the NSC_6 ion source is slightly lower than the SC15S3 super-cusp. On average the D^+ species yield is 2-3% lower across the ion source, with a central value of 86%. This however is still at an acceptable level for injection into JET.

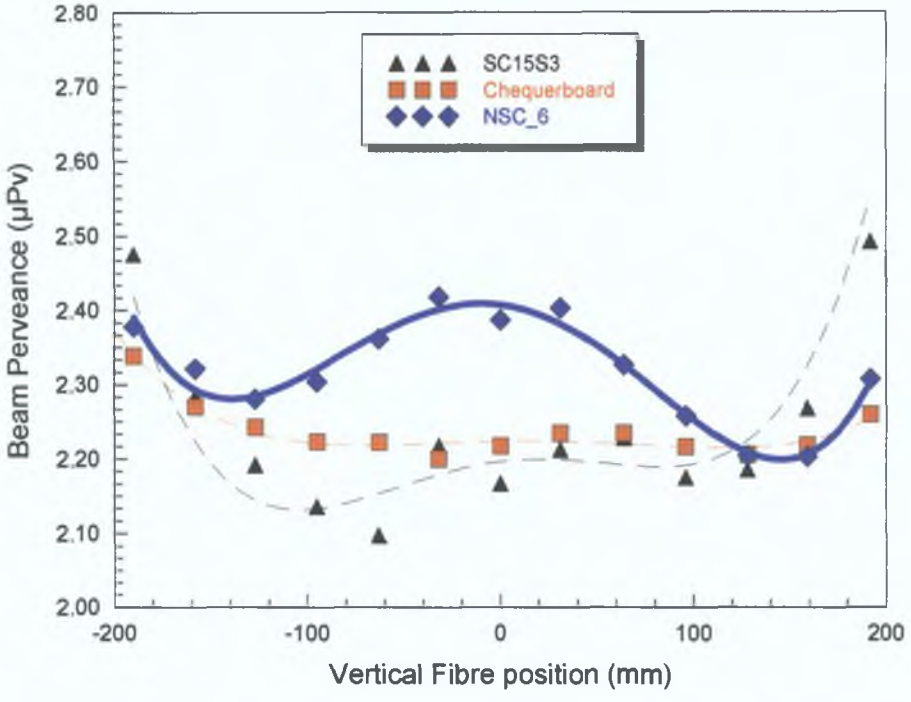

Figure 5.42 Comparison plots of the total beam perveance at the local minimum beamlet divergence for the NSC_6, SC15S3 and chequerboard ion sources. (Data corrected for the measured changing species composition across the beam)

Plotting the total beam perveance where the local minimum beamlet divergence occurs shows that the ion density is much more uniform over the extraction array than for the SC15S3 super-cusp ion source. The interpreted ion density profile appears to more closely resemble that obtained from the chequerboard ion source than the SC15S3 source. A more detailed quantitative analysis of this data is shown in the following chapter.

This source configuration has now been chosen to be used on two PINIs to be operated on the Octant 4 Neutral injector box through the May - August 2000 JET experimental campaign. The 2 PINIs are used in quadrant 2 of the injector, at PINI position 3 and 4. Comparing similar pulses from this quadrant with the previous experimental campaign shows a large reduction in the beamline scraper power load. Table 5.1 shows that for comparable 78kV pulses injecting in the JET plasma the power intercepting the box scraper falls from 212 to 140 kW per PINI, a 33% reduction in the power intercepting the box scraper. The operating

power limit for the box scraper is set at 250kW per PINI In previous campaigns this has limited the power that can be extracted from this quadrant, as this is already being approached at a beam of 78kV and will be exceeded by full power beams at 80kV

TABLE 5 1 Comparision of the box scraper power load for similar pulses injected to the JET plasma from campaigns using the SC15S3 ans NSC_6 ion source on the PINIs at quadrant 2 on the octant 4 injector

JET pulse number	**PINI voltage**	**PINI Pulse Length**		**Box scraper power load per PINI**
46815	78 kV	**3**	5 66 s	212 8 kW
		4	5 71 s	
50449	78 kV	**3**	4 17 s	140 3 kW
		4	5 71 s	

Previous studies of the power balances for the octant 4 injector show that for a total of 13 86MW neutral power generated 2 67MW is lost on beamline scraper elements (specifically the box scraper, calorimeter back panel and duct) Estimating that the lost power will be reduced by between 25 and 33% for all scrapers then the increase in the power transmitted to the JET plasma by using the NSC_6 ion source is between 5 and 8 % This would give an increase in the neutral power injected to the JET plasma of 0 75 to 1 0 MW if all PINIs used the NSC_6 ion source and are allowed operate at full electrical power, with no beamline power load restrictions

5.6 Chapter Conclusions

In a sequence of test on the JET Neutral Beam Test-Bed, beams were extracted from a variety of modified sources. We had previously observed an improvement in beam transmission when a chequerboard only source had been used, compared to the standard super-cusp source. It was thought that the more uniform ion density produced by the chequerboard source was the key to the improved beam transmission. However the disadvantage of using a chequerboard only source is the reduced monatomic species yield (65% D+) compared to the super-cusp source (88% D+).

In an effort to produce a more uniform ion source with good monatomic species yield a variety of source modifications were tested. Initially an extended version of the super-cusp ion source was constructed and tested. This source however did not perform anywhere near as well as had been hoped. The arc efficiency of the source was poor so that it could not be operated to full power beam extraction. Although the monatomic species yield was excellent (>90%) with good minimum beamlet divergence the ion density uniformity was similar to that seen in the standard super-cusp ion source. It was thus clear that moving the ion production region further away from the extraction plane was not in fact a good idea, so alternative solutions were tested.

The first alternative was to use line cusp magnet patterns to attempt to confine the primary electrons toward the walls of the ion source, but allow them to go close to the extraction plane. After a poor initial attempt, we produced two line cusp configurations that gave good arc efficiency, good monatomic species yield and some improvement in beam transmission. However these line cusp configurations didn't give large performance benefits over the standard super-cusp ion sources, so a new set of ion source bodies were specified to allow more flexibility in the design of the magnetic field configuration.

Using the new design of ion source body a magnet pattern was chosen with the assistance of the magnetic and particle trajectory models that appeared to produce a improved uniformity of the ion density. This prediction was proved to be correct when beam were extracted from PINIs using ion sources with this new (NSC_6) configuration. This source produces beams that have much improved transmission, with an acceptable level of monatomic species yield and arc efficiency. This source configuration now operates routinely on the Octant 4 injector.

The improved uniformity of the ion source gives a 33% reduction of the power interception on the beamline scrapers, which is estimated to give a 5-8% increase in the neutral power transmitted to the JET plasma

At this time it is not envisaged that any further development work will be carried out on the ion source configuration as the NSC_6 configuration appears to meet the aims of this source development program Any further work that may be carried out to find a fine cusp confinement pattern using the new ion source, that might give further improvement in source performance is now beyond the timescale of this thesis

6 QUANTIFICATION OF ION SOURCE PLASMA NON-UNIFORMITY

6.1 ANALYSIS OF THE SC15S3 SUPER-CUSP DATA

6.1.1 MULTI-CHANNEL SPECTROMETER

The data obtained with the multi-channel spectrometer has been outlined in Chapter 2 Here the vertical (y) beamlet divergence profiles obtamed by the fibre array are analysed in order to obtain a quantifiable measure of the ion source non-uniformity Inspecting the beamlet divergence data obtamed from a perveance scan shows some key characteristics of the beam extracted from a high current tetrode PINI using a super-cusp ion source that can be derived from these profiles

a) The beamlet divergences measured do not all reach the same minimum value, the beamlets towards the centre of the beam have a generally larger minimum divergence than the beamlets measured towards the edge of the source

b) The point in the perveance scan at which the minimum beamlet divergence is measured from each fibre location does not occur at the same value of total beam perveance

Figure 6 1 shows the distribution of the minimum divergences obtained across the beam, from the data measured in a perveance scan with PINI 18AT, corrected for the local variation in measured beam species composition

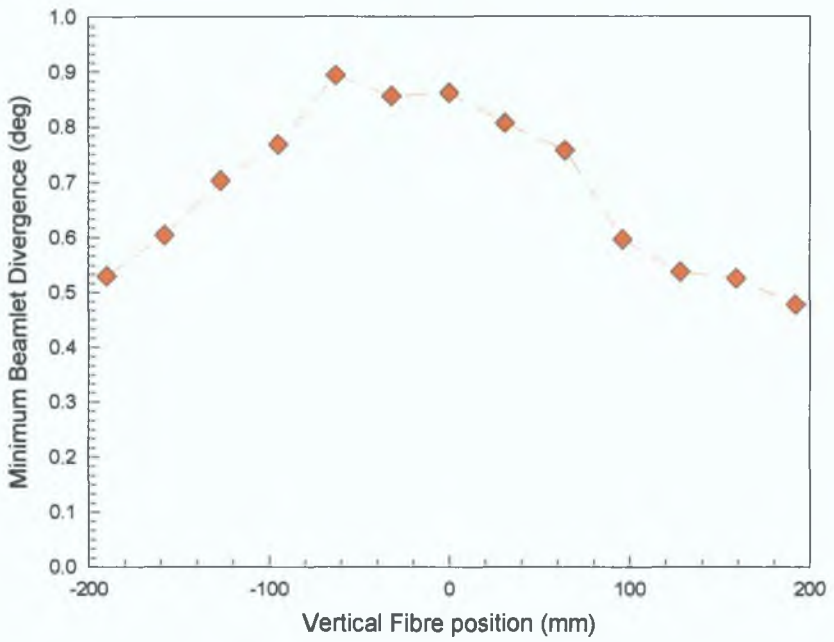

Figure 6.1. The measured minimum beamlet divergence distribution for a scan in beam perveance using PINI 18AT.

The differences in the minimum divergence value must be due to changes in the accelerator structure across the beam extraction array. For a given array of extraction apertures with constant gap lengths and extraction potentials then for whatever ion density distribution is provided by the ion source at some point the same minimum beamlet divergence must be observed. Recent investigations of the effect of the thermal load of the ion source arc on the first accelerator grid have shown that this grid distorts during a beam pulse [41, 42] The distortions predicted by thermodynamic models of the grid indicate that the first grid will bend towards the ion source in a dished shape. This produces a longer accelerator first gap at the centre of the ion source than at the edges of the grid. In the tetrode accelerator the function of the first gap is mainly optical, the bulk of the acceleration occurs in the second gap (90%). So varying the first gap length across the extraction array has a big impact on the local beam optics, modifying the local beamlet divergence. However as the second and third grids are not affected by the thermal distortion of the arc power load (only by the smaller contribution of beam heating) the second gap length is not distorted across the extraction array. Thus the beamlets will all have virtually the same divergence vs current characteristics, just that the value of the beamlet divergence is altered by the change in the first gap length. This has been

confirmed with a numerical simulation of the accelerator extraction system using the 2D Poisson equation solving code AXCEL-INP [22]

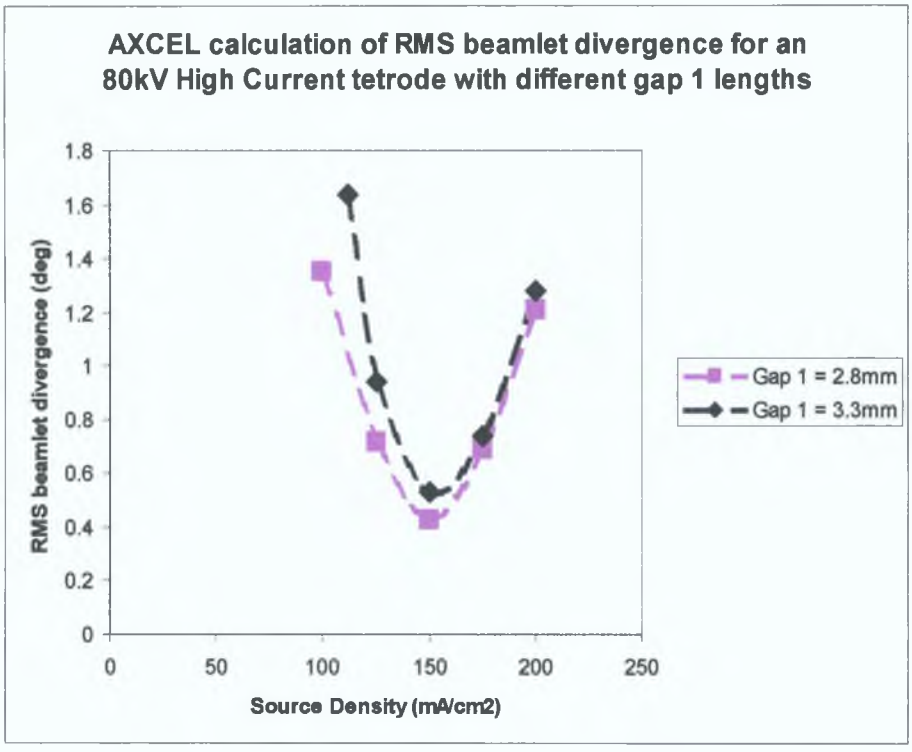

Figure 6.2 RMS beamlet divergence calculated from an AXCEL-INP model of a single aperture of the High Current Tetrode accelerator, with a 0.5mm change in the length of the first gap, to simulate the predicted distortion of the first grid.

The source ion density profile can be derived from the spectroscopic measurements by analysing where the minimum beamlet divergence occurs at each fibre location during the scan in beam perveance, correcting for the change in effective beam mass as the species composition varies. Given identical extraction conditions across the accelerator, or, in the case of the distortion of grid 1, conditions that do not change the ion density where the minimum divergence occurs - this only changes the value of the divergence achieved. It is clear that plotting the value of the total beam perveance where the minimum local divergence is measured gives information on the ion density distribution. For example where a lower ion density occurs the minimum beamlet divergence will occur at a high level of total beam current and vice versa for a high ion density. This can be visualised as a density profile by

plotting the inverse of the total beam perveance where the local minimum beamlet divergence is measured, Figure 6.3.

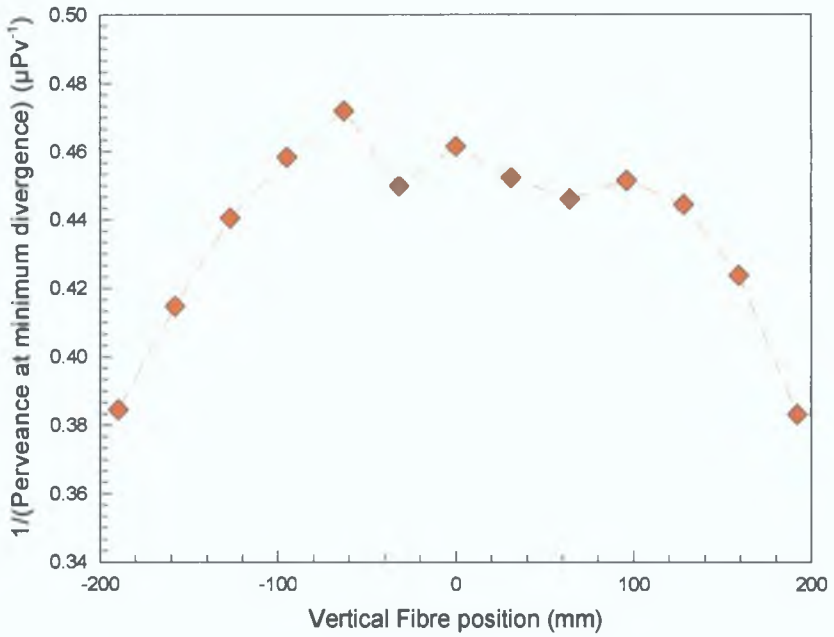

Figure 6.3 The inverse distribution of the beam perveance where the local minimum beam divergence occurs. For a fixed extraction gap and extraction potential this is equivalent to the beam current distribution. (Using the perveance scan of PINI 18AT)

Using the data from a scan in beam current the relation between the beamlet divergence and beam current is measured at one of the fibres closest to the point in where there is zero offset aperture steering (at +125mm). A quadratic polynomial is then used to produce a fit to the measured beam current – divergence relation. The measured profile of minimum divergences is then used to normalise the current - divergence relation for each fibre position. Both these spectroscopic measurements and accelerator modelling codes [KOBRA3-INP] show that the relation between beam divergence and beam current can be reasonably well approximated with a quadratic polynomial.

Figure 6.3 shows that the ion density is peaked towards the centre of the ion source, but with a reasonably constant value over the centre ±100mm of the profile. To recreate this profile 2

quadratic polynomials are used, the first is used to describe the outer part of the profile (from ±100mm to ±200mm), the second is used to generate the 'flat top' seen between ±100mm. The vertical (y) beam divergence distribution is simply derived from combining the beam current profile polynomial with the measured beam current – divergence relationships, normalised to each fibre position. The parameters of the 2 quadratic polynomials describing the beam current distribution are then solved, using a Microsoft Excel spreadsheet, to give the least squares best fit to the measured divergence distribution (which is corrected for the measure species composition distribution). Figure 6.4 shows the results of this fitting procedure to the beamlet divergence profile measured at the 'optimum' perveance. The 'optimum' perveance gives the minimum beam width seen on the TestBed beam dump 12m downstream.

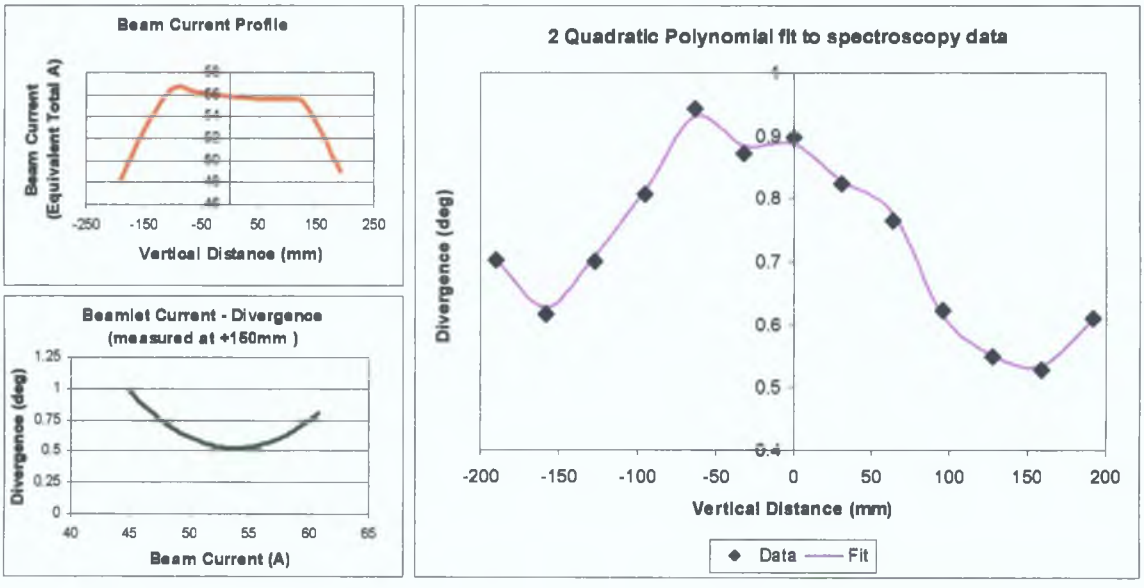

Figure 6.4. Fitting the measured beam divergence distribution with 2 quadratic polynomials describing the vertical (y) beam current profile (PINI 18AT Deuterium beam at 2.303μPv).

This method of determining the best-fit vertical (y) beam current profile is then used to simulate the other measured divergence profiles of the perveance scan, obtained by changing the beam current at fixed beam voltage. For consistency, the integral of each beam current profile is forced to follow the relative change in total beam current between each point in the beam current scan, using the solution to the 'optimum' perveance point as a reference. Figure

6.5 shows the beam current profiles required to produce a best fit to each divergence profile for the beam perveance scan.

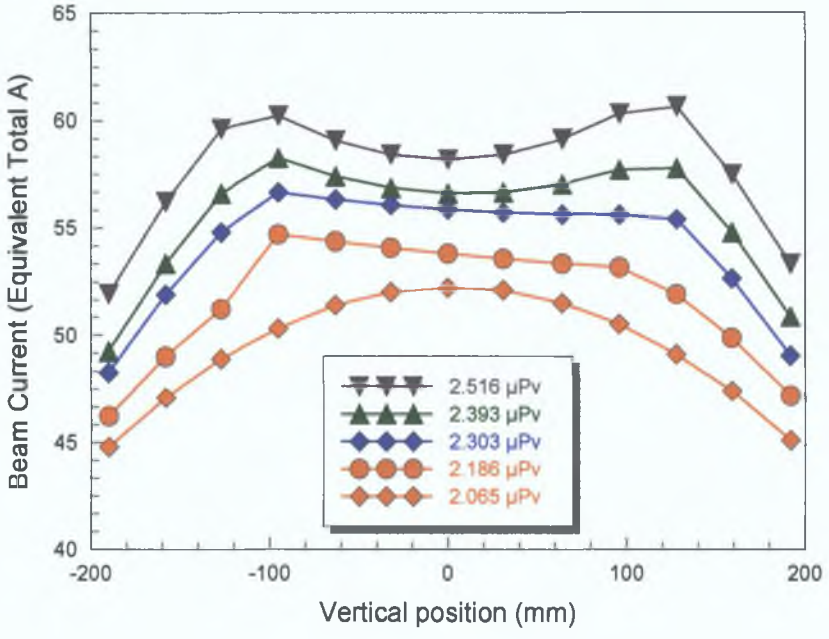

Figure 6.5 Best-fit solutions to the vertical (y) beam current profile for a perveance scan with the SC15S3 ion source. (Fixed beam energy, varying beam current)

For each of the profiles used to describe the beam current distribution a non-uniformity figure of merit is determined. This is defined as the root mean square (RMS) of the difference between the profile values and the mean (or uniform) value. Also calculated is the maximum value of the deviation of the profile from uniform, in both the positive and negative directions. Table 6.1 shows the non-uniformity deviation required to produce a best-fit for each of the cases shown in figure 6.5.

TABLE 6 1 Derivation of non-uniformity figure of merit for the best-fit current profiles shown in figure 6 5

Perveance (μPv)	Uniform Value (A)	Maximum Deviations		RMS Deviation
2 065	49 4	+5 2%	-9 4%	4 7%
2 186	51 7	+5 2%	-10 3%	4 8%
2 303	54 1	+4 2%	-11 2%	4 6%
2 393	55 6	+4 3%	-11 2%	4 4%
2 516	57 9	+4 3%	-10 4%	4 0%
			Mean :-	**4.5%**

The profiles show maximum deviations from uniform of +4 8%, and -10 5% as a result of the skewed distribution A mean RMS deviation of 4 5% in the vertical (y) beam current profile is required to recreate the observed non-uniformity in the beam divergence profile measured using the SC15S3 super-cusp ion source

6.1.2 CFC TILE CALORIMETER

For this measurement the CFC tile is located at a distance of 4 8m from the end of the accelerator grids, this is approximately the location of the beam scraper elements in the main injector boxes Having the tile located this close to the accelerator allows the beams from each grid half to be easily distinguished, with the tile at the previous location of 8 3m to 10 0 m downstream the beams from each grid half are no longer easily separated The optimum beam perveance as measured on the Test-Bed beam dump is 2 3μPv, the beam profile obtained by the CFC tile at 2 310μPv is shown, along with the simulated profile and the percentage deviation between the two in Figure 6 6

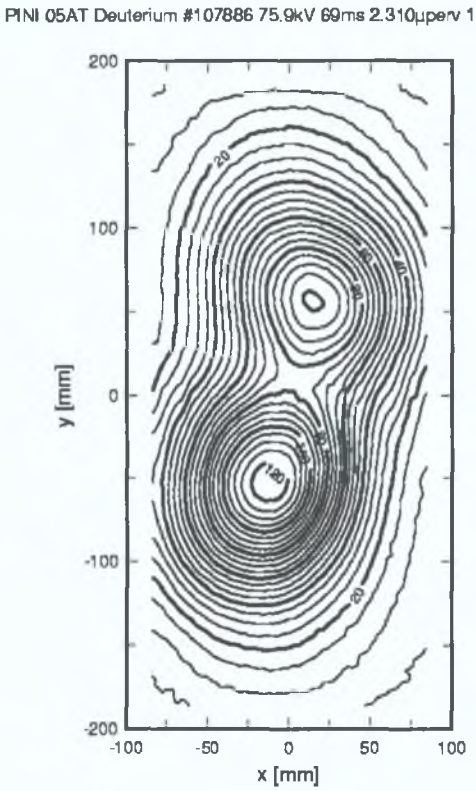

a) Measured

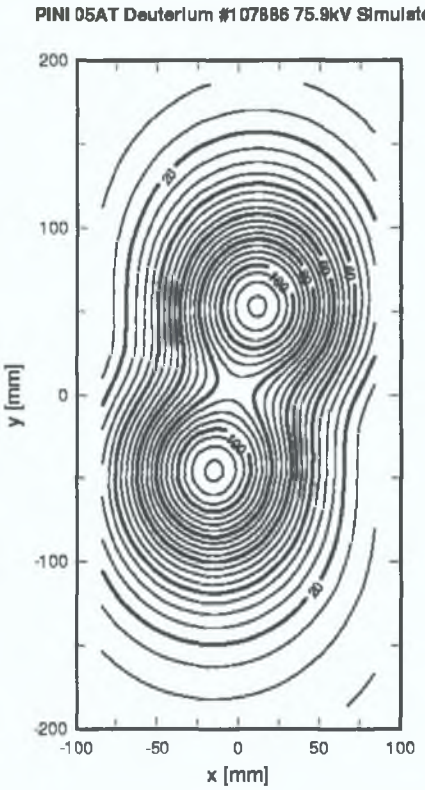

c) Simulated

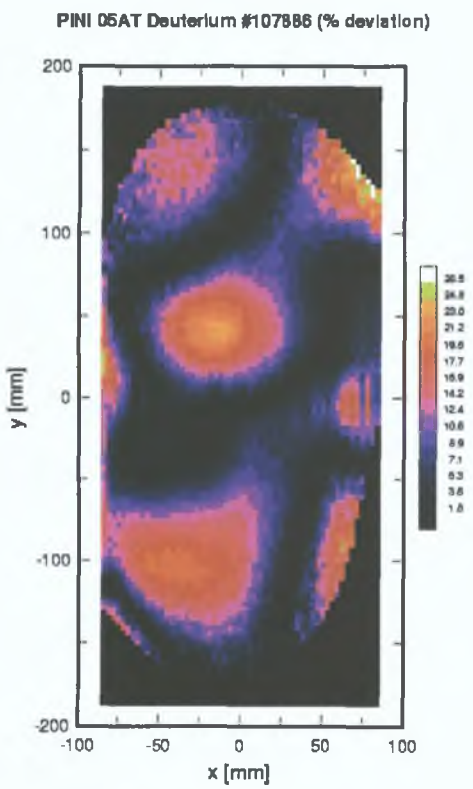

c) % deviation map

Figure 6.6. a) Measured and b) simulated beam power density profiles from an SC15S3 super-cusp ion source. c) shows the map of the deviation (in %) between the two profiles. The beam measured is mixed ions & neutrals from 05AT a high current tetrode accelerator at 4.8m downstream.

Comparing the measured and simulated beam profiles in figure 6.6 shows that the simulation reproduces the measured profile quite well. The difference between the measured profile and the profile produced by the 3Dfit simulation code is 8.2% averaged over the whole profile. It can be seen from the percentage deviation plot, and comparing the 2 contour plots, where the majority of this deviation occurs. The measured beam from the upper grid half in these plots is clearly asymmetric - the power density does not fall away equally from both sides of the peak. This asymmetry gives a peak error of 20% when compared with the symmetrical simulation. This asymmetry is thought to be due to the distortion of grid 1 under the high thermal loads present during beam extraction.

The beamlet current profile on the vertical (y) centre line that is used to generate the 3Dfit simulation of the beam power density profile is shown in figure 6.7. For this simulation the beamlet current-divergence relationship measured by the spectrometer at the fibre location closest to the point of zero offset aperture steering in used. Combining the beamlet current profile with the beamlet current - divergence relationship generates a beamlet divergence profile.

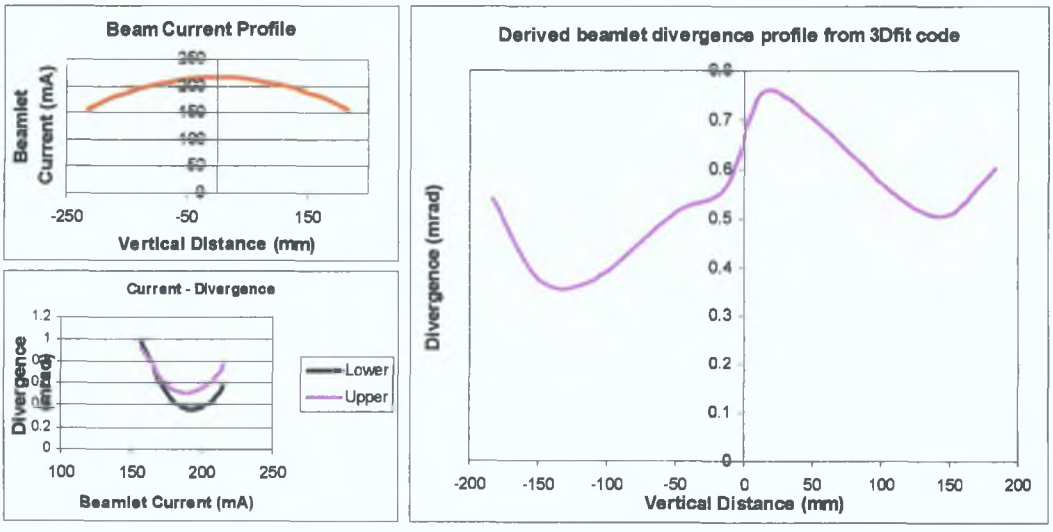

Figure 6.7. Vertical (y) beamlet current profile generated by the simulation of the profiles in figure 6.6. The vertical beamlet current profile generated is shown to compare with the spectroscopic data in figure 6.4.

This divergence profile shows the same general behaviour as that measured by the multi-fibre spectrometer (see figure 6.4). In both cases the beam minimum beam divergence is seen to occur towards the outer edges of the profile, with a maximum value toward the centre.

The 3Dfit code has been used to produce similar simulations of the beam power density footprint measured in a scan of beam perveance. The beamlet current profiles across the vertical (y) centre line are shown in figure 6.8. The divergence profiles generated with the 3Dfit simulation compare reasonably well with those measured by the multi-channel spectrometer, where generally the beamlets with minimum divergence move from the centre of the profile to the edges with increasing beam perveance.

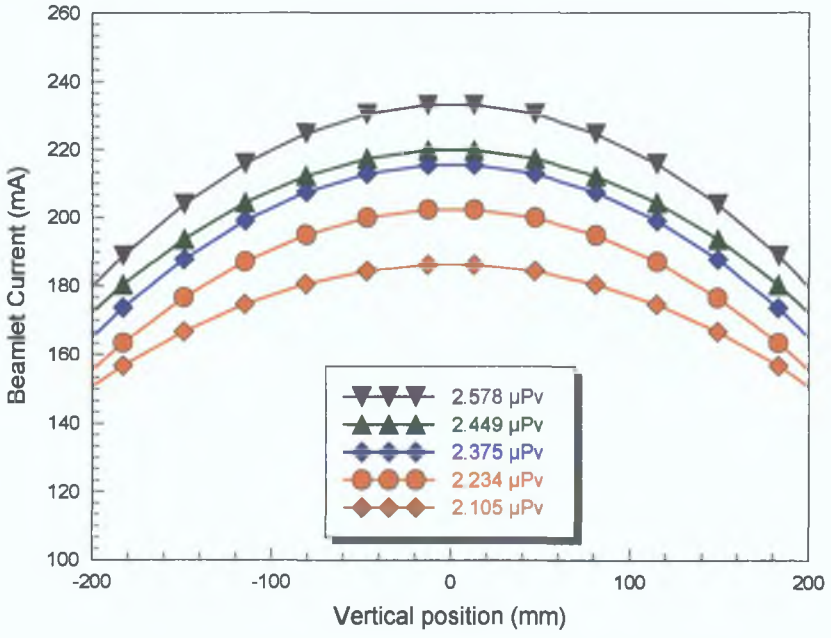

Figure 6.8. Vertical (y) beamlet current profiles generated by the simulation of the measured beam power density profiles in a perveance scan.

The results from the simulation of these beam power density footprints can be summarised in the same way as for the multi-channel spectroscopy. The same definition for the figure of merit for non-uniformity can be used to compare actual profile with the mean uniform profile.

Table 6.2 below shows a summary of the results of these simulations.

TABLE 6 2 Derivation of non-uniformity figure of merit for the 3Dfit simulations of the beam power density profiles, as shown in figure 6 8

Perveance (μPv)	Uniform Value (mA)	Maximum Deviations		RMS Deviation
2 105	174 8	+6 5%	-10 4%	5 9%
2 234	187 3	+8 0%	-12 8%	7 3%
2 375	199 3	+8 1%	-12 9%	7 4%
2 449	204 6	+7 4%	-11 9%	6 8%
2 578	216 1	+7 9%	-12 6%	7 2%
			Mean :-	6 9%

In this case a RMS deviation of 6 9% in the vertical (y) beam current profile is required to recreate the observed non-uniformity in the beam power density profile measured using the SC15S3 super-cusp ion source Also the skewed nature of the profile is reproduced with maximum absolute deviations of +7 6% and -12 1% These values compare reasonably well with the non-uniformity figure of merit obtained from the spectroscopic measurements of the perveance scan which generates a RMS deviation of 4 9% from uniform, with maximum deviations of +5 1% and -11 5%

6.1.3 MONTE CARLO MODEL OF H_2^+ ION TRAJECTORIES IN THE SC15S3 SUPER-CUSP

The Monte-Carlo model of the ion source has been used to trace the trajectories of primary electrons through the SC15S3 super-cusp ion source The primary electron calculations generate a map of the ionisation regions in the source, which is used as the starting point for tracing H_2^+ ion trajectories through the source The distribution of H_2^+ ion trajectories crossing a plane close to the extraction plane is then calculated

Figure 6 9 shows a plot resulting from simulating ~500,000 H_2^+ ion trajectories generated at the ionisation locations determined by running the primary electron trajectory simulation The ions are each given an initial energy randomly chosen from a normal distribution with a mean value of 0 5eV, with a standard deviation of 0 25eV The ion trajectories are traced until their energy falls below 0 01eV or a collision with a source wall is detected

The data for this plot takes ~10days of processing on the target 350MHz Intel Pentium II PC – this is shown here to illustrate the ion trajectory density distribution. Much of the work in this chapter however has been obtained from simulations with ~60000 trajectories which allowed the work to be completed in an acceptable time.

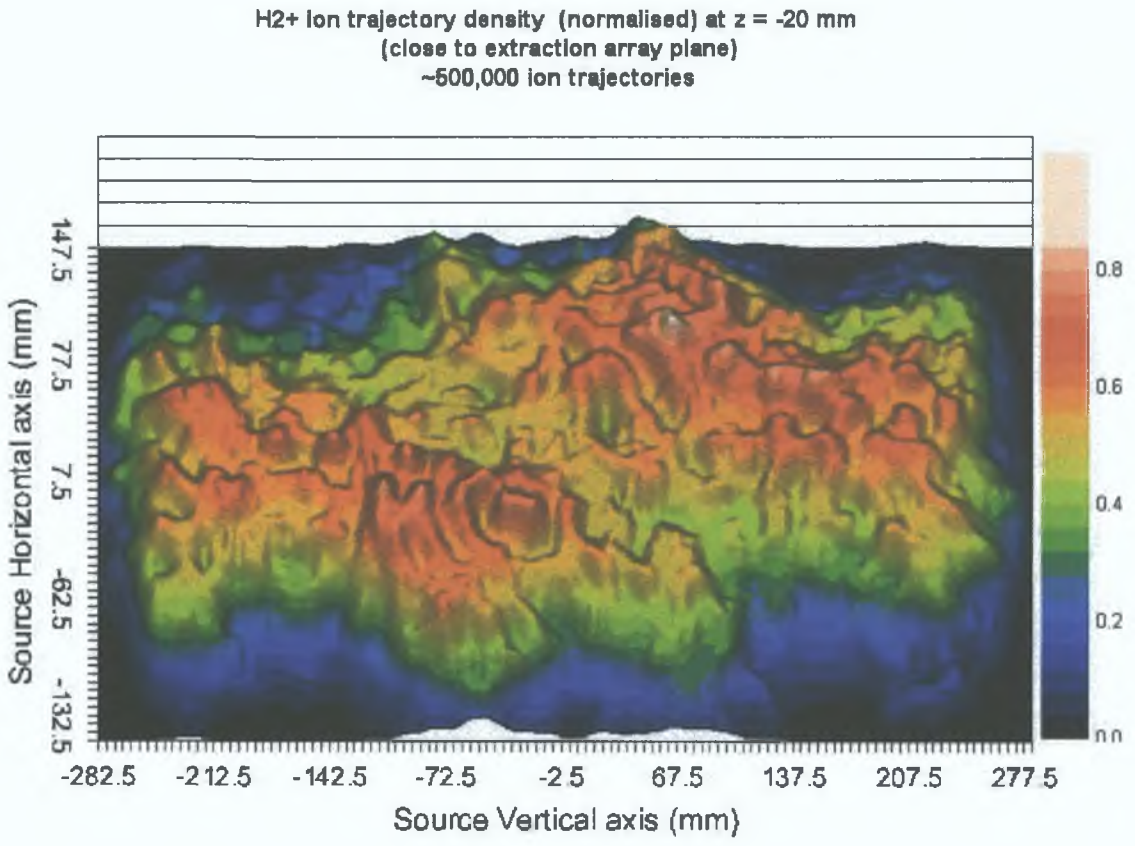

Figure 6.9. Distribution of H_2^+ ion trajectories close to the extraction plane SC15S3 Super-cusp ion source 500000 ions [0.5eV mean, 0.25eV std. dev.]

This density map clearly shows that the H_2^+ ion trajectories are not distributed uniformly over the extraction plane. There is a quite strong concentration of trajectories towards the centre of the source, mainly in two lobes offset across the centreline.

Integrating the 2D density distribution in the direction of the source horizontal (x) direction gives a vertical (y) ion density profile that can compared to that derived from the analysis of the spectroscopic measurements (and by the best fit to the calorimeter tile data). In order to

compare with the profiles generated from the measured data a quadratic polynomial is fitted to this profile over the vertical (y) distance range equivalent to the vertical extents of the extraction array. This vertical line density profile is plotted in figure 6.10.

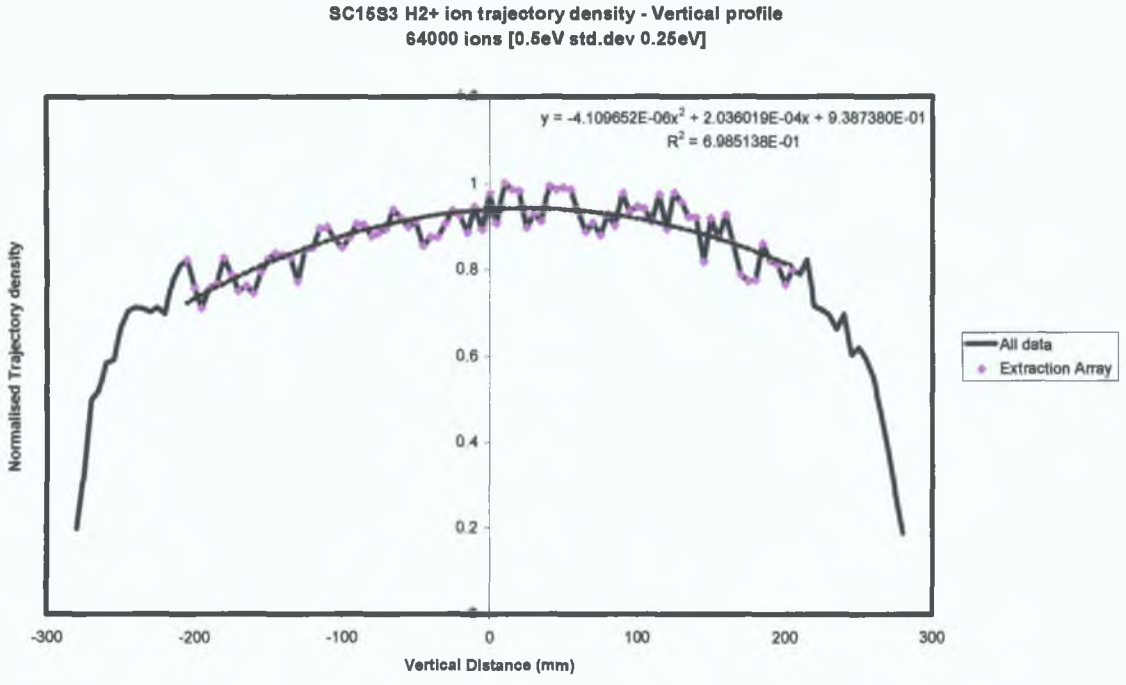

Figure 6.10. Vertical (y) profile of the trajectory density map, with a quadratic polynomial fit over the vertical extents of the Extraction Array. The solid line indicating 'All Data' shows the full vertical ion trajectory density profile given by the data in figure 6.9. [Data from a 64000 ion trajectory simulation]

Using the polynomial from the quadratic fit to calculate the deviation of the profile from uniform give a RMS deviation of 5.3%, with maximum deviations of +6.2% and -10.6%. The comparison of the modelled H_2^+ ion trajectory density with the measure data is shown in the summary below.

6.1.4 SUMMARY OF SC15S3 ANALYSIS

The table below shows the non-uniformity figure of merit for each of the 3 cases above The values agree well, showing a reasonably consistent RMS deviation in the ion density profile of 5% from uniform Also the skewed nature of the profile shows consistent maximum deviations of +6% and -11% from the equivalent uniform profile

TABLE 6 3 Comparison of the non-uniformity in the ion density derived from beam measurement and Monte-Carlo modelling of theSC15S3 super-cusp ion source

Description	**Beam non-uniformity (%)**
Multi-channel Spectroscopy	Mean over a perveance scan Maximum absolute deviations +4 8%, -10 5% RMS deviation **4.5%**
3Dfit to power density profile	Mean over a perveance scan Maximum absolute deviations +7 6%, -12 1% RMS deviation **6.9%**
Monte-Carlo H_2^+ ion trajectories	Maximum absolute deviations +6 2%, -10 6% RMS deviation **5.3%**

6.2 ANALYSIS OF THE CHEQUERBOARD SOURCE DATA.

6.2.1 MULTI-CHANNEL SPECTROMETER

As in the previous example of a super-cusp ion source, the beam divergence profile was measured during a scan in beam perveance Plotting the inverse of the beam perveance where each local minimum beamlet divergence occurs can show an impression of the ion uniformity This plot is shown in figure 6 11, plotted with the data from figure 6 3 to show a direct comparison with the super-cusp source This profile is much more uniform over the extraction array than the profile obtained for the super-cusp ion source

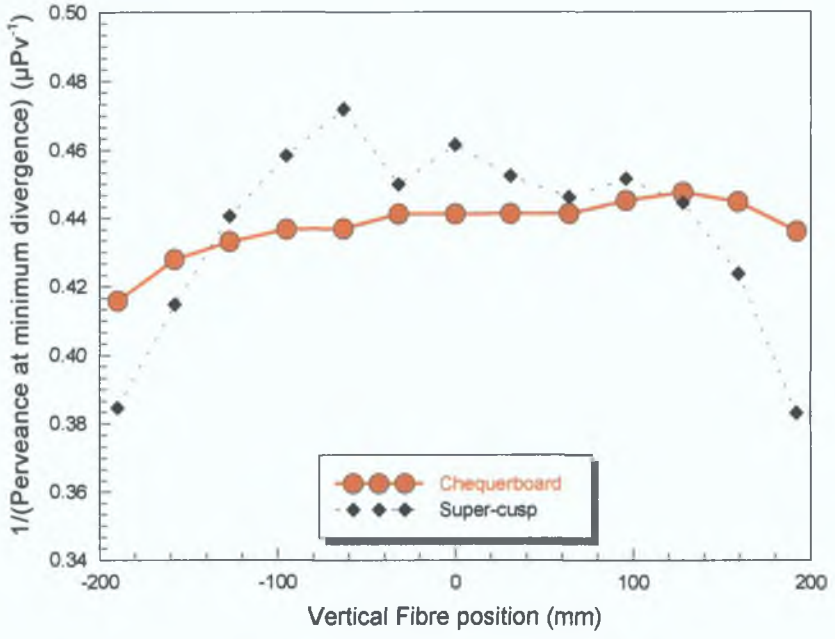

Figure 6.11. Comparison of the inverse distribution of the beam perveance where the local minimum beam divergence occurs, for the chequerboard and super-cusp ion sources. For a fixed extraction gap and extraction potential this is equivalent to the beam current distribution. (Using the data from the perveance scan of PINI 6AT with a chequerboard ion source and figure 6.3)

Using the same technique of finding the best fit current density profile to match the measured divergence profile, by using the measured current- divergence relation normalised to the relative value of minimum divergence obtained. Figure 6.12 shows the best fit current profile found for the divergence profile recorded at the optimum beam perveance.

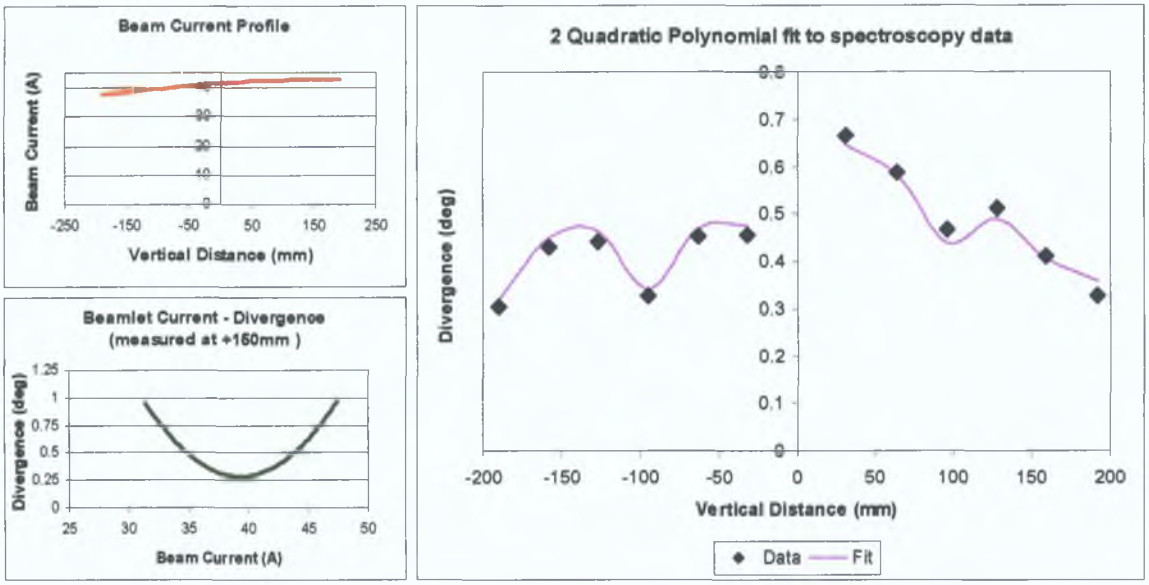

Figure 6.12. Fitting the measured beam divergence distribution with 2 quadratic polynomials describing a) the beam current - divergence relation at +150mm and b) the vertical beam current profile.

This analysis is repeated for the other divergence profiles obtained in scan of beam perveance. A summary figure of the beam current profiles is shown in figure 6.13.

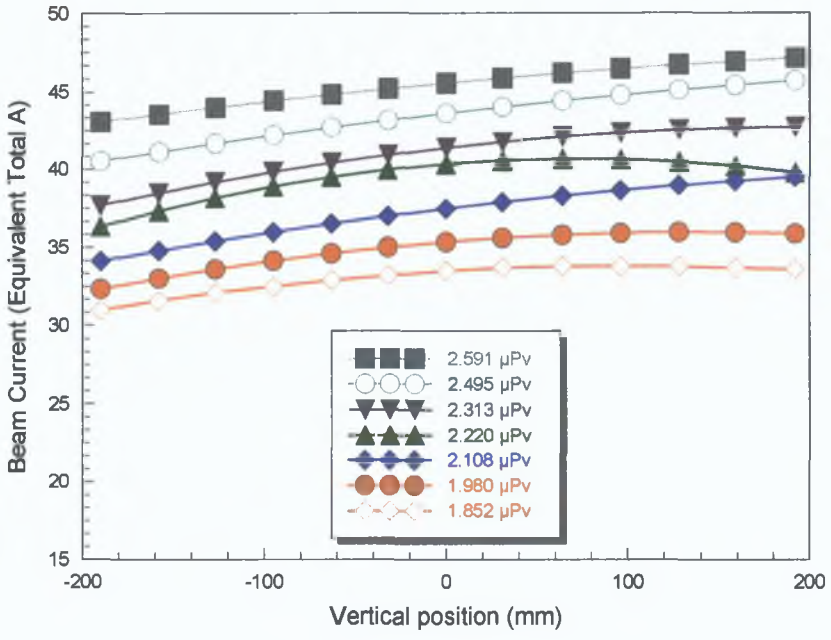

Figure 6.13 Best-fit solutions to the vertical (y) beam current profile for a perveance scan with the chequerboard ion source. (Fixed beam energy, varying beam current)

The results of the best-fit profiles to the perveance scan are summarised in table 6.4. Using the definition of the RMS non-uniformity described above, the mean RMS deviation from uniform is 1.0%. The profile derived from the chequerboard ion source is clearly less skewed that that for the SC15S3 super-cusp source with approximately equivalent maximum deviations of +1.1% and -1.8%

TABLE 6 4 Derivation of non-uniformity figure of merit for the best-fit current profiles show in figure 6 13

Perveance (μPv)	Uniform Value (A)	Maximum Deviations		RMS deviation
1 852	33 0	+1 4%	-2 3%	1 2%
1 980	34 9	+1 4%	-2 2%	1 3%
2 108	37 2	+0 7%	-1 1%	0 6%
2 220	39 4	+2 2%	-3 6%	2 0%
2 313	40 9	+1 1%	-1 8%	1 0%
2 495	43 4	+0 5%	-0 7%	0 4%
2 591	45 4	+0 4%	-0 6%	0 3%
		Mean		1 0%

6.2.2 CFC TILE CALORIMETER

The beam power density footprint is recorded during a scan in beam perveance with the tile located 4 8m from the end of the accelerator grids Figure6 14 shows the beam power density footprint measured at the 'optimum' perveance

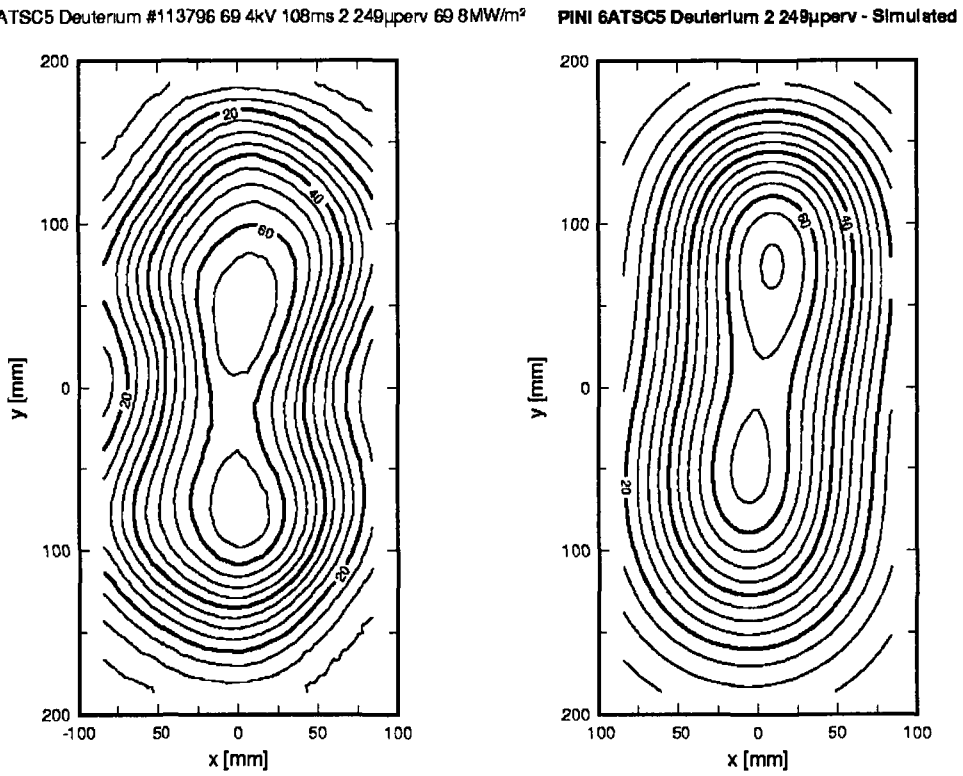

Figure 6 14 Measured and simulated beam power density profiles from a chequerboard ion source Beam measured is mixed ions & neutrals from 06AT a high current tetrode accelerator at 4 8m downstream

The 3Dfit simulation code is used to recreate this measured profile, and the vertical (y) beamlet current distribution is shown in figure 6 15 The averaged deviation between the measured and simulated profiles m figure 6 14 is 9 27%

The beamlet divergence distribution derived from the current profile is also shown in figure 6 15 This is similar to the divergence profile measured with the multi-channel spectrometer at this 'optimum' value of beam perveance

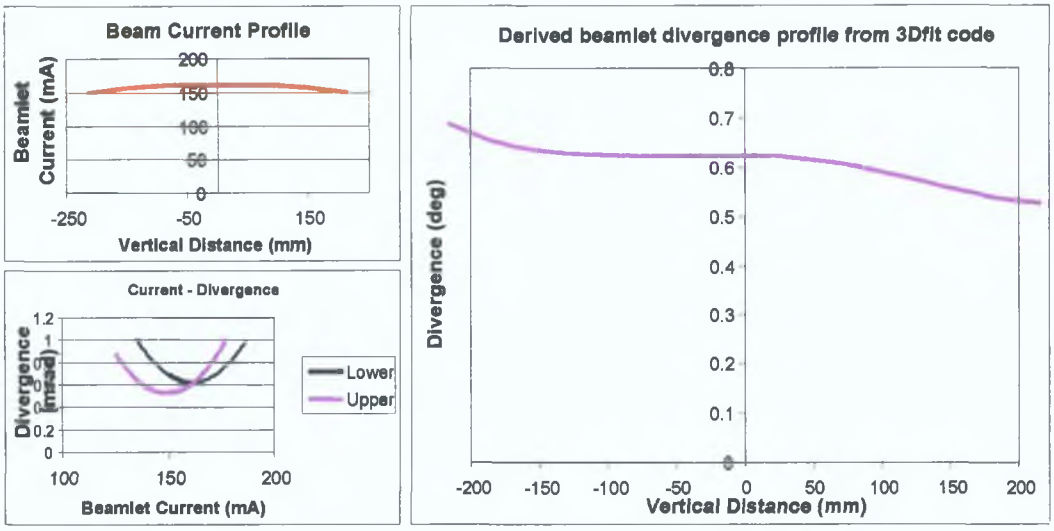

Figure 6.15. Vertical beamlet current profile generated by the simulation of the profiles in figure 6.14.

The beamlet current profile is reasonably uniform giving the expected equal beamlet divergence over the whole extraction array. In fact the RMS deviation of this profile from uniform is only 1.9%, with comparable maximum deviations of +2.0% and -3.3%.

Each of the beamlet current profiles generated by the 3Dfit simulation for the perveance scan show only a small deviation from a uniform profile. Table 6.5 summarises this data and shows that the mean RMS deviation for these profiles is only 1.8%, consistent with the 1.0% RMS value derived from the multi-channel spectroscopic measurements

TABLE 6.5 Derivation of non-uniformity figure of merit for the 3Dfit simulations of the beam power density profiles.

Perveance (μPv)	Uniform Value (mA)	Maximum Deviations		RMS Deviation
2.375	146.8	+2.7%	-5.8%	2.6%
2.449	158.9	+2.0%	-3.3%	1.9%
2.578	168.3	+1.1%	-1.8%	1.0%
			Mean:-	**1.8%**

6.2.3 MONTE CARLO MODEL OF H_2^+ ION TRAJECTORIES IN THE CHEQUERBOARD SOURCE

The chequerboard only magnetic field configuration was simulated and used by the Monte-Carlo code to derive the ionisation points generated by the primary electrons The difficulty with the chequerboard magnet pattern is that without the filter field to confine the primary electrons the trajectories move quickly to the extraction plane, where they are lost Thus very many primary trajectories are required to build up a meaningful number of interaction node to become significant It also appears that the few electron trajectories that get trapped in cusp fields around the end plates of the ion source contribute a large fraction of the interaction nodes, weighting the ion production density close to the end walls of the source

However taking these problems with the simulation of the chequerboard source into account an attempt was made to derive the ion trajectory density at the plane of the extraction aperture array The few ionisation node from the primary electron model were used to generate the initial conditions for a run of 63000 H_2^+ ion trajectories, again using the initial condition of choosing the initial ion energy randomly from a normal distribution of 0 5eV mean and 0 25eV standard deviation

The density of the ion trajectories close to the extraction plane is shown in the plot in figure 6 16

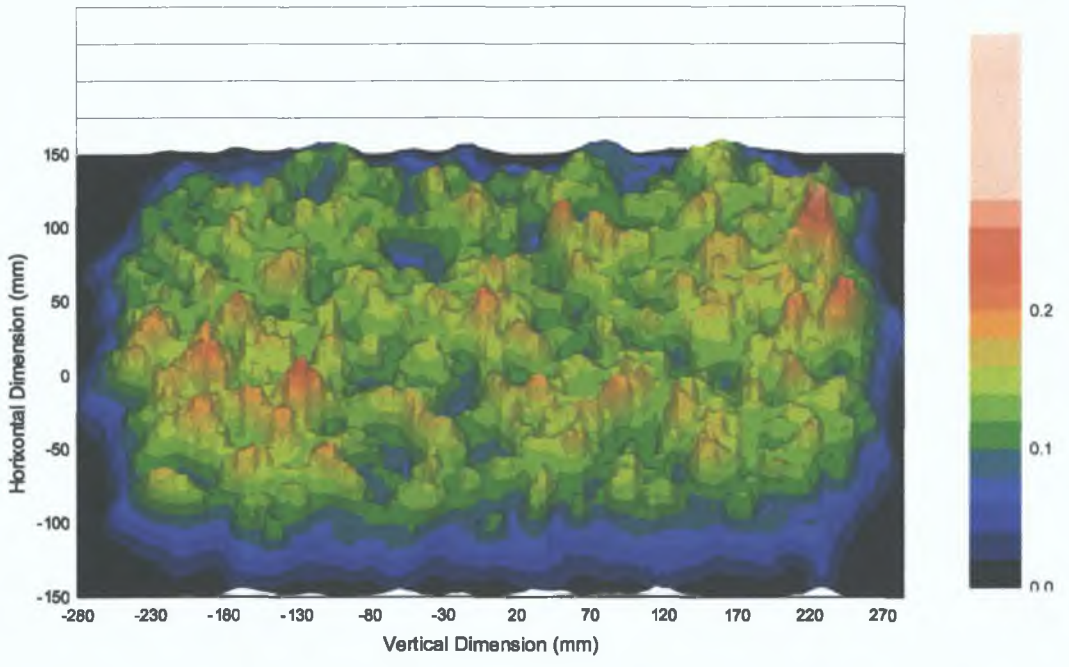

Figure 6.16 Distribution of H_2^+ ion trajectories close to the extraction plane Chequerboard (New Source Body), 63000 H_2^+ ions [0.5eV mean, 0.25eV std. dev.]

Although there is a very large amount of scatter in the trajectory density calculation, at first glance this does appear to be significantly more uniform than the SC15S3 super-cusp trajectory density map. This plot does show evidence of increased ion density towards the endplates of the source, where a few of the primary electron trajectories become trapped producing a relatively large number of ionisations.

Plotting the central line density profile for this simulation shows clearly the large scatter in the trajectory density. A quadratic polynomial is fitted over the vertical (y) range of the extraction aperture array and shows a RMS deviation from uniform of 1.1%, with maximum deviations of +2.5% and -1.0%. Although this is consistent with the values obtained from the analysis of the spectroscopic and calorimetric data, the large scatter of the data on the density profile does not allow this value to be given with any large degree of certainty.

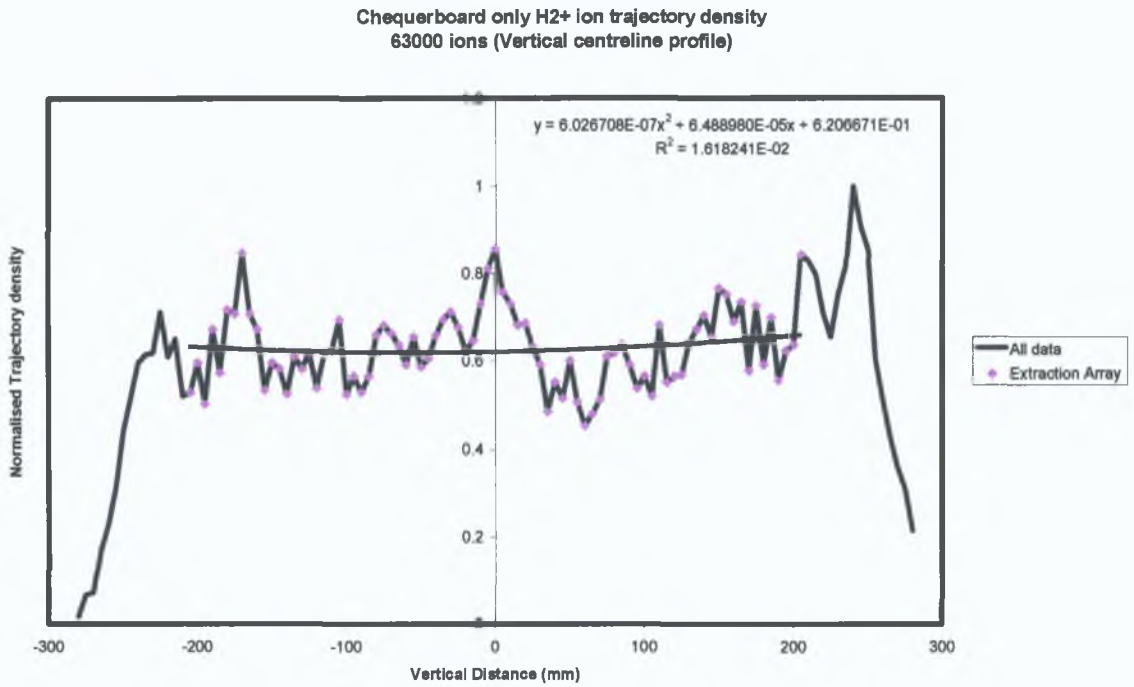

Figure 6.17 Vertical profile of the trajectory density map, with quadratic polynomial fit to a width of ±200 mm about the extraction array centre.

Although the Monte-Carlo model of the source appears to reproduce the ion density uniformity expected from the spectroscopic and beam profile analysis, the relatively poor statistics provided by the initial primary electron model make this difficult to be certain about.

6.3. LINE-CUSP ION SOURCES

6.3.1 MULTI-CHANNEL SPECTROMETER

As a main part of the source development programme the ion source was configured with a line cusp magnet pattern The purpose of this configuration is to produce a long range field along the side walls of the ion source, the filament are then placed so that they emit into this field The primary electrons are then confined to a region close to the source walls without being able to directly reach the extraction plane Thus the ionisation reactions occur primarily close to the walls of the ion source, with the intention of balancing the loss of ions to the source wall to obtain a more uniform ion density profile The first attempt at this configuration provided a line cusp field that was too effective at confining the primary electrons close to the source wall, producing an extracted beam that had a clearly lower density in the centre This case does however allow a good comparison between the measured beam profiles and the profile obtained from the Monte-Carlo model, in a case that is very different from the super-cusp and chequerboard configurations

The measurements from the multi-channel spectrometer taken during a perveance scan with this ion source, using a high current tetrode accelerator, shows the evidence for a beam with reduced centre density The key piece of evidence for this comes from the plot of the inverse of the total beam perveance where the minimum local beam divergence occurs for each vertical position, figure 6 18 As discussed previously this shows what is effectively the ion current density distribution For the super-cusp source the beam current density a profile is peaked towards the centre The opposite occurs for the line-cusp source showing a profile peaked towards the edges

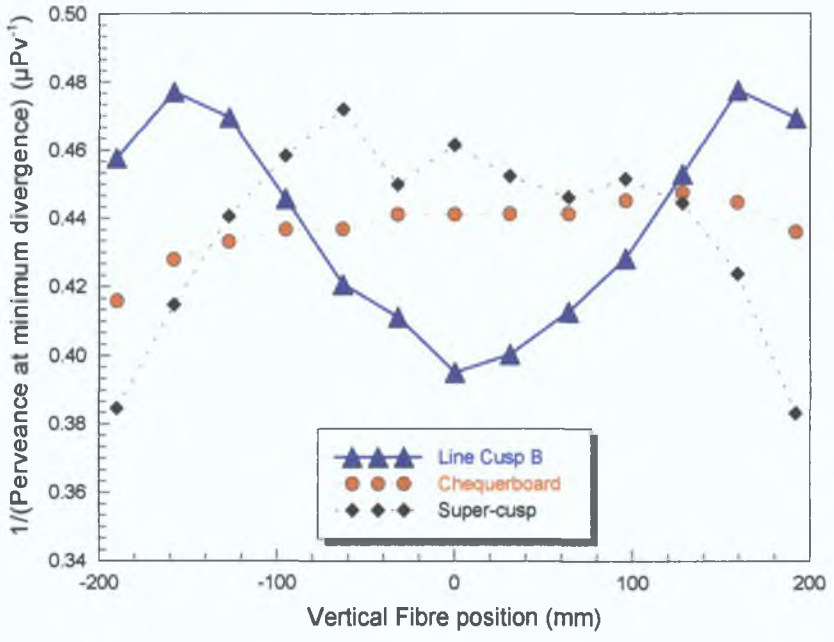

Figure 6.18. Total beam perveance required to produce the local minumum beamlet divergence for the line-cusp configuration compared with the super-cusp source

The spectrometer divergence profile for the beam perveance where the centre beam divergence is close to minimum is shown in figure 6.19. The profile is again re-created by using a quadratic definition of the beam current profile, and the measured divergence –current relation. In this case the best-fit solution is found only over a reduced range ±150mm (rather than ±200mm) as figure 6.18 shows a sharp change in the profile beyond these points, where the ionisation region is approached. The best-fit solution found in this case is with the minimum current at the centre of the profile, as compared to the solution for the super-cusp profile shown in figure 6.4.

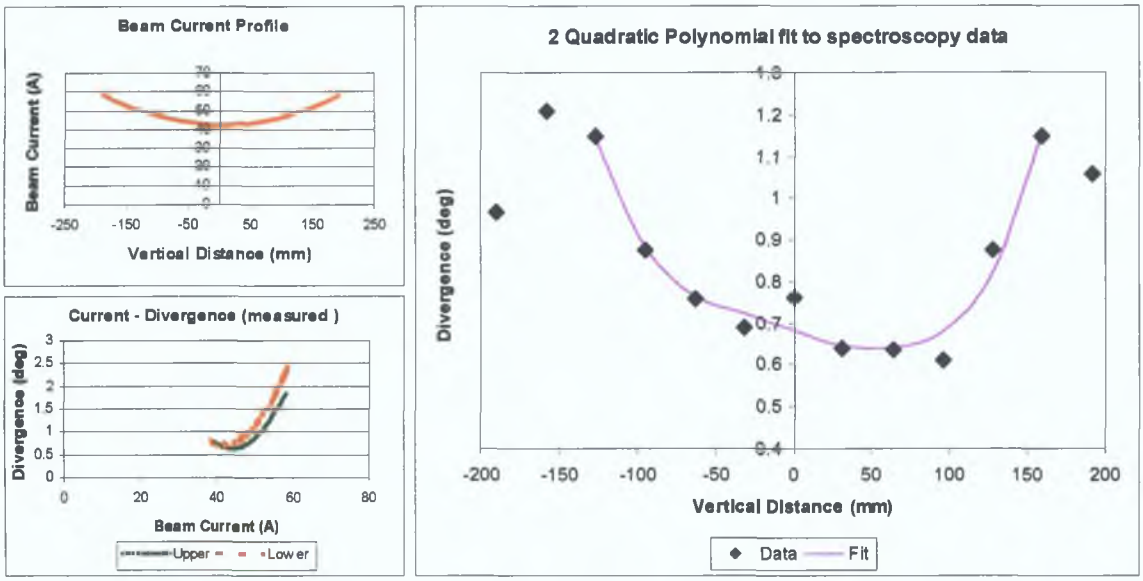

Figure 6.19. Fitting the measured beam divergence distribution with 2 quadratic polynomials describing a) the beam current - divergence relation and b) the vertical beam current profile.

Using this same method to find the best fit polynomial definition of the vertical (y) current profile for the other measurement of the beam perveance scan, generates the set of profile shown in figure 6.20.

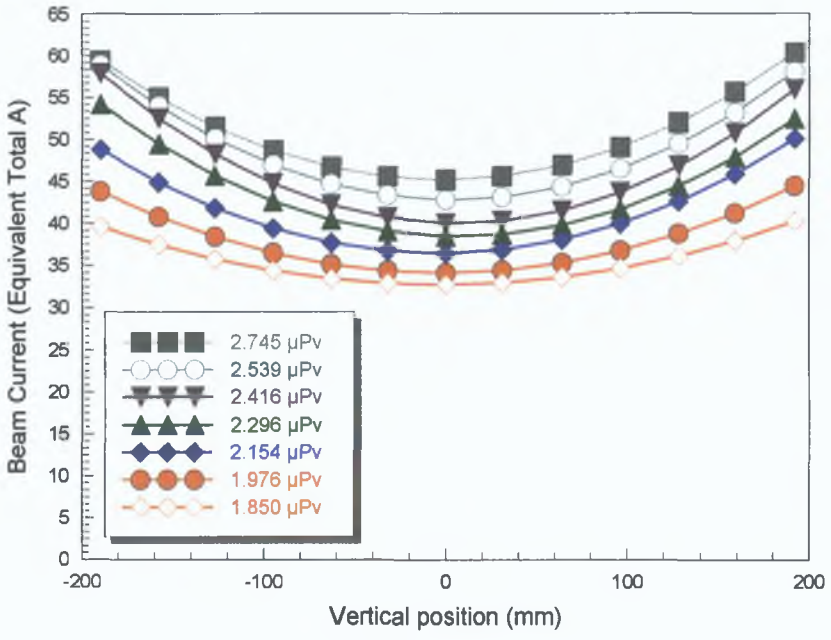

Figure 6.20. Best-fit solutions to the vertical (y) beam current profile for a perveance scan with the Line-cusp ion source. (Fixed beam energy, varying beam current)

Each of these current profiles can again be summarised by the RMS deviation of the profile from an equivalent uniform distribution. Also the values of the maximum deviations of the profile from uniform are calculated.

The summary table of these results is shown in table 6.6 below.

TABLE 6 6 Derivation of non-uniformity figure of merit for the best-fit current profiles show in figure 6 20

Perveance (μPv)	Uniform Value (A)	Maximum Deviations		RMS Deviation
1 850	34 71	-5 7%	+9 1%	5 0%
1 976	36 87	-7 5%	+11 8%	6 6%
2 154	40 01	-9 0%	+14 5%	8 0%
2 296	42 55	-9 7%	+16 3%	8 6%
2 416	44 66	-10 5%	+17 6%	9 3%
2 539	47 13	-9 2%	+14 5%	8 1%
2 745	49 24	-8 3%	+12 9%	7 3%
			Mean :-	**7.6%**

The mean RMS deviation from uniform for these best-fit profiles is 7 6% This is significantly more non-uniform than the super-cusp ion source, especially as this is over a distance of ±150mm, compared to the ±200mm used to derive the super-cusp non-uniformity Also this shows a skewed profile with mean values of the maximum deviation of -8 5% and +13 8%

6.3.2 CFC CALORIMETER MEASUREMENTS

Unfortunately when the tests were carried out with this PINI the CFC tile calorimeter was at a distance of 10 0m from the accelerator, although this still enables good profiles to be taken the simulation of the profiles by the 3Dfit code is very difficult At 10 0m downstream the beam focussmg has produced a beam profile that is difficult to accurately deconvolve So no useful quantifiable information about the source density distribution can be made from this data However looking at the evolution of the beam power density footprints through a perveance scan shows evidence that supports the observation of a lower density at the beam centre Figure 6 21 shows the profiles of a He beam at the tile distance of 10 0m at perveances below, at and above the optimum perveance for a He beam

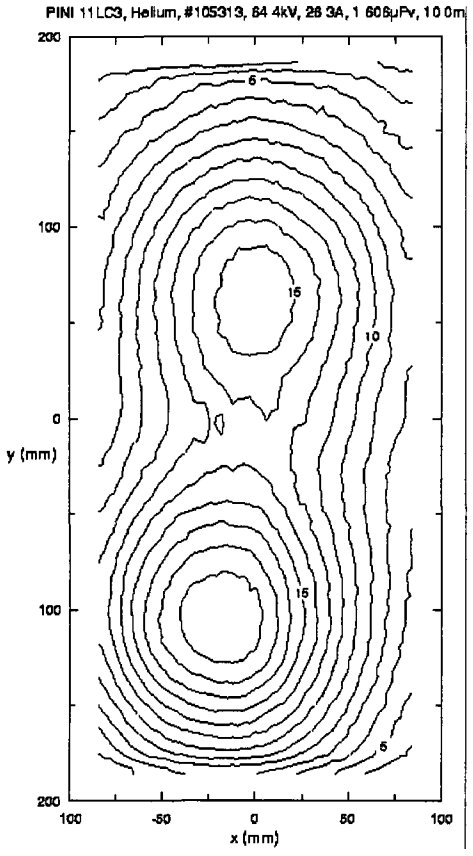

a) 1 606 µPv

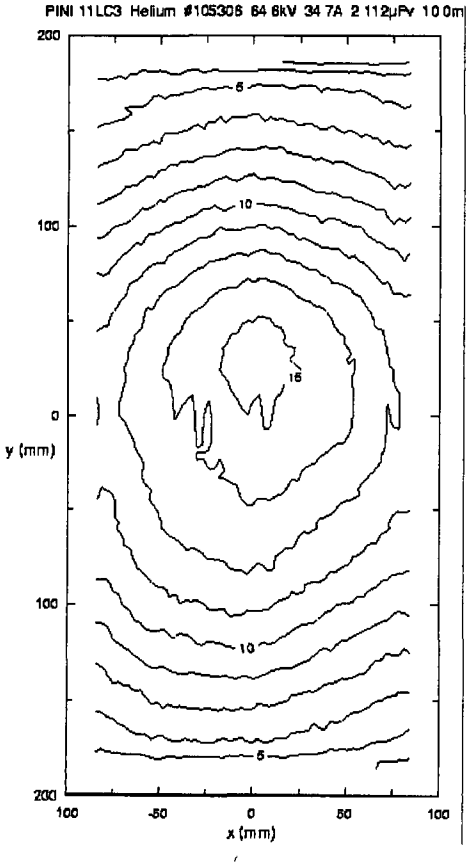

c) 2 112 µPv

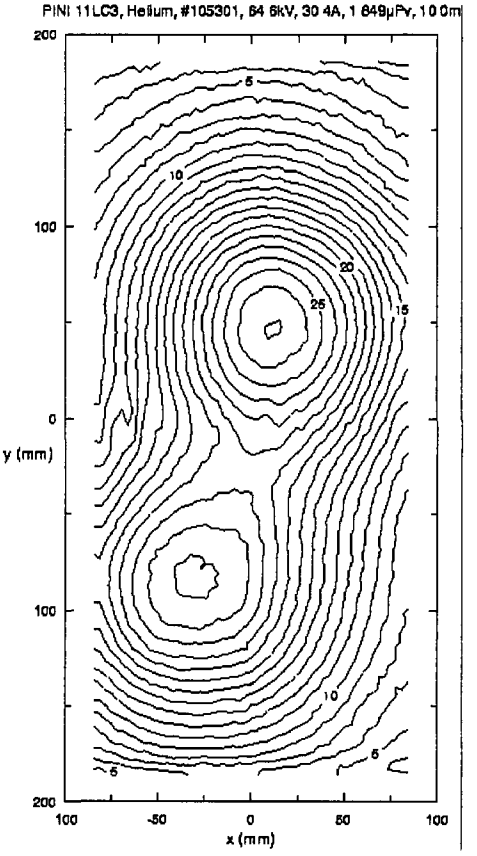

b) 1 649 µPv

Figure 6 21 Beam power density footprints measure for the Line Cusp B ion source magnet arrangement at a) below, b) at and c) above the optimum perveance Using PINI 11AT with the tile at a distance of 10 0m

Plotting the distance between the beam centres of each grid half, defined as the point where the maximum power density is seen, shows that this separation decreases with increasing beam perveance This has already been discussed in Chapter 2 for the super-cusp and chequerboard ion sources In the case of the super-cusp source the separation of the maximum power density peaks is seen to increase with increasing perveance, whereas for the chequerboard source no strong change in the separation is observed

Figure 6 22 shows the comparison of the separation of the maximum power density peaks for the three cases Although is should be noted that the line cusp source measurement were taken at 10 0m downstream, using a He beam, compared to the 4 8m measurements with a D2 beam for the super-cusp and chequerboard sources The interpretation of the increasing separation with increasing beam perveance seen for the super-cusp source was of the minimum beamlet divergence moving from the centre to the edge of the source with increasing perveance, indicating a current density profile peaked toward the source centre For the opposite effect to occur in the line-cusp source the ion density must be lower in the source centre than at the edges, exactly as observed with the multi channel spectrometer

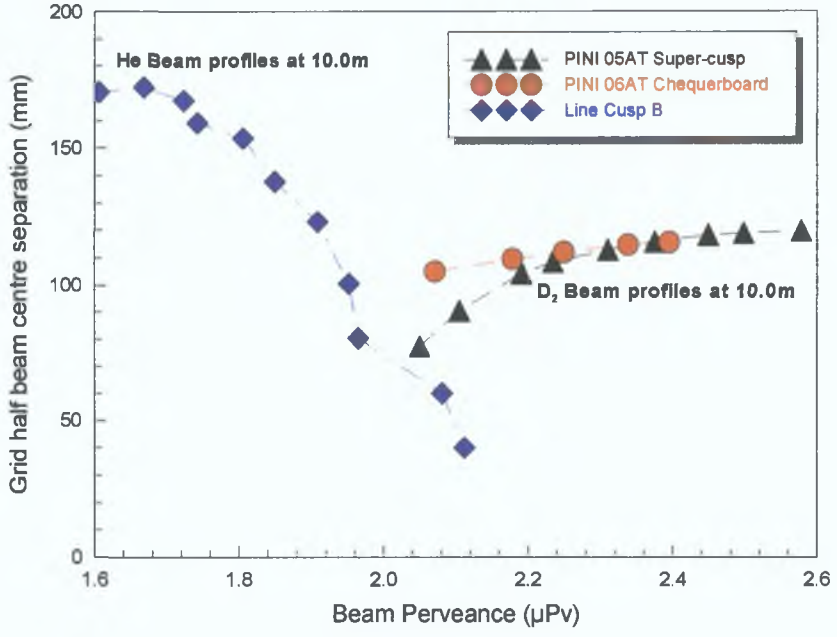

Figure 6.22. . The distance between the beam centres formed from each grid half as a function of the beam perveance. The data is shown from PINIs 11AT with the line cusp B ion source, 05AT with a super-cusp ion source and 06AT with a chequerboard ion source.

6.3.3 MONTE-CARLO MODEL

The model was used to trace a set of primary electron trajectories through the simulated magnetic field for the line cusp B magnet configuration. Once the ionisation points had been determined H_2^+ ions were traced with the same initial energy distribution as used for the super-cusp and chequerboard cases above. The H_2^+ ion trajectory density distribution is shown in figure 6.23 at a plane close to the extraction plane. This figure shows a clear reduction in ion density towards the centre of the ion source, with the majority of the ion trajectories concentrated in opposite corners of the ion source.

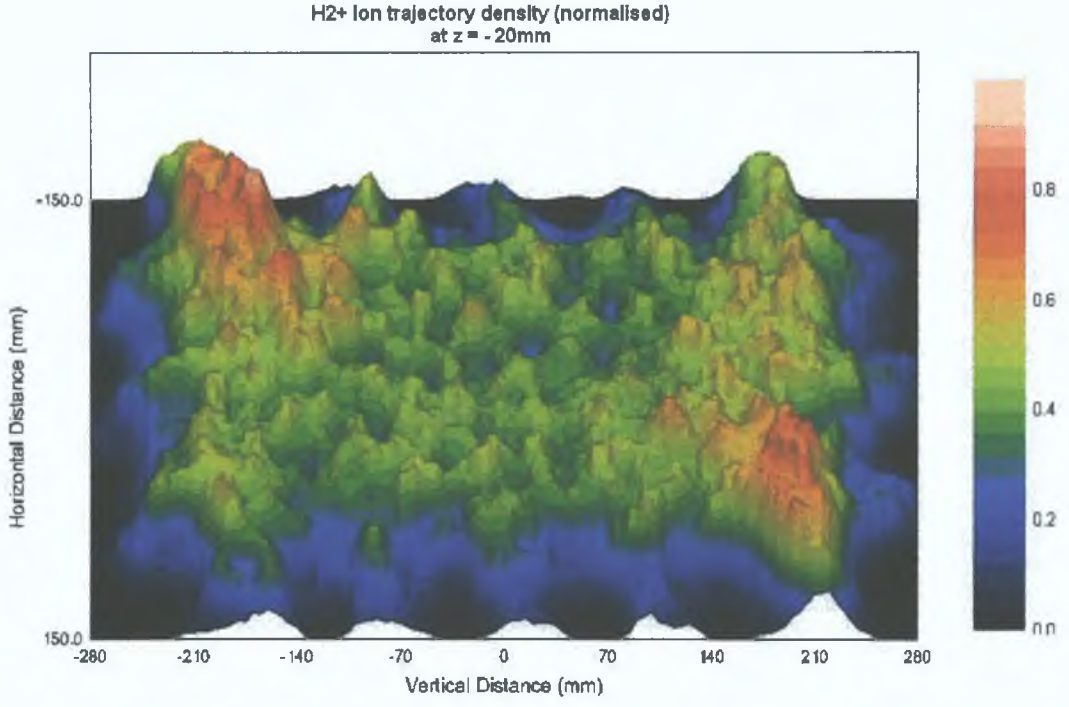

Figure 6.23. Distribution of H_2^+ ion trajectories close to the extraction plane Line Cusp B, 121500 H_2^+ ions [0.5eV mean, 0.25eV std. dev.]

The vertical (y) line trajectory density is derived from this distribution and shown in figure 6.24 The plot shows a quadratic fit to the points at ±150mm about the centre, to match the best-fit required from the multi-channel spectrometer data. This plot shows the sort of behaviour observed by the multi-channel spectrometer, the ion density rises from the centre toward the edges, then at between 150 and 200mm from the centre reaches a maximum and then start to fall towards the source wall.

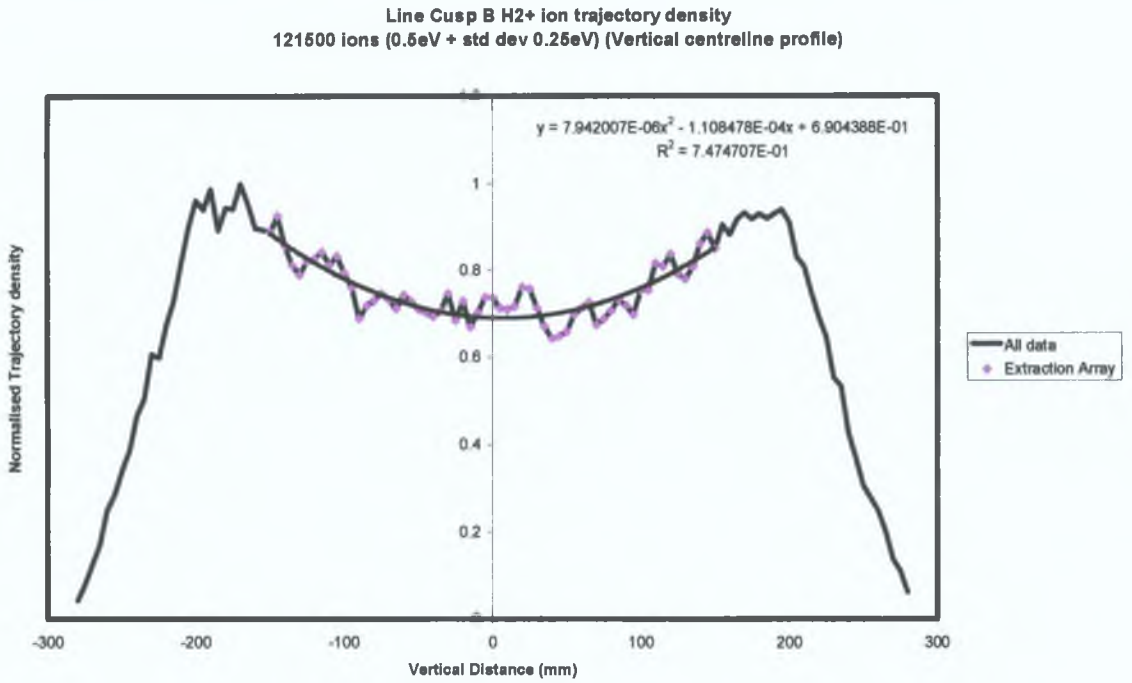

Figure 6.24 Vertical (y) profile of the trajectory density map, with quadratic polynomial fit to a width of ±150 mm about the extraction array centre.

Using the definition of non-uniformity over the ±150mm in this example gives a RMS deviation from uniform of 7.6%. This is identical to the value derived from the spectrometer data, averaged over a perveance scan. Also the maximum deviations of the profile of -7.9% and +15.9% agree well with the values derived from the spectrometer measurements.

6.4. NEW JET ION SOURCE CONFIGURATION

As part of the programme to improve the ion source performance, a new set of ion source bodies was designed and manufactured. The major change in the design of these source bodies over the previous version was to include an extra row of magnets, by reducing the spacing between each row. Previously the source bodies used 6 rows of magnets spaced 30mm apart, the new design has 7 rows of magnets spaced 23.5mm apart. This was design chosen to allow greater flexibility in the proposed modifications to the line cusp arrangements that had been tested using the older source body design. Another design decision was taken to fill each row with magnets of 27mm length, compared to 43mm in the old design, again with

the aim of allowing greater flexibility in arranging magnet patterns Improvements in the permanent magnet technology also meant that the new magnets were available with a stronger remnant field of 0 97T compared to the 0 85T magnets used in the old source bodies, allowing the possibility of longer range line cusp fields to be generated in the ion source

It was decided that for the first tests of this ion source, a super-cusp field that is as similar to the SC15S3 pattern as possible should be tested This would give us a baseline source magnet pattern that produces an ion source performance no worse than the current standard set of SC15S3 ion sources After this has been achieved it would then be possible to consider designs to improve the ion source performance At first replicating the SC15S3 magnet pattern did not give the required source performance, due to the increased strength of the magnet now used in the source body So modifications to the magnet pattern were required to effectively weaken the filter magnet row

6.4.1 MONTE-CARLO MODEL

As this code had started to give reasonable agreement with the measured properties of the SC15S3 super-cusp and line-cusp ion sources, this code was used to determine the effect of modifications to the magnet pattern on the new source body The final configuration, labelled NSC6 [New Super-Cusp version 6] was then tested on PINIs 2AT and 15AT due for installation on the Octant 4 Injector for the April 2000 JET restart and subsequent experimental campaign

As before, a set of 100eV primary electron trajectories were traced through the NSC6 pattern to obtain the H_2^+ ion trajectory starting points The H_2^+ ions were then followed through the ion source until they cross the measurement plane close to the extraction plane Figures 6 25 and 6 26 show the trajectory density plot and the line density plot across the vertical (y) centreline

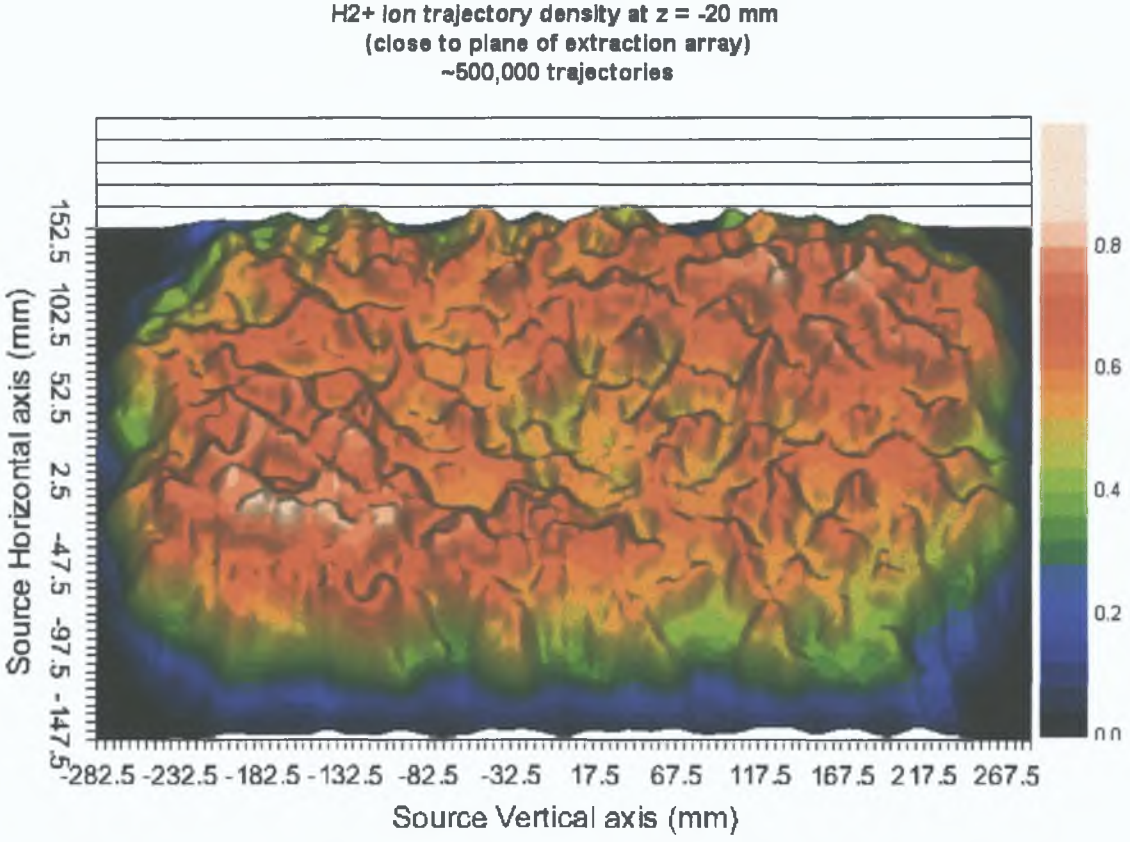

Figure 6.25. Distribution of H_2^+ ion trajectories close to the extraction plane New Super Cusp version 6, 500000 H_2^+ ions [0.5eV mean, 0.25eV std. dev.]

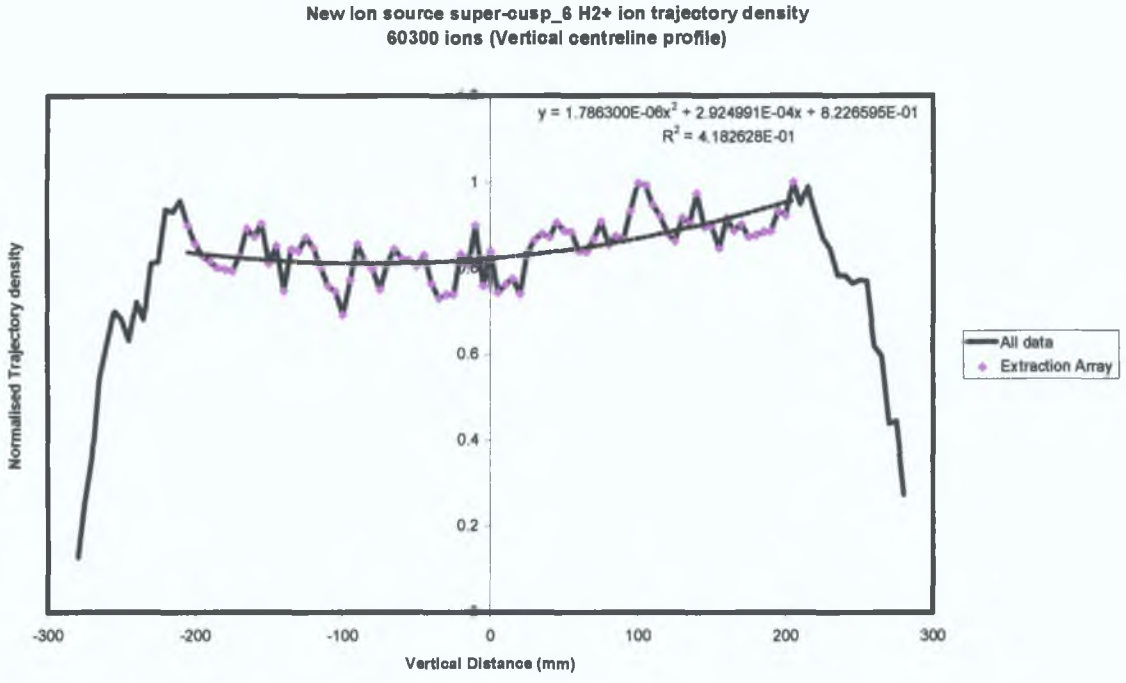

Figure 6.26. Vertical (y) profile of the trajectory density map, with quadratic polynomial fit to a width of ±200 mm about the extraction array centre. [Data from a 12000 ion trajectory simulation]

Using the previously described figure of merit for uniformity over the ±200mm about the vertical centreline profile gives a RMS deviation from uniform of 2.4%, with maximum deviations of-2.8% and +4.8%. This is a factor of two improvement on the 5.3% RMS deviation derived from the SC15S3 model, which agreed well with the measured profiles from this source. The maximum deviation also indicate that this source appears to produce a less skewed profile than the SC15S3 super-cusp

6.4.2 SPECTROSCOPY MEASUREMENTS

The magnet configuration used to produce the modelled uniformity in 6.4.1 above was applied to two ion source bodies and used during conditioning of 2 PINIs on the Neutral Beam Test Bed, both PINIs were of the high current tetrode type. The overall beam perveance at which the local minimum beamlet divergence occurs shows a different structure to that previously seen in the SC15S3 super-cusp source. Figure 6.27 shows this profile for both the

PINIs operated with the new ion source body design. As explained previously, these profiles show effectively the inverse of the ion source density profile, in these cases the density profile rises from the outer edges and the reduces slightly towards the profile centre. These profiles echo in a less severe way the profile observed with the line cusp arrangement.

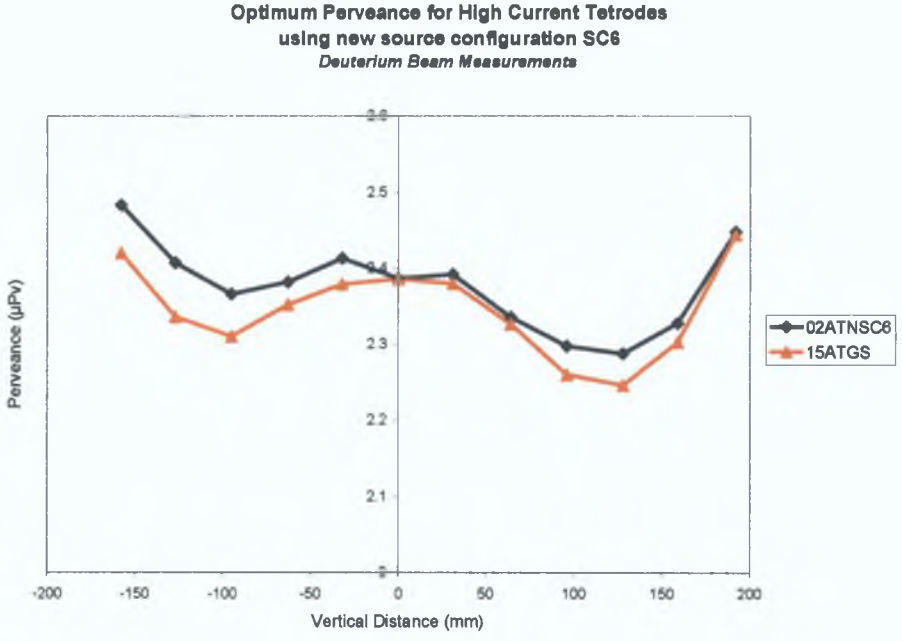

Figure 6.27 Local optimum perveance for the new source super cusp version 6 configuration, measured on PINIs 02AT and 15AT.

Using the same methodology as previously to find the best fit to the divergence profiles, by using 2 quadratic polynomials to describe the current profile (of the species corrected divergence profile), and a further quadratic polynomial to describe the current - divergence relationship, modified by the local value of the minimum divergence. Figure 6.28 shows the current profile required to recreate the divergence profile measured close to the 'optimum' perveance. The current profile required clearly shows the central dip that is evident from the plot of the beam perveance at the local minimum divergence.

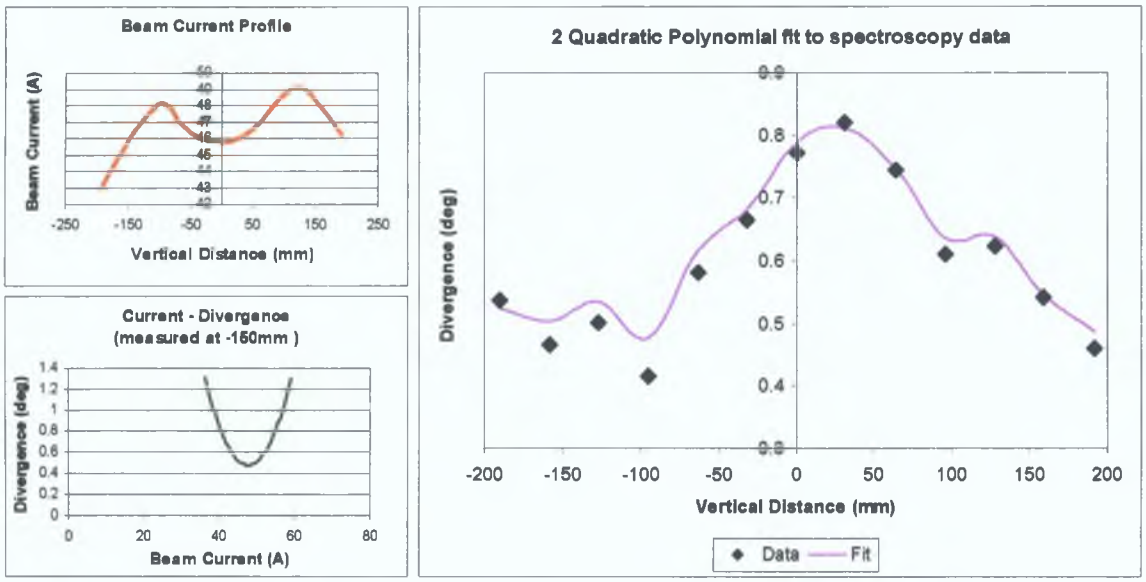

Figure 6.28. Fitting the measured beam divergence distribution with 2 quadratic polynomials describing the vertical beam current profile (PINI 02ATNSC6 Deuterium beam at 2.347μPv).

The best fit current profiles are found for each divergence profile measured in a scan of beam perveance, the required current profiles and the resulting best-fit divergence profiles are shown in figure 6.29. At the lowest value of beam perveance the best-fit solution is found without a dipped central part of the profile. As the perveance is increased the central dip in the profile becomes gradually more pronounced.

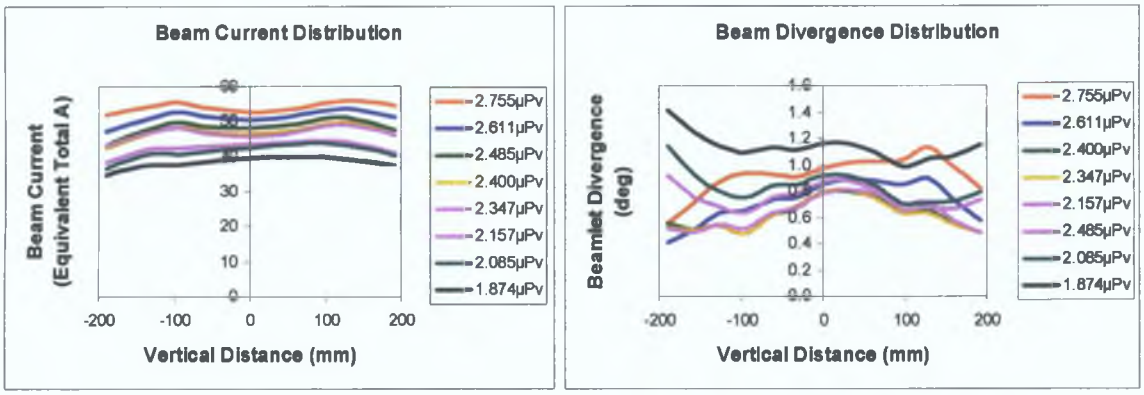

Figure 6.29 Best-fit solutions to the vertical (y) beam current profile for a perveance scan with the new version 6 ion source. (Fixed beam energy, varying beam current)

For each best-fit current profile the non-uniformity figure of merit is obtained, comparing the minimum and maximum values to the mean value. Table 6.7 shows a summary of this data and the resulting non-uniformity figures.

TABLE 6.7. Derivation of non-uniformity figure of merit for the best-fit current profiles shown in figure 6.29.

Perveance (μPv)	**Uniform Value (A)**	**Maximum Deviations**		**RMS Deviation**
1.874	38.3	-4.5%	+3.9%	2.6%
2.085	41.5	-5.6%	+5.2%	2.7%
2.157	42.7	-4.1%	+4.4%	2.6%
2.347	46.7	-2.7%	+4.3%	2.2%
2.4	47.0	-3.7%	+5.1%	2.5%
2.485	48.4	-4.5%	+5.2%	2.6%
2.611	51.2	-3.6%	+4.6%	2.0%
2.755	54.1	-2.2%	+3.4%	1.6%
			Mean :-	**2.5%**

The mean RMS deviation from a uniform profile calculated for these profiles is 2 5%, which compares well with the figure of 2 4% derived from the ion trajectory model of the ion source in this configuration The only discrepancy to note is that the ion trajectory model does not predict the shape of the current profiles generated from the measured divergence profiles Although the ion trajectory simulation does give a profile that has a dished shape this is over the full width of the profile rather than the central section This is also the case with the simulation of the SC15S3 super-cusp source where the ion trajectory model does not recreate the flat top seen across the central part of the profile It thus appears that the ion trajectory model can give a good estimate of the general profile shape but is unable to generate the details of the measured profiles

6.4.3 CFC CALORIMETER MEASUREMENTS

The beam power density footprint measured from PINI 2AT with the new version 6 source body design shows an unusual profile Typically at 4 8m the beams from each grid half are easily distinguished, in this case however the power density profile shows a single peak of very high power density at the centre of the profile This could not be adequately simulated within the existing capabilities of the 3Dfit code The code needed to be modified to take into account the variation in minimum divergence observed from the multi-channel spectrometer measurements A good approximation to the change seen in the value of the minimum beamlet divergence between the outer and central beamlets is to use a linear interpolation Figure 6 30 shows the difference in the minimum beamlet divergence measured for PINI 2ATNSC6, this is approximated in the 3Dfit code by using a central offset value of 0 3deg on the beamlet divergence The offset value used then falls linearly to zero at the maximum and minimum vertical extents of the extraction array

This modification to the 3Dfit code allowed a good solution to be obtained to the measured power density profile Figure 6 31 shows the measured and simulated power density profile for the beam measured close to the 'optimum' perveance in deuterium

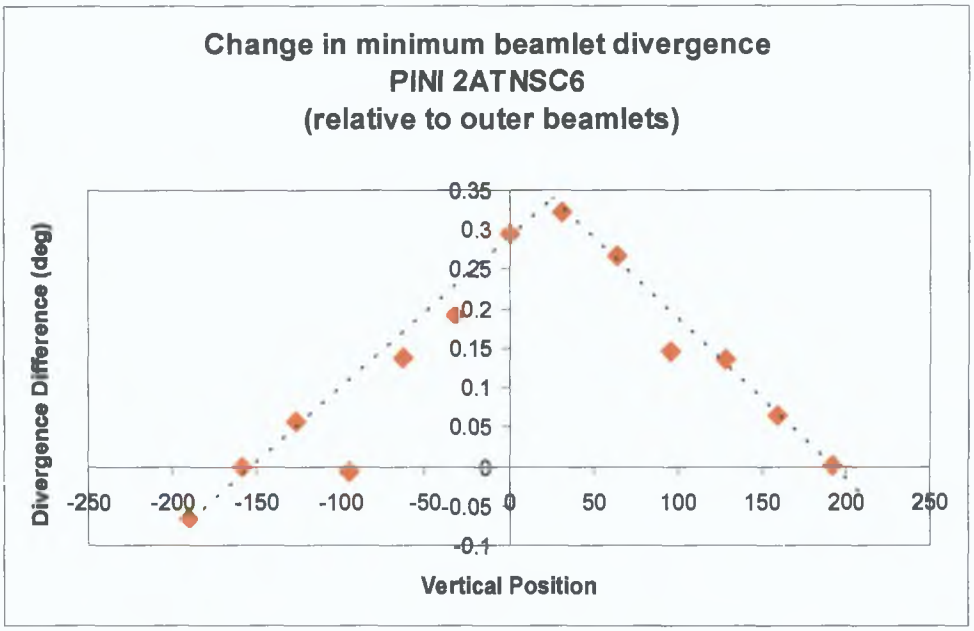

Figure 6.30 Measured difference in the minimum local beamlet divergence across the vertical (y) profile of PINI 02ATNSC6. Approximated in the 3Dfit code by a linear ramp from the centre to edges.

The average percentage deviation between the measured and simulated profiles in this case is 11.45%, not as good a solution as has been obtained from the previous simulations, but still of an acceptable level.

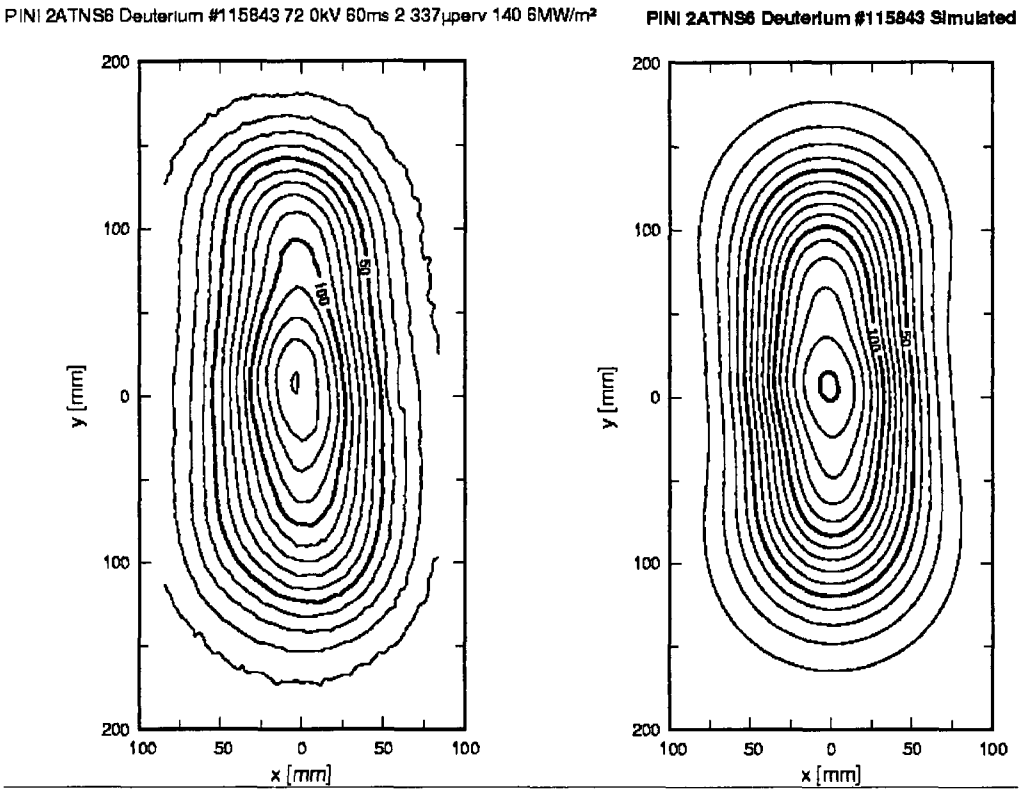

Figure 6 31 Measured and simulated beam power density profiles from the version 6 new super-cusp ion source, 4 8m downstream

The solution obtained by adding the extra beamlet divergence offset parameters uses a beam current density profile that has a RMS deviation from uniform of 2 5% over the extraction array, figure 6 32 Although the central dip in the profile, observed from the spectrometer measurements, is not reproduced in the 3Dfit simulation, the deviation required m the current density profile is similar to the values obtained from both the spectrometer measurements and the Monte-Carlo model

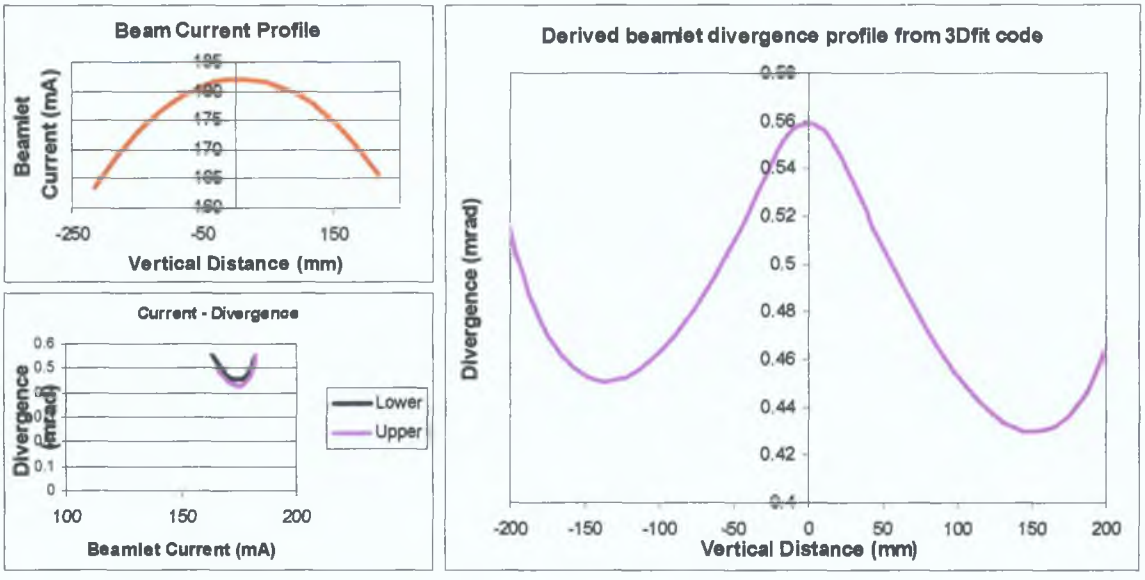

Figure 6.32. Beam current density profile required by the 3Dfit simulation to reproduce the power density footprint shown in figure 6.31.

The table below shows the RMS deviation non-uniformity figure of merit derived from the Monte-Carlo model and by the analysis of the measured beam profiles. The values agree well, showing consistent RMS deviation in the ion density profile of 2.3% from uniform. Which shows a significant improvement in the uniformity of this ion source compared to the RMS deviation of ~5.0% obtained from the standard SC15S3 super-cusp source.

TABLE 6.8 Comparison of the non-uniformity in the ion density derived from beam measurement and Monte-Carlo modelling of the new version 6 super-cusp ion source

Description	**Beam non-uniformity (Max, Min, RMS)**
Multi-channel Spectroscopy At 'optimum' perveance	**+4.5%, -3.9%** **RMS 2.4%**
3Dfit to power density profile At 'optimum' perveance	**+2.5%, -4.6%** **RMS 2.3%**
Monte-Carlo H_2^+ ion trajectories	**+3.6%, -2.1%** **RMS 2.2%**

The only difference in the ion density profiles derived from these three techniques is in the detail of the profile shape, otherwise the level of deviation from a uniform distribution agrees very well

6.5 CHAPTER SUMMARY

Beam profiles measured by the multi-channel spectrometer and CFC tile calorimeter on the Test-Bed have been used to derive a figure of merit for the uniformity of various ion sources The figure of merit used is the RMS deviation from the calculated source current density profile from the equivalent uniform profile This is then compared directly with the ion trajectory density profiles generated by the Monte-Carlo model close to the source extraction plane

The analysis has shown that the SC15S3 super-cusp source is indeed less uniform than the source using the chequerboard magnet pattern alone This analysis has also been used to compare the measured source ion density profile with the modelled profile m the line cusp source configuration Both the analysis of the data and the ion source model show a ion density profile with a 'hollow'centre

The analysis of data from the new NSC_6 super-cusp configuration has confirmed the mcreased uniformity of this source predicted by the Monte-Carlo model The RMS non-uniformity of the NSC_6 is shown to be a factor of 2 better than the SC15S3 super-cusp source

TABLE 6 9 Summary table of measured and modelled ion source non-uniformities

	Non-uniformity RMS deviation (max absolute deviations)		
Source Type	Multi-channel spectrometer	IR CFC tile calorimeter	Monte Carlo Model
SC15S3 super-cusp	4 5% (+4 8%, -10 5%)	6 9% (+7 6%, -12 1)%	5 3% (+6 2%, -10 6%)
Chequerboard only	1 0% (+1 1%, -1 8%)	1 8% (+2 0%, -3 3%)	1 1% (+2 5%, -1 1%)
Line cusp B	7 6% (-8 5%, +13 8%	N/A	7 6% (-7 9%, +15 9%)
NSC_6 super-cusp	2 4% (+4 5%, -3 9%)	2 3% (+2 5%, -4 6%)	2 4% (+4 8%, -2 8%)

7 A BRIEF COMPARATIVE ANALYSIS OF THE SC15S3 AND NSC_6 ION SOURCE MODELS

The previous chapters describe the development of the NSC_6 ion source configuration and the improvement obtained in the extracted beam performance This chapter attempts to provide some explanation in the difference in the performance of the original SC15S3 configuration with the NSC_6 source The models produced of the magnetic field and the Monte-Carlo model of the electron trajectories is analysed in greater detail to determine the difference between the sources

7.1 PRIMARY ELECTRON LOSS AREA

The log file created by the Monte-Carlo model keeps track of the endpoint of each calculated trajectory For the model of the primary electron trajectories the endpoints at a collision with the source wall will give a qualitative indication of the electron loss regions Since the same source backplate is used in the SC15S3 and NSC_6 configurations looking at the electron loss to the source side walls will be used to compare the different source body configurations

Initially it is useful to show the magnet patterns used for the side walls of the SC15S3 and NSC_6 source configurations This is best illustrated by a contour band plot of the magnetic field perpendicular to the side wall The plots shown in figures 7 1 and 7 2 show the orientations of the magnets used on the side wall in each configuration Where magnets of the same orientation are placed together to form a line cusp this appears as a long band of the same value The figures are plotted in the orientation of the axes used for the Monte-Carlo model where the plane of the extraction aperture array is located at the origin of the z-axis The backplate of the ion source is at a value of z = -210mm (using the convention that the +ve z-axis is in the direction of the extracted beam)

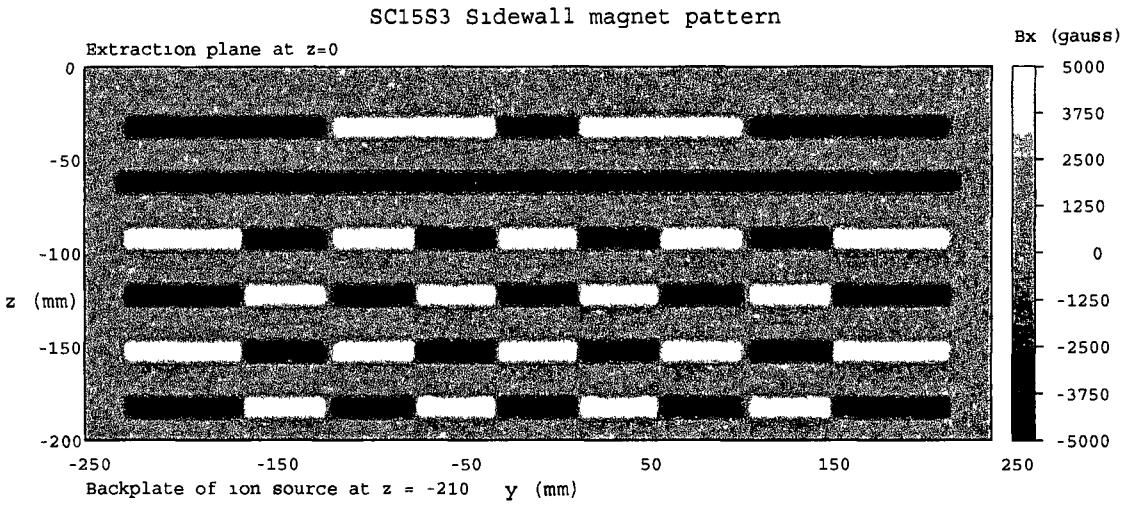

Figure 7 1 Contour band plot of the magnetic field perpendicular to the SC15S3 source sidewall The plot shows the arrangement and orientations of the sidewall magnets

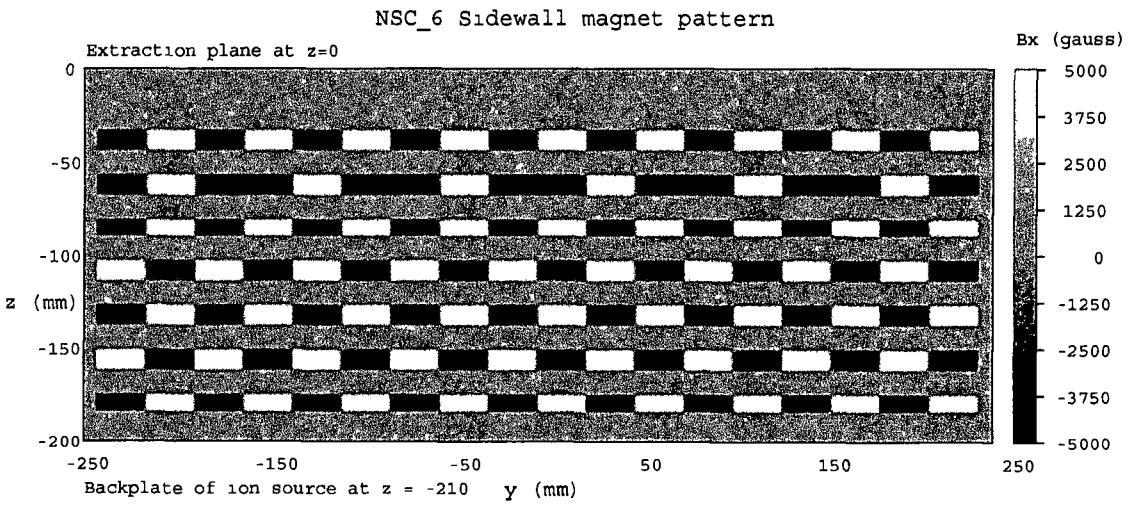

Figure 7 2 Contour band plot of the magnetic field perpendicular to the NSC_6 source sidewall The plot shows the arrangement and orientations of the sidewall magnets

For each of these configurations the Monte-Carlo model is run with a large initial number of 100eV primary electrons. All other initial conditions used in the model are identical (e.g.

neutral gas density, minimum electron energy). For each case the points where electron trajectories are detected to cross the boundary of the source sidewall are plotted in figures 7.3 and 7.4. This shows qualitatively the loss area of primary electrons to the walls of these ion source configurations.

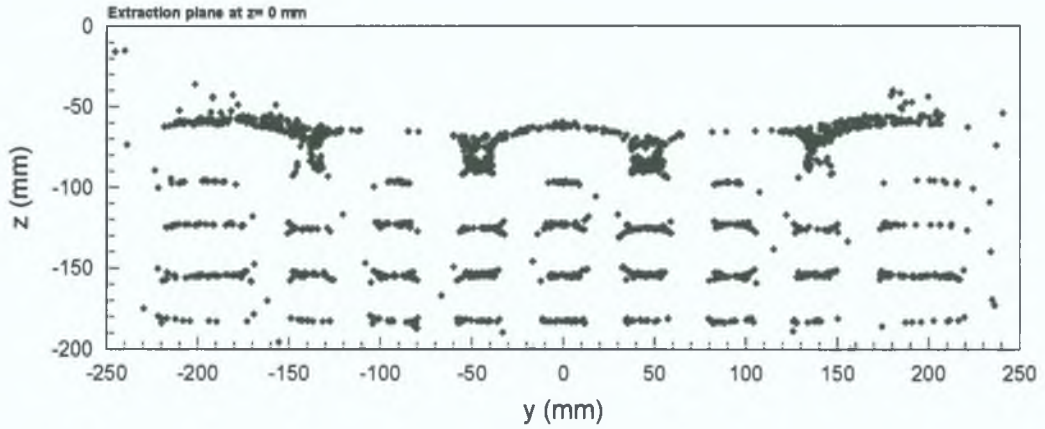

Figure 7.3 Plot of the points where electron trajectories intercept the SC15S3 source sidewalls. (at x = ±155 mm) (Average energy = 86.7eV)

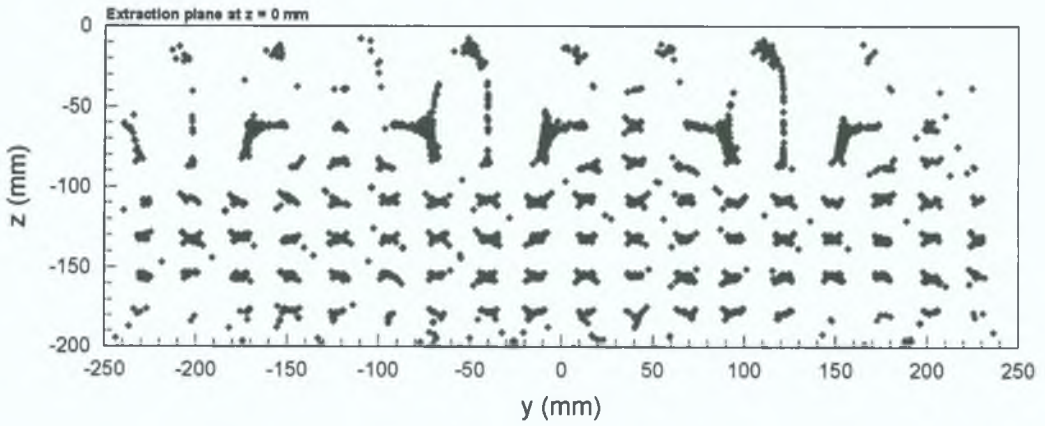

Figure 7.4 Plot of the points where electron trajectories intercept the NSC_6 source sidewalls. (at x = ±155 mm) (Average Energy = 82.6eV)

Generally these plots show the expected behaviour where the electrons can only reach the source walls at a narrow region across the centreline of each magnet [43]. Beyond the region of the super-cusp magnets (> z = -60mm) the field structure leads to a different pattern of

electron loss to the wall The point where the electrons intercept the source wall show the locations where the magnetic field has a component only in the direction perpendicular to the source wall. At these points there is an insufficient field component parallel to the source wall to reflect the electrons gyrating along the field lines into the cusp The pattern shown figure 7 3 is also very similar to the discoloration pattern seen on the walls of the ion sources after long period ion source operation at high arc power

The regions where the electrons are likely to intercept the source wall can thus be derived from the modelled map of the magnetic field in the source At the plane of the source wall the component of the perpendicular field (Bx) is calculated as a fraction of the total field at each point (Bx/Btot) By plotting the regions that have a Bx component that is >95% of the total field, i e where the magnetic field is close to perpendicular to the source wall surface, gives the patterns shown in figures 7 5 and 7 6

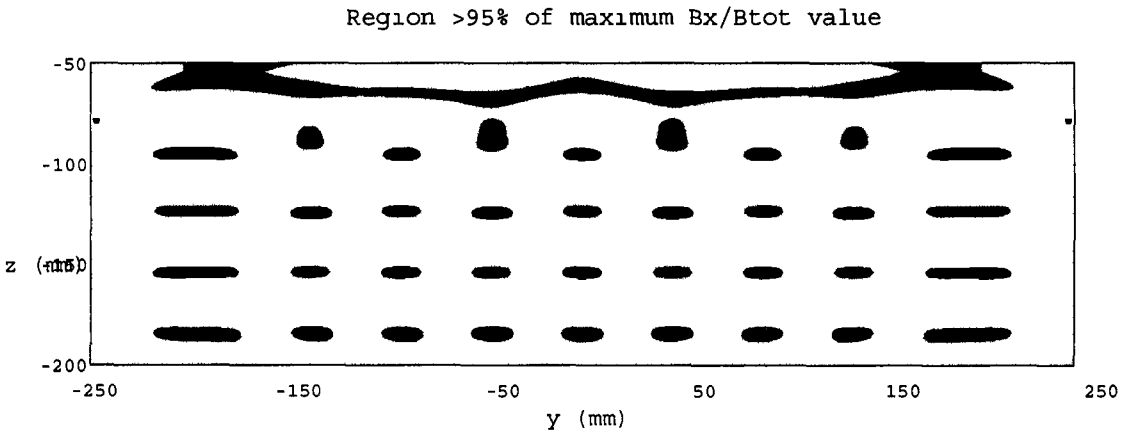

Figure 7 5 Band plot of the regions at the SC15S3 side wall where the normal component (Bx) is >95% of the total field at each point (at x = ±155 mm) The black regions show the areas where B_x/B_{tot} >95%, the light areas <95%

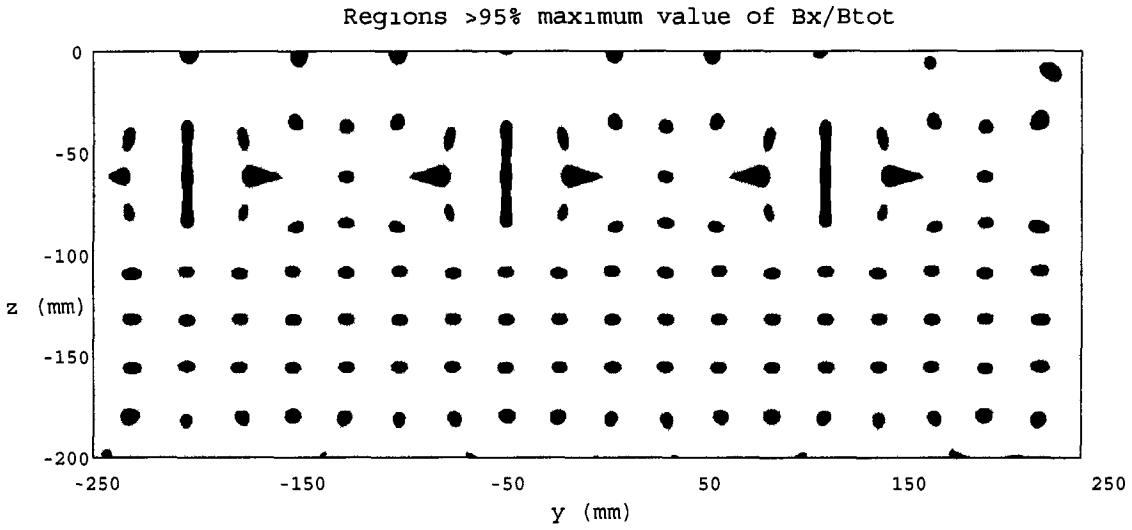

Figure 7 6 Band plot of the regions at the NSC_6 side wall where the normal component (Bx) is >95% of the total field at each point (at x = ±155 mm) The black regions show the areas where B_x/B_{tot} >95%, the light areas <95%

This analysis of the model field structure compares, qualitatively, well with the electron interception plots for each configuration, showing the same general pattern in each case To try to quantify this information the area covered by the regions shown in 7 5 and 7 6 is calculated The area is calculated as a function of the fraction of Bx/Btot for the two source configurations

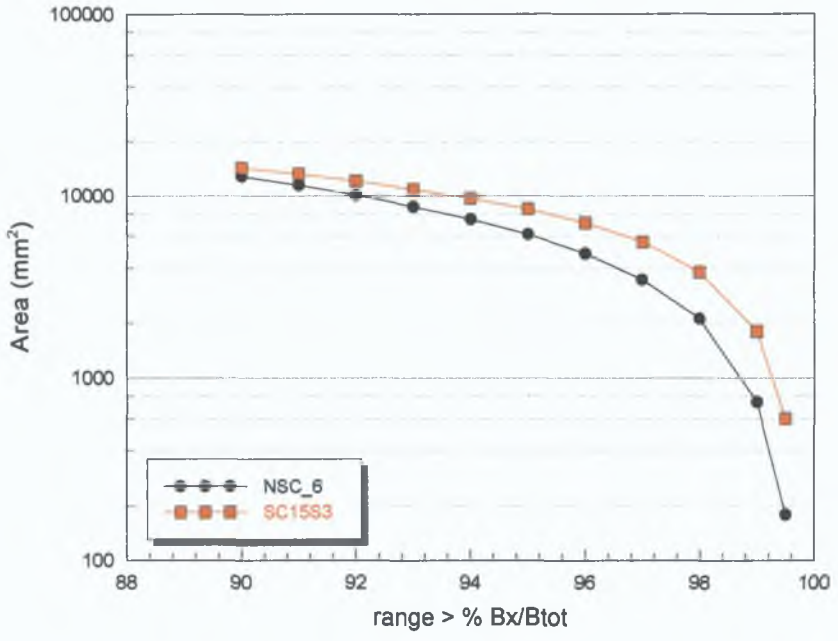

Figure 7.7 Comparison of the cusp loss areas calculated from the area of the Bx/Btot contours above a given fraction for the SC15S3 and NSC_6 configurations.

This plot shows that the SC15S3 configuration has a potentially larger surface area for loss of electrons than the NSC_6 configuration. This however gives a different impression than that given by comparing the ionisation efficiencies of the two configurations.

The table below compares the statistics of the Monte-Carlo primary electron model. For each configuration, using identical initial conditions for the model.

TABLE 7 1 Comparison of the output from the primary electron simulation of the SC15S3 and NSC6 super-cusp ion sources

	SC15S3		NSC_6	
Number of 100eV primaries	1194		1194	
Number ionisations	1069		1008	
Iomsation ratio	0 8953		0 844	
Total number of electrons (+ secondaries)	2263		2002	
Number <10eV	1641	72 5%	1705	85 2%
Number to grid 1 (energy >90eV)	131 (93)	5 8% (4 1%)	107 (58)	4 3% (2 9%)
Number to source walls	355	15 7%	507	25 3%

As has previously been shown the SC15S3 primary electron model produces a ratio of ionisations per primary of 0 90, compared to the value of 0 84 obtained from the NSC_6 model with the same initial conditions Analysis of the model output shows a greater fraction of the electrons lost to the source walls m the NSC_6 model than for the SC15S3 model In the case of the SC15S3 model 15 7% of the electron trajectories are lost to the source walls compared to 25 3% m the NSC_6 model, consistent with the experimentally observed reduction in ionisation efficiency It would thus be anticipated that the NSC_6 source configuration should show a larger cusp loss area than the SC15S3 source, which is not the case of figure 7 7

It thus appears that although the loss area on the surface of the NSC_6 wall is smaller more electron trajectories are collected on this area This can be illustrated by looking at the total magnetic field through a centreline section of the ion source perpendicular to the source wall In figures 7 8 and 7 9 below the contour of constant field at 100G is illustrated, at which a 100eV primary electron would have a Larmour radius of 3 4mm

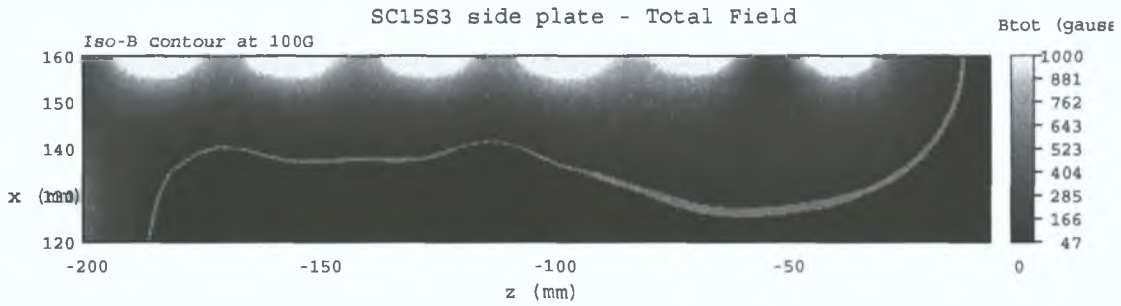

Figure 7.8 Total B field plotted on the centre ZX plane of the SC15S3 configuration. Shown is the 100Gauss iso-B contour.

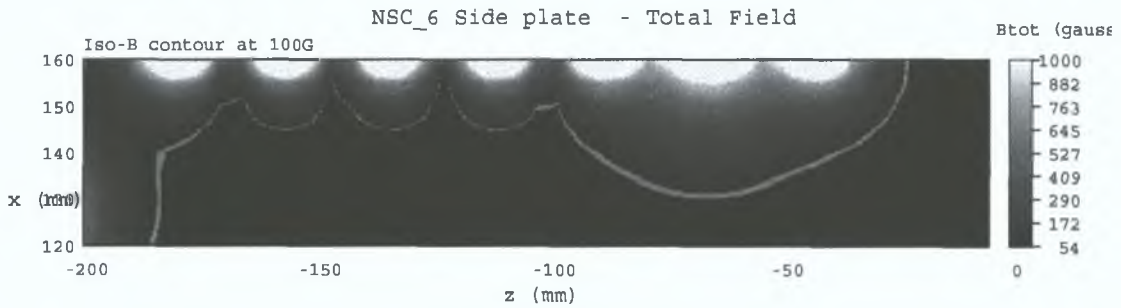

Figure 7.9 Total B field plotted on the centre ZX plane of the NSC_6 configuration. Shown is the 100Gauss iso-B contour.

In the case of the NSC_6 the source centreline is also along the line between magnets, this shows that there are regions where a field of <100G reaches very close to the source wall. This is not seen in the figure for the SC15S3 configuration as the source centreline passes through the centre of a column of magnets. It appears that the disadvantage of using shorter magnets, with a smaller magnet row spacing, in the NSC_6 configuration gives more opportunities for the electron trajectories to get close enough to the source wall to be caught in a cusp that leads to the source wall. With the larger magnets and wider spacing in the SC15S3 configuration the number of times that a low field reaches close to the source body is reduced. The advantage of the NSC_6 configuration is that with a greater number of magnet reversals in the chequerboard pattern the residual magnetic field at the extraction plane and centre of the ion source is much reduced. It can be seen in the figures above how much further

away the 100G contour is from the extraction aperture array, at z=0, in the case of the NSC_6 configuration.

It thus appears difficult to quantify the electron loss area looking by analysis of the magnetic field pattern alone as many factors influence the actual fraction of electron lost to the source walls. The magnetic field pattern can give some indication of where the electron losses will occur but the Monte-Carlo trajectory model is required to quantify the actual losses.

7.2 ION TRAJECTORY DENSITY COMPARISONS.

For each of the Monte-Carlo models of the ion trajectories in the SC15S3 and NSC_6 source configurations the ion trajectory density is plotted in the XY plane of the ion source (parallel to the plane of the extraction aperture array). The figures below show the ion trajectory density at z=-105mm (approximately halfway through the ion source) and at z=-15mm (close to the extraction aperture array). Each of the plot show the normalised ion density in each plane.

Comparing the trajectory density plots at z=-105mm show that at this point in the source the ion density in the NSC_6 source appears to be distributed more uniformly than for the SC15S3 source. The ion density at this point halfway through the ion source then seems to predetermine that the ion density will have a similar distribution at the plane of the extraction aperture array.

It appears that the NSC_6 produces a more uniform ion density at the extraction plane because the ionisation production region is inherently more uniform than for the SC15S3 configuration. It is difficult to find a single factor that sufficiently differentiates the primary electron trajectories in the models of the SC15S3 and NSC_6 configurations to explain the apparently more uniform ion production in the NSC_6 source. Some differences that could possibly explain this are :-

A) In the NSC_6 a combination of a weaker filter field and shorter range fields on the side walls, due to the decreased magnet row spacing, gives a larger low field volume for the electron trajectories to move in. If the primary electrons are not strongly tied to the filter

or wall fields then the probability of ion production will be spread over a larger volume of the source

B) In the SC15S3 configuration many of the electron trajectories are reflected from the transition between the side and end walls So these trajectories are not free to precess around the source and concentrate towards the corners of the ion source thus enhancing the ion production probability This can be seen in the two 'lobes' of ion density that can be seen in the SC15S3 ion density plot a z = -105mm

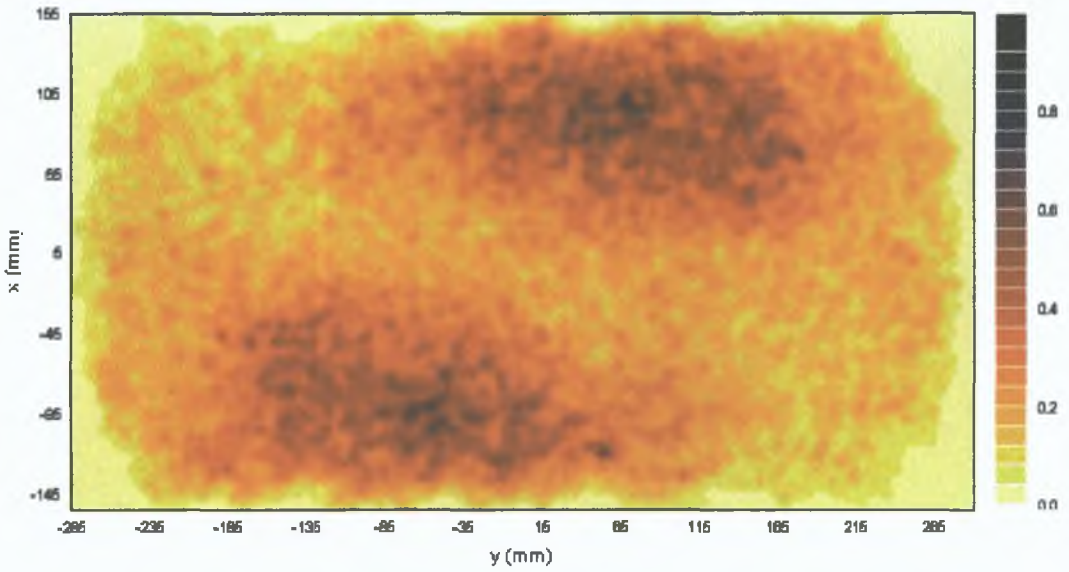

Figure 7.10 Normalised H_2^+ ion trajectory density distribution in the XY plane for a Monte-Carlo model of the ion trajectories in the SC15S3 source at a position z=-105mm, approximately half depth of the ion source.

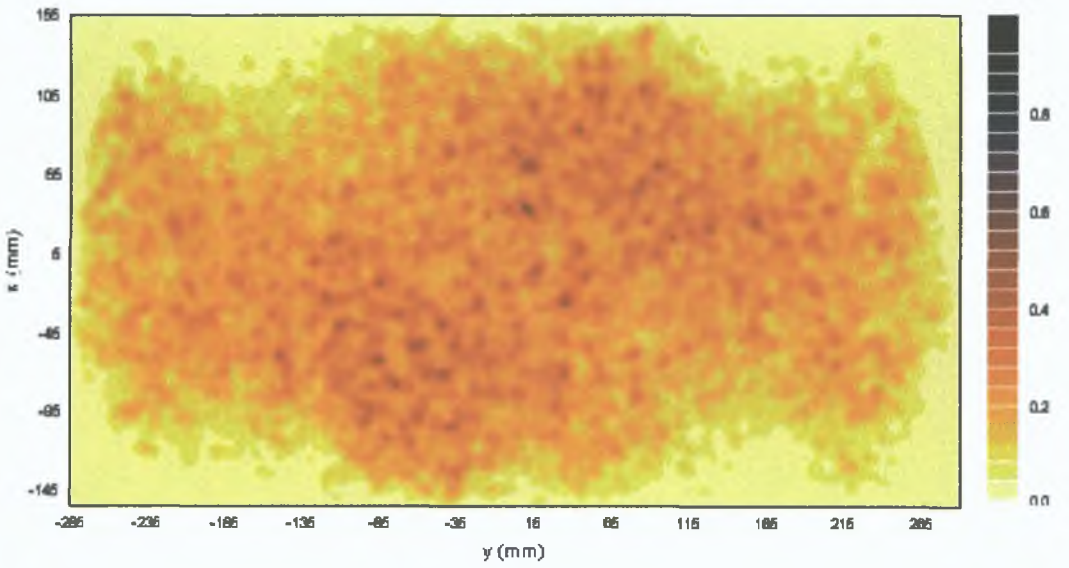

Figure 7.11 Normalised H_2^+ ion trajectory density distribution in the XY plane for a Monte-Carlo model of the ion trajectories in the SC15S3 source at a position z=-15mm, approximately at the plane of the extraction aperture array.

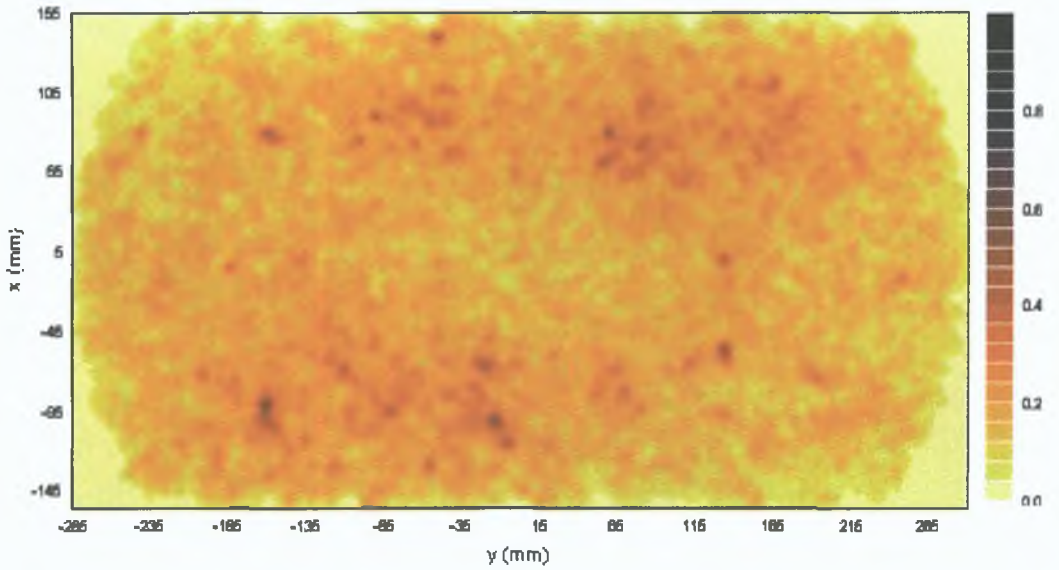

Figure 7.12 Normalised H_2^+ ion trajectory density distribution in the XY plane for a Monte-Carlo model of the ion trajectories in the NSC_6 source at a position z=-105mm, approximately half depth of the ion source.

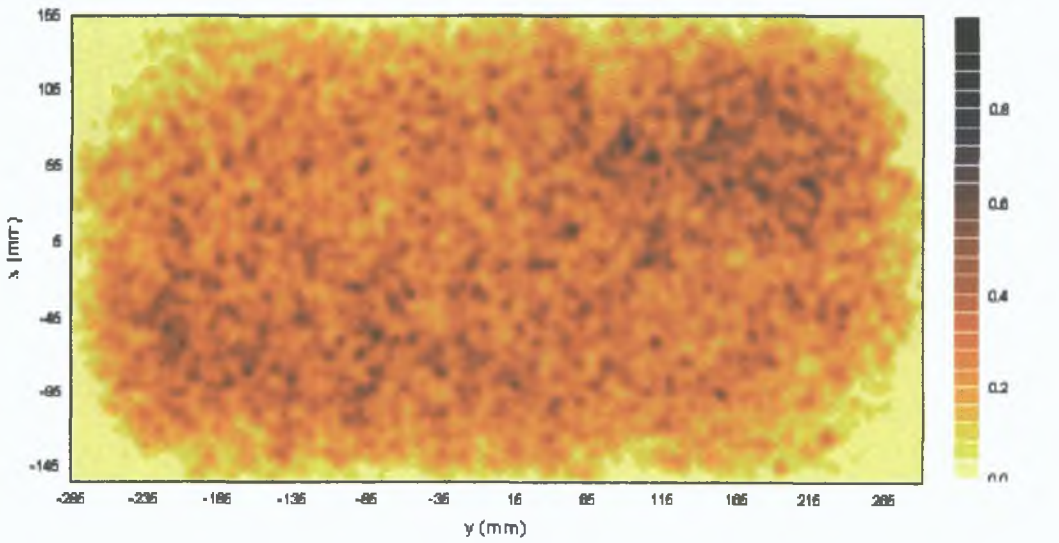

Figure 7.13 Normalised H_2^+ ion trajectory density distribution in the XY plane for a Monte-Carlo model of the ion trajectories in the NSC_6 source at a position z=-15mm, approximately at the plane of the extraction aperture array.

8 SUMMARY AND CONCLUSIONS

8.1 Non-uniformity

The experimental evidence, obtained from beams extracted on the Neutral Beam Test Bed, clearly shows that the ion source used on the JET PINI produces a non-uniform plasma It has been shown that the magnetic filter field, used in the ion source to produce an enhanced monatomic species fraction, is also responsible for the non-uniformity This was proven by comparing the beams extracted from sources with and without the filter field, using the same accelerator grids Although the source without the filter field produced an unacceptably low monatomic species yield the transmission of the beam power on the Test Bed was much greater than for the filter field source The increased beam transmission corresponded to a similar reduction of beam interception on the Test Bed beamline scraper elements

Further analysis of detailed measurements taken by a multi-channel spectrometer and Carbon Fibre Composite tile calorimeter revealed the difference in the uniformity of the ion sources The clearest evidence of this is given from the analysis of the multi-channel spectrometer data Across the vertical (y) axis of the beam the total beam perveance is calculated at which the local minimum local divergence occurs For a uniform extraction aperture array this is equivalent to the inverse of the local ion density Figure 8 1 shows the comparison of these plots for beams extracted from the SC15S3 super-cusp and chequerboard only sources

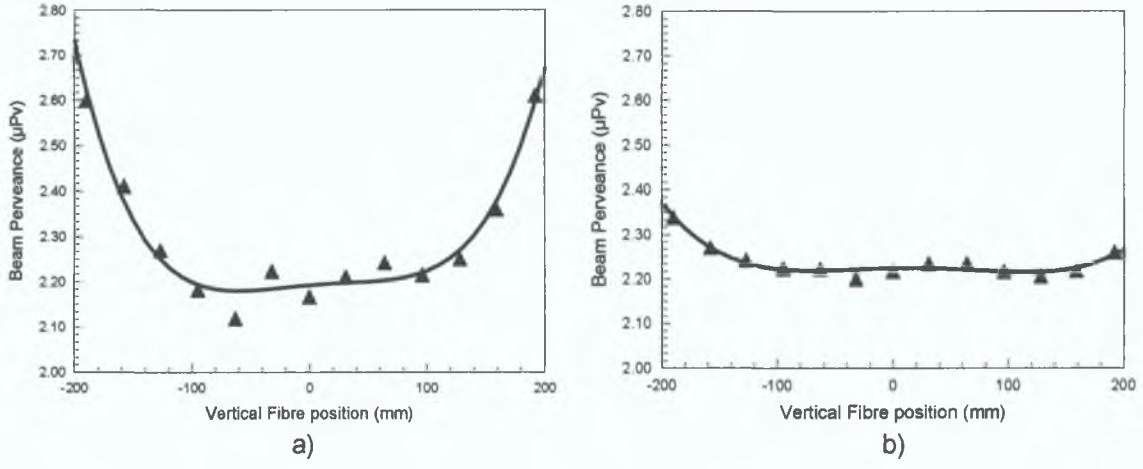

a) SC15S3 super-cusp

b) Chequerboard only

Figure 8.1. Comparison of the plots of the beam perveance where the local minimum beam divergence occurs across the vertical (y) axis of the beam. Reproduced from Chapter 5 (figure 5.7) with data from Chapter 2 (figures 2.7 and 2.11)

Analysis of beam profiles obtained from the spectroscopic and calorimetric diagnostics is used to derive a figure of merit for the root mean square (RMS) deviation of the measured profile from uniform. This figure of merit is summarised in table 8.1 below for the super-cusp and chequerboard only ion sources.

TABLE 8.1 Summary of non-uniformity figure of merit measurements for the super-cusp and chequerboard ion sources.

	Multi Channel Spectrometer	**IR tile calorimeter**
Super Cusp SC15S3	**4.5%**	**6.9%**
Chequerboard only	**1.0%**	**1.8%**

Considering the effect of a non-uniform plasma density produced by an ion source at the multi-aperture extraction array showed how the beam transmission was affected. Essentially for a non-uniform source there will always be some fraction of the apertures that are not producing beams at the minimum possible divergence for any given total beam current. This effectively increases the minimum divergence that is possible for a beam combined from a

multi aperture array Clearly for a perfectly uniform source there will be a given extracted beam current where all aperture produce the minimum divergence, giving a combined beam of overall low divergence It is this that leads to increased beam interception on beamline scraper elements, with the consequential reduction in transmission of the beam through the beamline The maximum power injected into the JET plasma from the Octant 4 Neutral Beam Injector is often limited by excessive beam interception on beamline scraper elements and not by the limits of the electrical power supplies It was thus realised that if a source could be produced with improved uniformity, but without degrading the monatomic species fraction, then it would be possible to reduce the scraper power loads in the octant 4 injector This would have the double benefit of allowing beams to be injected at the limit of the power supplies, and give a higher transmission of the beam power to the JET plasma It is for this reason that a programme of source uniformity enhancement was initiated on the Neutral Beam Test Bed by -

A) Developing a Monte-Carlo computer model of the ion source
B) Running experimental tests of different ion source configurations

8.2 Monte-Carlo model of the JET PINI ion source

A computer model was developed to simulate the ion source used in the JET PINI The model calculates the trajectories of charged particles through a map of the three dimensional magnetic field of the ion source The magnetic field map is created by superimposing the solution of the analytical expressions for the magnetic field vector from each magnet The first part of the model traces the primary electrons launched from the filament cathodes through the ion source A Monte-Carlo method is used to calculate the interactions of the primary electrons with the neutral source gas The highest probability reactions of the primary electrons with the source gas are the elastic, ionisation and dissociation reactions Running many trajectory calculations builds a map of the points where the ionisation of the source gas occurs The next step is to calculate the trajectories of the ions with the initial starting locations given by the primary electron model The uniformity of the ion source is then quantified by determining the density of ion trajectories crossing the plane of the extraction aperture array

The primary electron model was benchmarked against the known behaviour of the super-cusp ion source The model correctly reproduces the observed dependence of ionisation efficiency

on the density of the neutral source gas. The primary electron model also reproduces the known behaviour where the source arc efficiency does not increase significantly above an arc potential of 80V in this ion source. In addition the primary electron model produces many qualitative comparisons with the ion source, plotting the inelastic interactions nodes gives an indication of how the filter field isolates the primary electron from the region close to the extraction aperture array. This gives a qualitative indication of the monatomic species yield since primary electrons must be excluded from this region for an enhancement in the monatomic species ratio to occur.

The density of the ion trajectories crossing the plane of the extraction aperture array was calculated for the super-cusp ion source, using the initial conditions produced by the primary electron model. The density map is used to generate a profile of the ion density that is used to compare directly with the experimental measurements.

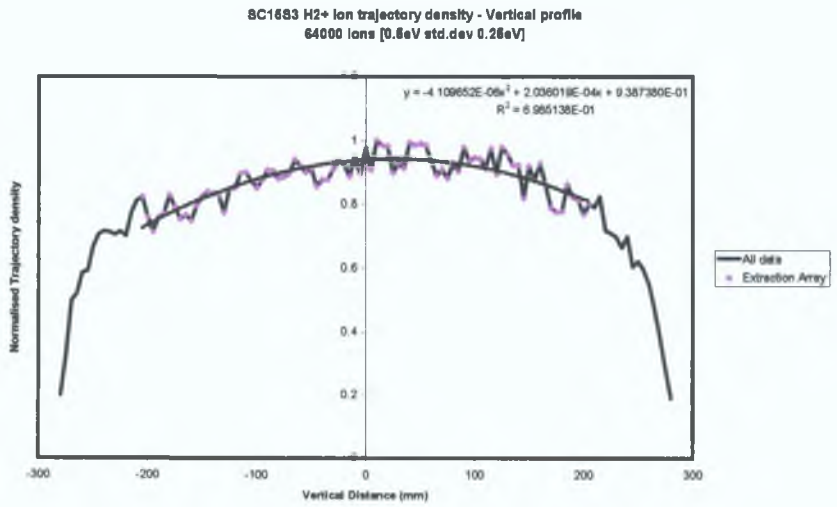

Figure 8.2. Vertical (y) profile of the trajectory density map, with quadratic polynomial fit to the width of the extraction array.

Figuire reproduced from Chapter 6 (figure 6.10)

Over the vertical range of the extraction aperture array the Monte-Carlo model gives a RMS deviation in the ion trajectory density of 5.3% from uniform. This agrees very well with the values obtained from the measurements of the super-cusp ion source, table 8.1.

The simulation of the chequerboard only source is not as successful however - without the filter field to confine the trajectories of the primary electron the model looses these particles very quickly to the plasma-facing grid This does not enable good statistics of the primary electron interactions to be established in the central region of the ion source Thus the initial conditions of the ion trajectories are incorrectly weighted to regions very close to the source wall where a few of the primary electron trajectories become trapped

8.3 Experimental Source development

Initially it was thought that stray magnetic field present at the extraction plane, from the magnet used to create the filter field, was a contributing factor to the non-uniformity To test this a source body was constructed with a 33% increase in depth The extra depth was covered in a chequerboard only pattern, with the rest of the source configured in the super-cusp pattern This source however gave a no improvement in plasma uniformity over the standard depth ion source In addition this source showed a significant reduction in the ion current extracted per unit of input arc power, giving only 30A of beam at full arc power

Following a review of alternative source configurations a variety of line-cusp magnet configurations were investigated In these configurations the filaments are rotated so that the emission is closer to the source walls Line cusp magnet configurations were then used to produce a filter field that extends over the depth of the ion source wall Thus the ionisation region of the source covers the walls of the source so that ions will move towards the centre of the ion source, with sufficient ion production close to the source wall to balance the ion loss Some variation of the line-cusp configuration showed potential improvement in ion uniformity (line-cusp A 2) but in general it was difficult to produce a sufficient ion density in the centre of the ion source These particular configurations (e g line-cusp B) produced an ion density non-uniformity that was dipped towards the centre of the ion source The Monte-Carlo model was used to simulate the line cusp configurations and was able to successfully reproduce the observed ion density non-umformity (e g line-cusp B)

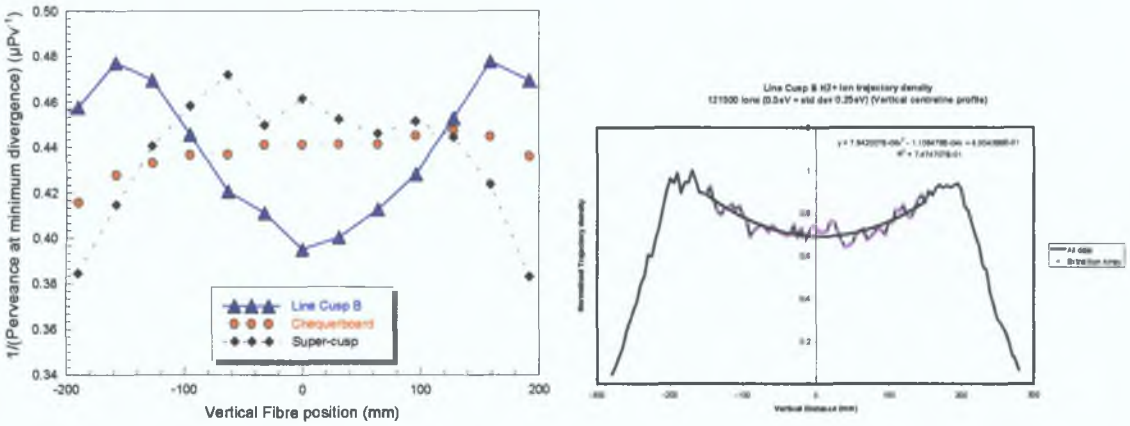

Figure 8.3. Comparison of the ion source non-uniformity profile recreated from spectroscopic measurements for the line cusp B configuration and the Monte-Carlo model. The measure line-cusp B profile is, shown with the similarly derived profiles for the super-cusp and chequerboard sources
Data taken from chapter 6.

8.4 Development of the NSC_6 source configuration

A new ion source body design was specified for further magnet configuration tests. This design used the same depth as the original source bodies but the number of magnet rows was increased from 6 to 7 by reducing the row interspace from 30 to 23.5mm. In addition new magnets of a shorter length but higher remnant field were specified to allow greater flexibility in the choice of magnet configuration.

For the first configuration of this source a pattern similar to the original SC15S3 super-cusp was used. This was intended to provide a fallback position should the work on further configurations be unsuccessful. This initial configuration, NSC_1, however gave a very poor ion uniformity, but with a larger monatomic species yield. Investigating the model of the magnetic field map of the NSC_1 configuration shows that the stronger magnets specified for the new source configuration result in a stronger filter field. The Monte-Carlo model was then used to simulate variants of the super-cusp configuration to find a configuration that would give the required source performance. As a result of these simulation a configuration, NSC_6 was developed that actually appeared to give an ion uniformity that was a factor of two better than for the original SC15S3 configuration. The RMS deviation of the predicted ion density

profile from uniform was 2.2%, compared to the 5.3% given by the model of the SC15S3 super-cusp source.

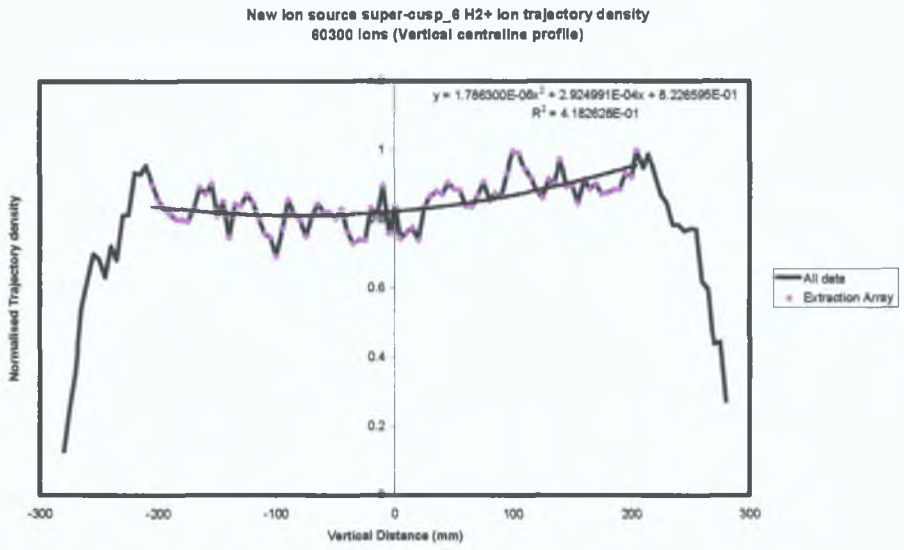

Figure 8.4 predicted ion density uniformity for the NSC_6 configuration. Reproduced from Chapter 6 (figure 6.26)

The Monte-Carlo model of the NSC_6 configuration indicated that the monatomic species yield should be similar, but that a reduced arc efficiency would be likely. The key feature of the NSC_6 configuration is a filter field that is weaker than both the NSC_1 and SC15S3 configurations.

PINIs with the NSC_6 source configuration were then tested on the Neutral Beam Test Bed. Immediately it was clear that the arc efficiency was lower, however increasing the gas flow to the ion source easily compensated this. The source gas flow used was comparable with that used routinely on the Octant 4 injector so no vacuum problems would be caused by operating a source that required this gas flow. The transmission of beam power to the Test Bed beam dump from the NSC_6 source was comparable to that previously measured with the chequerboard ion source. This was supported by the analysis of the spectroscopic and calorimetric diagnostics that both showed improved ion density uniformity.

TABLE 8 2 Comparison of the predicted and measured ion uniformity for the NSC_6 source configuration

Description	Beam non-uniformity (%)
Multi-channel Spectroscopy At 'optimum' perveance	**2.4%**
3Dfit to power density profile At 'optimum' perveance	**2.3%**
Monte-Carlo H_2^+ ion trajectories	**2.2%**

The monatomic species fraction of the NSC_6 configuration was found to be reduced by 2%, to 86% D^+ This however is still above the minimum level required for neutral beam injection to the JET plasma

It is thought that the NSC_6 magnet pattern gives improved ion uniformity for the following reasons Looking at the magnet pattern, the filter magnets appear to be a small perturbation of the overall strong chequerboard pattern This produces a filter field that is weaker than for the SC15S3 pattern but still strong enough to give good monatomic species yield Since the filter field is weaker and surrounded by a good chequerboard pattern there is a significantly reduced stray magnetic field, in fact more closely resembling the chequerboard only source at the extraction array The magnet row used for the filter field on the side walls is also now 13mm closer to the extraction plane than in the SC15S3 design Combined with the weaker filter field this means that the region in which the primary electrons are contained extends further along the wall of the source towards the extraction plane This, in common with the line-cusp patterns, gives an ion production region along the source wall to compensate for the loss of ions to the walls It is believed that this prevents a gradient building in the ion density from the centre of the source to the walls, thus reducing the non-uniformity at the plane of the extraction aperture array

It is interesting to compare the key quantities of the super-cusp configuration ion sources tested Figure 8 5 shows how the measured monatomic species yield and ion density non-uniformity vary with the strength of the filter field For this plot the line integral of total magnetic field from a filament stem location to the centre of the extraction plane is used to provide a quantitative comparison. The data for the chequerboard source are also shown for

comparison. This plot shows a general principal for the ion sources of the super-cusp type in that the ion density non-uniformity is closely linked to the monatomic species yield. To produce a monatomic species fraction >80% appears to inevitably require a filter field strength that will degrade the ion uniformity.

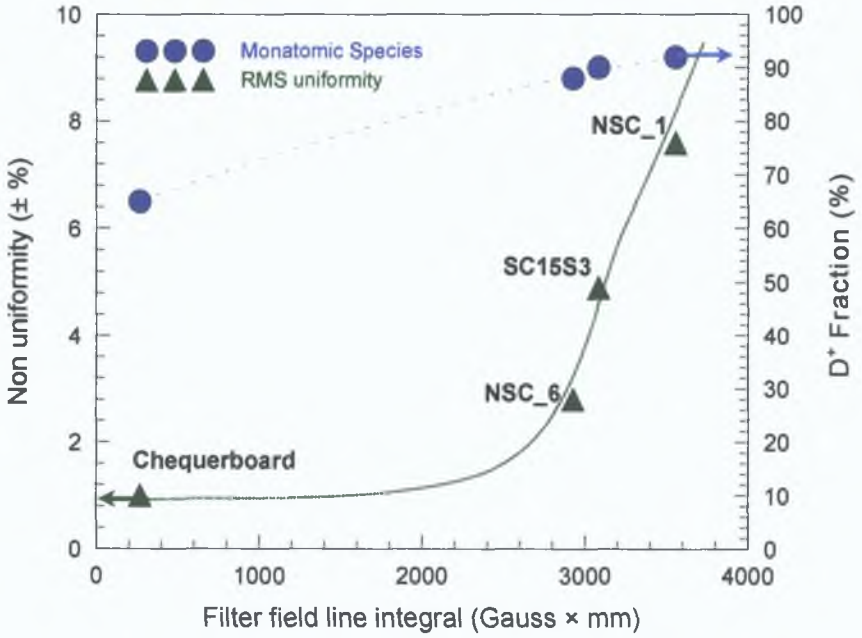

Figure 8.5 Summary of the comparison of the super-cusp magnet patterns.

Figure 8.5 of course does ask the question whether using an NSC configuration with a filter field further weakened, to say 2400 G×mm, would produce still further improvements in the RMS ion uniformity, perhaps to 1.5% - with a monatomic species fraction still >80%?

8.6 Conclusions

- The experimental evidence from the Neutral Beam Test Bed clearly showed that in the ion source used for the JET PINI the enhanced monatomic species yield was achieved at the expense of a non-umform ion density

- A Monte-Carlo model of the ion source was developed that successfully reproduced the observed features of the JET PINI ion source, including the ion density non-uniformity

- This model in conjunction with an experimental programme of source modification lead to the production of an ion source design with improved uniformity, without degrading the monatomic species yield

- 2 PINIs with the new ion source have been operated on one quadrant of the Octant 4 Neutral Injector for the May - August 2000 JET experimental campaign This quadrant shows a 33% reduction in box scraper power load compared to the PINIs used in the previous campaign This is estimated to give a 5-8 % mcrease in the neutral power injected from this quadrant into the JET Plasma Importantly the reduction in beamline power interception allows this quadrant to routinely inject at the limit of the electrical power supply

- Extrapolating this mcrease in transmission, and ability to routinely operate at the power supply limit, to all 4 quadrants gives an approximate 1 MW increase m the neutral power injected mto the JET plasma from Octant 4 at full power

- Current estimates for constructing a third positive ion Neutral Beam Injector for JET give a price of 2 8million € per MW of new neutral power A 1MW increase in power by reconfiguring the ion source to produce improved uniformity is thus a very cost-effective way of enhancing the power neutral power to JET

APPENDIX A

OPERATION OF THE MONTE CARLO MODELLING CODES

A1 PERMAG32.EXE - 3D MAGNETIC FIELD MAPPING CODE (D CIRIC)

This program calculates three components of the vector of the magnetic induction in the specified three-dimensional volume Current version supports only permanent magnets of rectangular cross section Magnets can be oriented arbitrarily and there are no requirements for any symmetry of the magnetic field structure There is no limit to the number of magnets or to the number of points in which the field is calculated - it is only limited by the memory of your system Take care that the RAM required to store e g 1 million points is 3 × 4 bytes × 10^6 points ~ 12 Mbytes To reduce round-off errors calculation is performed in 8 byte precision, but data storage is done in 4 byte precision

Magnetic configuration file

The first step in defining specific magnetic structure geometry is to choose appropriate reference Cartesian coordmate system (x, y, z) which should reflect the symmetry of the magnetic configuration - the logical choice is to use then beam axis as the z-axis of the system Once the reference frame is selected the position and orientation of each magnet is defined with respect to that coordinate system

Geometry of the magnetic structure is defined in the geometry file (default extension " MAG") This file is an ASCII file which can be created using any suitable text editor A freeware program "Programmer's File Editor" (*PFE32 EXE)* is copied to the application root directory during the installation and you can use that one to create configuration files The structure of a magnetic geometry file is shown in the table below

---

D Description of the magnetic field structure (up to 256 characters long)

P

X_C Y_C Z_C

A_{11} A_{12} A_{13} A_{21} A_{22} A_{23}

D_X D_Y D_Z B_R θ

The first line of the file can contain the description of the specific magnetic structure This line is recognised by the program by the letter "*D*" in the first column This description is used by several codes as the identifier of a specific magnetic structure geometry

The remaining lines contain definition parameters of permanent magnets Each permanent magnet is described by the group of four lines of text which contain the information on the position and the orientation of the magnet in the reference coordinate system and the dimensions, and remanent induction of the permanent magnet Blank lines can be used to separate individual magnets Blank lines are not allowed within the group of text lines defining one single magnet

- Each permanent magnet is recognised by letter "*P*" in the first column The remaining columns of this line of text can contain additional description of the magnet (used only for identification of the magnet and ignored by the program)
- The second line contains the coordinates of the centre of the permanent magnet in millimetres
- The third line defines the orientation of the permanent magnet in the reference coordinate system A_{ij} are the first six elements of the rotational matrix which uniquely define the orientation of the magnet in the three-dimensional reference frame (see Figure 1) A local Cartesian coordmate system (x', y', z') is associated to each permanent magnet, with z' axis being parallel to the easy axis of the magnet Elements of the rotational matrix are defined as

$$A_{11} = \cos\angle(x',x) \qquad A_{12} = \cos\angle(x',y) \qquad A_{13} = \cos\angle(x',z)$$
$$A_{21} = \cos\angle(y',x) \qquad A_{22} = \cos\angle(y',y) \qquad A_{23} = \cos\angle(y',z)$$
$$A_{31} = \cos\angle(z',x) \qquad A_{32} = \cos\angle(z',y) \qquad A_{33} = \cos\angle(z',z)$$

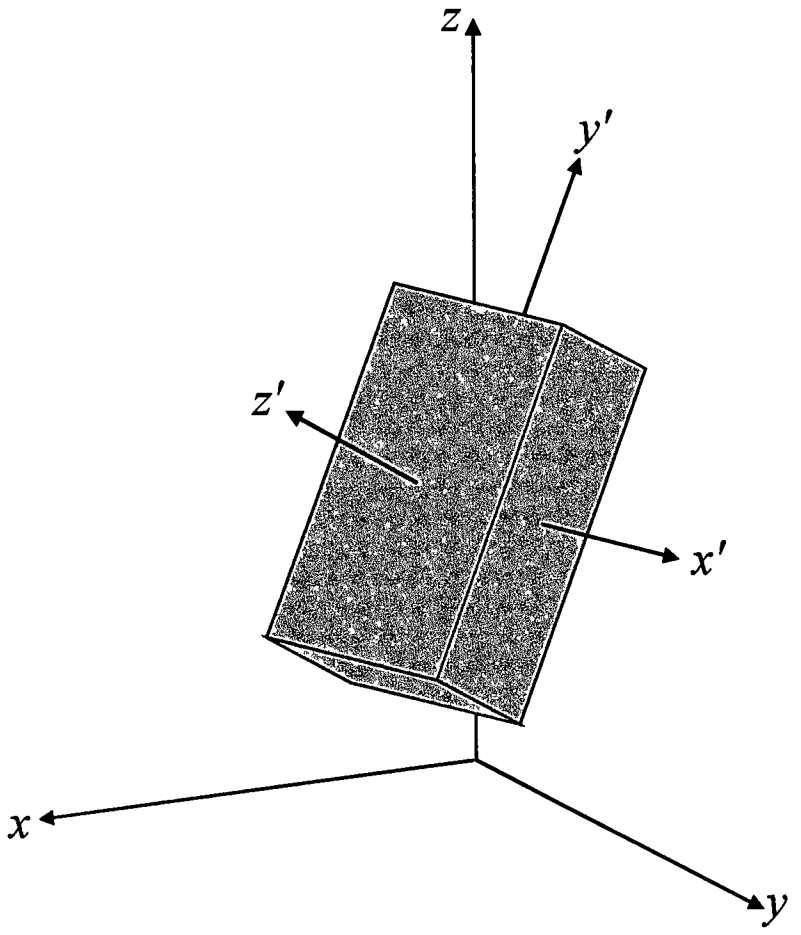

Figure A1 1 Permanent magnet orientation in the reference Cartesian coordinate system

- The fourth line defines the dimensions of the permanent magnet and its remanent induction D_X, D_Y and D_Z are the dimensions of the magnet (in millimetres) parallel to x', y' and z' axis of the magnet respectively B_R is the remanent induction of the magnet (in Teslas), and θ is the angle (in degrees) between the z' axis of the magnet and the vector $\boldsymbol{B}_R$ in the $x'z'$ plane In the current version of the program the inclined remanent induction vector is not supported and value θ must be zero! This means that the remanent induction vector is collinear with the z'-axis of the magnet

Very often a group of magnets will have the same size and/or orientation and you can create a complicated magnetic field structure by copying a group of lines defining one magnet and by

changing position coordinates and/or elements of the rotational matrix Bare in mind that the value B_R can be also negative and to create magnets with alternate orientation it is easier to change only the sign of B_R then the change the corresponding elements of the rotational matrix

Accurate value of the remanent mduction BR is required for accurate calculation of the magnetic field distribution Since this value is not always known, you can determine it experimentally m the following manner

a) Measure the B_z coinponent at several points along the z'- axis of the permanent magnet at distance two to three time larger than the dimensions of the magnet (to avoid huge field gradients) Precise alignment of the Hall probe is quite important in these measurements
b) Calculate the field along the z'-axis of the magnet by assuming 1 Tesla for the remanent mduction
c) The actual B_R value is the normalisation factor between measured and calculated values You can then repeat the measurement along some other axis of the magnet and compare it the calculated values

Using Permag32.exe

To create the three-dimensional field map for specific magnetic filed structure follow these steps

1) Open previously created magnetic structure file by clicking on the " " on the *Geometry* page
2) Type the boundaries of the of the volume (Xmin, Xmax,) and the increment between data points (DX,) All values should be given in millimetres To check the total number of points and estimated calculation time click on the "Check Region" command button When you run the program for the first time calculation time will be unknown Later on, the calculation time will be calculated from the total number of data pomts and total number of permanent magnets and the speed of your computer Be aware that even on very fast machines calculation might last many hours! Initially, use moderate size data sets (few planes only)
3) Select the output file name (default extension **MAP*) by clicking on the " " command button on the *Output* page, and type the description for the current session into the corresponding field Output map file is the binary file which contains the description of the

current session, number of data points along three axes, etc You can get information on the structure of this file by clicking on the "?" command button Volume boundaries in this file are in SI units (metres)

4) Choose the output file format by selecting the corresponding check box If you select binary option three files will be created They will have the same name as the map file and extensions *Bx*, *By* and *Bz* related to three different components of the magnetic field vector Magnetic induction is stored in SI units (Teslas) Information on the binary file structure can be obtained by clicking on the "?" command button If you select ASCII output file, this one will have the same name as the mapping file and the extension *TXT* You can select output units for the ASCII file ASCII file is a multiple column file containing x, y and z coodinates and components of the magnetic field vector Use ASCII format only for maps of moderate size (along the line, or within one plane) as this file can easily exceed 1 MByte

A2 XYZTRACE.EXE - PARTICLE TRAJECTORY SIMULATION

This program calculates the trajectories of given particles through a magnetic field map generated by the program permag32 exe (4 A1)

Step 1

The magnetic field map created by the 3D magnetic field mapping code must be loaded Click 'Open Magnetic Field Map' to start a dialogue box that allows the user to select the required * map file The files of the magnetic field components (* bx, * by and * bz) must be present m the same directory as the * map file

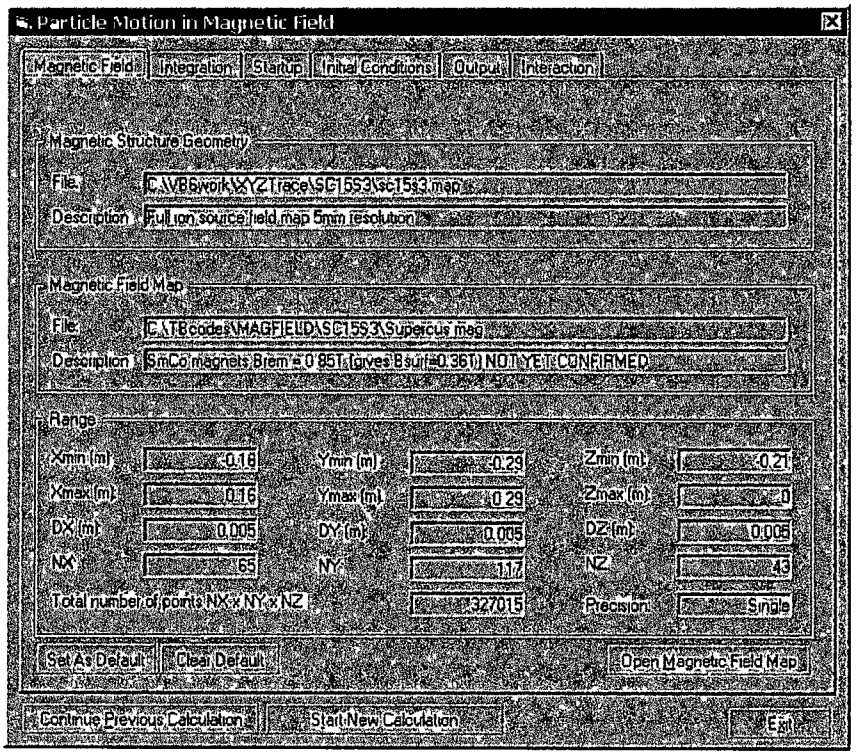

Figure A2 1 XYZTrace magnetic field map input tab

Step 2

The integration parameters for the model are given on the next tabbed page The boundary of the magnetic field map is used as the default for the model, the user can then specify different boundary walls or used the pre-programmed definition of the PINI ion source with the curved

end walls Trajectories that exceed the values of the boundary are deemed to have collided with the source wall and are terminated at that point The trajectory tracing is controlled by the 'Initialization parameters', the accuracy defines the maximum difference that is allowed between successive iterations of the stepwise controlled Runge-Kutta integration When the difference between successive iterations is below this value the trajectory is solved and the model continues to the next trajectory step The trajectory steps are controlled by the next two values that specify the initial trajectory step length, and the minimum, step length that the model is allowed to reduce to in order to solve the particle trajectory The maximum number of iterations that the integration routine can use to solve the trajectory is specified in the final value of this panel Careful choice of the trajectory solver 'Initialization parameters' can have a dramatic effect on the computational time required to model a particular trajectory In the case of small magnetic fields or low charge/mass ratio particles then largee trajectory step lengths, and a non-zero minimum trajectory step can be used to speed up the trajectory computation The trajectory calculation is terminated when the number of trajectory steps calculated, or the maximum path length values specified in the 'Termination Parameter' panel are exceeded These parameters are set to terminate trajectories that are not otherwise ended by interactions with the boundary walls or other particles Finally the Magnetic field can be trimmed to specify when zero magnetic field can be used - to speed up computational time in very low field regions, or where the field in one particular component is very low The integration parameter setting can be stored as the default setting for subsequent operations of the model

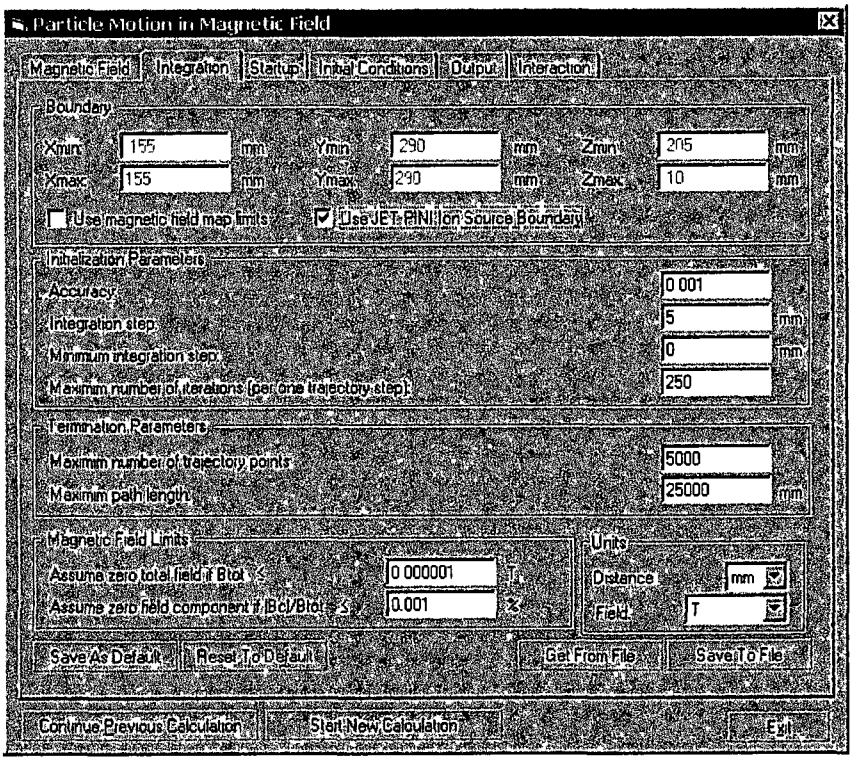

Figure A2 2 XYZTrace Integration parameter input tab

Step 3

The initial conditions for the trajectories are setup via this tab page, this is not necessary if an input dataset, * inp, has previously been calculated and stored (go to Step 4) A database is used to store the charge, mass and description of a range of particles generally used in these simulations A single reference number in the input dataset defines each particle The trajectory conditions are entered into the spreadsheet table by either typing directly, pasting from the clipboard or opening a tab delimited ASCCII file The input dataset must be in the form where the colmmn order is -

Particle ID, Xinitial, Yinitial, Zinitial, X'initial, Y'initial, Z'initial, Energy

Where the distance and energy units are defined on the page The particle directions are defined by the cosines of the initial trajectory angles with the direction of each of the Cartesian axes The input dataset is the converted into a common input format, by standardising the units and normalising the input cosines The user is requested to give a filename for the *.inp file that will be created from the input initial conditions

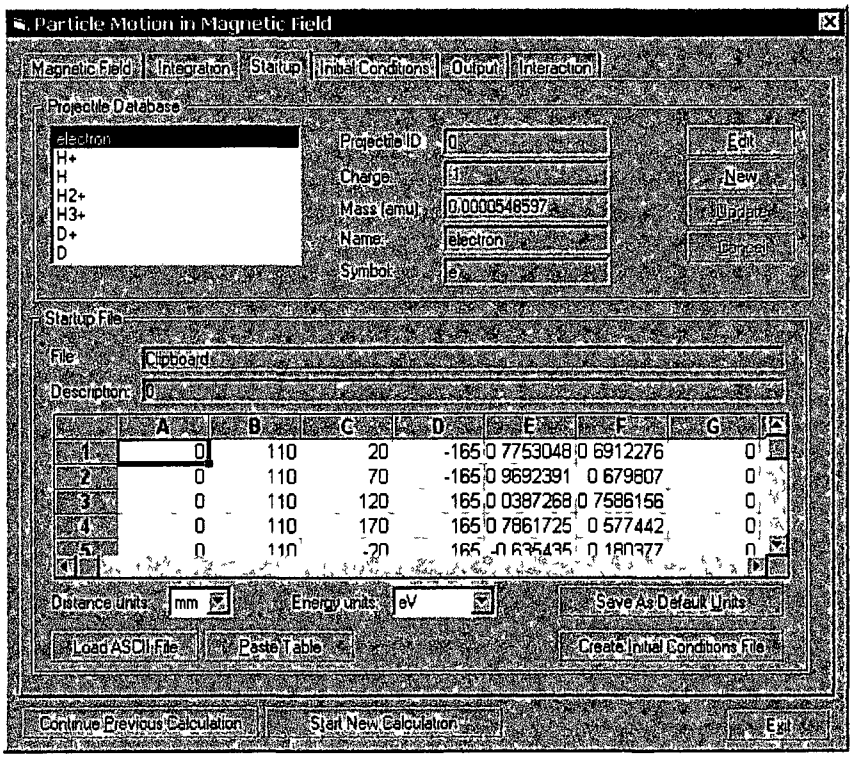

Figure A2 3 XYZTrace Startup parameter input tab

Step 4

An initial conditions input file, * inp, is opened via this tab page, either one previously created or one that has just been created from the previous data entry tab page A default input dataset can be defined for subsequent repeated opeartions of the simulation

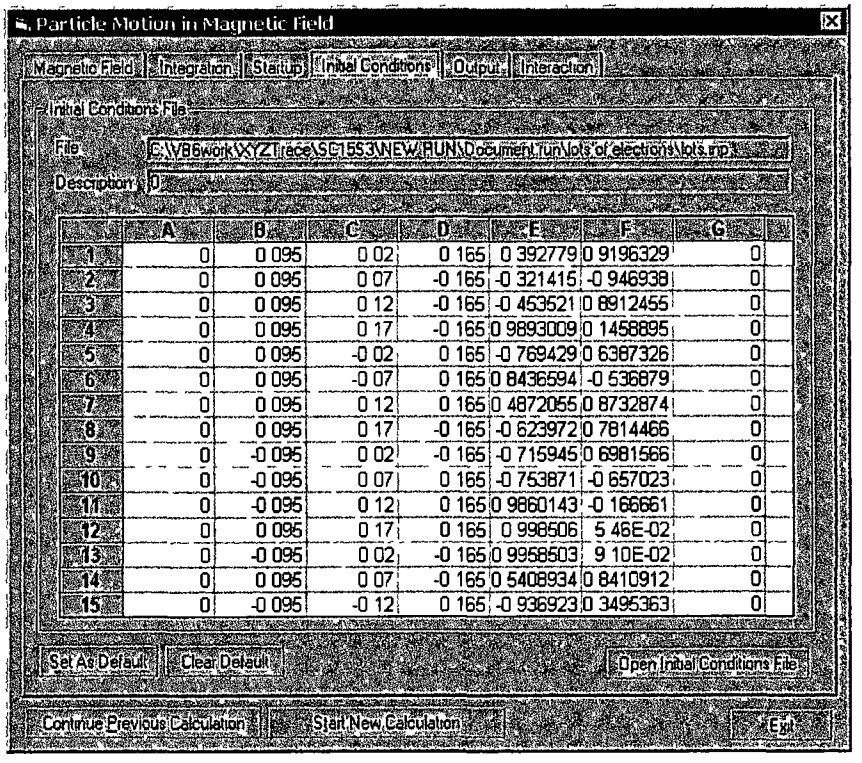

	A	B	C	D	E	F	G
1	0	0 095	0 02	0 165	0 392779	0 9196329	0
2	0	0 095	0 07	-0 165	-0 321415	-0 946938	0
3	0	0 095	0 12	-0 165	-0 453521	0 8912455	0
4	0	0 095	0 17	-0 165	0 9893009	0 1458895	0
5	0	0 095	-0 02	0 165	-0 769429	0 6387326	0
6	0	0 095	-0 07	0 165	0 8436594	-0 536879	0
7	0	0 095	0 12	0 165	0 4872055	0 8732874	0
8	0	0 095	0 17	-0 165	-0 623972	0 7814466	0
9	0	-0 095	0 02	-0 165	-0 715945	0 6981566	0
10	0	-0 095	0 07	0 165	-0 753871	-0 657023	0
11	0	-0 095	0 12	0 165	0 9860143	-0 166661	0
12	0	0 095	0 17	0 165	0 998506	5 46E-02	0
13	0	-0 095	0 02	-0 165	0 9958503	9 10E-02	0
14	0	0 095	0 07	-0 165	0 5408934	0 8410912	0
15	0	-0 095	-0 12	0 165	-0 936923	0 3495363	0

Figure A2 4 XYZTrace Initial Conditions file input tab

Step 5

The parameters to be used by the model for the particle interactions is the setup via the 'Interaction' tab page The Monte-Carlo model uses the interactions of electron and H_2^+ ions with the neutral source filling gas A pressure (in mtorr) and temperature (in K) define the neutral gas density, this method of entry is chosen to be more relevant to measured, or estimated, source gas conditions For each trajectory calculation the energy below which the trajectory will be terminated is given, so that once particles are below the energy range of interest the next particle trajectory can be started The energy loss of primary electrons with the 'background' plasma electrons through coulomb collisions is defined by giving the fraction of the source filling gas that is ionised, with the mean plasma electron temperature

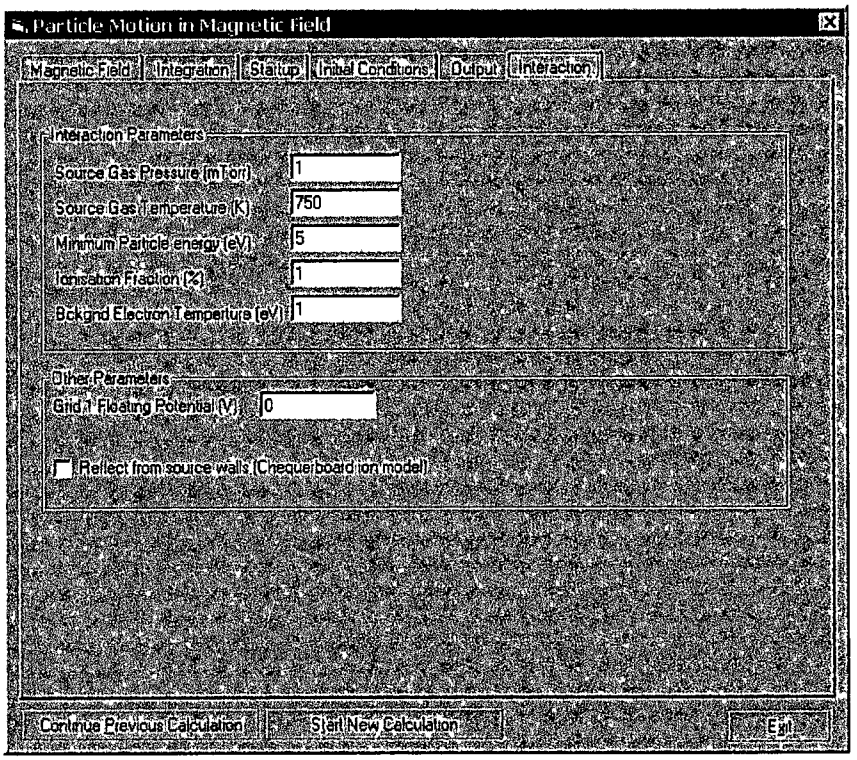

Figure A2 5 XYZTrace Interaction conditions input tab

Step 6

The parameters for the output of the trajectory simulation are given on the final tab page The program will write trajectory data at the initial and endpoint of each trajectory to the specified log file For particle interactions the interaction type and location is also written to the log file Optionally a binary file containing the full trajectory of each particle used in the model can be written, warning - this can be a very large file! The file of the trajectory endpoints only can also be created if required, although this information appears in the log file as well Finally the graphical display of the trajectories is setup on this page by specifying which two planes the trajectories should be plotted in, along with the refresh rate of the trajectory and text output To significantly speed up the computation of the trajectories the graphical output can be suppressed, if no longer required

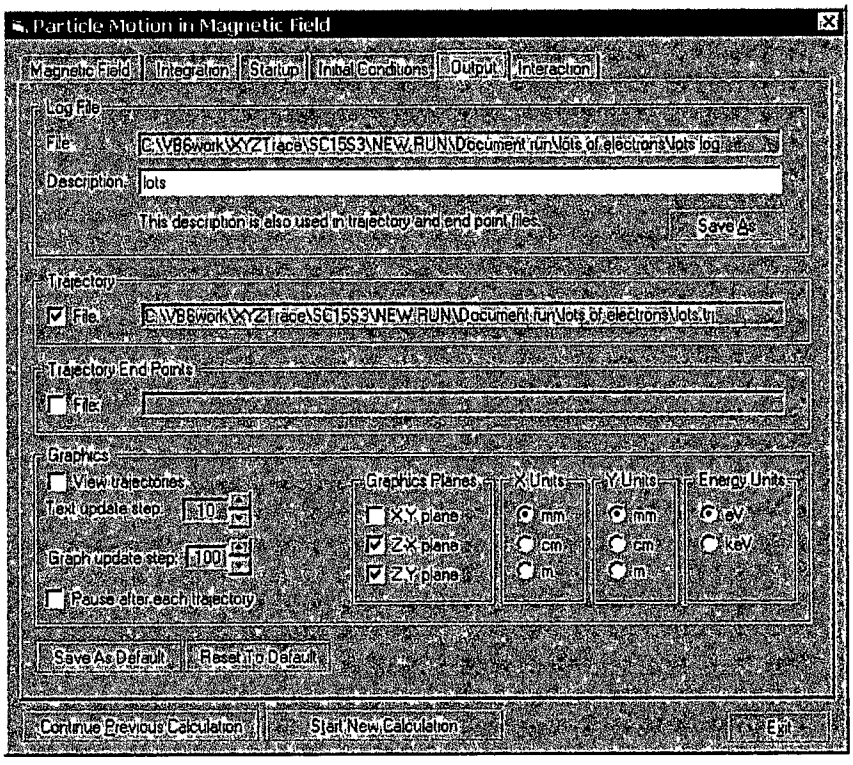

Figure A2 6 XYZTrace Trajectory output conditions tabbed page

Step 7

Once all the conditions for the operation of the trajectory and interaction calculations have been entered the model is started by pressing 'Start New Calculation' This launches the output display page and starts the trajectory simulation The 'Continue Previous Calculation' button is used to restart calculations that have been paused by the user This is done by pressing the Pause/Resume button on the output page and then exiting from the output page The user can view the trajectories as they are calculated and is given the information on the initial condition of each trajectory and the details of particle interactions or trajectory terminating conditions

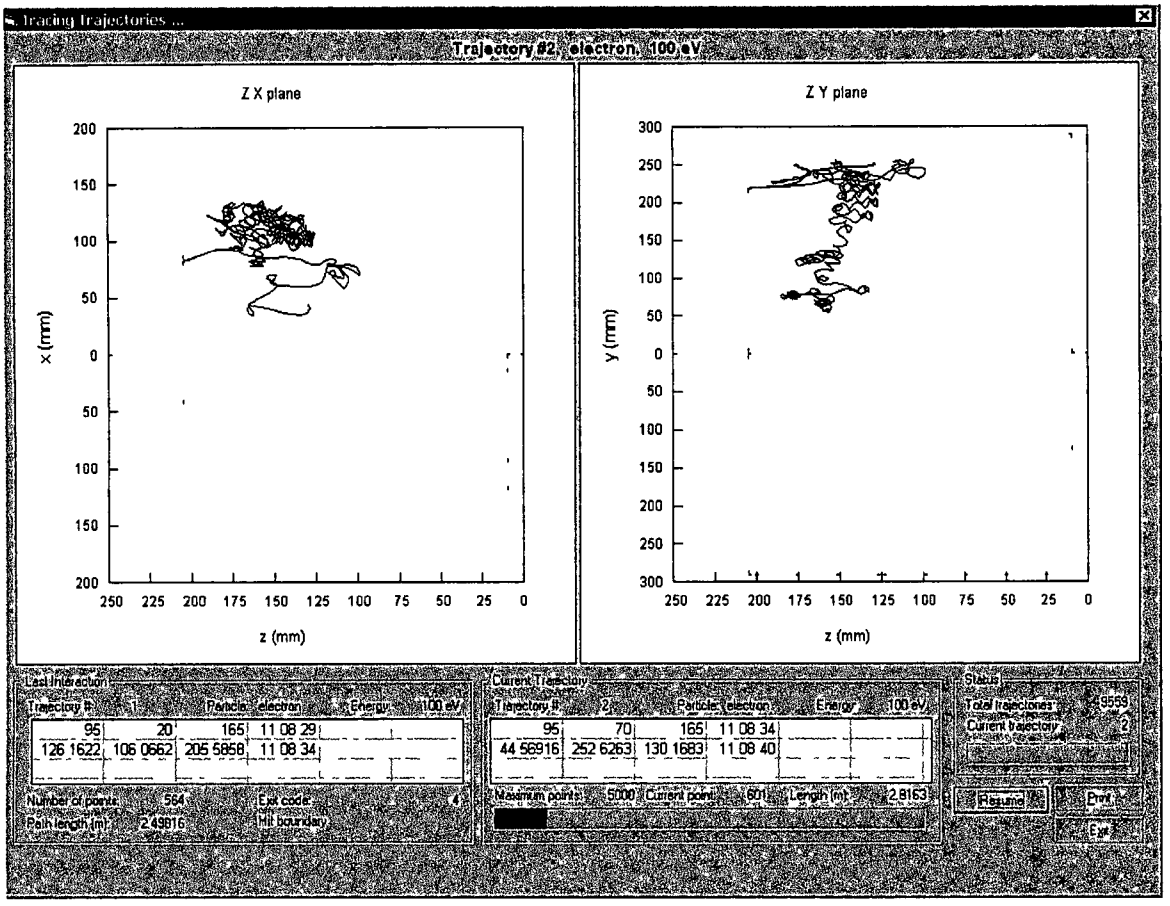

Figure A2 7 XYZTrace Trajectory display page

Analysis of XYZtrace output.

Generally the logfile is used to produce an analysis of the output from the model This is in a tab delimited ASCII format and is easily imported to a spreadsheet, such as Microsoft Excel for analysis The trajectory points can be identified by the exit code assigned to each trajectory, table 4 A2 1 For example selecting all trajectories with exit code 13 give the point where the electron ionisation of the H_2 source gas has occurred

Table 4 A2 1 Trajectory simulation exit codes

EXIT CODES	**0**	Initial condition
	1	Step too small
	2	Too many iterations
	3	Step too small
	4	Hit boundary
	5	Path too long
	6	Too many points
	9	Energy below threshold
	12	Elastic Collision (electron)
	13	Ionisation (electron)
	14	Dissociation (electron)
	22	H2+ Elastic
	23	H2+ Charge Exchange
	24	H2+ Dissociation
	25	H2+ to H3+

The file containing all trajectories can be used to calculate the density of particle trajectories crossing a given measurement plane by using the program trajdecode exe

REFERENCES

[1] Wesson J, Tokakmaks 2nd Edition, 1997, Oxford University Press

[2] Green T S, Reports on Progress in Physics, 1974, 37, 1257-1344

[3] Pamela J, 1995, Plasma Phys Control Fusion, 37, A325-A336

[4] Kuriyama M et al 1999, 18th Symposium on Fusion Engineering, Albuquerque, NM, 133

[5] Kuriyama M et al 1998, Proceedings of the 19th Symposium on Fusion Technology, Marseille, France, 391

[6] Stork D, 1990, Proceedings of the 16th Symposium on Fusion Technology, London, UK

[7] Duesing G, Altmann H, Falter H-D, Goede A, Haange R, Hemsworth R S, Kupschus P, Stork D and Thompson E, 1987, Fusion Technology, 11,163

[8] Jones TTC et al , 1999, Fusion Engineering and Design ,47, 205}

[9] Keilhacker M, 1999, Fusion Engineering and Design, 46, 273

[10] Holmes A J T, Green T S and Newman A F, 1987, Rev Sci Instrum 58,1369

[11] Holmes A J T, Green T S, Martin A R, Hemsworth R S and Thompson E, 4th Symposium on heating in Toroidal plasmas, 1984, Rome, 1065

[12] Ehlers K W and Leung K N, 1982, Rev Sci Instrum , 52, 1452-1456

[13] Green T et al, 1984, Proceedings of the 13th Symposium on Fusion Technology, Varese, Italy, 693

[14] Green T S, Coupland J R, Hammond D P, Holmes A J T, Martin A R, Hemsworth R S and Thompson E, 1984, 10th Int Conf On Plasma Phys And Contr Nucl Fus Res , (IAEA-CN-44/H-I-5) Vol 3, 319

[15] Falter H-D et al, 1984, Proceedings of the 13th Symposium on Fusion Technology, Varese, Italy, 571

[16] Ciric D, Falter H-D, Fanthome J G A, Massmann P and Mellon K N, 1994, Proceedmgs of the 18th Symposium on Fusion Technology, Karlsruhe, 827

[17] Ciric D, Falter H-D and Godden D J, 1998, Proceedings of the 20th Symposium on Fusion Technology, Marseille, France, 469

[18] Cottrell G A, 1984, Rev Sci Instrum 55(9) 1401

[19] Martin A R, 1984 Vacuum (34), 17

[20] Godden D J, JDC 1/96, JET, May 1996

[21] Coupland J R and Green T S, Nuclear Instruments and Methods 125, 1975, 197

[22] Spàdtke P, KOBRA3-INP, Extended-DOS Versıon 3 35, INP, Wıesbaden

[23] Godden D J, JET-DN-C(97)140, Beam Focusıng ın the JET PINIs (ıncludıng upgraded scenarıos), NB Internal Dıvısional note, 1997

[24] Holmes A J T and Thompson E, Rev Scı Instr 1981 52 172

[25] Martın D, Watson M J and Meuhleısen M, Proceedıngs of the 18th Symposıum on Fusıon Engıneerıng, 1999, Albuquerque, NM, 253}

[26] Ido S, Hasebe H and Fujıta Y, 1993, Jpn J Appl Phys Vol 32, 4761

[27] Ido S and Hasebe H, 1994, Jpn J Appl Phys Vol 33, L380

[28] Kashıwagı M and Ido S, 1998, Rev Scı Instrum ,69,2,1117

[29] Holmes A J T, 1981,Rev Scı Instrum 52(12) 1814

[30] Smıth K and Glasser A H, 1989, Computer Physıcs Communıcatıons, 54, 391

[31] Rudd M E, Hollman K W, Lewıs J K, Johnson D L, Porter R R

[32] Fagerquıst E L, 1993, Phys Rev A, 47, 3, 1866

[33] Huba J D, 1998, NRL Plasma Formulary

[34] Anders A, A Formulary for Plasma Physıcs, 1990, Akademıe-Verlag, Berlm

[35] Chan C F, Burrell C F, Cooper W S, 1983, J Appl Phys 54(11), 6119

[36] Goede A P H, Green T S, Martın A R, Mosson G A G and Sıngh B, Int Symp Heatıng Tor Plasmas, 1978, Grenoble, 77

[37] Hemsworth R S, JET-DN-C(85)3, Internal Dıvısional Report

[38] Data obtaıned from copıes of the logbooks of the PINI ıon source development tests on the F4/G23 facılıty at Culham, Feb 1984

[39] Horıike H et al, Phys Fluıds 30 (10), October 1987, 3268

[40] Okumura Y et al, Rev Scı Instrum, 55 1, 1984

[41] Martın D, Watson M J and Meuhleısen M, Proceedıngs of the 18th Symposıum on Fusıon Engıneerıng, 1999, Albuquerque, NM, 253

[42] Hughes D A, McLachlan R C, Mıtchell N A, 1988, 15th Symposıum on Fusıon Technology, Utrecht, The Netherlands, 568

[43] Uhlemann R, Phys Plasmas 2 (6), June 1995, 2141